Synthesis and self-assembly of plasmonic nanoparticles

Jieli Lyu

université
PARIS-SACLAY

Synthesis and self-assembly of plasmonic nanoparticles

Synthèse et auto-assemblage de nanoparticules plasmoniques

Thèse de doctorat de l'université Paris-Saclay

École doctorale n°564, Physique en Ile-de-France (PIF)
Spécialité de doctorat : Physique
Graduate School : Physique. Référent : Faculté des sciences d'Orsay

Thèse préparée dans l'unité de recherche **Laboratoire de Physique des Solides** (Université Paris-Saclay, CNRS), sous la direction de **Doru CONSTANTIN**, Directeur de recherche, la co-direction de **Cyrille HAMON**, Chargé de recherche, et le co-encadrement de **Marianne IMPÉROR-CLERC**, Directrice de recherche

Thèse soutenue à Paris-Saclay, le 5 Juillet 2022, par

Jieli LYU

Composition du Jury

Emmanuelle LACAZE Directrice de recherche, Sorbonne Université, Institut des NanoSciences de Paris	Présidente
Mona TRÉGUER-DELAPIERRE Professeure, Université de Bordeaux, Institut de Chimie de la Matière Condensée	Rapporteure & Examinatrice
Guillaume BROTONS Maître de conférences (HDR), Université du Maine, Laboratoire de Physique de l'Etat Condensé	Rapporteur & Examinateur
Brigitte PANSU Professeure, Université Paris-Saclay, Laboratoire de Physique des Solides	Examinatrice
Jorge PÉREZ-JUSTE Professeur, CINBIO, Université de Vigo, Département de chimie physique	Examinateur
Doru CONSTANTIN Directeur de recherche (HDR), Université de Strasbourg, Institut Charles Sadron	Directeur de thèse

THÈSE DE DOCTORAT

NNT : 2022UPASP071

université PARIS-SACLAY | ÉCOLE DOCTORALE Physique en l'Île-de-France (PIF)

Titre : Synthèse et auto-assemblage de nanoparticules plasmoniques

Mots-clés: nanoparticules plasmoniques, auto-assemblage, remodelage, génération de seconde harmonique, diffusion des rayons X aux petits angles, spectroscopie d'absorption.

Résumé: Les nanoparticules (NPs) de métaux nobles (par ex. l'or ou l'argent) ont attiré beaucoup d'attention par leurs propriétés optiques fascinantes, comme des résonances de plasmon de surface. Ces propriétés optiques dépendent fortement de la morphologie des NPs, ainsi que de la distance entre les particules et de l'environnement local. En particulier, la mise en forme de NPs distinctes dans des nanostructures assemblées rend possible le couplage entre les plasmons des particules individuelles et l'émergence de propriétés collectives. Le travail présenté dans cette thèse peut être divisé en quatre parties.

Dans la première partie, la croissance hétéro-épitaxiale d'argent sur des nanosphères et des bipyramides d'or a été étudiée en détail par plusieurs techniques comme la microscopie électronique environnementale (LCTEM), la diffusion des rayons X aux petits angles (SAXS) et la spectroscopie d'absorption (AS). Parmi les faits marquants, nous avons montré que l'acide ascorbique (AA) a un effet thermodynamique (en stabilisant les facettes {100}) et joue ainsi un double rôle (dans la réduction du précurseur et dans la définition de la forme des nano-objets) en présence de CTAC.

Nous avons révélé le mécanisme de remodelage de nanotétrapodes d'or (GNTPs) par AS, LCTEM, et SAXS dans la deuxième partie. La cinétique de remodelage est contrôlée par la température, la présence ou l'absence d'un environnement liquide, et par l'ajout d'ions iodure, alors que des GNTPs recouverts d'argent sont très stables. Nous avons aussi exploré la génération de seconde harmonique par des solutions de GNTPs à symétrie tétraédrique. Alors que le réseau cristallin de l'or est centrosymétrique, la forme des particules ne l'est pas, ce qui confère à la première hyper-polarisabilité une symétrie presque parfaitement octupolaire. En laissant les GNTPs évoluer vers des sphères, nous montrons que leur réponse non-linéaire est contrôlée par leur morphologie. Ces résultats ouvrent la voie vers de nouveaux types de plateformes plasmoniques non-linéaires et de marqueurs pour l'imagerie.

Dans la troisième partie, nous avons suivi la cinétique d'assemblage de GNPs recouvertes de tensioactif dans des chaînes unidimensionnelles en présence d'ions sulfate. Leur évolution en deux étapes a pu être élucidée uniquement en combinant AS et SAXS. Qui plus est, il y a des différences significatives en termes de rendement et de constante de réaction entre des sphères, des bâtonnets et des bipyramides, mettant en valeur l'influence de la courbure de surface sur la formation de contacts. En outre, le processus d'auto-assemblage a pu être arrêté à tout moment par l'ajout de tensioactif en excès au milieu de réaction. Au niveau du contact, l'interaction est forte et très directionnelle, comme on a pu le prouver par LCTEM. De plus, on peut cibler avec précision les « points chauds » des chaînes plasmoniques et déposer un deuxième métal à ces endroits. Nous avons suivi la formation des chaînes et la déposition du deuxième métal (argent ou palladium) par AS, et nous avons résolu les propriétés plasmoniques à la nano-échelle en utilisant la technique EELS.

Finalement, nous avons obtenu des supracristaux (SCs) tridimensionnels bien ordonnés de bipyramides pentagonales d'or (GBPs). En combinant SAXS, tomographie FIB-SEM et simulations Monte Carlo (MC), nous avons prouvé que les SCs ont une symétrie triclinique, avec deux particules par maille et une densité de 0,835. De surcroît, la réponse optique des SCs dépend de l'orientation des facettes : les surfaces "à pointes" et "lisses" ont respectivement des rendements SERS élevés et réduits. Ce résultat ouvre la perspective de la détection sélective d'analytes très dilués.

université PARIS-SACLAY | ÉCOLE DOCTORALE Physique en l'Île-de-France (PIF)

Title: Synthesis and self-assembly of plasmonic nanoparticles

Keywords: plasmonic nanoparticles, self-assembly, reshaping, second harmonic generation, small-angle X-ray scattering, absorption spectroscopy

Abstract: Noble metal (e.g. gold or silver) nanoparticles (NPs) have been attracting considerable attention because of their fascinating optical properties such as localized surface plasmon resonances. These optical properties are strongly dependent on the NPs' morphology as well as on the interparticle distance and the local environment. In particular, integrating discrete NPs into assembled nanostructures enables interparticle plasmon coupling, thereby generating new collective properties. The work described in this thesis can be separated into four parts.

In the first part, the heteroepitaxial growth of silver on gold nanospheres and bipyramids was studied in detail using techniques such as liquid-cell transmission electron microscopy (LCTEM), UV-Vis-NIR absorption spectroscopy (AS) and small-angle X-ray scattering (SAXS). We revealed that ascorbic acid (AA) has a thermodynamic effect (by stabilizing the {100} facets) and thus plays a double role (i.e. both reducing and shape-directing agent) in the presence of CTAC.

The reshaping mechanism of gold nanotetrapods (GNTPs) is demonstrated by AS, LCTEM, and SAXS in the second part. The reshaping kinetics is controlled by the temperature, the presence/absence of a liquid environment, and the addition of iodine, while GNTPs coated with silver are shown to be very stable. We also explored the second harmonic scattering response from colloidal GNTPs with tetrahedral symmetry. While the crystal lattice of gold is centrosymmetric, the particle shape is not, conferring to the first hyperpolarizability an almost purely octupolar symmetry. By reshaping the GNTPs into spheres, we show that their nonlinear response is controlled by the morphology. These results open the way for new kinds of nonlinear plasmonic platforms and imaging probes.

In the third part, the assembly kinetics of surfactant-stabilized GNPs into one-dimensional chains in the presence of sulfate ions was investigated. Their two-step evolution could only be revealed by combining AS with SAXS. Moreover, there are marked differences in reaction yield and rate constant between spheres, rods, and bipyramids, highlighting the role of surface curvature in contact formation. In addition, the self-assembly process can be stopped at any stage by adding an excess surfactant to the reaction mixture. The contact interaction is strong and highly directional, as shown by LCTEM. Furthermore, the "hot spots" in the plasmonic chains could be precisely targeted and a second metal deposited at their location. We followed the chain formation and the deposition of the second metal (i.e. silver or palladium) via AS, and the plasmonic properties could be mapped at the nanoscale using electron energy loss spectroscopy (EELS).

In the end, we obtained well-ordered three-dimensional supercrystals (SCs) of pentagonal gold bipyramids (GBPs). Combining SAXS, focused ion beam-scanning electron microscopy (FIB-SEM) tomography analysis and Monte Carlo (MC) computer simulations, we proved that the SCs have a triclinic symmetry, with two particles per unit cell and a packing fraction of 0.835. Moreover, the SCs exhibit a facet-dependent optical response, with spiky and smooth facets displaying respectively high and low SERS efficiency. This result opens the perspective of selectively detecting trace-level analytes.

Résumé en français

Par rapport aux métaux en volume, les nanoparticules (NPs) de métaux nobles (par exemple, l'or ou l'argent) ont attiré une attention considérable en raison de leurs propriétés optiques fascinantes, telles que les résonances localisées des plasmons de surface. Ces propriétés optiques dépendent fortement de la morphologie des NPs, ainsi que de la distance interparticules et de l'environnement local. En particulier, l'intégration de NP discrètes dans des nanostructures assemblées permet le couplage des plasmons individuels, générant ainsi un champ électromagnétique plus fort dans les espaces interparticules, appelés « points chauds », engendrant de nouvelles propriétés collectives. Par exemple, ces points chauds peuvent grandement améliorer l'intensité vibratoire des molécules présentes à la surface des NPs d'or. La polarisabilité des molécules est affectée en raison du fort champ électrique, de sorte que nous pouvons augmenter l'intensité de la diffusion Raman de plusieurs ordres de grandeur, un effet appelé « diffusion Raman exaltée en surface » (SERS).

Par conséquent, la morphologie des NPs influe sur leurs propriétés et leurs applications. Il est assez intéressant de travailler et de comprendre la fabrication de NPs avec un bon contrôle de la taille et de la forme. Dans notre travail, plusieurs types de NPs d'or ont d'abord été préparés par la méthode de croissance germée impliquant deux étapes distinctes : la nucléation et la croissance. Nous utilisons d'abord un agent réducteur très puissant (borohydrure de sodium) pour réduire rapidement le chlorure d'or en très petites graines d'or. En utilisant des graines monocristallines, nous pouvons obtenir des nanosphères d'or (GNS), des nanotiges d'or (GNR) et des nanotétrapodes d'or (GNTP) en utilisant différents additifs. Les GNTP branchés à longs bras peuvent être cinétiquement contrôlés et obtenus en quelques minutes en augmentant le pouvoir réducteur de l'acide ascorbique (AA) à pH élevé. La cristallinité des graines influencera également la morphologie finale des NP, car une polycristallinité de la graine fournit suffisamment d'anisotropie pour briser la symétrie des particules pendant la croissance. Par exemple, des bipyramides d'or pentagonales sont préparées à partir de graines penta-maclées. En plus des produits chimiques et des protocoles de synthèse, je présente également les principales techniques de caractérisation physique au chapitre 2. En particulier, la diffusion des rayons X aux petits angles (SAXS) est une technique de caractérisation très puissante, qui peut fournir des informations non seulement sur la

forme et la taille des NPs isolées en solution, mais aussi sur la structure des NPs agrégées.

Par rapport aux NPs homogènes, les NPs cœur-coque sont prometteuses pour la fabrication et la réalisation de nouvelles fonctionnalités en introduisant d'autres composants, avec par ex. des propriétés semi-conductrices ou magnétiques. Le contrôle fin de la forme des NPs cœur-coque peut également être utilisé pour ajuster leurs propriétés optiques. Cependant, bien que les états initiaux et finaux des NPs cœur-coque aient été bien étudiés, leurs états intermédiaires sont encore inconnus. Ainsi, nous avons étudié la croissance d'une coque d'argent sur un cœur d'or au chapitre 3. Premièrement, la croissance de nanosphères d'or enrobées d'argent a été étudiée à l'aide de quatre techniques complémentaires ex-situ. L'estimation de la morphologie et de la concentration en particules des solutions obtenues nécessite une analyse fine du SAXS enregistré pour des solutions ayant un rapport molaire croissant d'argent sur or (K = Ag/Au, estimé lors de la synthèse et en accord avec l'analyse chimique *a posteriori*). De manière remarquable, les populations de particules ont une excellente monodispersité *p* (entre 5 et 10%) mesurée par SAXS et TEM et confirmée par l'accord entre l'épaisseur de coque calculée et prédite. L'analyse des images TEM montre une transition entre des formes quasi-sphériques et cubiques entre K = 1, 4 et 2, alors que la qualité des ajustements SAXS trouve la transition vers K = 2: les deux techniques sont en très bon accord! Les valeurs de la concentration en particules *n* obtenues par trois techniques sont en bon accord (à 40 % près de leur moyenne), à l'exception de quelques points SAXS de faible valeur. La différence systématique entre les techniques est inférieure à l'écart des valeurs pour chaque technique, soulignant l'importance d'utiliser des protocoles d'échantillonnage soigneux : agitation des échantillons pour assurer l'homogénéité et éviter l'apparition de gradients de concentration, contrôle de la température pour éviter la cristallisation des tensioactifs, peser des aliquots plutôt que s'appuyer sur les volumes de pipetage (qui ne sont pas toujours précis pour les solutions de tensioactifs). Parmi les quatre méthodes utilisées, la SAXS donne le plus d'informations sur les particules : la taille, la polydispersité, la forme et la concentration sont déterminées avec précision, comme le montre un très bon accord avec les autres techniques. Ce résultat valide l'utilisation de SAXS pour l'étude de nano-objets complexes (bimétalliques et asphériques), en statique ou au cours de leur croissance. Cependant, les particules doivent être raisonnablement monodisperses pour profiter

pleinement de cette technique. Bien sûr, les méthodes de diffusion ne donnent que des informations indirectes et les techniques d'imagerie restent essentielles pour identifier les formes des particules et choisir le modèle approprié: la TEM doit donc toujours être utilisée en complément. Dans la deuxième partie, nous avons discuté des aspects cinétiques de la croissance de l'argent sur les bipyramides d'or. Nos investigations LCTEM confirment le rôle directeur de l'AA dans la croissance de l'argent sur l'or. Communément décrit comme un agent réducteur doux, nous démontrons ici que l'AA, combiné à des ions halogénures, est également un agent de direction de forme qui favorise la formation de NRs en arrêtant la croissance cristalline le long des directions ⟨001⟩. Plus généralement, le travail présent montre que de telles études multimodales in situ permettent de mieux appréhender les mécanismes de croissance des nanomatériaux. Premièrement, corroborer les investigations à grande échelle et à l'échelle nanométrique nous permet de contourner les limitations inhérentes et les artefacts associés à chaque technique. Deuxièmement, cette approche permet de déterminer si la croissance cristalline est sous contrôle cinétique ou thermodynamique et, enfin, elle fournit un moyen d'identifier le rôle individuel des produits chimiques dans les mécanismes de croissance, aidant notre compréhension de la synthèse des nanomatériaux.

Les nanotétrapodes d'or (GNTP) avec des bras pointus proéminents et régulièrement espacés ont attiré notre attention, car leur taille et leur homogénéité de structure les distinguent des nanoétoiles d'or étroitement apparentées. Les GNTP sont généralement instables et ont tendance à se remodeler en d'autres morphologies à température ambiante, modifiant ainsi leurs propriétés plasmoniques. Par conséquent, nous avons exploré les processus physico-chimiques qui régissent la stabilité des GNTP au chapitre 4. Ce processus de remodelage des GNTP est fortement lié aux températures, à la présence/ou à l'absence d'un solvant et à l'ajout éventuel d'iodure. À savoir, le processus de remodelage est plus rapide à température élevée. De plus, le remodelage des GNTP se produit également à l'état sec (suggérant un mécanisme de migration des atomes), mais la cinétique est beaucoup plus lente que celle en solution. Le taux de remodelage augmente considérablement lors de l'ajout d'iodure, indiquant que l'évolution de la déformation de la forme est bien liée à la présence de divers solutés, confirmant le mécanisme de dissolution et redéposition. Une caractéristique intéressante est que le processus de remodelage peut être bloqué avec une fine couche d'argent (Ag/Au = 0.2)

à toute étape de l'évolution. De cette manière, la morphologie des GNTPs peut être parfaitement stabilisée, empêchant également l'évolution des propriétés optiques. De plus, les GNTP recouverts d'argent sont très stables à température ambiante pendant 2 mois, ainsi que pendant quelques heures à 70°C. Cette stabilisation à long terme nous permet de consacrer la deuxième partie de ce chapitre aux mesures optiques par une approche d'optique non linéaire. Les GNTP présentent une forte génération de seconde harmonique (SHG), essentiellement due à leur forme (et donc avec la même symétrie octupolaire que les objets eux-mêmes) et qui diminue à mesure qu'ils se reforment en sphères, atteignant un plateau dont l'origine est due à des défauts de surface. Initialement, le retard est faible et la réponse SHG est dominée par la non-centrosymétrie de forme. Au fur et à mesure que les GNTPs évoluent vers des sphères, cette source s'affaiblit et se complète par une origine due au retard. La longueur des bras (et donc le spectre d'extinction) des GNTPs peut être réglée sur une large plage, ce qui est très intéressant du point de vue des applications. Par exemple, on pourrait placer soit la valeur maximale (le pic) soit la pente la plus raide de la bande longitudinale de plasmon à la fréquence d'excitation pour une efficacité ou une sensibilité maximales, respectivement. La présence de deux bandes plasmon ouvre la voie vers des systèmes à double résonance, où les fréquences fondamentale et harmonique coïncident respectivement avec les bandes longitudinale et transversale. Des applications possibles à l'imagerie non-linéaire peuvent également être envisagées, puisque le signal SHG est spectralement pur et cohérent, contrairement à la luminescence à deux photons, par exemple. Ces avantages ont déjà incité l'utilisation de matériaux ferroélectriques (par exemple le $BaTiO_3$) comme sondes de microscopie. Les nanoparticules d'or ont l'avantage supplémentaire d'une chimie de surface très polyvalente, ce qui les rend adaptables à pratiquement tous les milieux d'intérêt (biologiques ou autres).

Dans le chapitre 5, la cinétique d'assemblage des GNP stabilisés par un tensioactif en chaînes unidimensionnelles en présence d'ions sulfate a été étudiée. Leur évolution en deux étapes n'a pu être révélée qu'en combinant l'AS avec du SAXS. Le processus d'assemblage des GNPs est induit en diminuant la concentration de CTAB bien en dessous de la CMC : immédiatement (quelques minutes, au plus) après cette étape, de gros objets sont présents dans la solution, comme le révèle l'augmentation du signal SAXS aux petits angles. À ce stade, l'AS est toujours inchangée, car les distances interparticules sont supérieures à quelques nm, vraisemblablement imposées par les

bicouches de tensioactifs qui les recouvrent. Les chaînes, si elles sont présentes, n'ont pas un espacement bien défini (nous n'observons aucun pic dans les données SAXS). De plus, il existe des différences marquées dans le rendement de la réaction et la constante de réaction entre les sphères, les tiges et les bipyramides, soulignant le rôle de la courbure de surface dans la formation de contacts. De plus, le processus d'auto-assemblage peut être arrêté à tout moment en ajoutant un excès de tensioactif au milieu de réaction. Divers oligomères aux propriétés optiques définies ont ainsi été stabilisés pendant une longue période (au moins 15 jours). Les assemblages sont très stables sous dialyse, et l'interaction entre particules est assez forte, tel que montré par la LCTEM. Après traitement des données AS en utilisant la méthode SVD, l'assemblage peut être simplement décrit comme la conversion de l'espèce initiale (particules isolées) vers l'espèce finale (chaînes), avec une cinétique apparemment du premier ordre. Cette conclusion vaut très bien pour les bâtonnets et les sphères, mais pas pour les bipyramides, où l'évolution est plus compliquée, à la fois en termes de nombre d'espèces impliquées et d'évolution temporelle. Nous avons postulé qu'une telle évolution en deux étapes, qui ne peut être découverte qu'en combinant l'AS avec une technique structurelle (par exemple SAXS), peut aussi avoir lieu dans d'autres processus présentant une cinétique apparemment du premier ordre, par exemple lorsque des NP d'or s'assemblent en raison de l'induction d'un dipôle électrique à leur surface. De plus, nous pouvons ajuster le décalage de la bande plasmon vers la gamme de l'infrarouge moyen et générer avec précision les « points chauds » dans les assemblages de NP en concevant des jonctions conductrices utilisant divers métaux. Des catalyseurs tels que le palladium et le platine peuvent également être déposés aux « points chauds ». Bien que la réponse plasmonique soit amortie, une telle configuration est idéale pour la photocatalyse car des porteurs de charge chauds seraient générés au voisinage du catalyseur. De même, notre méthode pourrait être appliquée pour déposer des matériaux semi-conducteurs à l'emplacement des points chauds pour former des doubles barrières Schottky. Dans l'ensemble, cette méthode de préparation est simple et évolutive et donne des nanostructures à rapport d'aspect élevé avec des propriétés optiques qui peuvent être adaptées sur une très large gamme spectrale, du visible à l'infrarouge moyen. Nous pensons que ce travail constitue un saut en avant pour toutes les applications plasmoniques qui peuvent bénéficier de la conception précise des « points chauds » dans les polymères plasmoniques.

Enfin, nous avons obtenu des supracristaux (SC) tridimensionnels bien ordonnés de bipyramides d'or pentagonales (GBP). En combinant le SAXS, l'analyse par tomographie par microscopie électronique à faisceau ionique focalisé et les simulations Monte Carlo, nous avons prouvé que les SC ont une symétrie triclinique, avec deux particules par maille et une fraction de volume de 0.835. De plus, les SC présentent une réponse optique dépendante des facettes, avec des facettes pointues et lisses affichant respectivement une efficacité SERS élevée et faible. Ce résultat ouvre la perspective d'une détection sélective d'analytes à l'état de trace.

Dans l'ensemble, les travaux de recherche élaborés dans cette thèse ont porté sur divers aspects concernant le contrôle synthétique de la taille, de la forme et de la composition des nanoparticules, ainsi que sur la conception de nanostructures auto-assemblées avec des applications prometteuses telles que la diffusion Raman exaltée en surface.

Acknowledgments

Writing here indicates that my doctoral journey is really coming to an end. Incredibly, I spent four years at Orsay, France, and got my Ph.D. During the four years of winter and summer, no matter the joys or sorrows, all the experiences are gifts to me, and all the encounters are treasures to me. I have been fortunate enough to meet many lovely people on this journey, and without their tireless guidance, help, and support, it would not be possible for me to present this thesis to you. I'm not very expressive, but at this moment, I would like to take this opportunity to express my sincere gratitude to all of you.

First and foremost, I would like to give my sincerest thanks to my supervisor, **Doru Constantin**, the director of my thesis. You picked me up at the bure station, helped me with my accommodation, familiarized me with the lab route, drove me to the supermarket, and prepared a lot of daily necessities with your family for me as if it happened yesterday. In the past few years, whether in life or in scientific research, you have always been so patient to help me solve many problems. Especially in experimental details, data processing, and analysis, you always provided me with a lot of ideas, which broadened my in-depth understanding of my subject. In addition, I learned from you how to organize laboratory notebooks, how to classify experimental data and samples, how to better show my work to others and how to make a detailed plan, etc. These good scientific literacies will benefit me for a lifetime. You are not only my scientific supervisor but also my mentor. You have given me a lot of guidance on my scientific path and future career plans, and I am grateful for the endless encouragement you have been giving me in whatever I want to do. Your careful and rigorous scientific attitude has given me a lot of inspiration, and your patient guidance and concern for students have also given me a lot of warmth. A few words cannot express how grateful I am to you, everything you have done during this journey is deeply rooted in my heart and I will cherish it for the rest of my life and learn to be as good a supervisor as you are if possible.

Similar gratitude belongs to my co-supervisor, **Cyrille Hamon**, thank you for your help and support whenever I need it, no matter from the topic selection to the design of the specific experimental scheme, from the experimental operation process to the analysis of the data results, from the writing and revision of the article to the finalization of the

final thesis. Without your careful guidance and patient explanation, it would be not possible for my doctoral dissertation to be completed on schedule and the fruits I have achieved today. I'm also very grateful that you always asked my opinion first and respected my opinion throughout this process, and the occasional humor has added a lot of fun to my scientific work. I thoroughly enjoyed our fruitful discussions and collaboration. **Marianne Impéror-Clerc**, my co-supervisor, I am very grateful that you responded to my PhD application email four years ago and offered me the opportunity to work and study in our group. Thank you for your patient help and encouragement over the past few years, especially after countless repeated work, you still smile and solve problems with me, which really gave me a lot of encouragement and motivation. I think this will have a great impact on my later life and research work.

I thank all the jury for participating in my special defense. I would like to thank the two reporters: **Mona TRÉGUER-DELAPIERRE** from Université de Bordeaux and **Guillaume BROTONS** from Université du Maine. I thank them for their insightful remarks and encouragement. I also thank the president of my defense, **Emmanuelle LACAZE** from Sorbonne Université as well as two examiners: **Brigitte PANSU** from LPS of Université Paris-Saclay and **Jorge PÉREZ-JUSTE** from Université de Vigo, who put forward a lot of constructive questions and jointly declare that I have passed my defense. It’s a great honor to present my works to all of you.

I’d like also to thank my colleagues in the MATRIX group in LPS. Especially, **Claire Goldmann**, you are like a superhero and you seem to be able to solve any problem I have in the lab. You not only imparted your valuable experimental experience to me but also gave me a lot of help in every detail. I am also very grateful to you for helping me teach that bad guy that summer, as well as your intentions, and the gifts you chose for me on behalf of everyone, and it is no exaggeration to say that each one directly hit my heart. **Wajdi Chaâbani**, you are a very good collaborator, and we have been able to accomplish a lot of work together. I am very grateful for your help in experiments and for the many experiences you often tell me. **Stéphan ROUZIERE**, thank you very much for your prompt help whenever we have problems with SAXS. As well as **Patrick DAVIDSON**, **Patrick JUDEINSTEIN**, **Erwan PAINEAU**, **Wengen ZHENG**, **Jiuxiang ZHANG**, **Yifan PAN**, **Jianan QIAN**, **Kiran Hidayat**, **Jules Marcone**, **Yassine Naciri** and **Camille Mahyaoui**, thank you for all your encouragement and help. **Kinanti Aliyah**, I miss working with you, and thank you so much for helping me

even after leaving Orsay. It's a pity that I didn't see you on the day of my defense, and I hope you are all well in your PhD. **Karin EL RIFAII**, I really enjoy chatting with you every time and sharing the ups and downs of scientific research with you. I am grateful to have a pleasant and friendly atmosphere at LPS.

I would like to express my sincere gratitude to our collaborators. **Thomas BIZIEN**, many thank you for the synchrotron-based SAXS measurements at the SWING beamline of the SOLEIL synchrotron. **Damien ALLOYEAU**, thank you for the liquid-cell TEM measurements at Université de Paris. **Evgeny MODIN** and **Andrey CHUVILIN**, thank you for the focused ion beam-scanning electron microscopy (FIB-SEM) tomography analysis at Electron Microscopy Laboratory and Basque Foundation of Science (Spain). I thank **Pierre-François BREVET** and **Fabien RONDEPIERRE** for the second-harmonic scattering experiments at Université Lyon 1, **Valérie GEERTSEN** for the inductively coupled plasma mass spectrometry (ICP-MS) measurements at CEA, **Lauren MATTHEWS** and **Thomas ZINN** for the synchrotron-based SAXS measurements at European Synchrotron Radiation Facility (ESRF) as well as **Xiaoyan LI** and **Mathieu KOCIAK** for the STEM-electron energy loss spectroscopy (EELS) experiments and **Frank SMALLENBURG** for the Monte Carlo computer simulations at LPS. I also thank **Claire BOULOGNE** and **Cynthia GILLET** for your help with the TEM measurements. Thank you very much for your kind help, without your help my work could not have been completed smoothly.

My sincere thanks also go to my mentor **Rohart STANISLAS** and my scientific tutor **Walls MICHAEL** for your concerns and encouragement in the annual suivi comité de thèse.

I am also very grateful to many of my Chinese friends for their care and love in France. Sorry for not being able to thank them one by one, but I am really grateful to have your company to make my life happier. I am also very grateful to my best friend in China, **Ting XIE**, who we met by chance when we were teachers ten years ago and became good friends in the end. I am very happy to have opened my heart to you in these ten years and have nothing to say, thank you very much for your continuous support and encouragement! **Guanqun DU**, our bachelor's and master's studies are spent in the same places, although your PhD is in Sweden, we are still very closely connected. It's amazing that not only do we look alike, but we also always understand each other's

emotions. Thank you very much for your positivity and optimism that have always inspired me. I am also very lucky that I have a good friend who has the same frequency during this long journey.

I would like to thank the **China Scholarship Council (CSC)** for their funding support of my PhD study. I would like also to thank my Master thesis supervisor **Junxia PENG** at Shaanxi Normal University for your endless help and encouragement during my CSC scholarship application.

In addition, I would like to thank my family who has been my strong supporters. Thank you for your unconditional support and kindness to enable me to successfully complete my studies. I am very grateful to Mr. Shi for always giving me comfort and encouragement when I was lost. I also thank him for his care and love for my family when I was studying abroad in China, so that I can move forward without any worries.

此外，我要感谢我的家人们，他们一直是我坚强的后盾。感谢你们无条件的支持和厚爱使我能够顺利完成我的学业。在这里非常感谢史先生在我失落的时候总是给我安慰和鼓励，也感谢在我国外留学时他对家人们的照顾和关爱，让我能够没有后顾之忧地一直往前走。

Last but not least, many thanks to all of you that I have met.

Table of contents

Abbreviations

1D	One-dimensional
2D	Two-dimensional
3D	Three-dimensional
4-ATP	4-aminothiophenol
5-BrSA	5-bromo salicylic acid
AA	Ascorbic acid
AR	Aspect ratio
AS	UV-Vis-NIR absorption spectroscopy
CCD	Charge-coupled device
CTAB	Cetyltrimethylammonium bromide
CTAC	Cetyltrimethylammonium chloride
CV	Crystal violet
DMF	N, N-dimethylformamide
EELS	Electron energy loss spectroscopy
EF	Enhancement factor
EM	Electromagnetic
FCC	Face-centered cubic
FFT	Fast Fourier Transform
FIB	Focused ion beam
FWHM	Full width at half maximum
GBPs	Gold bipyramids
GNPs	Gold nanoparticles
GNPs@Ag	Silver coated gold
GNstrs	Gold nanostars
GNRs	Gold nanorods
GNSs	Gold nanospheres
GNTPs	Gold nanotetrapods
GRDs	Gold rhombic dodecahedrons
HAADF	High-angle annular dark-field
HCP	Hexagonal close-packed
HMT	Hexamethylenetetramine

HRS	Hyper Rayleigh scattering
HQ	Hydroquinone
ICP-MS	Inductively coupled plasma mass spectrometry
LCTEM	Liquid-cell transmission electron microscopy
LSPR	Localized surface plasmon resonance
MC	Monte Carlo
MEA	2-mercaptoethanol
$NaBH_4$	Sodium borohydride
NaPSS	Sodium polystyrene sulfonate
NCs	Nanocubes
PVP	Polyvinylpyrrolidone
R6G	Rhodamine 6G
RD	Rhombic dodecahedron
SAXS	Small-angle X-ray scattering
SD	Standard deviation
SHG	Second harmonic generation
SERS	Surface-enhanced Raman spectroscopy
SERRS	Surface-enhanced resonant Raman scattering
SEM	Scanning electron microscopy
SVD	Singular value decomposition
TEM	Transmission electron microscopy
UV-Vis-NIR	Ultraviolet-visible-near infrared

1 General introduction

1.1 Nanoscale and nanotechnology

Nanotechnology, considered by many to be the third industrial revolution, is one of the most exciting scientific domains and has attracted the attention of researchers within interdisciplinary areas, from physics to chemistry to biology and engineering.[1] Indeed, nanotechnology is one of the largest technological leaps in human history and promises breakthrough solutions to many of the challenges that threaten our future. For instance, lightweight, high-strength nano-composite materials and ceramics are exploited for aerospace and defense as well as stronger hip prostheses for increased life quality are one of the numerous benefits offered in the biomedical field.[2] As a matter of fact, in the survey of the 2011 investigation of the Engineering and Physical Sciences Research Council on the grand challenges of material science for the next century, two of four indications are extremely concerning to nanotechnology, namely "assembly and control at the nanoscale" as well as the "smart design of functional materials".[3]

The scientific and technological challenges at the nanoscale were first proposed by American physicist Richard Feynman, who gave his famous lecture *"There is Plenty of Room at the Bottom"* in 1959 at Caltech.[4] Starting from both the "top to down" and "bottom to up" methods, he brought forward the possibility of molecular writing, miniaturizing the computer as well as rearranging individual atoms. This discovery would open up a whole new world and his prediction was regarded as a herald of nanotechnology. Based on this cogitation, the term "nanotechnology" was coined by Norio Taniguchi in 1974, he described that "nanotechnology mainly consists of the processing of separation, consolidation, and deformation of materials by one atom or one molecule" to define the "top to down" fabrication of semiconductor.[5] Later, Eric Drexler[6] popularized the word "nanotechnology" through his biologically inspired "bottom to up" visions of building molecular machines and initiated the germ of the idea of the assembler, a universal nanoscale assembling machine, is capable of creating not only nanostructured materials but also other machines, including duplicating itself. This vision tells us the nano-era would certainly arrive when a large number of assemblers laboriously built atom-by-atom with universal manufacturing capability became available, which was indeed seen as the ultimate purpose of nanotechnology.[7]

What is nanotechnology? Is it simply "technology at the nanoscale"? If so, we only need to define "nanoscale" to properly understand nanotechnology. In general, "nanoscale" describes a physical length scale that is on the order of a billionth of a meter long, or nanometer (nm), which is four times the size of an atom and much smaller than one-thousandth the length of a single bacterium.[2,8] However, this definition does not explicitly include the aspects of "fundamentally new properties" or "novel" and "unique" that nanotechnologists usually insist upon. As a consequence, the US National Nanotechnology Initiative declares that "nanotechnology is concerned with materials and systems whose structures and components exhibit novel and significantly improved physical, chemical, and biological properties, phenomena, and processes due to their nanoscale size".[9] In the same vein, the US Foresight Institute specifies that "nanotechnology is a group of emerging technologies in which the structure of matter is controlled at the nanometer scale to produce novel materials and devices that have useful and unique properties". Or stressed in: "the design, synthesis, characterization and application of materials, devices and systems that have a functional organization in at least one dimension on the nanometer scale". This is emphasized even more strongly in "nanotechnology pertains to the processing of materials in which structure of a dimension of less than 100 nm is essential to obtain the required functional performance".[2] All these definitions insist on the novel combination that emerges as the size is reduced. We can conclude that such groundbreaking properties have to be intimately related to the dimensions of the research objects and that they must be size-dependent and different from those on the atomic and macroscopic scales.[10]

In the essence, nanotechnology relies on the assertion that "less is different", indicating that, as the size decreases, a whole family of new phenomena arises, with the need for a new level of description.[7] However, the specificity of nanomaterials is determined by their atom-scale structure, but also by their specific interface and surface structures.[11] For instance, the emission color of semiconductor CdSe nanoparticles (NPs) can be continuously tuned from red to blue by changing their size, owing to the quantization of electron energy levels.[12] Not only do semiconductors, metals, insulators, and semi-metals absorb and emit light, but they also have electrical and magnetic properties. These properties are greatly affected by quantum confinement and the discreteness of states just as with the aforementioned optical properties.[1] Because of the special graphite layer structure, carbon nanotubes exhibit quantum conduction effects at room

temperature, in stark contrast with ordinary wires.[13] Moreover, the melting point of gold is lowered from 1337 K in the bulk to 700 K in 2 nm NPs due to surface atomic effects.[14] Furthermore, the optical properties or commonly referred to as plasmonic properties of gold nanoparticles (GNPs) also depend on size but not only.[15–17] Additionally, crystalline catalysts can exhibit better performance resulting from a decrease in interatomic spacing despite the size-dependent nature of the lattice parameters.[18,19] Plasmons properties,[20–24] among the more striking properties, will be described in the following section, as they represent one of the main topics of this thesis.

How to fabricate nanomaterials? A great number of methodologies and tools have been exploited by scientists and engineers over the years. Two distinguished approaches "top to down" and "bottom to up" are also mentioned above. Briefly, the "top to down" approach refers to the methods of fabrication via etching away bulk material to achieve the required smaller architectures, generally achieved by lithographic processes.[25,26] This "top to down" approach is dominantly used to fabricate a variety of artificial materials, a prime example being the semiconductor industry, where features of metal oxide semiconductor field-effect transistor are imprinted onto a silica wafer via a lithography-based procedure termed photolithography.[27] The miniaturization of transistors was described by Moore's law,[28] a term postulated in 1965 that the number of transistors that can be packed into a given unit of space will double about every two years. The goal was to miniaturize electronics equipment to include increasingly complex electronic functions in limited space with minimum weight. However, experts agree that computers should reach the physical limits of Moore's Law at some point in 2020.[29] In a 2007 interview, Moore himself admitted that "...the fact that materials are made of atoms is the fundamental limitation and it's not that far away...We're pushing up against some fairly fundamental limits so one of these days we're going to have to stop making things smaller."[30] The slowing of Moore's law has prompted many to ask, "Is Moore's law dead?" This in fact is not occurring. While Moore's law is still delivering exponential improvements, the results are being delivered at a slower pace. Jim Keller,[29] who took over as Intel's head of silicon engineering in 2018, noted that keeping Moore's Law going can involve more than a hundred variables, each offering different benefits and facing its own limitations. That means there are many ways to keep doubling the number of devices on a chip-innovations such as three-dimensional (3D) architectures and new transistor designs. This new design trend donated as "more

than Moore" is driven by systemic complexity.[31] This ideology of multidimensional nanomaterial fabrication is enlightened by an opposite approach text where the nanostructures can be built up atom-by-atom or molecule-by-molecule through covalent or supramolecular interactions[25,32] in a similar manner to how a house is built brick by brick, so-called the "bottom to up" method.[33] Such multidimensional architectures increase the complexity of the whole system and in the emergence of intriguing structures and collective properties. P.W. Anderson[34] wrote a paper entitled "*More is different*", in which he developed the idea of qualitative changes emerging when a sufficient number of particles are aggregated together. That's the foremost proposition of assemblers in the emergence of new collective electronic, magnetic, and optical properties which are unattained from the individual components, especially the appearance of a new electromagnetic field owing to the collective plasmonic properties that have attracted numerous attention[35] (see Chapter 5 and 6).

To date, nanomaterials such as metals, ceramics, semiconductor materials, etc. have been fabricated and utilized maturely. In this thesis, we will focus on the metal NPs, gold nanoparticles (GNPs) in particular. A variety of innovative procedures for GNPs synthesis have been explored, including advanced nanolithography techniques and sacrificial templates, etc. These techniques furnish high-quality nanomaterials, whereas scale-up fabrication and precise control are challenges because of potentially complicated and expensive processes.[36] In this respect, the "bottom to up" strategy as a complementary and alternative approach was originated, which does not suffer in principle from such limitations and is thus of immense interest in plasmonic NPs design. The "bottom to up" method for the synthesis and assembly of plasmonic NPs is exploited in our works.

1.2 Plasmonic properties of metal nanoparticles

The vivid optical properties of noble metal NPs have been fascinating since ancient times. The most famous examples are the Lycurgus cup[37] fabricated in the late Roman period and medieval stained glasses windows[38] with ruby red tints which arise from the use of GNPs as coloring agents (see Figure 1.1). These characteristics have aroused people's interest for hundreds of years, while the first scientific research on metal NPs should be traced back to the work of Michael Faraday, who published an extensive paper on the optical properties of thin films and colloidal suspensions of GNPs.[39] In

this work, he attempted to explain the properties of the Purple of Cassius[38] and concluded that the distinct optical properties were directly related to the dimensions of the GNPs and the thickness of the thin films.[40] He first discovered the synthetic and stabilization process of GNPs in water.[41] The unique optical properties of such small metal NPs displaying collective electronic resonance were later widely known as plasmonic properties.[42]

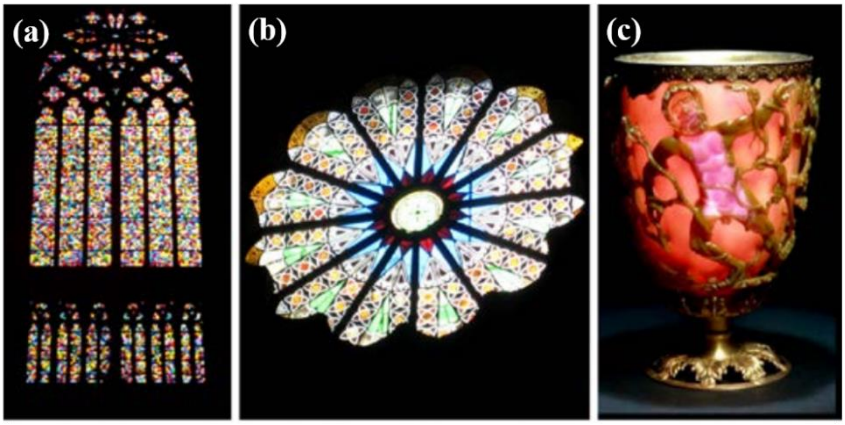

Figure 1.1 Photographs of stained glass from (a) Cologne Cathedral, (b) Santa Maria Sopra Minerva church in Rome, and (c) the Lycurgus cup. Adapted from Ref. 36.

1.2.1 The Drude theory of metals

When dealing with the plasmonic properties of metal NPs, we can start by considering only the negatively conduction electrons, assumed to move freely against a fixed positive background of heavy immobile ions.[43–46] The transport properties of the free electron gas define its response to applied electromagnetic (EM) fields. When a metal is irradiated by incident light characterized by an electric field $E_0(\omega)$, with a wavelength much larger than the NP dimension ($\lambda(\omega) \gg r$), the electron cloud is polarized and creates surface charges that accumulate on opposite ends of the particles, engendering a dipole moment.[35] This oscillating polarization creates an electric field opposed to the excitation field and results in a restoring force arising from Coulomb attraction between electrons and ions, the electron cloud oscillates thus in response to the oscillating electric field of the incident wave.[44] When these two oscillations meet resonant conditions at a specific wavelength, generating a plasmon wave. Surface plasmons can thus be defined as collective coherent oscillations of the conduction band electrons of metal at the metal-dielectric interface. The interaction between electrons and the electric fields is described by the dielectric function $\varepsilon(\omega)$ of the material.

Applying kinetic theory to the free electron gas yields a very simple and useful description of the dielectric function of metals: the Drude-Lorentz-Sommerfeld model (generally known as the Drude model).[47,48] The Drude dielectric function can be written as:

$$\varepsilon(\omega) = 1 - \frac{\omega_p^2}{\omega^2 - i\Gamma\omega} \approx 1 - \frac{\omega_p^2}{\omega^2} \tag{1-1}$$

where Γ is the damping constant, and ω_p, the plasma frequency, is given by

$$\omega_p^2 = \frac{4\pi n e^2}{m} \tag{1-2}$$

m is the mass of the conduction electrons and n is the electron density. The Drude dielectric is generally rewritten as:

$$\varepsilon(\omega) = \varepsilon'(\omega) + i\varepsilon''(\omega) \tag{1-3}$$

separating the real part $\varepsilon'(\omega)$, which describes how strongly the material is polarized upon exposure to an external electromagnetic field, from the imaginary part $\varepsilon''(\omega)$, which quantifies how strongly the plasmons are damped, e.g. due to electron-phonon collisions and electron scattering from the surface.[49,50] Note that the very simplified Drude model only accounts for the free electrons (intraband transitions) and completely neglects the contribution from the bound electrons (interband transitions). Since interband transitions play an important role for GNPs, corrections to the Drude model are often used.[48]

The electron cloud of the NPs is entirely affected by the electric fields owing to a size comparable to the metal skin depth which means the electric field of incident light can penetrate the metal and polarize the conduction electrons, resulting in a plasmon oscillation distributed over the whole particle volume, called localized surface plasmons resonance (LSPR).[45,46] For instance, in the case of a spherical NP (isotropic) with a size much smaller than the wavelength of light (quasistatic approximation), a dipole is induced along the electric field vector of the incident light wave[44] (see Figure 1.2). This corresponding moment μ_{ind} is determined by the incoming EM field $E_0(\omega)$ and the polarizability α of the NP: $\mu_{ind} = \alpha E_0(\omega)$.[35]

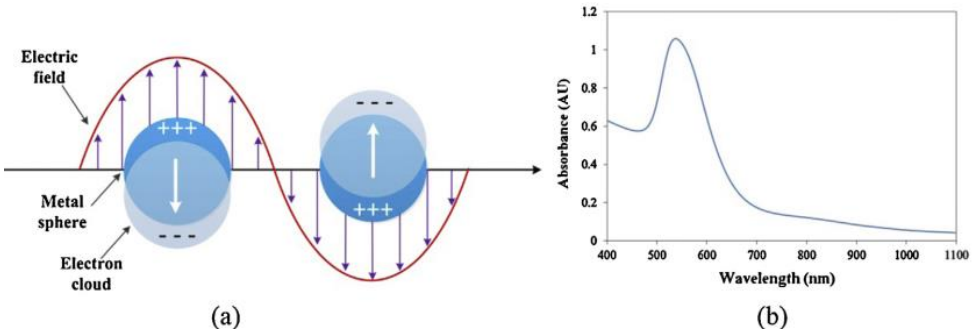

Figure 1.2 (a) Schematic illustration of LSPR excitation for spherical NP. (b) A typical LSPR absorption band of spherical NP. Adapted from Ref. 15,44.

How about anisotropic NPs? A gold nanorod (GNR) for example, as shown in Figure 1.3, exhibits two dipole modes resulting in two different plasmon peaks. Electron oscillation perpendicular to the GNR main axis gives the transverse LSPR, the longitudinal LSPR corresponds to the electron oscillation parallel to the main axis of the GNR.[15,51] The wavelength of the longitudinal mode is significantly red-shifted with respect to that of the transverse mode because of a higher α.[52,53]

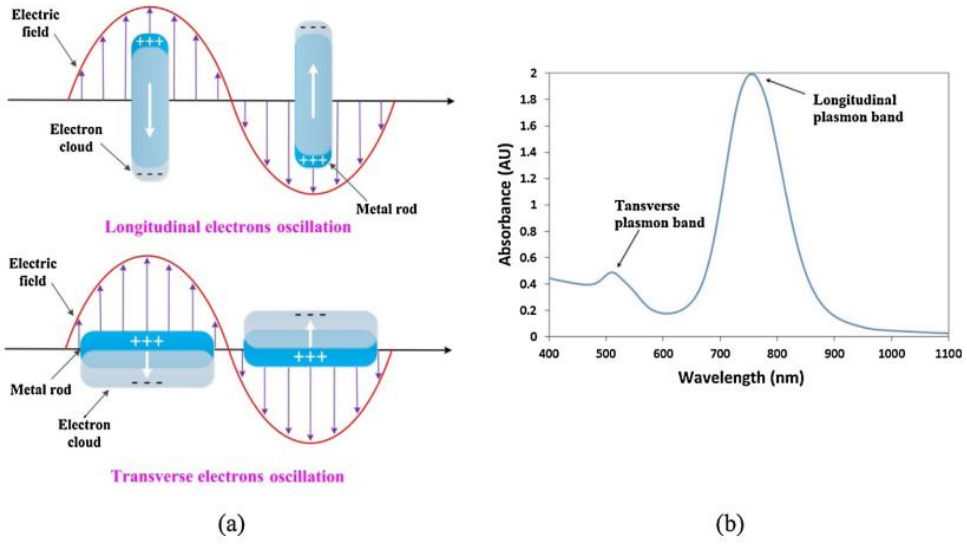

Figure 1.3 (a) Schematic illustration of LSPR excitation for GNRs, longitudinal (top) and transverse (bottom) electron oscillations and (b) LSPR absorption bands of GNRs. Reprinted from Ref. 44.

1.2.2 Factors affecting the plasmon resonance of metal nanoparticles

Tunable plasmonic properties are not only their size dependence but also the morphology of the NPs as well as changes in the interparticle distance and local environment.[42,54] Engineering of plasmon resonances in metal NPs is of great interest for numerous applications, such as sensing, light and energy harvesting, optoelectronics,

biomedicine and catalysis.[35] In this section, we will then give the details on how the plasmon resonance wavelength and bandwidth are affected.

1.2.2.1 The nature of metal

As we mentioned above, the plasmonic properties of nanomaterials are defined by their dielectric function $\varepsilon(\omega)$. For instance, silver and gold NPs exhibit different dielectric constants, for similar NP sizes, the positions of the plasmon peak will be different.[45,55,56] The comprising two parts of dielectric constants are shown in Figure 1.4, providing us the first approximation of the position of the maximum of the plasmon peak for gold and silver NPs. The plasmon peak position is 520 nm for gold whereas 390 nm for silver.

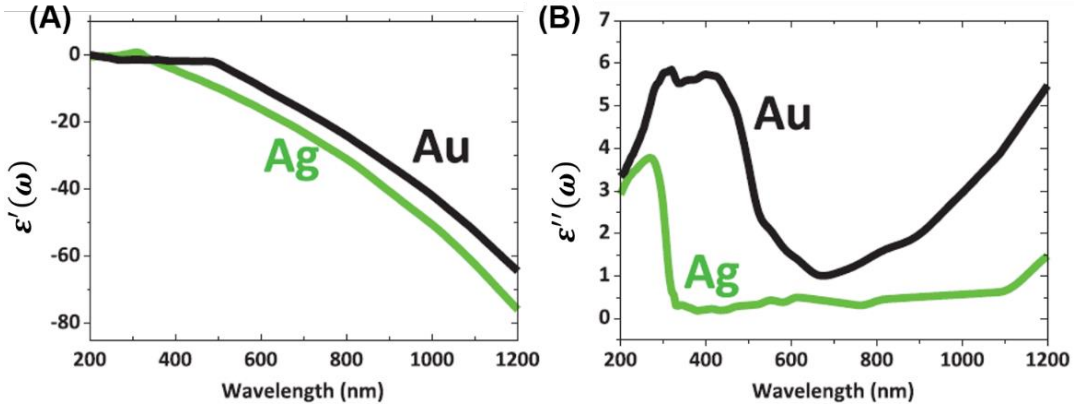

Figure 1.4 Plot of the real part ε'(ω) (A) and the imaginary part ε''(ω) (B) for gold (black) and silver (green), as reported in Ref. 55. Adapted from Ref. 45.

1.2.2.2 Plasmon resonances and particle morphology

The features of the extinction spectra, such as the number, position, and width of the plasmonic peaks vary significantly with the NP's morphology.[57] Various morphologies of NPs and their corresponding extinction spectra are shown in Figure 1.5. Advances in the synthesis of plasmonic nanostructures made it possible to produce NPs with many different shapes, such as nanospheres, nanorods, nanoshells, nanowires, nanocubes, nanostars, nanotriangles, etc.[45] In addition, size tuning will also be capable of modifying the plasmon resonance. Murphy et al.[58–61] have shown that the larger aspect ratio (AR) of the GNRs, the more red-shifted their plasmon peak is. Furthermore, the experimentally observed size dependence of the plasmonic bandwidth can be explained by electron collisions with the particle surface and the retardation effects.[62]

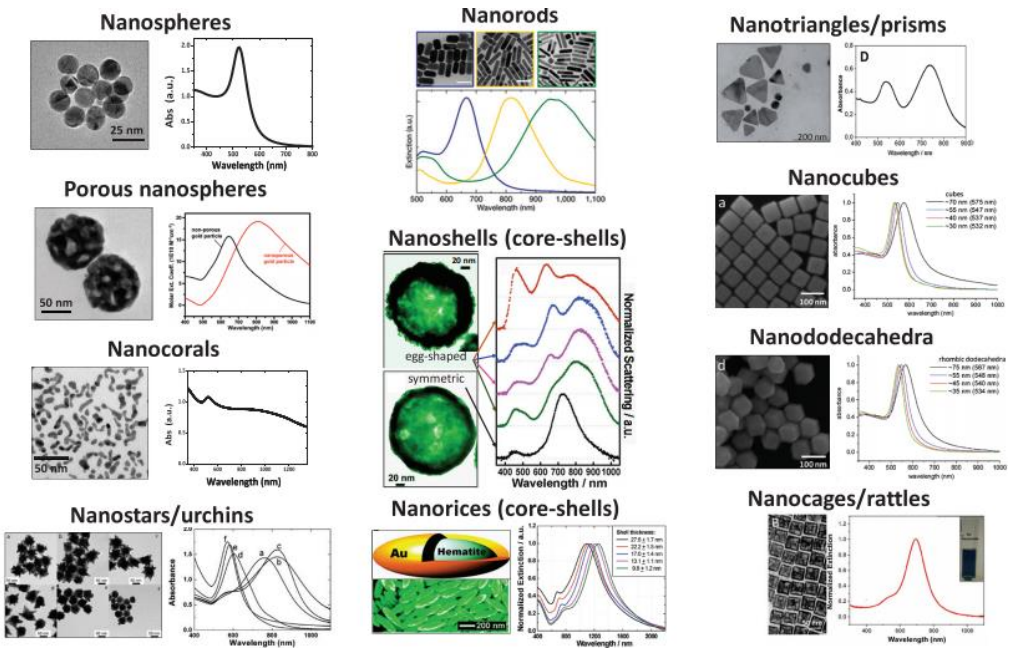

Figure 1.5 GNPs with different morphologies and corresponding optical extinction spectra. Reprinted from Ref. 45.

Branched GNPs, such as nanostars, have drawn particular interest since their sharp tips can lead to a strong localized electric field (the so-called lightning rod effect)[63] and a significant enhancement in the Raman signal.[64–66] Recently, a class of branched particles known as nanotetrapods (GNTPs), with prominent and regularly spaced sharp tips have attracted our attention, since their size and structure homogeneity distinguish them from gold nanostars.[67] Monodisperse GNTPs with tunable arm lengths were synthesized via a seed-mediated growth method by K. Liu's group.[68] Adjusting the arm length makes it possible to control their longitudinal plasmonic resonance properties (see Figure 1.6).

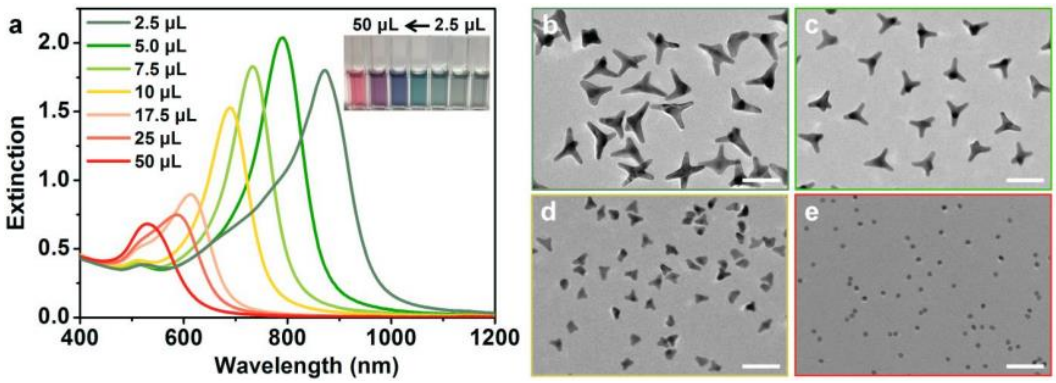

Figure 1.6 (a) Extinction spectra of GNTPs with different sizes were obtained using different amounts of seed solution. (b-e) TEM images of GNTPs. Scale bars: 50 nm. Reprinted from Ref. 68.

The nature of the metal itself can affect the optical performance, the optical properties of NPs containing two or more metals are of course distinct from their homogeneous counterparts. One of the notable examples is core-shell NPs, whose surface plasmon resonance depends not only on the overall size and shape but also on the relative size of the individual components.[69,70] Therefore, one can tune the properties of any core-shell nanostructures by varying the dimensions of the core or shell individually.[71] As an example, GNRs@Ag core-shell NPs were produced by our group (see Figure 1.7). The silver shell was epitaxially grown onto GNRs and its thickness was controlled by adjusting the silver to gold ratio. A strong color shift of the colloidal suspensions is observed, due to the blue shift of the longitudinal plasmon peak and the appearance of new peaks as the silver shell grows thicker.[72]

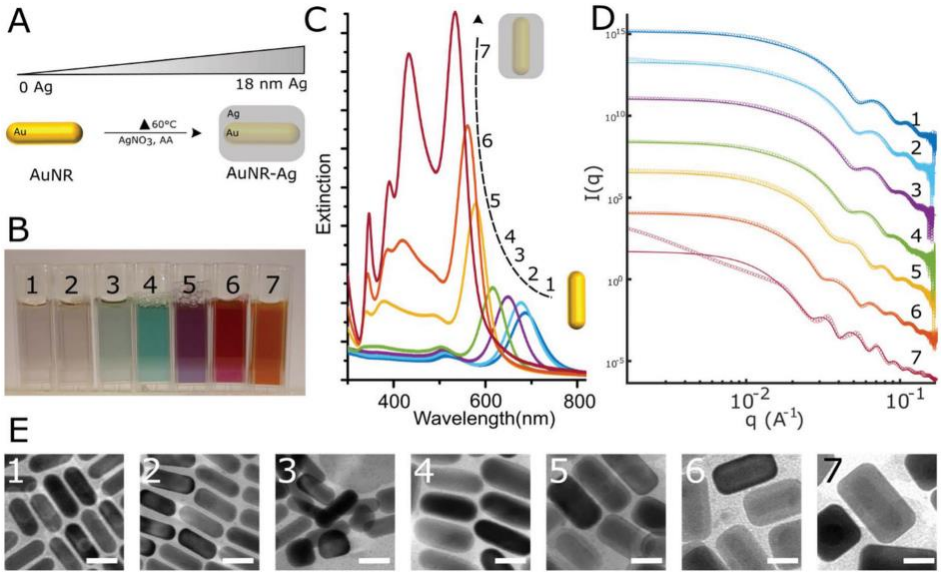

Figure 1.7 (A) Scheme depicting the preparation of GNRs@Ag. (B) Photograph of the GNRs@Ag suspensions. (C) Corresponding AS spectra, (D) SAXS curves (dots) with full-curve fits (full lines) and (E) TEM images. Scale bars: 20 nm. Reprinted from Ref. 72.

The LSPR band of gold bipyramids coated with silver NPs (GBPs@Ag) can also be tuned by controlling the amount of silver grown over the GBPs, see Figure 1.8. The authors also indicated that the SERS enhancement of core-shell GBPs@Ag using 4-MBA as the analyte was found to be 4 times higher than that of single AgNRs because of the very high EM field contribution as well as the much wider surface area for adsorption of the analytes.[71] The cited work used a simple, low-cost synthesis of core-shell Au@Ag NRs with very high yield, better stability, and a new approach for plasmon tuning over a wide range and higher sensitivity and has strong implications in

SERS applications. Moreover, the remarkable changes in the structure and optical features of epitaxially-grown core-shell Au@Ag NPs have motivated our inquiry into the growth kinetics of such objects and their applications.

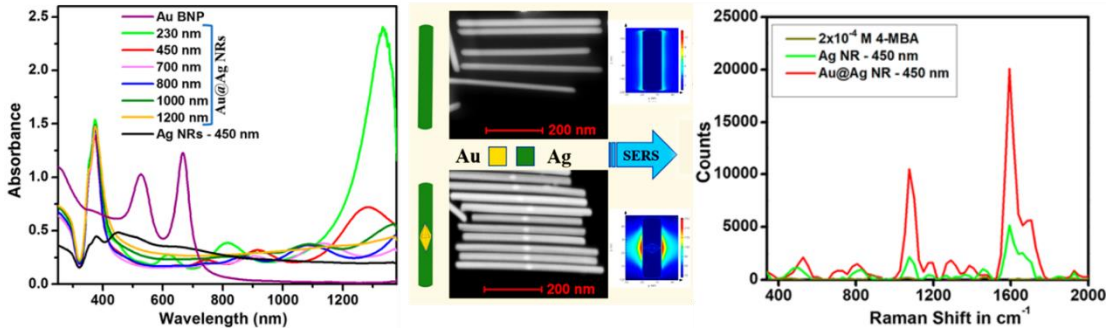

Figure 1.8 AS spectra, TEM images and SERS spectra of 4-MBA taken for single AgNRs and GBPs@Ag NRs, respectively. Adapted from Ref. 71.

1.2.2.3 Optical response of coupled nanoparticles

Plasmons of distinct NPs can reciprocally influence each other, depending on the interparticle distance, arrangement, geometry, and relative light polarization, with the emergence of "coupled" plasmon modes, quantitatively and qualitatively distinct from the isolated plasmon modes observed when the NPs are far from each other in the suspensions.[73,74] When the NPs are close together, this coupling generates a strong electric field in the interparticle gaps, so-called "hot spots".

The simplest case of coupling between two NPs is that of gold nanosphere (GNSs) dimers.[75] The representative extinction spectra of randomly oriented GNS dimers are shown in Figure 1.9 for different interparticle distances (from infinitely far away to 0.2 nm). These GNSs 40 nm in diameter, are irradiated with unpolarized light. When the interparticle distance is large enough, there is a single plasmon peak resulting from the isolated particles (isolated mode) in the extinction spectrum (spectrum a). As the distance gradually decreases, the plasmon peak first becomes a little wider and then red-shifts relative to the isolated mode, with the generation of new plasmon peaks.

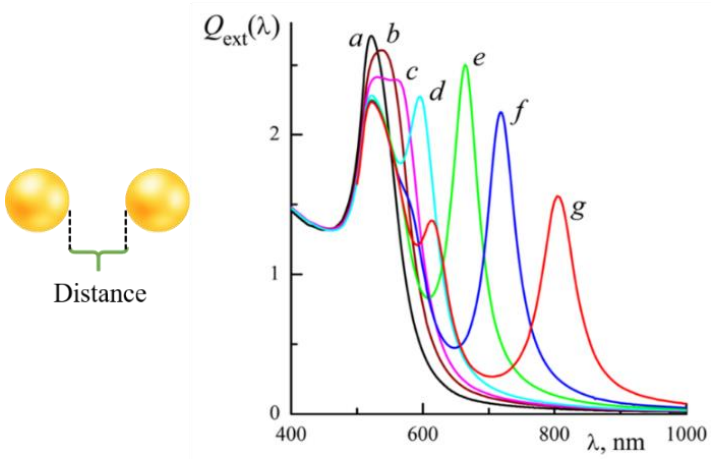

Figure 1.9 Extinction efficiency, Q_{ext}, simulated in the scope of the generalized multiparticle Mie theory for pairs of coupled 40 nm GNSs with different distances between their surfaces: ∞ (a), 7 (b), 4 (c), 2 (d), 0.7 (e), 0.4 (f), and 0.2 nm (g). Adapted from Ref. 75.

To better understand the plasmon coupling phenomenon for various NP shapes, the plasmon modes of typical GNR and GNS dimers under linearly polarized light are represented in Figure 1.10. We assume here that the dimers are randomly oriented in the medium so that we measure average overall configurations in AS, the final absorbance is thus equivalent to the sum of contributions from three equivalent space directions (x, y, z). The incident light is linearly polarized along z and propagates along x, from left to right of the Figure. Due to NP coupling, a new coupled plasmon mode (highlighted in red) appears next to that of isolated NPs. GNSs coupling, for instance, a new coupled-mode appears when the coupling direction is parallel to the polarized direction, we could thus observe two plasmon peaks in the AS spectrum (see Figure 1.10a). As for anisotropic GNRs, there are two plasmon peaks, transverse and longitudinal for isolated nanorods. After coupling, the new longitudinal peak is contributed from the coupling peaks, while the transverse plasmon peak is insensitive (see Figure 1.10b). Noted we just discuss the dimers here but ignore the angle and distance between them.

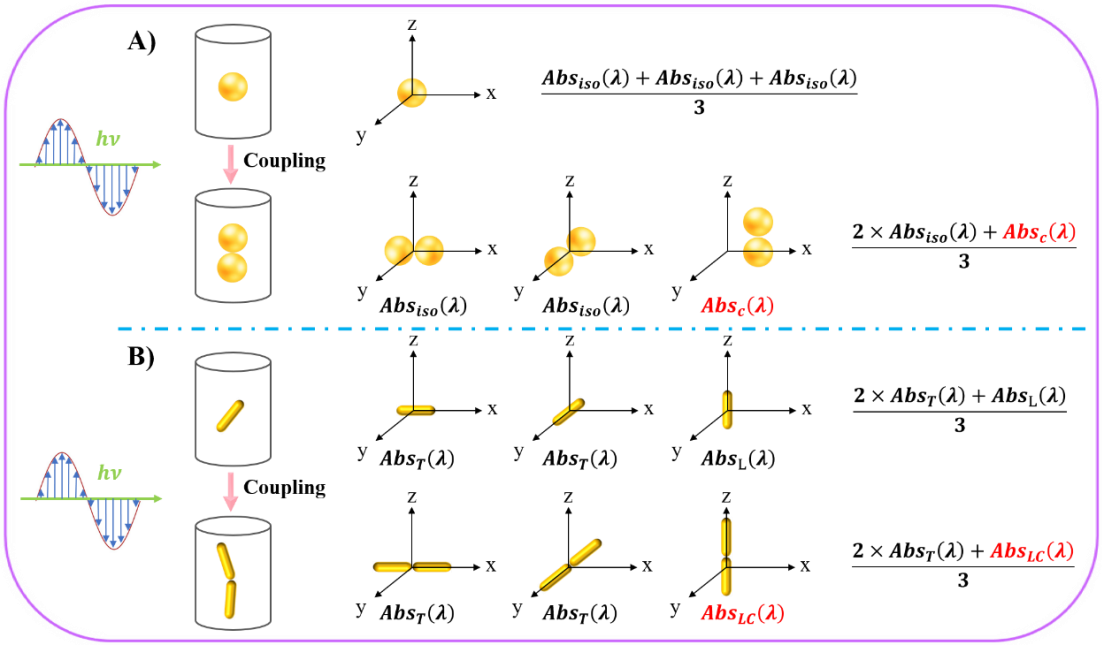

Figure 1.10 The different plasmon modes of GNPs under incident light, with and without coupling, A) GNSs and B) GNRs. The propagation direction of the light is along the x axis and the polarization direction is along the z axis.

NPs coupling causes a change in polarizability, so the position of the coupling plasmon peak shifts as the number of coupled NPs increases. In Ref. [76], the authors showed the extinction band for end-to-end GNRs configuration, giving us the information that the longitudinal plasmon peak shifted towards the longer wavelengths gradually known as the red shift when the number of coupled NPs increases.

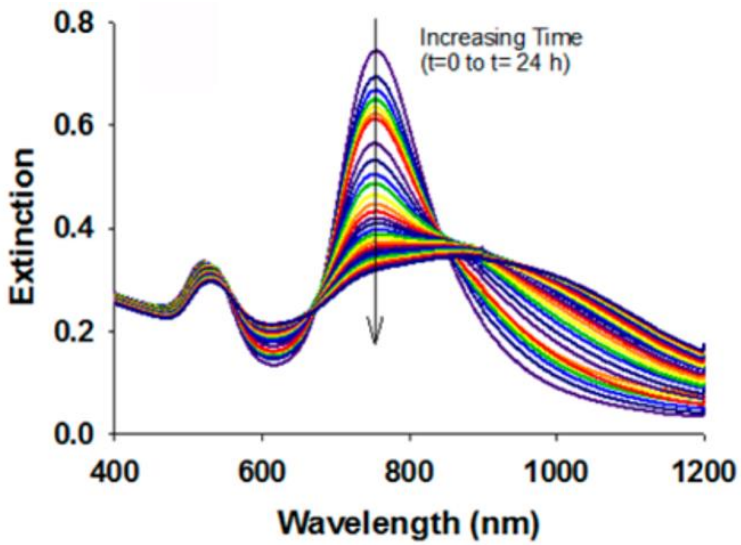

Figure 1.11 AS spectra of end-to-end CTAB-GNRs assemblies. Adapted from Ref. 76.

1.2.2.4 Influence of the environment

The position and amplitude of the plasmon peak are linked to the refractive index n of the surrounding medium as well. Figure 1.12 displays simulations of the plasmon response of GNSs in three different surroundings: air, water, and silica, respectively. As the refractive index increases, the intensity of the extinction peak increases and its position red shifts.[77]

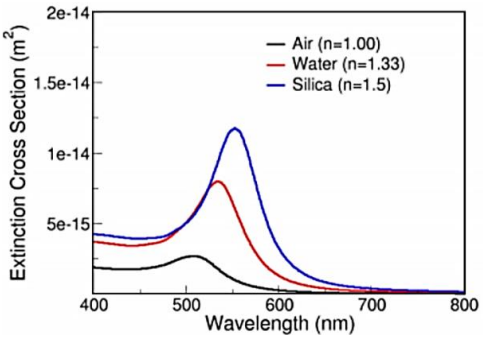

Figure 1.12 Calculated extinction spectrum of GNSs 50 nm in diameter as the local refractive index is increased. Reprinted from Ref. 77.

In addition, the variation in optical properties due to pressure and temperature results from the deformation or reshaping of the NPs. T. Cui and co-workers[78] fabricated GNPs into new shapes and tuned the LSPR of GNPs under pressure. J. Yang et al.[79] studied the evolution of the plasmon resonance through the thermal reshaping of GNRs in an aqueous solution. Liz-Marzán and co-workers[80] studied the thermal reshaping of sub-monolayer GNRs on a glass slide: the GNRs would rapidly contract into spherical particles as the temperature increased (see Figure 1.13), although the temperature was much lower than the melting point of bulk gold.

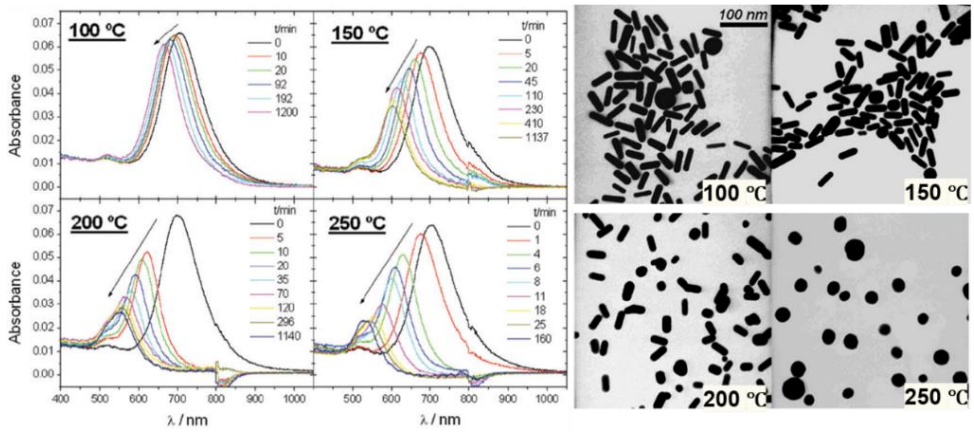

Figure 1.13 Time evolution AS of GNRs after heating at different temperatures and the TEM images of the final state of the nanorods after 20 h of heating. Adapted from Ref. 80.

On the other hand, gold nanobranches are generally unstable and tend to reshape into other morphologies at room temperature, thereby changing their plasmonic properties.[81] The variation rate of reshaping depends not only on the temperature but also on subtle changes in solution composition. Liz-Marzán et al.[82] demonstrated a strong dependence of the nanostars' reshaping process on the presence of different chemicals in the solution, such as halide ions. The reshaping rate was following the order $I^- CTA^+ > Br^- CTA^+ > Cl^- CTA^+$, so the fastest reshaping rate was achieved when iodide was added. Moreover, the reshaping process can be completely quenched by simply adding Ag^+ ions, thereby obtaining NPs with any intermediate morphology and LSPR wavelength. Novel Gold nanotetrapods (GNTPs) also displayed poor stability at room temperature, resulting in quick changes in their morphology and corresponding LSPR peaks over a few hours, see Figure 1.14a.[68] This reshaping process can be quenched by the addition of monome-thoxy-poly(ethylene glycol)-thiol (mPEG-SH). The LSPR of PEGylated GNTPs showed negligible peak shifts at room temperature for a month, or 75°C for 30 min, while the peak width was a little broadened relative to that of initial GNTPs, see Figure 1.14b. These results prompted us not only to reveal the reshaping mechanism but also to prevent it, thereby obtaining stable GNTPs with the desired morphology and optical properties.

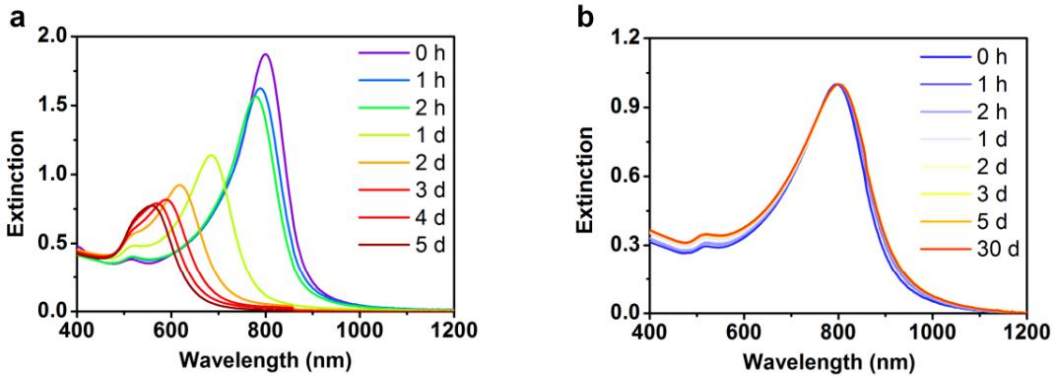

Figure 1.14 The stability of GNTPs. (a) Time evolution AS of aqueous GNTPs, the blue-shifting of LSPR indicated the shape change of GNTPs to more rounded structures. (b) AS of PEG-modified GNTPs stored at 25°C. Adapted from Ref. 68.

1.2.3 Surface-enhanced Raman scattering

Raman scattering, inelastic light scattering by the vibrational excitations of molecules and materials, can provide a rich variety of information on the structure and composition of matter by revealing its vibrational fingerprints. This information can be obtained by monitoring the frequency shifts between excitation and scattering light.[83]

However, the Raman effect is an extremely inefficient process: the Raman cross-section of molecules ranges from 10^{-30} to 10^{-25} cm^2, whereas fluorescence spectroscopy, based on the absorption and emission of light, exploits effective cross-sections between 10^{-17} cm^2 and 10^{-16} cm^2.[84] This obstacle can however be overcome when the molecules are located near rough metal surfaces or metal NPs, which results in enhanced Raman scattering via a process referred to as surface-enhanced Raman scattering (SERS).[35] This effect was first observed in 1974 by Fleischmann et al., who reported an unexpectedly strong Raman signal from a monolayer of pyridine adsorbed on an electrochemically roughened silver electrode.[85] To date, SERS has become an attractive and powerful technique that exploits the interaction of light and molecules on the metallic nanostructures to boost the Raman signal, in some cases up to a remarkable 14 orders of magnitude! It opens the perspective of ultrasensitive detection, identification and, sometimes, quantitation of a broad range of molecules, even at the single-molecule level. Furthermore, SERS has contributed to the development of plasmonic and the related field of near-field optics, which are revolutionizing optics and spectroscopy.[83,86]

Researchers have revealed that the excitation of surface plasmons resonances in the metal NPs could explain the enhanced Raman signals, which is known as an electromagnetic mechanism.[87–89] As described above, the interaction with the electric field ($E_0(\omega)$) of incident light induces an electromagnetic field (LSPR) inside the NPs. The presence of LSPR excitation $E_{loc}(\omega)$ increases the polarizability α by 1 to 3 orders of magnitude of the molecule compared to free molecules, resulting in the mutual excitation between induced dipole in the molecule and NPs, shown in Figure 1.15 (bottom).[35] By comparison, the ordinary Raman scattering can be described by the modulation of the incident field through a molecule vibrating with an eigenfrequency ω_{vib} by irradiating field with a shifted frequency $E_0(\omega_R)$, as schematically shown in Figure 1.15 (top). The SERS intensity I_{SERS} thus depends on both the incident (incoming) $E_0(\omega)$ and the scattered (outgoing) fields $E_{loc}(\omega_R)$ and SERS enhancement is achieved when incoming and outgoing fields are in resonance with the LSPR of the GNPs, known as an electromagnetic mechanism, it can be written as:

$$I_{SERS} = \left(E_{loc}(\omega)\right)^2 \times \left(E_{loc}(\omega_R)\right)^2 \qquad (1\text{-}4)$$

As molecular vibration frequencies ω_{vib} are small compared to the excitation frequency ω_0, the shift ($\omega_R = \omega_0 - \omega_{vib} \approx \omega_0$) of the outgoing field is also small and the

enhancement factor (EF) can be approximated to the fourth power of the local EM field enhancement at the NP surface:

$$EF = \frac{I_{SERS}}{I_{Raman}} = \frac{\left(E_{loc}(\omega)\right)^2 \times \left(E_{loc}(\omega_R)\right)^2}{\left(E_0(\omega)\right)^2 \times \left(E_0(\omega_R)\right)^2} = \left(\frac{E_{loc}(\omega)}{E_0(\omega)}\right)^4 \qquad (1\text{-}5)$$

which illustrates how LSPR enhances the SERS output. A 100-fold enhancement in the plasmon electromagnetic field would rise the SERS intensity by 10^8.

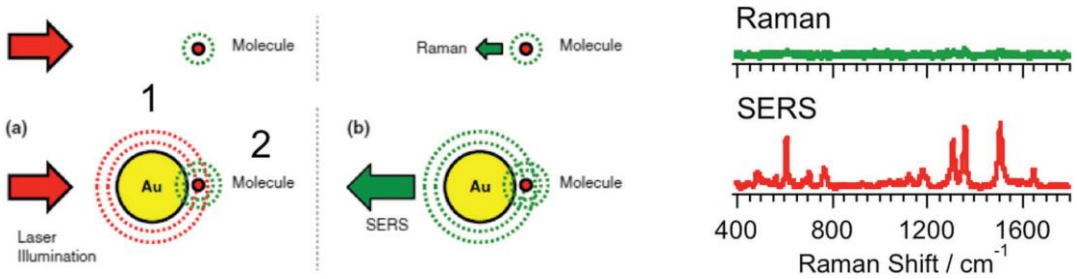

Figure 1.15 Ordinary Raman scattering and SERS measuring without and with GNP as substrate. Reprinted from Ref. 35.

The high electromagnetic enhancement can be strongly amplified by NPs coupling because of "hot spots", which is of great interest in detecting molecules. The Raman scattering spectra collected from the individual and end-to-end assembled NPs are shown in Figure 1.16, there are more significant Raman signals that can be observed in the assembled NPs spectra compared to in the individual ones. More interesting, the amplification of the Raman signal is higher for both individual and assembled bipyramids than those of the nanorods because of sharper tips.[90]

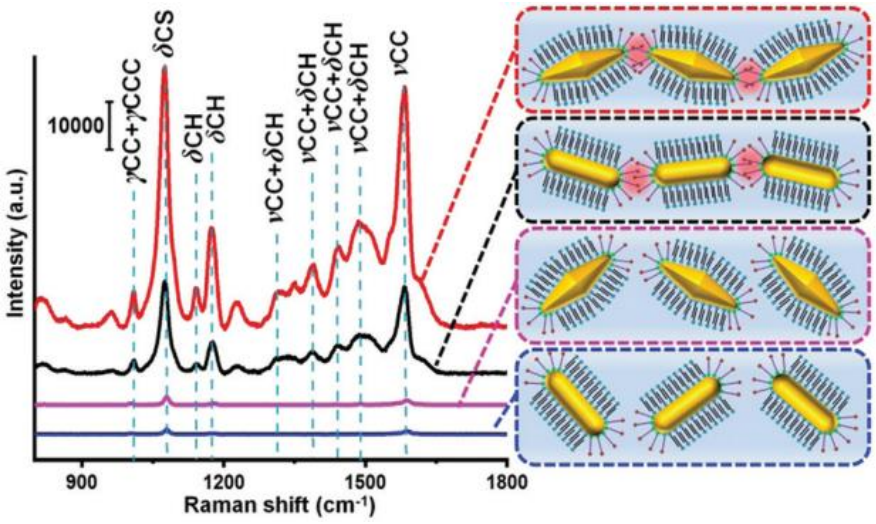

Figure 1.16 SERS spectra of 4-aminothiophenol (4-ATP) modified from individual GNRs and GBPs and end-to-end assembled GNRs and GBPs. Reprinted from Ref. 90.

Another attractive example of SERS in the biomedical field is 3D supercrystals assembled from GNPs as substrates due to their larger area of "hot spots". For instance, the SERS signal of a prion protein at low concentrations was obtained using GNR supercrystals.[88]

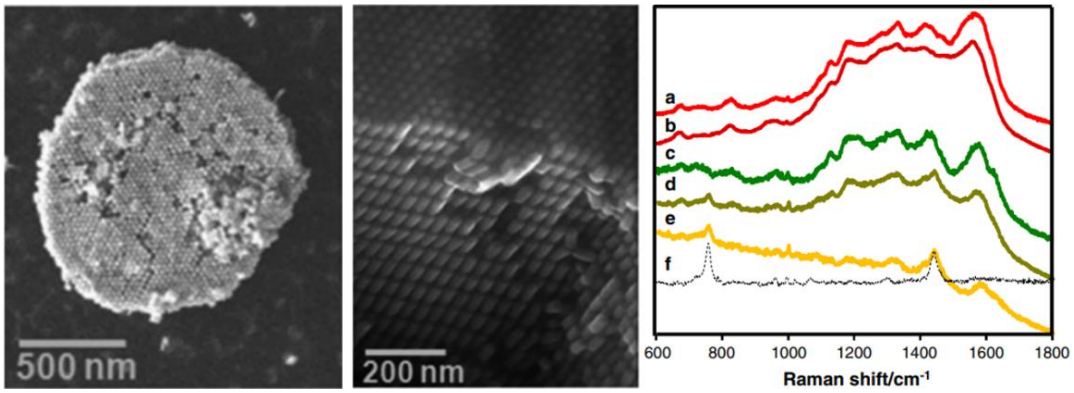

Figure 1.17 SEM images of a typical nanorod supercrystal island film and SERS spectra of (a) natural and (b) spiked human blood; (c) natural and (d) spiked human plasma. (e) SERS spectra spiked human plasma after spectral subtraction of the matrix (human plasma). (f) SERS spectra of the scrambled prion. Adapted from Ref. 88.

In addition to the electromagnetic enhancement owing to the LSPR of GNPs we described above, there is another contribution, the charge transfer between intermolecular and intramolecular, i.e. resonance Raman, known as the chemical mechanism. Whereas chemical mechanism only applies to substances whose surfaces have already formed chemical bonds, so cannot explain all the observed enhanced signals. Therefore, in particular, when a molecule binds to the GNPs surface, the electronic interaction between the molecular orbital and the conduction band of the GNPs can generate a new charge transfer resonance, which can be coupled to the vibrational state of the molecule, leading to additional SERS enhancement with EF of $10^1 - 10^3$. This combinational enhancement, so-called surface-enhanced resonant Raman scattering (SERRS), is generally much smaller than the electromagnetic effect but can improve significantly the sensitivity of the SERS signal.[35]

1.3 Synthesis strategy of plasmonic nanoparticles

The design of a general method for the synthesis of plasmonic NPs with well-defined and controllable morphologies is needed to exploit fully their unique properties for practical applications. Numerous synthesis approaches have been developed to prepare plasmonic NPs, including electrochemical, photochemical, sonochemical, and

microwave-assisted methods as well as chemical reduction. Generally, the chemical reduction method occurs in the liquid phase with the advantages of large-scale synthesis and precise control to provide uniform and monodisperse NPs.[91]

1.3.1 Chemical reduction of gold precursors

The reduction of gold salts is a relatively simple operation that requires the mixing of several chemical reagents under well-controlled conditions. These conditions include the type of the reducing agent and stabilizer, as well as the reaction temperature that can affect the final morphology of the particles.[91] The first preparation method of metal NPs in an aqueous medium was presented in a lecture at the Royal Institution by Faraday in 1857. He synthesized aqueous dispersions of small GNPs by reducing a chloroauric salt with white phosphorous and recognized that the resulting color of the solution was due to the small size of the NPs in the dispersion.[41] Since then, a large number of synthetic protocols have been developed for metal NPs. In 1951, Turkevich et al.[92] reduced gold salts with sodium citrate forming monodisperse colloids in water, in the range of 10-20 nm. In this method, the citrate behaves both as a reducing agent and as a capping agent that stabilizes the NPs. Starting from Turkevich's results, Frens[93] refined this protocol in 1973 by adjusting the molar ratio of citrate to gold to achieve a better size tunability of the particles. This readily accessible synthesis often denoted as the citrate reduction method is still popular nowadays. Another well-known synthesis procedure is the Brust-Schiffrin method published in 1994,[94] using two-phase (water-toluene) reduction of gold salts by sodium borohydride ($NaBH_4$) in the presence of an alkanethiol to yield GNPs 1-3 nm in diameter bearing a surface coating of thiol. During the past two decades, C. Murphy and El-Sayed[58–61] have worked on the seed-mediated synthesis of GNRs by exploiting ascorbic acid (AA) reduction of gold salts in the presence of cetyltrimethylammonium bromide (CTAB). The sizes of GNRs can be easily manipulated by varying the ratio of seed to the metal salt, the concentration of the reducing agent, and the tail length of surfactant CTAB. This approach used for the large-scale synthesis of GNRs is the most prevalent at present in an aqueous medium. Moreover, other synthetic conditions exist such as the so-called Polyol process.[95] In addition, the preparation of silver NPs by reduction of Ag^+ ions in/by N, N-dimethylformamide (DMF), in the presence of polyvinylpyrrolidone (PVP) was reported.[96]

Among the different available approaches for NP synthesis, seed-mediated growth methods are most commonly used for the preparation of monodisperse NPs. In general, the growth mechanism of plasmonic NPs involves nucleation and growth steps, and the nucleation step must be separated from the growth step to prevent simultaneous secondary nucleation and growth.[97,98] An artificial separation between the nucleation and growth processes can be achieved by introducing seed particles into the precursor solution below the critical supersaturation, see Figure 1.18.

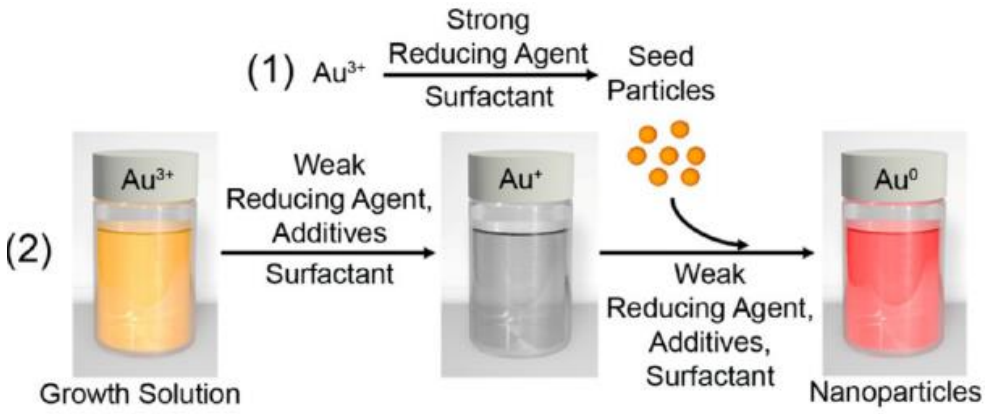

Figure 1.18 Simplified schematic representation of the two steps of the seed-mediated synthesis of GNPs: (1) nucleation, rapid reduction of Au(III) to Au(0); (2) slow growth, controlled deposition of gold onto the preformed seeds in the presence of shape-directing additives. Reprinted from Ref. 98.

The different mechanisms[99] that explain the formation of uniform NPs are presented in Figure 1.19. LaMer and Dinegar et al. (curve I) proposed the classical concept of "burst nucleation", where many nuclei are simultaneously generated as the concentration of constituent species reaches critical supersaturation, and the existing nuclei are allowed to grow uniformly by diffusion of solute to their surface until the final size is reached.[100] Nevertheless, uniform NPs can also be obtained after multiple nucleation events by a self-sharpening growth process, called Ostwald ripening[101] (curve III), which corresponds to the growth of larger NPs at the expense of smaller NPs, which gradually dissolve. Moreover, uniform NPs can also be obtained from the aggregation of smaller subunits[102] (curve II). Ostwald ripening or aggregated growth can be avoided by precise control of reaction conditions involving strongly stabilizing ligands that passivate the NPs surface.[36]

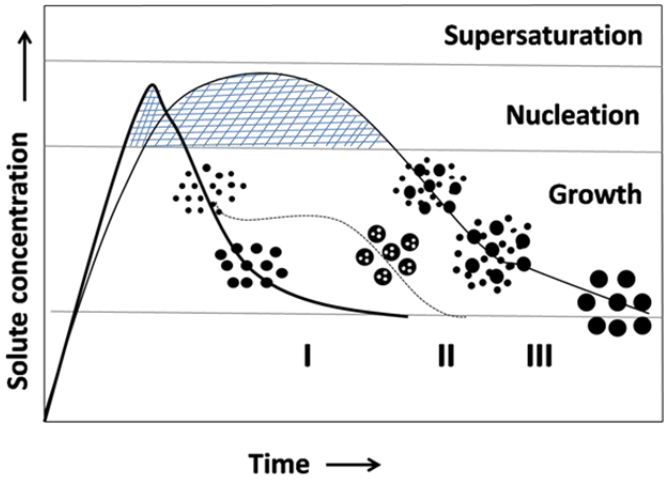

Figure 1.19 Different growth mechanisms of uniform particles in solution: curve I represents single nucleation and uniform growth by diffusion; curve II displays the nucleation, growth and aggregation of smaller subunits; curve III shows multiple nucleation events and Ostwald ripening growth. Adapted from Ref. 99.

1.3.2 Shape control of plasmonic nanoparticles

Plasmon resonances in isotropic spherical NPs can only span a relatively small wavelength range (a few tens of nm) by varying the NP diameter, whereas anisotropic NPs are capable of providing an additional degree of freedom that allows controlling the plasmon resonance wavelength, ranging from the visible through the near-infrared region as a function of NPs size, shape as well as aggregation state and local environment.[35] Moreover, the presence of sharp edges or tips significantly promotes electric field enhancement, which can enhance the catalytic, electronic, and optical properties of the NPs such that they can be used in a broader range of applications.[42,103,104] In addition, the morphology of the NPs can also determine their assembled structures, as well as emerging collective properties which provide promising applications and motivate a growing number of structural studies on the packing of novel assemblies and their applications.[105] Gold and silver, in particular, are face-centered cubic (FCC) lattices, therefore, anisotropic structures can be obtained using a symmetry breaking from the monocrystalline seeds, as well as control over the growth kinetics.[91] The factors that determine the final morphology of NPs will be elucidated below.

1.3.2.1 Nucleation and formation of seeds

As shown in Figure 1.18, metal salts are firstly reduced with a strong reducing agent $NaBH_4$ to yield 1-5 nm small "seed" particles at room temperature. These faceted seeds

can be monocrystalline or polycrystalline, the latter being characterized by the presence of stacking faults and/or twin boundaries in the lattice structure. In the seed-mediated growth process, the crystallinity of the seeds capped with a variety of stabilizing agents (citrate, surfactants, etc.) is very important for directing NP's morphology. Y. Xia et al.[106,107] summarized most major shapes that have been grown from different seeds under different experimental conditions (see Figure 1.20).

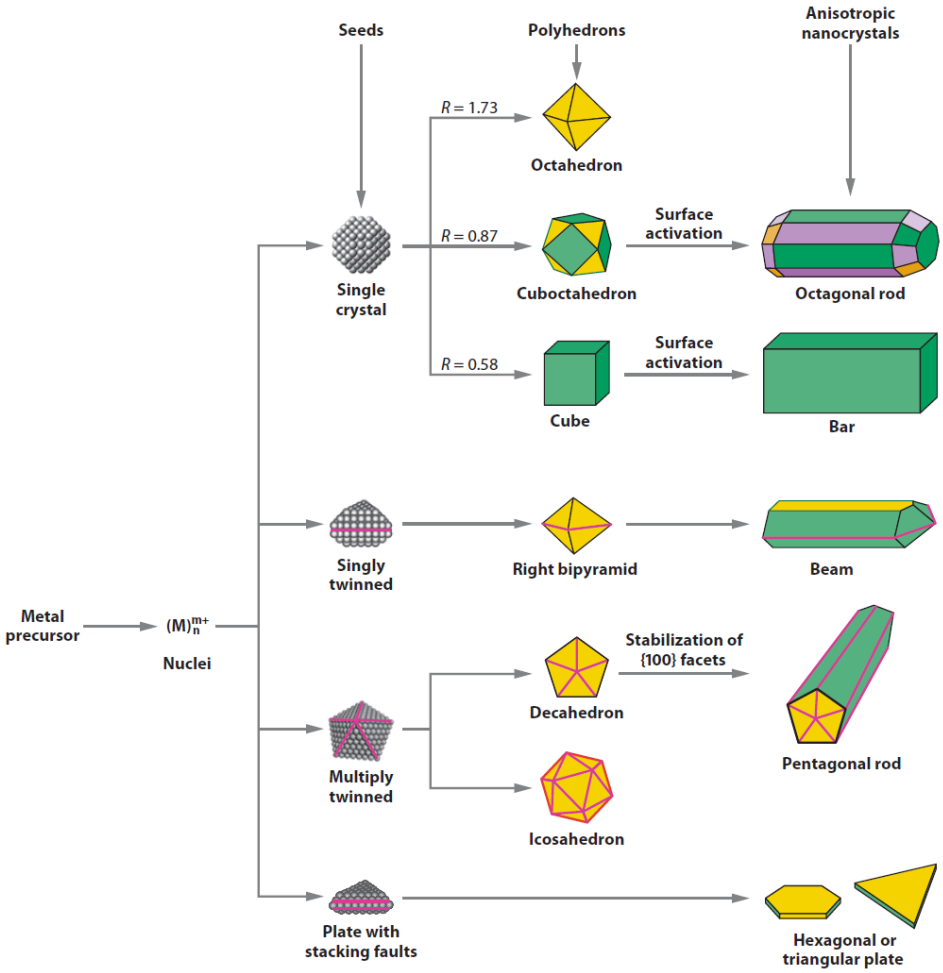

Figure 1.20 Scheme illustrating most major shapes obtained from the different seed crystallinity. Seeds grow from the initial nuclei into either monocrystalline or polycrystalline structures, which in turn can be singly twinned or multiply twinned and/or contain stacking faults. The green, orange, and purple colors represent {100}, {111} and {110} facets, respectively. Twin planes are delineated in the drawing with red lines. The parameter *R* is defined as the ratio between the growth rates along [100] and [111] directions. Reprinted from Ref. 107.

For instance, a single-crystal seed capped with hexacethyltrimethylammonium bromide (CTAB) can grow into an octahedron, cube or cuboctahedron with corner truncation by controlling the ratio of growth rates along the [100] and [111] directions, which is

typically achieved through the introduction of a capping agent,[108] see Figure 1.21. Additionally, single-crystal cuboctahedrons and cubes can be made to grow anisotropically into one-dimensional nanorods with octagonal cross-sections and nanobars with rectangular cross-sections, respectively, by the activation of a specific side face through oxidative etching.[109] From singly twinned seeds, right bipyramids or nanobeams are typically produced.[110] Multiply twinned seeds such as pentatwinned capped with citrate can be directed to grow into pentagonal nanorods or bipyramids.[111] Finally, plate-like seeds will evolve into hexagonal and then eventually triangular plates whose top and bottom faces are {111} facets and whose side surface is enclosed by a mix of {100} and {111} facets.[112] From these examples, it is critical to control the crystallinity of the seeds to produce the plasmonic NPs with the desired shape. Furthermore, the addition of the number of seeds is also crucial to regulate the size of NPs during the synthetic process. Introducing a larger amount of seeds at a given concentration of precursor ions results in smaller particles, while for anisotropic NPs both the AR and the peak absorption wavelength generally decrease. Conversely, larger NPs are generated when fewer seeds are used.[17]

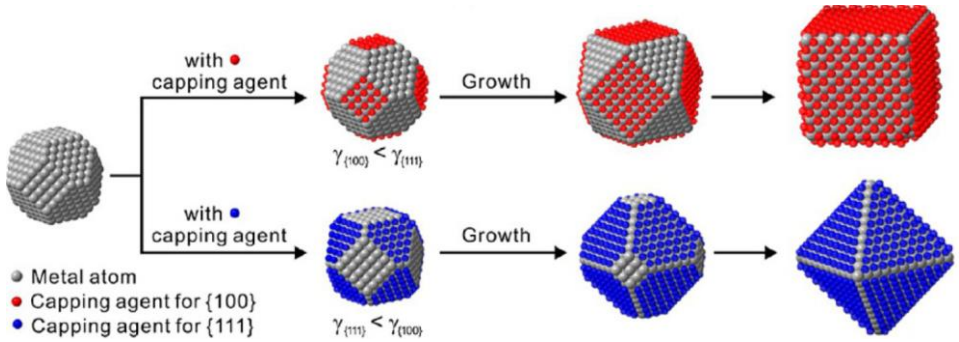

Figure 1.21 Schematic illustrations showing the role of capping agents in directing the growth of a single-crystal seed made of an FCC metal. The shape of resulting nanocrystals can be manipulated in a controllable fashion through the introduction of a capping agent (represented by red or blue dots) that can selectively bind to a specific type of facet, altering the order of surface free energies and eventually leading to the formation of a nanocube enclosed by {100} facets and an octahedron enclosed by {111} facets, respectively. Reprinted from Ref. 108.

1.3.2.2 Reducing agent

In the second step, the seeds are rapidly injected into a growth solution including more metal precursors, stabilizing, reducing agents and shape directing agents. At this moment, the following reaction occurs in the growth solution:

$$Au^{3+} + 2Au^{0} \rightleftharpoons 3Au^{+} \quad (1\text{-}6)$$

which means that the equilibrium is displaced toward the comproportionation between Au(III) and Au(0), therefore, Au(0) from GNPs will still be oxidized in the presence of Au(III).[113,114] In this case, selecting a rational reducing agent to keep the Au(I) as the most stable species plays a central role in obtaining the final particles.

The weak reducing agent, ascorbic acid (AA), is one of the most popular choices, which by itself is not capable of reducing completely the metal salt to the elemental metal, but upon addition of the seeds, the reaction is thought to take place on the seed surface and be autocatalytic, to produce larger NPs.[104] Specifically, AA can reduce Au(III) into Au(I), as reflected in the solution color change from yellowish to colorless.[115,116] AA commonly functions as a one-electron reducing agent because of the ascorbate radical, the one-electron ($1e^-$) oxidation product of ascorbic acid is relatively unreactive with nonradical species.[117] The Pourbaix diagram for the first $1e^-$ oxidation of AA in water is shown in Figure 1.22. At higher pH, its electrochemical potential decreases, enhancing its reduction strength. Therefore, the reduction strength of AA can be easily tuned via adjustment of the solution pH.[118] But noted if the pH is above 9, AA will be able to reduce Au(I) into Au(0) directly, even in the absence of seeds, thus compromising the seeded growth mechanism.[16]

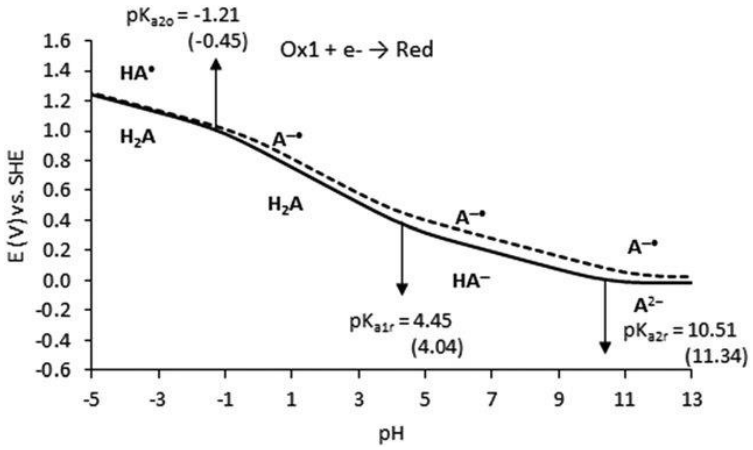

Figure 1.22 Pourbaix diagram for the first $1e^-$ oxidation of ascorbic acid in water. The solid line and dashed line are calculated and obtained from experiment values of the pH-dependent reduction potential, respectively. Adapted from Ref. 117.

1.3.2.3 Shape-directing agents

As we discussed above, capping agents can adsorb onto certain families of crystal facets and passivate them, so that the resulting particle overexpresses such facets, thereby

directing the particle's shape. Specifically, there are two effects of halides (denoted as X) on particle growth, namely, on the reduction rates of the gold ion species and the binding of the halide to the gold particle surface.[119] Firstly, the halides will complex gold ions, thereby affecting the reduction potential and solubility of the gold ions in the $[CTA\text{-}X\text{-}AuX_2]^-$ complexes and thus changing their reduction rate.[120] The reduction potentials and the solubility for $[AuX_2]^-$ complexes follows the sequence $[AuCl_2]^- > [AuBr_2]^- > [AuI_2]^-$.[121] Secondly, halides can also bind to the surface of the GNPs, inhibiting the subsequent growth of the particles. The binding strength of the halides to particles surface follows the order $I^- > Br^- > Cl^-$.[122] Thus, the addition of bromide or iodide will slow the rate of GNPs formation as compared to the rate in the presence of chloride alone, both by lowering the reduction potential and solubility of the gold ion species in solution and by binding strongly to the surface of the GNPs.[119] Additionally, it appears from experimental evidence that the halide ion Cl^- is used widely in isotropic particles synthesis like nanospheres,[104] Br^- is often claimed to induce the formation of anisotropic NPs such as nanorods and bipyramids, whereas I^- preferentially stabilizes the {111} facets and promotes the growth of nanoplates (such as triangular NPs) while preventing the growth of oblong NPs.[112,123] Moreover, the tail length of the surfactant is surprisingly important for GNPs synthesis: it was found that as the length of the surfactant chain increased, the resulting GNRs' AR increased.[60]

The shape of the GNPs can also be controlled by introducing silver ion additives in a growth solution. One interpretation of the mechanism is the so-called silver underpotential deposition, in which a silver layer would be deposited preferentially on high-index facets. Once silver deposits onto a particular facet, it slows further growth of that facet by inhibiting gold deposition, and therefore that facet is retained in the final NP's morphology.[124,125] Note that the effects of halides on particle growth are more complicated once silver ions are added, because the halides interact not only with the gold ions in solution and the GNP surface but also with the silver ions and the silver layer, forming AgX.[126] In addition, Murphy and co-workers[59] have demonstrated the highest AR of high-yield GNRs obtainable with silver ion is about 6, whereas low-yield GNRs obtainable with the highest AR 25 in the absence of silver.

It is worth noting that AA is not only a common reducing agent: we demonstrated in our work that AA, combined with halide ions, is also a shape-directing agent that favors

the formation of nanorods by stabilizing the {100} facets of the silver cubic lattice, see Section 3.4.

1.3.3 Core-shell bimetallic nanoparticles

The seed-mediated growth of NPs is based on slow growth at the surface of preformed nanocrystal seeds. This approach is promising for fabricating core-shell nanocrystals with new functionalities by introducing other components, e.g. semiconductor or magnetic properties. The growth of platinum or palladium as shells on gold or silver cores has also been widely used to tune or enhance their optical and catalytic properties. In this text, we will take gold and silver as examples. Silver coated onto GNPs (core-shell GNPs@Ag) can be easily prepared by seed-mediated growth in which gold seeds are injected rapidly into a growth solution comprising silver salt as well as mild reducing, shape directing and stabilizing agents. Nevertheless, fabricating core-shell Ag@GNPs is still challenging, because of the oxidation of the silver core by the gold ions. This effect is well known as galvanic replacement reaction in which the silver core acts as a sacrificial anode for the cathodic reduction of gold ions.[127]

As described above, the crystallinity of the seeds will also determine the final morphology of the core-shell NPs (Figure 1.23). How the silver shell grows will not only depend on the surface energy of the exposed seed facets but can also be further tuned through the addition of halides or other additives. Furthermore, silver shells can also be adjusted into different morphologies by tuning the silver to gold ratio. GNPs@Ag cubes are readily generated from isotropic gold seeds, such as octahedrons[128] as well as spheres[129]. The silver shell could be easily discerned from the gold core by high-angle annular dark-field scanning TEM (HAADF-STEM) (Figure 1.23D), in which the contrast is due to variation of the atomic number between the two different components. In addition, the silver will overgrow preferentially at the sides or the ends on either single crystalline or pentatwinned nanorods and bipyramids as seeds. Since halides stabilize the {100} silver facets, they lead to preferential growth of other silver facets.[128,130,131] Apart from the tunable morphology, core-shell GNPs@Ag exhibit a higher extinction cross-section compared to the initial individual GNPs, and thus enhanced optical properties. Also, GNPs@Ag show a more complex set of plasmon resonances than those in any single-metal nanoparticles. Notably, the plasmon resonance peaks of the gold cores are shifted toward higher energy as the silver shell

thickness increases and additional higher energy peaks develop due to the better plasmonic performance of silver.[130] Although numerous core-shell NPs have been produced, the growth mechanism, the role of agents, and the process of morphological evolution are still of considerable interest.

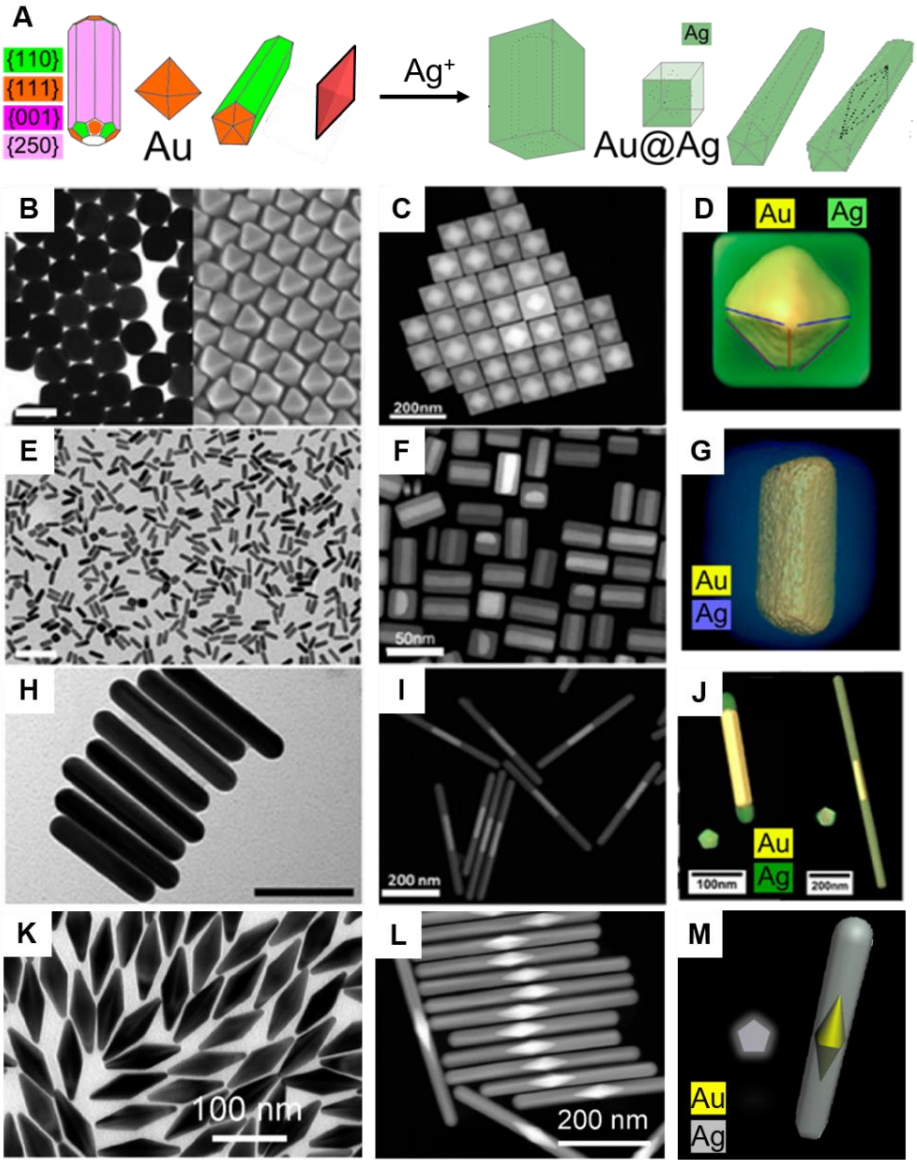

Figure 1.23 Core-shell GNPs@Ag synthesis. (A) Scheme illustrating the distinct types of seed crystallinity to define the shape of the silver shell: single crystalline rods, octahedrons, pentatwinned rods and pentatwinned bipyramids are represented before and after silver deposition. Adapted from Ref. 127. (B)-(L) electron microscopy images characterizing the above-mentioned particles. GNPs@Ag were prepared from gold seeds of different crystallinity (B)-(D) octahedrons, (E)-(G) single crystalline rods, (H)-(J) pentagonal twinned rods and (K)-(L) pentagonal twinned bipyramids. Three types of electron microscopy techniques were used: (B)-(K) TEM (and SEM in B), (C)-(L) STEM-HAADF, (D)-(J) Electron tomography. (M) 3D visualizations of the reconstructed GBPs@Ag. (B-M) were adapted from Refs. 128, 130, 131.

It is well known that the plasmonic properties of NPs are very sensitive to particle morphology. Therefore, determining the morphology and concentration of NPs is a crucial step towards understanding their formation and a prerequisite for any applications. While measuring these parameters for single-metal NPs is by now rather routine, reliably characterizing bimetallic NPs is still a challenge. In addition, understanding the individual contributions of additives would benefit the rational nanoparticle design. Through the combination of various complementary characterization techniques, we expect to gain some novel information during bimetallic synthesis, see Section 3.3 and Section 3.4.

1.4 Self-assembly of plasmonic nanoparticles

Self-assembly of colloidal NPs into superstructures offers a flexible and promising pathway toward materials with the increased overall size, dimensionality, and complexity and thus toward the emergence of new collective electronic, magnetic and optical properties which are unattainable with the individual components. These assembly structures could be one-dimensional (1D) chains, two-dimensional (2D) sheets and three-dimensional (3D) supercrystals (see Figure 1.24).

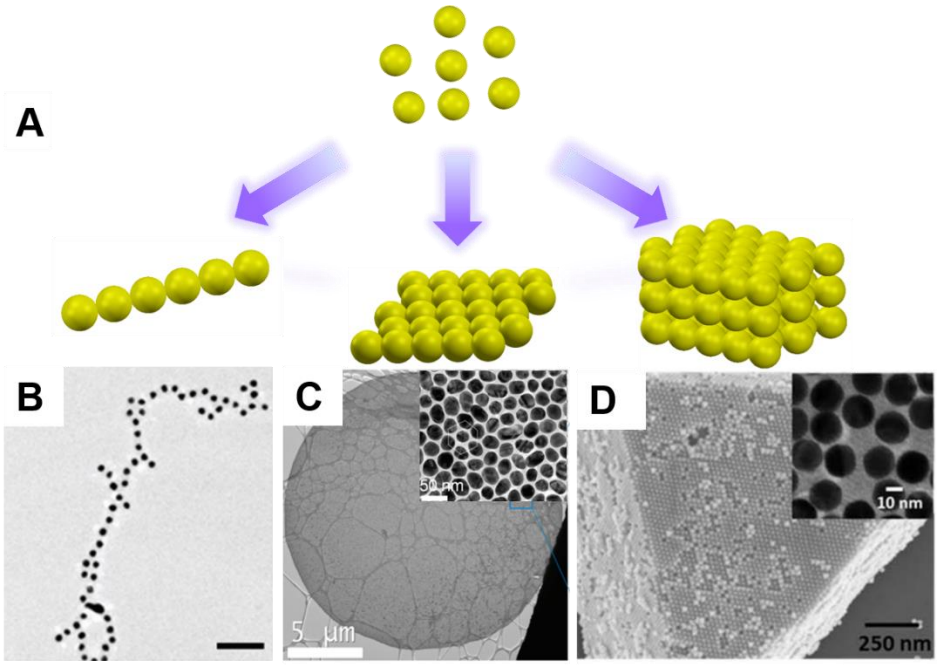

Figure 1.24 A typical illustration of NPs self-assembly. (A) Schematic illustration of the organization of nanospheres into 1D chains, 2D sheets and 3D supercrystals. TEM images of 1D chain (B) and 2D monolayer sheet (C) and SEM image of 3D supercrystal (D), the insets in C and D show the TEM images of NPs. Adapted from Ref. 132, Ref. 133 and Ref. 134, respectively.

In addition, “hot spots”, the electric field enhancement, are utilized widely in numerous applications, such as SERS, plasmon-enhanced fluorescence, amplification of non-linear optical signals, nanoscale lasing, plasmon assisted photolithography, light-harvesting, photocatalysis, and chemical and biological sensing.[132–134] Furthermore, the structures of assemblies with directionality and long-range order could also be investigated if the spacing and alignment of individual NPs can be controlled.[135]

1.4.1 Driving forces for self-assembly

Self-assembly can provide a simple and low-cost procedure for producing NP assemblies in a controllable manner, in which pre-existing isolated components form an organized structure or pattern.[136] All self-assembly processes are typically driven by a minimum in the free energy of the final assembled structure, which will exist in equilibrium or metastable states at least.[137,138] The free energy landscape is governed by the balance of attractive and repulsive interactions, such as Van der Waals, Coulomb, hydrogen bonding or hydrophobic interactions, to name a few.[10] Many routes have been explored to fabricate NP assemblies, but they can all be divided into three categories: interparticle interactions, applied external field forces, and spatial confinement strategies that use templates and solvent evaporation.[139]

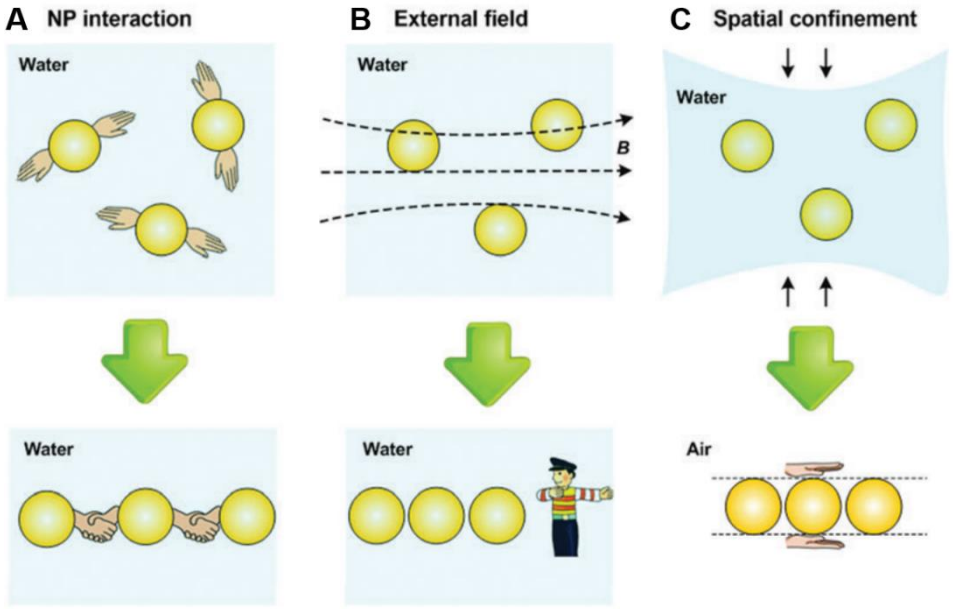

Figure 1.25 Schematic illustration of NP self-assembly driving forces: (A) inter-particle interaction, (B) external field and (C) spatial confinement strategies. Adapted from Ref. 139.

The assembly initiated by internal forces is strongly related to the morphology and surface chemistry of NPs. This driving force can be classified as physical, such as

hydrophobic,[140] electrostatic interactions[141] and depletion attractions[142] or chemical, for instance, hydrogen bonding,[143] covalent or non-covalent interaction,[144] and even biological, including DNA hybridization,[145] antibody-antigen recognition[146] and avidin-biotin bonding.[147] Moreover, diverse NP assemblies have also been successfully produced in the presence of external fields, such as electric field,[148] magnetic field[149] and flow field.[150] In addition, solvent evaporation as a simple method has been widely utilized to drive assembly at a solvent-air drying interface by depositing NPs on a solid substrate such as a glass coverslip, carbon-coated copper grid or silicon wafer.[151] During evaporation, the volume of solvent is reduced and the NP concentration is gradually increased until a certain threshold, where the NPs undergo a transition from the disordered state to ordered assemblies driven by the relatively weak Van der Waals force and ligand-substrate chemisorption interaction.[152] Multidimensional superstructures with large scales can be achieved by increasing the NP concentration in droplets and by using a relatively slow evaporation rate.[153] In this way, 2D thin films can be readily generated on the substrate and 3D supercrystals can be obtained in a sealed environment at a significantly slower drying rate as well.[154] Furthermore, the template approaches (complementary to the evaporation) are capable to guide the assembling NPs into desired configurations via spatial confinement.[155] To achieve well-defined 3D assemblies, cavities of discrete sizes were patterned into Si wafers through a soft lithography technique and then NPs were brought into these wells and yielded assemblies via evaporation,[156,157] see Figure 1.26.

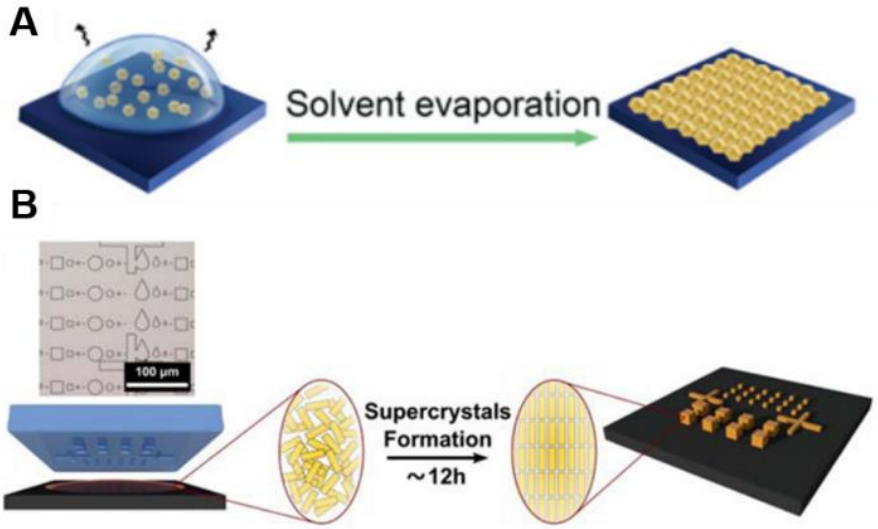

Figure 1.26 Schematic of spontaneous assembly of NP superstructures through slow solvent evaporation (A) without and (B) with templates. Adapted from Ref. 153 and Ref. 157.

1.4.2 One-dimensional chains

Fabricating one-dimensional (1D) assemblies chains is of particular interest since NPs' 1D assemblies can directionally transport excitons, photons, or phonons, and shows considerable applications in waveguiding, highly sensitive sensors, microcircuits, logic computations, biomedicine, etc.[139,146,158] When the interparticle distances are short enough (1-10 nm), a collective plasmon mode emerges in the extinction spectrum. Elongated or facetted NPs particularly, such as nanorods (GNRs), bipyramids (GBPs), nanocubes, and nanotriangles, generate strong "hot spots" concentrated at their sharp tips.[159] For instance, the 1D assembly of anisotropic GNPs like GNRs or GBPs in the end-to-end configuration causes a redshift in the longitudinal plasmonic band compared to the isolated particles (see Figure 1.27D), while the side-by-side configuration causes a blueshift.[146,160] End-to-end assemblies are of particular interest for biological sensing and SERS applications, which usually take place in solution.[89,161,162] Various approaches have been developed to assemble anisotropic GNPs into 1D chains (Figure 1.27). For example, Z. Bao et al.[163] aligned nanorods within the hydrophilic region of a template. J. Zhu et al.[164] demonstrated the confined assembly of polymer-tethered gold nanorods in cylindrical nanopore channels with the assistance of an electric field. In addition, molecular recognition methods were exploited to connect GNPs. J. J. Gooding et al.[90] showed that GNR or GBP chains can be induced by coordination between copper ions and the amino group of 4-aminothiophenol (4-ATP) molecules attached via their thiol group to the tips of the particles (where they replaced the CTAB). These assembled chains are capable of detecting the SERS signal of 4-ATP molecules due to the Raman activity. Furthermore, the use of Hg^{2+} as a bridge connecting nanorods functionalized with DNA was demonstrated.[165]

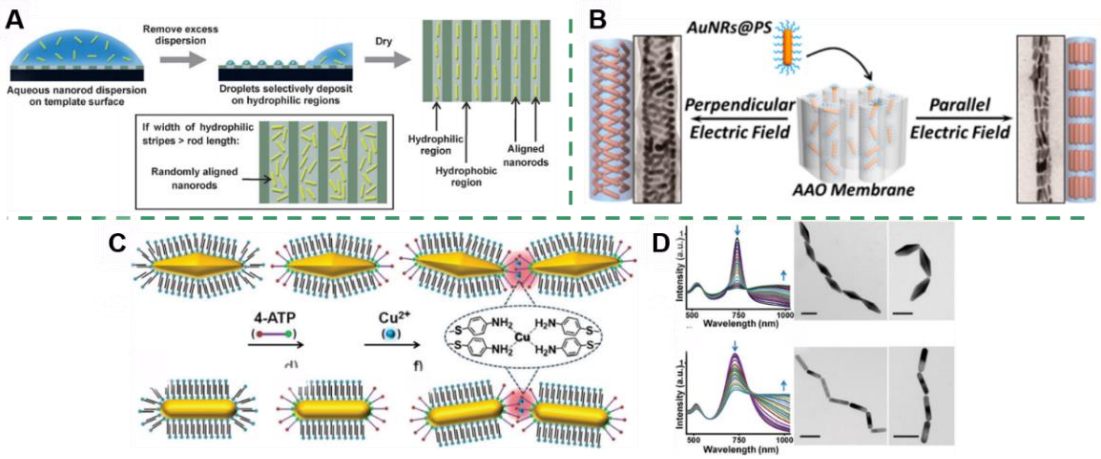

Figure 1.27 Schematic illustration showing the assembly strategies for one-dimensional chains: (A) template-assisted, (B) external electric field, (C,D) molecular recognition method for chains and corresponding extinction spectra and TEM images. Adapted from Ref. 163, Ref. 164 and Ref. 90.

Although these strategies are well established and yield assembled chains, the removal of templates, introduction of an external electric field, or the functionalization of the NPs require extensive additional procedures to the fabrication process. S. Mann et al.[166] investigated the mechanism of GNS chains associated with the induction of electric dipole-dipole interactions arising from the partial ligand exchange of surface-adsorbed citrate ions by facile addition of 2-mercaptoethanol (HS-$(CH_2)_2$-OH, MEA). They confirmed a first-order kinetic process of chain assembly by analyzing the evolution of the extinction peaks at 520 nm and 730 nm. Peter J. Vikesland et al.[76] illustrated a simple method in which sulfate ions are used to facilitate end-to-end GNR chains in aqueous suspension. In this case, sulfate as a divalent anion effectively interacts with the quaternary ammonium headgroup of CTAB on the GNRs surface and bridges the tip facets of adjacent GNRs. This bridging produces chainlike end-to-end assemblies of GNRs and the length of chains can be controlled by the sulfate ion concentration, the particle concentration, and the reaction time. In contrast with end-to-end assembly, side-by-side and end-to-side assemblies are hindered by strong electrostatic repulsion between the dense CTAB bilayers present on the side facets. Furthermore, the authors track the formation and growth of the chains over time by analyzing separately the evolution of the extinction spectrum for both the transverse and longitudinal bands using a simple second-order aggregation model.

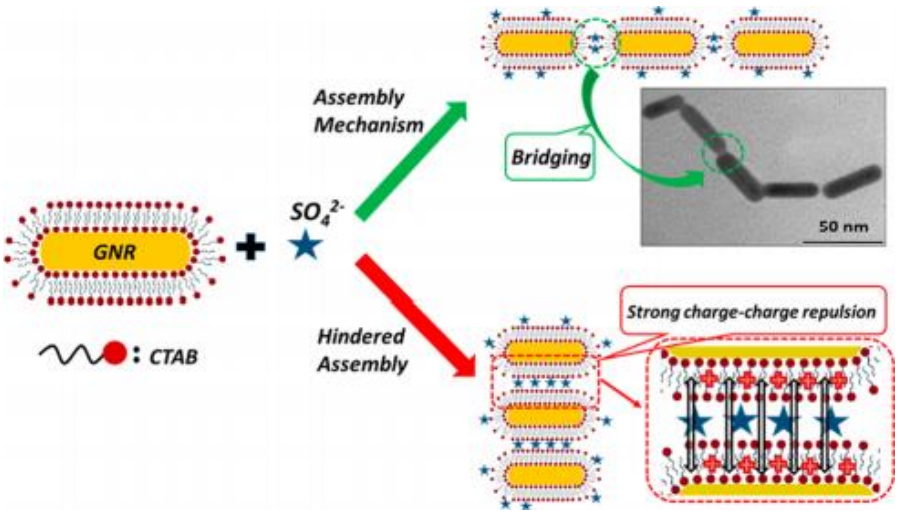

Figure 1.28 Sulfate-mediated end-to-end assembly of GNRs. Reprinted from Ref. 76.

Comprehending the mechanism of NP self-assembly is of critical significance in developing synthetic strategies for complex nanostructures, whereas the capability to visualize and analyze emerging nanostructures using characterization techniques can provide insight into intelligent molecular design and the mechanisms of chemical reactions. So far, monitoring the assembly process via AS and the subsequent analysis of the extinction bands as the function of reaction time has been widely reported.[76,166,167] However, the new plasmon bands comprise two different plasmon modes when the NPs coupled (see Figure 1.10), discriminating those modes is thus essential for understanding the assembly mechanism since their analysis is capable of providing information about the assembly kinetics, the yield of assembly, and the distribution of each species in the reaction system. In this respect, the singular value decomposition (SVD) method has been exploited to analyze the absorption spectrum quantitatively for extracting the time-dependent fraction of the principal components. This method reduces all the information to a few principal components and allows extracting the relative importance of each component as a function of time.[168–170] Conventional TEM provides direct-space images and yields a statistical description of the NP assemblies on a local scale. Liquid-cell TEM displays the assemblies in the suspension solution and gives useful information on the position and the orientation of the objects. Synchrotron-based SAXS provides further insight by revealing the evolution of the structure factor of the assemblies. Understanding the assembly mechanism, controlling the kinetics, and thereby obtaining the desired 1D assemblies is one of our goals. The study of NP assemblies using techniques such as UV-Vis-NIR absorption spectroscopy (AS), electron microscopy and synchrotron-based small-angle X-ray scattering (SAXS) measurements is demonstrated in Chapter 5.

1.4.3 Two-dimensional sheets

Freestanding 2D plasmonic superlattice nanosheets also termed plasmene nanosheets,[171] have attracted a lot of attention because of GNPs coupling producing unconventional collective properties including enhanced conductivity,[172] coherent vibrational modes,[173] unusual mechanical properties,[174] magnetic properties and plasmonic properties.[175,176] Several assembly strategies have been exploited, including the drop-casting method,[177] DNA-mediated self-assembly,[178] the Langmuir-Blodgett technique[179] and fluid-fluid interface assembly, including air-liquid,[180] vapor-liquid[181] and liquid-liquid as media combinations.[182]

Encouraging progress has been made in the fabrication of 2D assemblies over the past decade, with current achievements extending from simple GNSs[133] to binary[183] and other more complex NP shapes, such as GNRs,[176] core-shell GNPs@Ag nanocubes (NCs),[171] gold rhombic dodecahedrons (GRDs) and gold nanostars (GNstrs).[184] The plasmenes fabricated from some elongated NPs, such as GBPs and GNRs, have led to ordered arrays with different orientations.[176,185] More interestingly, the interparticle spacing in the plasmene nanosheet can be controlled by tailoring the size of the NPs or the ligand length, thereby adjusting their optical properties.[185,186] W. Chen et al.[151] summarized the development of the 2D assembly fabrication (see Figure 1.29).

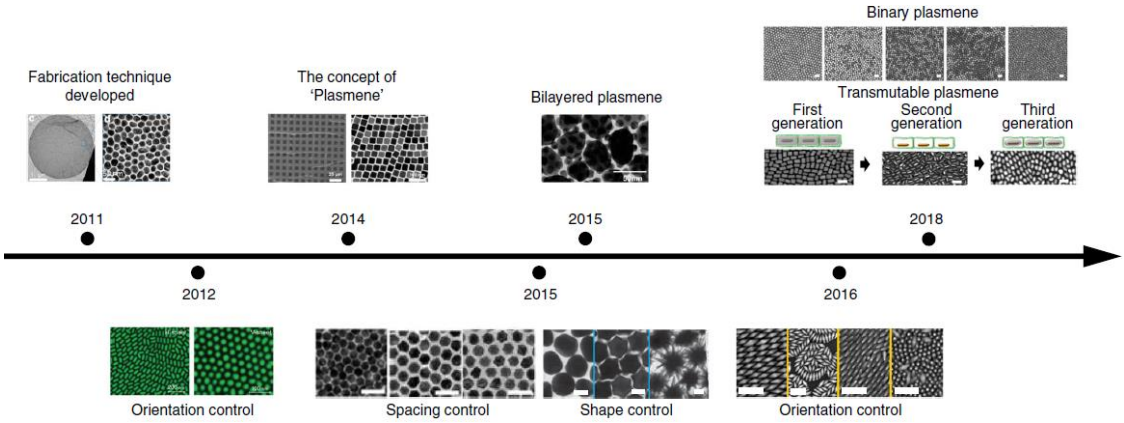

Figure 1.29 Development of plasmene superlattice nanosheets. The first plasmene nanosheet was obtained in 2011 using GNSs;[133] The concept of "plasmene" was introduced in 2014;[176] The complex NP shapes, such as GNRs,[176] core-shell GNPs@Ag NCs,[171] GRDs and GNstrs[184] were then developed from 2012 to 2015. A binary plasmene system[183] was built in 2018. Control of plasmene orientation, spacing and shape was realized.[176,184,185] Reprinted from Ref. 151.

1.4.4 Three-dimensional supercrystals

The organization of NPs into 3D supercrystals with both long-range translational and orientational order not only offers exciting opportunities to design a variety of intriguing and complex superstructures but also provides access to the emerging collective properties deriving from their ordered arrangements. Supercrystals, a class of ordered structures obtained by arranging individual NPs in lattices with a well-defined order, are sensitive to the morphology and concentration of NPs as well as to the type of surfactant and solvent used in the process.[187–190] In general, spherical NPs are organized into face-centered cubic (FCC) or hexagonal close-packed (HCP) superlattices.[153,191] On the other hand, anisotropic NPs with asymmetric shapes and inequivalent particle orientations are capable of producing far richer (and intriguing)

packing structures. For instance, the symmetry shift of the GNR superlattice from a typical hexagonal to a tetragonal by Rhodamine 6G (R6G) modification has been successfully achieved by Y. Liang and co-workers, the unit cell parameters were obtained by SAXS measurements (see Figure 1.30).[192] Recently, the self-assembly of uniform GdF_3 nanoplates with defined shapes via a liquid interfacial method has led to the formation of diverse ordered superstructures over large areas.[193] In addition, Zhang et al.[194] reported that gold triangular nanoplate@Ag right bipyramids are capable of self-assembly into a four-leaf-clover-like structure with a face-to-face configuration. Such behavior was explained by a depletion attraction mechanism.

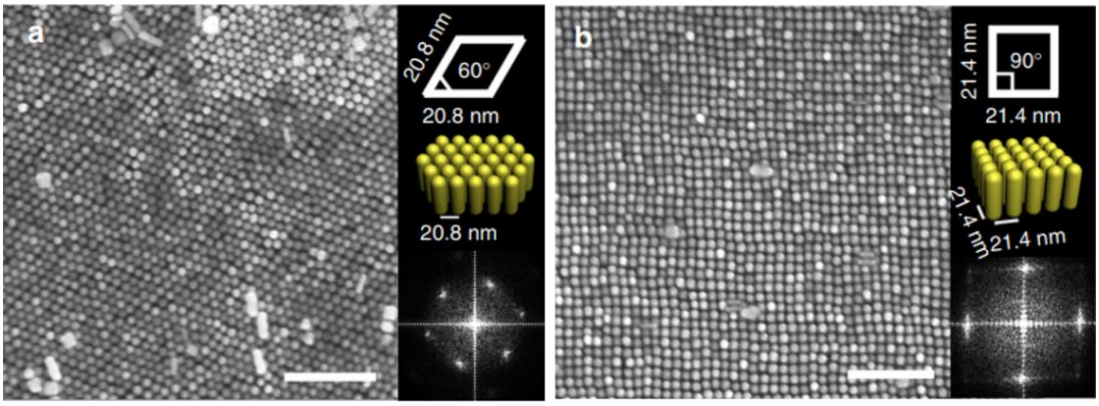

Figure 1.30 Symmetry control of the GNR superlattice from a typical hexagonal to tetragonal order by Rhodamine 6G (R6G) modification. In a typical SEM image of the hexagonal superlattice (a) and tetragonal superlattice (b), the scale bar is 200 nm. Reprinted from Ref. 192.

Controlling the symmetry of GNRs@Ag supercrystals with tunable cross-section was investigated by our group.[72] The hexagonal arrangement shifts to a square superlattice as the thickness of the silver coating increases, as demonstrated by SAXS. Moreover, the shift in lattice symmetry is also confirmed by the Fast Fourier Transform (FFT) analysis of the TEM images, which reveals six-fold symmetry shifts to four-fold symmetry (see Figure 1.31). This work opens the way toward an optimized architecture design for a broad range of plasmonic applications.

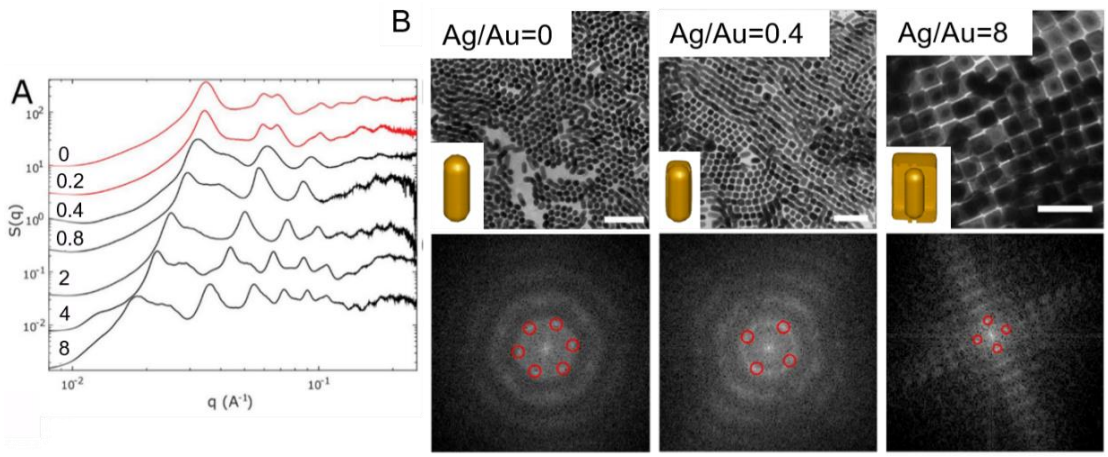

Figure 1.31 (A) Structure factors of GNR@Ag supercrystals with tunable silver to the gold ratio obtained from SAXS. The ratio is arranged on each SAXS spectra. The two spectra in red correspond to a hexagonal arrangement whereas the ones in black exhibit square symmetry. (B) Typical TEM images and associated FFT of GNR@Ag monolayers. The scale bar is 100 nm. Adapted from Ref. 72.

Moreover, in polyhedral particle assemblies, NPs with well-defined facets and high shape symmetries tend to mutually align with the flat facets towards their neighbors to maximize entropy.[153] In the past few years, experimental investigations on polyhedral NPs have included nanocubes, nanotetrahedra, nanoctahedra, dodecahedra and other polyhedral NPs with more complex facets. Z. Tang et al.[195] investigated the entire self-assembly process from disordered suspensions of spheres, cubes, octahedra and rhombic dodecahedra to large-scale ordered superlattices induced by nanocrystal sedimentation and eventual solvent evaporation (see Figure 1.32). For instance, each rhombic dodecahedron (RD) contacts with twelve neighbors' facet-to-facet (Figure 1.32a-d), and diffraction peaks of RD with varying sizes were indexed to the FCC lattice (sRD, mRD and lRD) (Figure 1.32q-s). The superlattices of the smallest particles (sRD) exhibit the sharpest and most intense diffraction spots of a single crystalline character (Figure 1.32q). This suggests that, despite the relatively small size of sRDs, their ordered domains are the largest. SAXS patterns of octahedron supercrystals have several well-defined peaks that cannot be assigned to a single lattice type (Figure 1.32o,t). The SEM analysis reveals octahedron NPs frequently assemble in two crystallographically distinct stacking modes of close-packed hexagonal layers, a base-centered monoclinic superlattice with a two-particle unit cell (Figure 1.32e,h) and a simple hexagonal superlattice (Figure 1.32e-g). In addition, it is evident from SEM images that cubes arrange into a simple cubic lattice (Figure 1.32i,j). SAXS data

demonstrates that it is more challenging to achieve order with cubes over large areas as compared with rhombic dodecahedra and octahedra (Figure 1.32p,u). Among the possible polymorphs for the octahedron supercrystals, the simple hexagonal arrangement was most frequently observed. Visual inspection shows that the size of the ordered domains of octahedron superlattices typically reaches only 100 microns, much smaller than sRD, mRD and lRD domains indicating that shape, rather than size, determines the quality of the assembly.

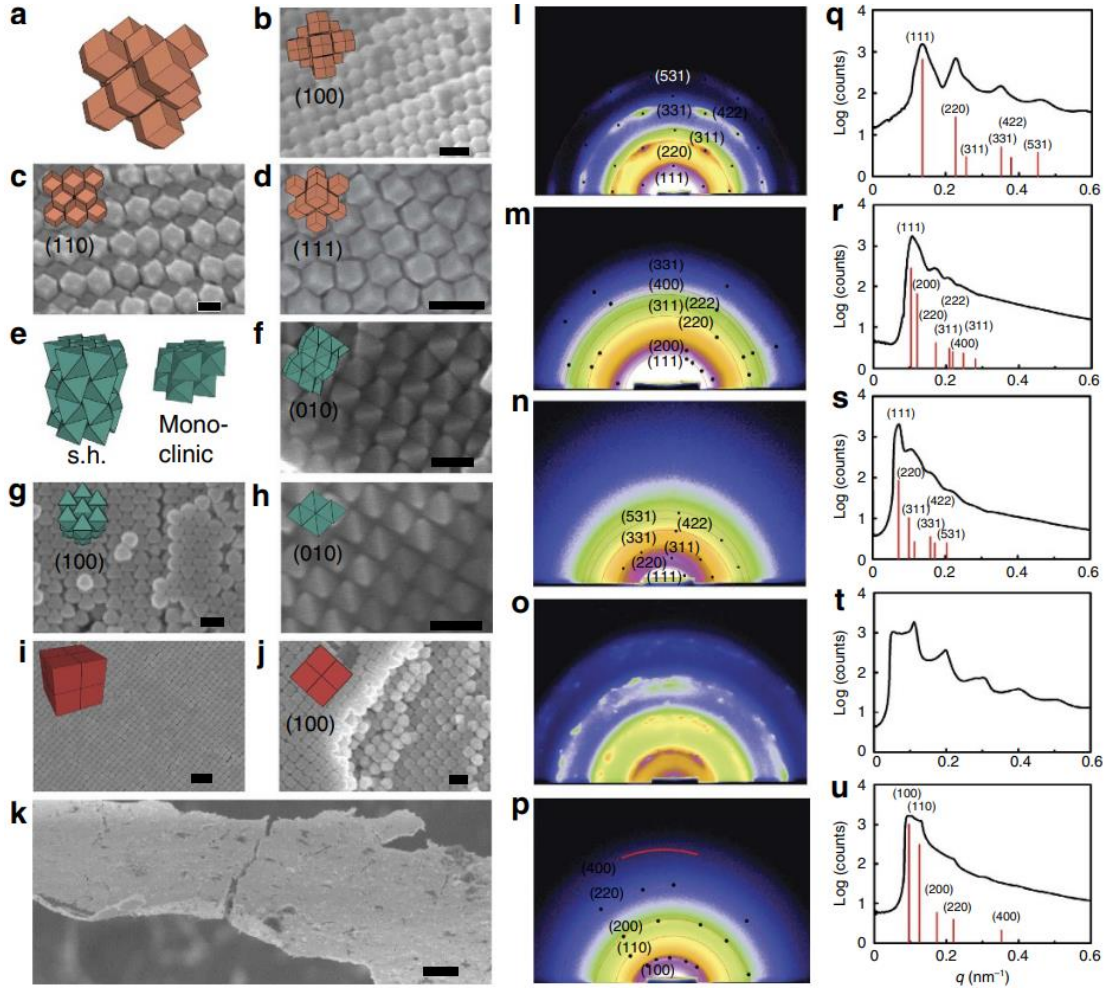

Figure 1.32 Determination of the symmetry of gold supercrystals using SEM and SAXS. (a-d) Rhombic dodecahedra form a face-centered cubic superlattice visible along with different projection directions. (e-h) Octahedra are found predominantly in two crystallographically distinct superlattices: simple hexagonal (e-g) and monoclinic (e, h). (i, j) Cubes assemble into a simple cubic lattice. (k) A macroscopic view shows a complete superlattice film. (l-p) Two dimensional and (q-u) radially averaged SAXS images of assembly products exhibit clear diffraction spots and peaks, respectively, highlighting long-range order in superlattices of sRD (l, q), mRD (m, r), lRD (n, s), octahedra (o, t) and cubes (p, u). Scale bars, (i) 200 nm; (k) 10 mm; all others are 100 nm. Reprinted from Ref. 195.

Designing high-quality dense supercrystals with increased structural complexity assembled by some particularly shaped nanoparticles is of notable interest. However, to date, the vast majority of the efforts have focused on isometric particles (with a similar size along with the three space directions, as we described above) and elongated shapes have received much less attention.[157,196] Pentatwinned gold bipyramids (GBPs) with pentagonal cross-section and shape anisotropy are outstanding due to the high-yield synthesis as well as the tunability of the optical properties and the sharper tips.[111,197] The self-assembly of GBPs has been studied within 1D chains and 2D monolayers, which both exhibit high SERS enhancements.[90,185] The first SEM images of 3D supercrystals have been reported by J. Wang group,[198] which reveals the surface arrangement of the particles, but this technique does not provide effective 3D information. Therefore, the complex packaging structure remains unknown and even more fascinating to date. In addition, high-quality crystallization also requires a high size and shape homogeneity of the particle assemblies, as well as a favorable set of experimental conditions, including the concentration of particle and of stabilizing surfactant. Moreover, investigating the structure of the supercrystals by electron microscopy in real space is challenging, as the electrons typically interact too strongly with the NPs to penetrate the bulk of supercrystals and reveal their 3D packing order. Therefore, self-assembly of pentagonal GBPs of varying truncation into 3D supercrystals was carried out by tuning the concentrations of particles and surfactants. Using a combination of experimental characterizations and computer simulations, we expect to reveal their 3D arrangement, see Chapter 6.

1.5 Scope of the thesis

This thesis work has been carried out within the frame of the Memorandum of Understanding between the Chinese Scholarship Council and Université Paris-Saclay (CSC NO. 201806870029), which focused on the fabrication of plasmonic NPs and the self-assembly of NPs. More specifically, the thesis was first oriented toward the observation of the growth of core-shell GNPs@Ag (gold nanospheres@Ag and gold bipyramids@Ag) and the characterization of their growth process through various experimental techniques. We then revealed the reshaping kinetics and the nonlinear optical properties of acicular gold nanotetrapods (GNTPs). The plasmonic NPs were finally assembled into one-dimensional (1D) and three-dimensional (3D) structures. In

particular, the enhanced electric field “hot spots” were exploited to detect molecules by the surface-enhanced Raman scattering (SERS) spectroscopy.

The experimental part was carried out mainly in the Laboratoire de Physique des Solides (LPS) at Orsay. Importantly, part of some major results included in the thesis stem from collaborations with external groups, mainly regarding the synchrotron-based small-angle X-ray scattering measurements with our collaborator Dr. Thomas Bizien at the SWING beamline of the SOLEIL synchrotron, liquid-cell TEM measurements with our collaborator Dr. Damien Alloyeau at Université de Paris, focused ion beam-scanning electron microscopy (FIB-SEM) tomography analysis with our collaborators Dr. Evgeny Modin and Dr. Andrey Chuvilin at Electron Microscopy Laboratory and Basque Foundation of Science (Spain), second-harmonic scattering experiments with our collaborators Prof. Pierre-François Brevet and Dr. Fabien Rondepierre at University Lyon 1, as well as the inductively coupled plasma mass spectrometry (ICP-MS) measurements by our collaborator Dr. Valérie Geertsen at CEA, the STEM-electron energy loss spectroscopy (EELS) experiments by our collaborators Dr. Xiaoyan Li and Dr. Mathieu Kociak and the Monte Carlo computer simulations by our collaborator Dr. Frank Smallenburg at LPS.

We give a brief outline of each chapter in the following:

In Chapter 1, we presented the general introduction about the main concepts that will be addressed throughout this thesis. Initially, we gave a brief description of nanotechnology and nanoscale phenomena, then focused on presenting a broad overview and the factors affecting the plasmonic properties of metal nanoparticles, introducing the importance of the assembly to obtain novel optical features, and their application in surface-enhanced Raman scattering (SERS) spectroscopy. We then continued with a detailed description of the synthesis strategy of plasmonic nanoparticles via the seed-mediated growth method, in particular the shape control of gold nanoparticles. We finally moved into the self-assembly of gold nanoparticles to produce plasmonic structures with novel optical properties.

In Chapter 2, we gave the details of all the chemical materials as well as the synthesis approaches for the various plasmonic NPs (i.e. gold nanospheres, nanorods, bipyramids, tetrapods and core-shell objects) and characterization techniques in this thesis.

Then, in Chapter 3, we focused on monitoring the growth of core-shell GNP@Ag nanoparticles, determining the morphology and concentration of core-shell gold nanospheres@Ag nanoparticles and then observing the anisotropic growth of Ag on gold bipyramids in-situ, revealing the roles of additives (AA and CTAC).

We next revealed the reshaping mechanism of GNTPs by demonstrating their reshaping kinetics, as well as controlling their stability with a thin silver layer. We also studied their nonlinear optical properties, i.e. the second harmonic generation signal of GNTPs.

Various types of surfactant-stabilized GNPs (spheres, rods and bipyramids) were assembled into 1D chains using sulfate ions in Chapter 5. We investigated the assembly kinetics by AS and SAXS, controlling the process with excess CTAC and then tuning the nature of the chains junction by depositing a metal at the hot spots' location in chains.

In Chapter 6, we obtained long-range 3D supercrystals of pentagonal gold bipyramids and revealed their structure via a combination of several characterization techniques: synchrotron-based SAXS and focused ion beam-scanning electron microscopy (FIB-SEM) tomography analysis, in agreement with the Monte Carlo (MC) computer simulations. The crystalline order of the GBPs supercrystals results in a facet-dependent optical response, which is demonstrated by SERS spectroscopy.

As a whole, this thesis presents significant advancements in both the synthesis and self-assembly of different plasmonic nanoparticles, improving the knowledge of core-shell NPs growth as well as assembly mechanisms and arrangements.

2 Materials and methodology

This chapter starts by covering the chemical reagents we used, as well as general protocols and tips for the synthesis of various nanoparticles (NPs), i.e. gold nanorod (GNRs), gold nanospheres (GNSs), gold bipyramids (GBPs), gold nanotetrapods (GNTPs), and core-shell GNPs@Ag. Furthermore, we present the main characterization and measurement techniques used in our work. UV-Vis-NIR absorption spectroscopy (AS) is an essential tool for providing information on the plasmon peak positions, gold concentration and the density of the particles from the extinction spectrum of the suspensions. Scanning electronic microscopy (SEM) and transmission electron microscopy (TEM) were used to obtain direct images of the samples. *In situ* liquid-cell TEM (LCTEM) is an emerging technique for interpreting the mechanisms of formation of nanostructures with nanoscale resolution in real time. Focused ion beam-scanning electron microscopy (FIB-SEM) tomography analysis revealed the internal structure of NPs assemblies. Synchrotron-based small-angle X-ray scattering (SAXS) was utilized to investigate the morphology, polydispersity, concentration and organization of the NPs under a realistic environment throughout almost the entire thesis, helping us achieve a deeper understanding of the systems. Inductively coupled plasma mass spectrometry (ICP-MS) was carried out to yield the individual elemental concentration of the GNPs@Ag solution. To gain knowledge of the nonlinear optical properties and the second harmonic generation signal of GNTPs, hyper Rayleigh scattering (HRS) was employed. Additionally, surface-enhanced Raman scattering (SERS) spectroscopy is a sensitive technique that allows detecting trace amounts of molecules deposited on the GNP supercrystals.

2.1 Synthesis protocols of nanoparticles

All the starting materials were obtained from Sigma-Aldrich and used without further purification: hydrogen tetrachloroaurate trihydrate ($HAuCl_4 \cdot 3H_2O$, ≥99.9%), hexadecyltrimethylammonium bromide (CTAB, ≥99%), silver nitrate ($AgNO_3$, ≥99.0%), hexadecyltrimethylammonium chloride (CTAC, 25 wt % in H_2O, 90%), 5-bromosalicylic acid (5-BrSA, 90%), L-ascorbic acid (AA, ≥99%), sodium borohydride ($NaBH_4$, 99%), trisodium citrate dihydrate ($C_6H_3Na_3O_7 \cdot 2H_2O$, ≥99.0%), sodium hydroxide (NaOH), and hexamethylenetetramine (HMT) were purchased from Sigma-

Aldrich. Magnesium sulfate ($MgSO_4$, ≥ 95%) was purchased from Prolabo. Water purified by reverse osmosis with a resistivity (>15 MΩ.cm) was used in all experiments.

Gold nanoparticles (GNPs) were synthesized via the seed-mediated method according to the previously reported works.[199–201] As we mentioned in Section 1.3, the final morphology of the GNPs is governed by various parameters, including the crystallinity of the seeds,[57] the type of surfactants with different halide ions as capping agents and reducing agents and the ratio of the metal salt to reductant.[202,203] In addition, changing the redox potential by adjusting the pH of the reducing agent can also affect the shape of the NPs.[118] Various GNPs have been synthesized in our work, see Figure 2.1. Among them, GNSs, GNRs and GNTPs can grow on monocrystalline spherical seeds, while the GBPs are formed with pentatwinned seeds. In growth solution, the surfactants CTAB and CTAC act as capping agents and $AgNO_3$ acts as a shape-directing agent. Especially, AA typically as a reducing agent also plays a shape-directing role. HMT is widely used as a surface capping agent, and it also acts as a reducing agent for $HAuCl_4$ in the process of GNTPs synthesis. The details of synthesis protocols will be presented below.

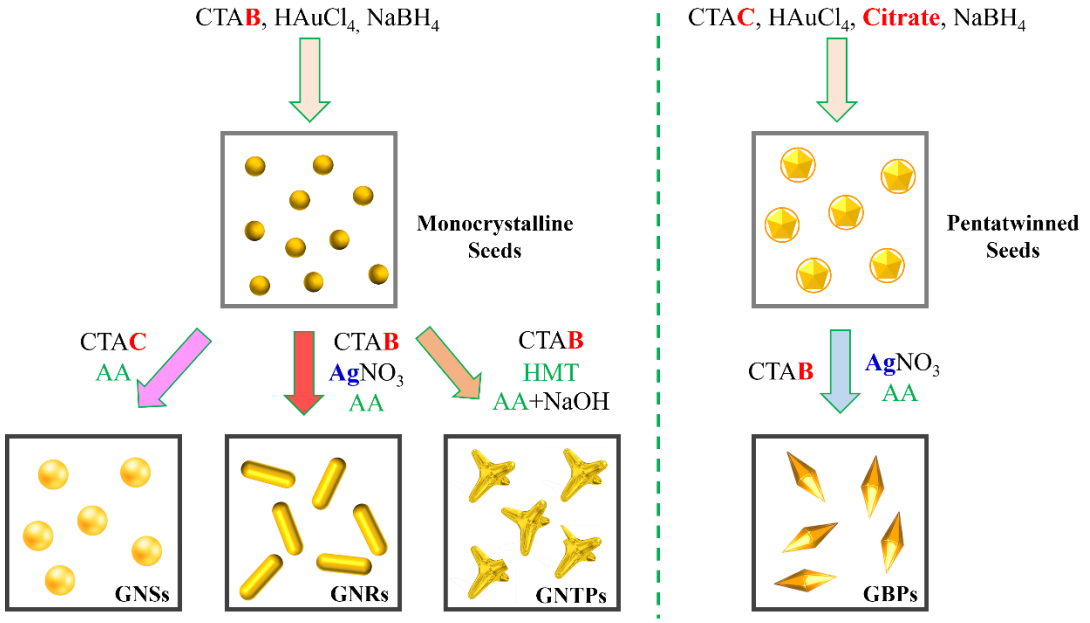

Figure 2.1 Schematic representation of GNPs synthesis with different shapes.

2.1.1 Monocrystalline gold nanorod synthesis

Gold nanorods (GNRs) were synthesized according to previously reported methods.[113,204] For the preparation of the seeds, 50 µL of 0.025 M $HAuCl_4$ solution was

added to 4.7 mL of 0.1 M CTAB solution, after mixing, 300 µL of freshly prepared 0.01 M $NaBH_4$ solution was injected under vigorous stirring. The color of the solution changed from yellow to brownish-yellow and then stirring was stopped after 2 min. The seed solution was aged at 30°C for at least 30 min before injection into the growth solution.

The growth solution was prepared by mixing 50 mL of 0.05 M of CTAB with 45 mg of 5-BrSA dissolved, 480 µL of 0.01 M $AgNO_3$ and 1 mL of 0.025 M $HAuCl_4$ solution. The process of prereduction was monitored by AS, when the absorbance at 396 nm reached 0.65 (the optical path of the cuvette is 1 cm), 130 µL of 0.1 M AA solution was injected quickly under fast stirring. When the solution turned colorless, 80 µL of previously synthesized seed solution was added quickly as well, the mixture was then kept at 30°C for 4 h. After synthesis, the suspension was purified by 2 rounds of centrifugation (6000 rpm, 40 min) to remove the excess CTAB and then re-dispersed in 1.8 mM CTAB solution.

2.1.2 Gold bipyramid synthesis

Gold bipyramids (GBPs) were synthesized following the publications.[111,205] For the preparation of pentatwinned seeds, 2645 µL of 0.756 M CTAC, 32.96 mL of purified water and 400 µL of 25 mM $HAuCl_4$ were injected into the flask in sequence, then 4 mL of 50 mM sodium citrate was added under vigorous stirring. The solution was kept in a water bath at 30°C for 10 min. 1 mL of freshly prepared 25 mM $NaBH_4$ solution was injected under vigorous stirring, then the reddish-purple seed solution was obtained after aging at 40°C for 5 days. The seed solution can be stored for at least one month at room temperature.

The growth solution was prepared by adding successively 100 mL of 0.1 M CTAB, 1 mL of 10 mM $AgNO_3$, 2 mL of 25 mM $HAuCl_4$ and 2 mL of 1 M HCl. Then 800 µL of 100 mM AA solution was added quickly under vigorous stirring, followed by the addition of 600 µL of seed solution when the solution turned colorless. The mixture was left undisturbed at 30°C for 4 h. After synthesis, the particles were purified by at least 2 rounds of centrifugation and pellet redispersion in 1.8 mM CTAB.

2.1.3 Gold nanosphere synthesis

Gold nanospheres (GNSs) were obtained following three steps as in the literature.[206] Specially, S0 seeds: 50 µL of 0.025 M $HAuCl_4$ solution was added to 4.7 mL of 0.1 M CTAB solution. After mixing, 300 µL of freshly prepared 0.01 M $NaBH_4$ solution was injected under vigorous stirring, the seed solution was then kept at 30°C.

S1 spheres: 120 µL of 0.025 M $HAuCl_4$ solution and 10.38 mL of purified H_2O were added to 1.5 mL of 0.756 M CTAC solution, then 4.5 mL of 100 mM AA solution was added quickly under vigorous stirring, followed by the addition of 300 µL of S0 seed solutions when the solution turned colorless. The solution was kept at 30°C.

S2 spheres: 120 µL of 0.025 M $HAuCl_4$ solution and 10.38 mL of purified H_2O were added to 1.5 mL of 0.756 M CTAC solution, then 4.5 mL of 100 mM AA solution was added quickly under vigorous stirring, followed by the addition of 300 µL of the solution of S1 spheres when the solution turned to colorless. The mixture was left undisturbed at 30°C for 1 h. After synthesis, the particles were purified by at least 2 rounds of centrifugation and pellet redispersion in 1.8 mM CTAB.

2.1.4 Gold nanotetrapod synthesis

The gold nanotetrapod (GNTPs) were prepared by a method reported previously.[68] Seed solution: 3.5 mL of a 0.14 M CTAB solution was mixed with 125 µL of 15 mM $HAuCl_4$ and 0.50 mL of freshly prepared 10 mM $NaBH_4$. The brownish-yellow solution was kept at 30°C.

Solution A: 0.38 mL of 15 mM $HAuCl_4$, 3.0 mL of 0.10 M CTAB, 3.0 mL of 0.10 M HMT, 1.0 mL of 10 mM AA, and 0.62 mL of purified water were added in turn to a 50 mL centrifugation tube. Solution B: 6 mL of purified water, 60 µL of 1.0 M NaOH and 5 µL of seeds solution were added to a 20 mL glass. Solution B was added quickly to solution A under rapid stirring. The mixture went from colorless to deep blue in a few minutes, indicating the complete formation of GNTPs.

After synthesis, 8.44 mL of a 29 mM CATC was injected into the mixture, the final gold concentration was 0.25 mM and the CTAC concentration was 10 mM. This step not only prevents the crystallization of CATB in the solution at room temperature to help us continuously monitor the reshaping of the GNTPs with AS but also facilitates our subsequent experiments of introducing a thin layer of silver.

2.1.5 Synthesis of core-shell gold@silver nanoparticles

Core-shell gold@silver were prepared by depositing silver onto the GNPs, AA as a reducing agent and a shape-directing agent and the thickness of silver can be tuned by adjusting the amount of silver precursor and AA in the reaction mixture.[207,208] As shown in Figure 2.2, taking GBPs coating with silver as an example, the specific experimental process refers to the previous work of our group,[72] 0.25 mM GNP solution purified with 10 mM CTAC was put into a centrifugation tube, followed by the addition of $AgNO_3$ and AA. The molar ratio between the silver precursor and AA was fixed to 4 in all experiments. After mixing, the solutions were kept at 60°C for 3 h. After synthesis, the particles were purified by 2 centrifugation rounds (6000 rpm, 40 min) to remove the excess of reactant and pellet redispersion in 1 mM CTAB. The final gold concentration of all samples was 0.25 mM.

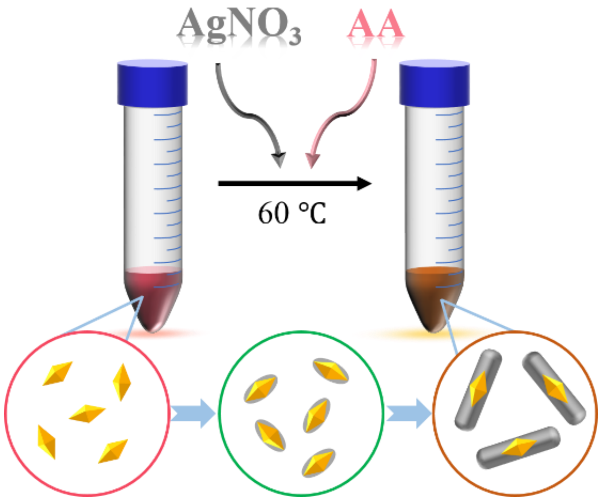

Figure 2.2 Schematic description of GBPs@Ag synthesis.

What needs special mention here is the preparation of gold nanotetrapods@Ag (GNTPs@Ag). As described earlier, the branched GNPs show poor stability and tend to reshape their morphology, which can change their plasmonic properties.[81] Therefore, maintaining the shape of GNTPs in the shortest time is essential for further application. Here the reducing power of AA was increased by increasing the pH in the solution, thus the silver thin layer can be formed and stop the reshaping of GNTP in several seconds. Specifically, 0.25 mM GNTPs solution purified with 10 mM CTAC was put into a centrifugation tube, followed by the addition of 10 mM $AgNO_3$, 40 mM AA and 0.2 M NaOH. GNTPs@Ag were obtained at room temperature after a few minutes. The thickness of silver can also be adjusted by tuning the amount of silver precursor and AA.

2.1.6 General tips for gold nanoparticles synthesis

Every step in the synthesis process plays an important role in the quality of particles and reproducibility of the results. The following general practical tips are displayed combined with the recommendations from Ref. [16] and our experience.

- Stock Solutions:

- CTAB - stable over a long time in a 30°C water bath to prevent crystallization at low temperature.
- $HAuCl_4$ - prepared by dissolving all contents in a sealed bottle due to hygroscopicity. Then the stock can be split into small glass vials and stored in the refrigerator, protected from sunlight, and kept for several months.
- $AgNO_3$ - weigh silver salt with a plastic spatula to avoid contact with metal surfaces. The solution should be freshly prepared every week, stored in the fridge protected from sunlight.
- AA - freshly prepared every week, stored in the fridge protected from sunlight.
- HCl - stable over a long period at room temperature.
- $NaBH_4$ - freshly prepared every time and weighed quickly as the powder is hygroscopic.
- Stock solutions should be discarded if significant changes are observed, e.g. dark lid for $AgNO_3$, yellowish color for ascorbic acid and dark insoluble matter for $HAuCl_4$.

- CTAB/CTAC foam:

Shaking or stirring the solution causes CTAB or CTAC to form foam above the solution. When adding reagents with a micropipette, the micropipette tip should be inserted directly into the solution. Because the reagents entering the foam may not be properly mixed, thereby affecting the synthesis conditions.

- Seed solution:

The reducing agent ($NaBH_4$) should be injected instantly into the solution to achieve the simultaneous generation of all nuclei so that they are evenly distributed throughout the solution volume.

- Growth solution:

AA is injected into the solution under rapid stirring. After the solution and foam have completely turned colorless, then add quickly the seed solution.

- Centrifugation step:

After synthesis, centrifuge the particles solution at least twice to re-disperse the particles in a low concentration of surfactant. For larger-sized nanoparticles, lower-speed centrifugation should be used to avoid the aggregation of nanoparticles. The size of the nanoparticles can be estimated based on the position of the LSPR peak in the AS.

- Glassware and stirring bar cleaning:

All glass bottles and stirring bars must be washed with soap and water firstly, then soaked in aqua regia, rinsed thoroughly with water, ethanol, acetone and then dried.

2.2 UV-Vis-NIR absorption spectroscopy

The extinction spectrum of all dispersion GNPs was measured using the Cary 5000 UV-Vis-NIR absorption spectroscopy (AS) at room temperature, using disposable polystyrene cuvettes (VWR European Cat. NO. 634-0675) with an optical path of 1 cm. The absorbance of purified water in the same cuvette used for the solution was measured in a double-beam configuration and used as a reference in all experiments. The AS spectrum of monocrystalline GNRs is shown in Figure 2.3 as s typical example, which exhibits two different plasmon peaks and the position of the longitudinal peak compared to the transverse peak gives us a quick estimate of the aspect ratio (AR =length/width).[16] How the dispersion of the particles can be known from the full width at half maximum (FWHM), which is fitted by the Lorentzian function. The GNPs concentration can be derived from the absorbance at 400 nm, as well as the presence of a shoulder on the transverse band shows the presence of by-products.[16,209]

In addition, the reshaping process of GNTPs was monitored by a V-630 UV-Vis spectrophotometer (Jasco) in a double-beam configuration to measure the absorption spectrum of dilute particle solutions between 250 and 1000 nm. The solutions were held in quartz cuvettes (Hellma) with a 1 cm optical path, at a temperature fixed by a Lakeshore 340 temperature controller.

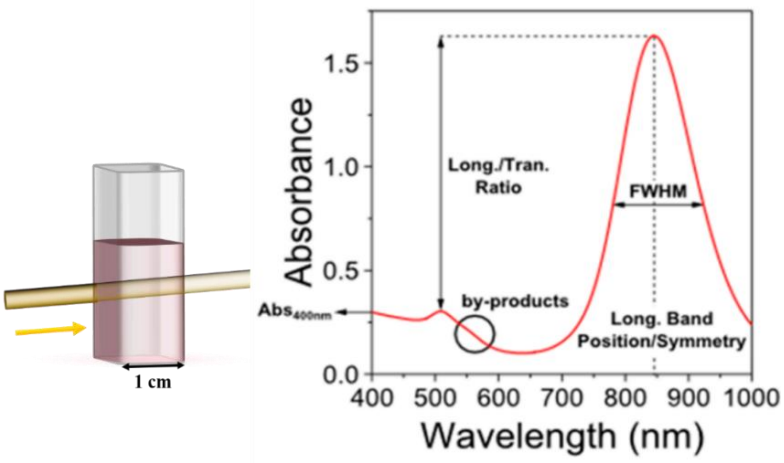

Figure 2.3 Typical AS spectrum of monocrystalline GNRs. Adapted from Ref. 16.

2.3 Microscopy techniques

2.3.1 Standard transmission electron microscopy

The morphology of NPs is commonly performed by standard transmission electron microscopy (TEM). TEM images were obtained on 300 mesh carbon-coated copper grids using a JEOL 1400 microscopy, operating at an acceleration voltage of 120 kV. Transmitted through the grids of the deposited sample, a broad beam of electrons arrived at a detector below and then the 2D images were created directly on a fluorescent screen or onto a computer screen using a charge-coupled device (CCD) camera. The microscopy images are recorded using Gatan Digital Micrograph software.

The visual state of the samples is extremely related to the preparation process. Re-disperse and concentrate the particles in a surfactant solution with a low concentration (below 0.5 mM) by mild centrifugation at 2300 rpm, the final gold concentration is around 1 mM. 10 µL of particle deposition was dropped on a carbon-coated grid and dried fast at 70°C to prevent particle aggregation during the drying process.

2.3.1.1 Particle analysis

The dimensions of NPs were extracted by using the ImageAnalyzeParticles operation in Igor Pro 7.0. GNSs for example, the individual particles were modeled as ellipses with half-axes a and b, their equivalent radius R was computed as $R = \sqrt{a \times b}$. Due to the low relative contrast between gold and silver, only the outer boundary of the particles was detected, so R corresponds to the radius of the complete object. The size

distribution of the GBPs or GNRs was determined by manual TEM image analysis using the ImageJ software.

As for GNTPs with obvious arms, the size distribution of particles was obtained manually using the ImageJ software. The core diameter $2R$ was estimated by drawing the inscribed circle centered on the particle, while the arm length L was estimated as the distance from this circle to the tip of the arms and corrected for the arm tilt α with respect to the substrate (with a tilt angle of α =19.5°). Whereas for the GNTPs (where the arms are no longer present), the analysis procedure was the same as what we dealt with for GNSs.

The distribution of 1D chains was obtained using the ImageJ software as well. We determined the average area of the isolated particles and used it to normalize the area of all identified objects. The objects were sorted according to the normalized area and the number of chains with n monomers was calculated by summing objects between $n - 0.5$ and $n + 0.5$. The contact distribution was obtained by manually counting all the contacts in 5 images.

Note that the dimensions of NPs are represented as $\bar{X} \pm \sigma$, where $\bar{X}$ is their mean value $\bar{X} = \frac{1}{N}\sum_{i=1}^{N} X_i$, X_i are the values of each measurement and N is the number of measurements. The standard deviation, σ, is determined as follows:

$$\sigma = \sqrt{\frac{1}{N-1}\sum_{i=1}^{N}(X_i - \bar{X})^2} \qquad (2\text{-}1)$$

2.3.1.2 Electron energy loss spectroscopy

Electron energy loss spectroscopy (EELS) available on TEM is a common spectroscopy technique and is in principle capable of measuring the amount of energy loss owing to some of the electrons undergoing inelastic scattering, resulting in lost energy and having their paths slightly and randomly deflected. A prominent form of inelastic scattering in solids involves plasmon excitation. This phenomenon arises from the fact that outer-shell electrons (conduction electrons in a metal, valence electrons in a semiconductor or insulator) are only weakly bound to atoms but are coupled to each other by electrostatic forces.[210] In our case, the plasmonic response of the

nanostructures was studied using EELS in the NION CHROMATEM monochromated Cs-corrected scanning transmission electron microscope. The 15 nm thick Si_3N_4 support membrane grids were used for NPs deposition to provide a carbon-free background at the low energy range for a better observation of the plasmonic peaks. The EELS spectrum images were acquired at 60 keV, with a spatial resolution of 0.5 nanometers and a typical energy resolution of 20 meV. The EELS spectra were extracted by summing a few hundreds of spectra in a region of interest close to the nanostructures and normalized by the intensity of the zero-loss peak (ZLP).

2.3.2 Liquid-cell transmission electron microscopy

LCTEM imaging was performed on a JEOL ARM 200F microscope operating at 200 kV, using a liquid-cell TEM holder (Poseidon select, Protochips inc.). The microscopy was operated in scanning transmission electron microscopy (STEM) mode with a beam current of 225 pA using a high-angle annular dark-field (HAADF) detector. The geometry of the scanning electron beam, liquid-cell and HAADF detector[211] are shown in Figure 2.4a, the electron beam passes through two SiN membranes which separated the liquid from the microscope vacuum. Compared with standard TEM, the specimen is preceded by deflection scan coils and the objective lens in the STEM mode[212] (see Figure 2.4b) and a parallel beam used enables focus on a small part of the sample and scanning uniformly the samples.

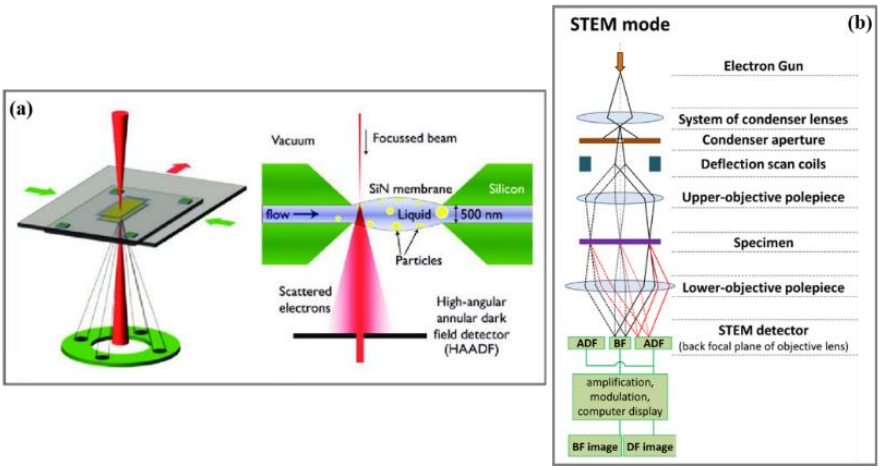

Figure 2.4 (a) Schematic of the LCTEM geometry (left) and a cross-sectional schematic of the arrangement of the SiN membranes (right). (b) Experimental setup of STEM mode. Adapted from Ref. 211 and Ref. 212.

For the growth of GBPs@Ag, a colloidal suspension of GBPs seeds (with a gold concentration of 0.25 mM) dispersed in a CTAC aqueous solution (10 mM) was

encapsulated in the liquid cell by using the conventional loading process.[213,214] When AA was present in the reaction media, its concentration was 2.25 mM. The gold spacers of the liquid cell were 150 nm thick and the experiments were performed in the corners of the observation window, where the liquid thickness is minimum. The liquid cell was used in static mode. Growth experiments were performed before and after the formation of a hydrogen bubble in the liquid cell improves the signal-to-noise ratio of images. We did not notice any difference in the growth processes of GNPs@Ag with or without the hydrogen bubble. STEM HAADF imaging was performed with a pixel dwell time of 5 µs and probe current ranging from 7.7×10^7 to 4.7×10^8 electron/s. The electron dose rate of each growth experiment was calculated in electrons.s^{-1}·nm^{-2} by dividing the probe current by the irradiated area (i.e. the image area in STEM mode). STEM diffraction was performed after the formation of the hydrogen bubble with a probe current of 10^8 electron/s.[215]

In the case of 1D chains, a colloidal suspension of chains (with a gold concentration of 2.5 mM) dispersed in a CTAC aqueous solution (10 mM) was encapsulated in the liquid cell by using the conventional loading process. Videos were acquired with a frame rate of 25 frames per second. From each movie, we extract every third frame and determine the outlines of the two particles using the ImageAnalyzeParticles operation in Igor Pro 7.0 (we discard the frames where the algorithm identifies more or less than two objects). The useful information is the position of the center of mass and the orientation of the objects, given by the angle of the major axis for the fitted ellipse. In the videos, the center of mass is indicated by a red dot and the ellipse is drawn in blue.

2.3.3 Scanning electron microscopy

Scanning electronic microscopy (SEM) characterization for supercrystals was performed at the Laboratoire de Physique des Solides (LPS, Orsay, France) with a Zeiss Supra55VP with an acceleration voltage of 5 keV.

Focused ion beam scanning electron microscopy tomography (FIB-SEM) was performed at CIC Nanogune (San Sebastian, Spain), in a Helios Nanolab 450 FIB-SEM (Thermo Fisher Scientific). After defining the area of interest, a standard preparation protocol was followed: deposition of an ≈ 1 µm Pt protective layer (starting with electron beam-induced deposition to prevent surface damage and followed by ion beam-induced deposition), trenches were milled around the examined volume and the

cross-section was polished to reveal the structure and perform a final optimization of imaging conditions in the electron beam. Slicing was then performed with the ion beam at an accelerating voltage of 30 kV and a beam current of 24 pA. After each FIB cut, an electron image was acquired using the high-resolution mode at 5 kV and 25 pA. The resulting image had a field of view of 2.1 × 1.4 μm^2 at 1536 × 1024 px resolution, which corresponded to a pixel size of 1.4 × 1.4 nm^2. A series of 200 slices were acquired, with a target slice thickness of 7 nm. Further data processing, including alignment, filtration, and visualization was performed using the Aviso 8.1 software (Thermo Fisher).

2.4 Small-angle X-ray scattering

Small-angle X-ray scattering (SAXS) is a structural characterization technique that enables researchers to investigate NPs' behavior in solution as well as crystal growth and hierarchical structure at nanometer and angstrom length scale in real-time and under a realistic environment.[216,217] In addition, X-ray scattering makes use of the variation of a sample's electron density to generate contrast. A typical SAXS experimental set-up[218] is shown in Figure 2.5, a monochromatic X-ray beam of the incident wave vector k_i is selected and passes though the sample, one part of this beam is absorbed and transformed into heat and/or fluorescence radiation, another part is scattered into another direction of propagation.

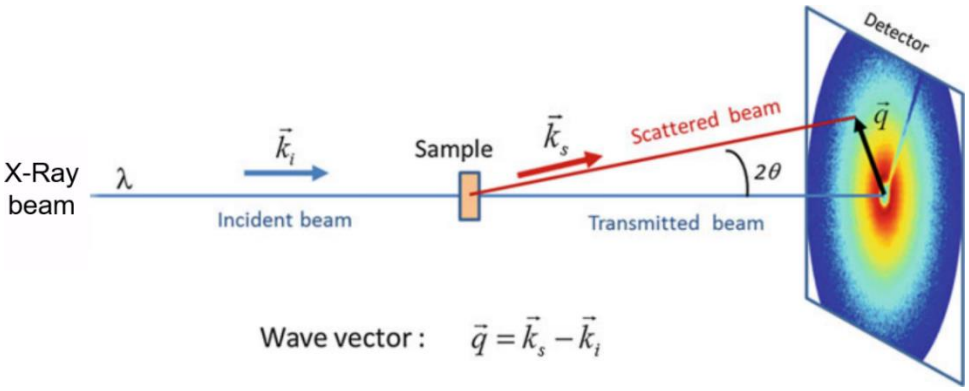

Figure 2.5 Schematic for the optical components of the SAXS beamline. Adapted from Ref. 218.

Generally, a two-dimensional (2D) area detector is used to collect the angle-resolved SAXS signal that is elastically scattered by the sample.[218] Elastic interactions are characterized by zero energy transfers, such that the final wave vector k_s is equal in modulus to k_i. The relevant parameter to analyse the interaction is the momentum transfer or scattering vector $q = k_s - k_i$, defined by:

$$q = \frac{4\pi \sin\theta}{\lambda} \tag{2-2}$$

where λ is the wavelength of the X-ray and 2θ is the scattering angle.

After the scattered signal is recorded by a 2D detector, a series of standard 2D data correction processes are performed, including dark current subtraction, image distortion and linear correction, and flat field correction. Then, the position of each pixel on the 2D image is converted into the 1D profile via a simple integration.[216] The process of data conversion and a typical 1D profile are shown in Figure 2.6.[219]

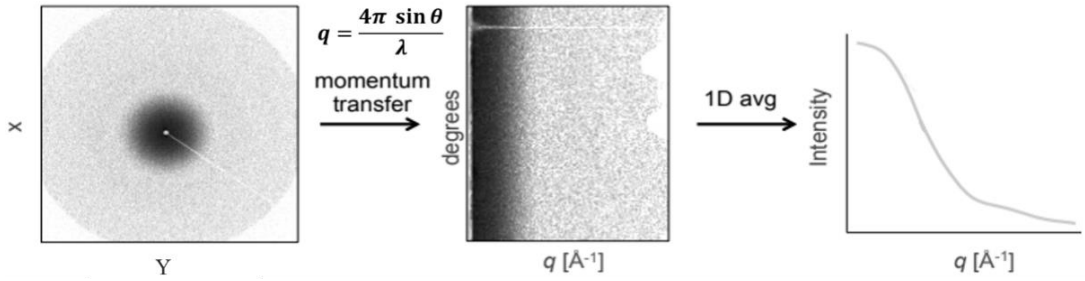

Figure 2.6 The process of data conversion in SAXS experiments. Adapted from Ref. 219.

The intensity $I(q)$ is plotted versus q, in the range $q_{min} - q_{max}$ defined by the experimental set-up and usually fixed by geometric limitations, a measurement made at a given q_0 allows investigating the density fluctuations in the sample on a distance scale $D_0 = \frac{2\pi}{q_0}$. It is equivalent to observing the system through a $\frac{2\pi}{q_0}$ diameter "window" in real space.[220] It is well known that $I(q)$ can be obtained by calculating the squared modulus of the amplitude function, defined in the reciprocal space (q space), of those waves scattered over the whole volume i.e. $I(q) = \frac{|F(q)|^2}{V}$. The scattering amplitude $F(q)$ is given by the Fourier transform of the electronic density $\rho(r)$:

$$F(q) = \int_V^0 \rho(r)\, e^{-iqr} dr \tag{2-3}$$

which corresponds to the probability to find a scattered at position r in the sample and the reference scattered at position 0, revealing the spatial correlations in the sample. When the particles are randomly oriented, the $I(q)$ can be represented as:

$$I(q) = \frac{1}{N_p} \left| \sum_1^{N_p} F(q)\, e^{-iqr} \right|^2 \tag{2-4}$$

where N_p is the number of identical particles, $F(q)$ and r is the form factor amplitude and position of the particle, respectively. The exponential term e^{-iqr} is called the phase factor.

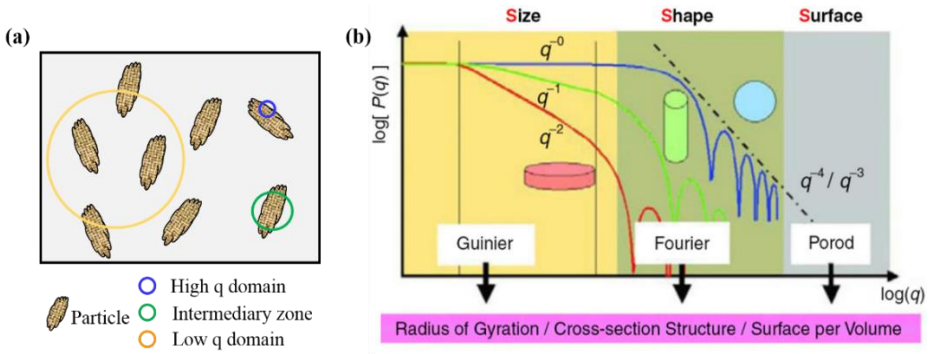

Figure 2.7 (a) Illustration of different q region at different observation windows. (b) Three distinct regions of the SAXS profile. Adapted from Ref. 217.

The SAXS profile is generally divided into three distinct regions, according to the range of q (see Figure 2.7). The high q domain (blue zone) with a small window provides information about surfaces such as the surface-to-volume ratio and specific surface estimation for compact particles. There is a contrast only at the interface between the two media, the so-called Porod's region. In the intermediary zone (Fourier region), the window is of the order of the elementary bricks in the system, which gives significant information about the size, shape and internal structure of one particle. And the pair distribution function $p(r)$ can be given by an indirect Fourier transformation of the experimental form factor $P(q)$, which refers to the distribution of electrons averaged over the radius r:

$$p(r) = \frac{1}{2\pi^2 r}\int_0^\infty qP(q)\,sin(qr)\,dq \qquad (2\text{-}5)$$

The left is the Guinier region at the low q region gives information about the radius of gyration (R_g) of the particles by fitting a line to the natural log of the intensity as a function of the square of the scattering vector q.[217] The structural order can also be obtained, it is the so-called structure factor $S(q)$, which allows to calculate the interactions in the system. After assembly of NPs, the NPs come closer to each other, and their relative interparticle distance may no longer be random. Thus Eq. (2-4) should be:

$$I(q) = \frac{1}{N_p} P(q) \left| \sum_{1}^{N_p} F(q)\, e^{-iqr} \right|^2 \tag{2-6}$$

and then the sum of the absolute square of the phase factor is defined as the structure factor:

$$S(q) = \frac{1}{N_p} \left| \sum_{1}^{N_p} F(q)\, e^{-iqr} \right|^2 \tag{2-7}$$

to this end, the $S(q)$ can be represented as:

$$S(q) = \frac{I(q)}{P(q)} \tag{2-8}$$

In general, a quantitative analysis of $S(q)$ can provide the strength and range of the potential of mean force between the NPs' variety of ordered states, revealing their structure and long-range order in the case of high-resolution synchrotron-based SAXS such as supercrystals. The common lattices are extracted by the Bragg peaks position ratios of $S(q)$. That is calculating the ratio of $\frac{q}{q_0}$, where q_0 denotes the first-order scattering peak with the largest interparticle distance. Typically, Bragg peaks in a $1: 2: 3: 4: 5$ progression signal lamellar symmetry, the $1: \sqrt{3}: 2: \sqrt{7}: 3$ progression is characteristics of the hexagonal arrangement, the $1: \sqrt{2}: \sqrt{3}: 2: \sqrt{5}$ sequence indicates a body-centered cubic symmetry and the $1: \sqrt{2}: 2: \sqrt{5}: \sqrt{8}$ progression indicates a square lattice arrangement.[72,219]

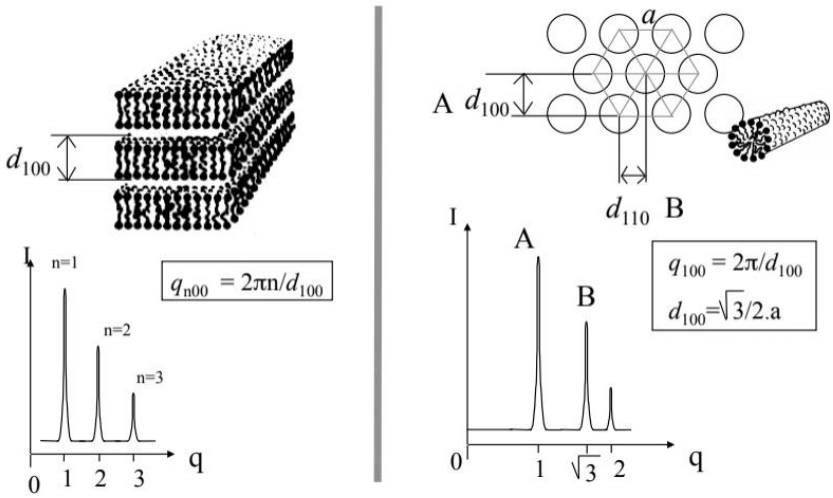

Figure 2.8 The lamellar and hexagonal arrangement. Adapted from Ref. 219.

As for our measurements, the SAXS data was collected at the SWING beamline of the SOLEIL synchrotron (Saint-Aubin, France), at a beam energy of 16 keV and two sample-to-detector distances (1.42 and 6.52 m). The beam size was approximately 500 × 200 μm^2 ($H \times V$). The solutions were filled into round glass capillaries (Mark-Rörchen, Germany), and placed vertically in a motorized holder. The capillaries were filled with the sample solution and sealed at the top using a glue gun to prevent evaporation. The scattered signal was recorded by an Eiger 4 M detector (Dectris Ltd, Switzerland) with a pixel size of 75 μm. Preliminary data treatment (angular averaging and normalization) was done using the software Foxtrot developed at the beamline and yielded the intensity as a function of the scattering vector $I(q)$ in absolute units. Subsequent data modeling was done in Igor Pro 7.0 using functions available in the NCNR SANS package.[221]

Some SAXS data were collected at the LPS using a rotating anode (Cu Kα, λ =1.542 Å), and a sample-to-detector distance of 1.396 m. Data treatment (angular averaging and normalization) was done using the Nika 2D SAS macros in Igor Pro 7.0.[222]

Moreover, the SAXS/WAXS measurements of GNTPs reshaping were performed on the ID02 beamline of the ESRF synchrotron (Grenoble, France) at a sample-to-detector distance of 3.0 m, with a photon energy E = 11.5 keV.

2.5 Inductively coupled plasma mass spectrometry

Inductively coupled plasma mass spectrometry (ICP-MS) yields the elemental concentration in solution with very few assumptions.[223] It is therefore a very robust technique, but it provides no information as to the size and shape of the objects. The gold and silver concentrations were determined using an iCAP Q Thermo Electron instrument after external calibration by dilution of multi-element standard solutions (SPEX, MS3 for gold and MS2 for silver). Measurements were repeated six times before averaging. All dilutions (samples and standards) were prepared by weight. Gold determination was performed at mass 198 in hydrochloric media. Silver was measured at mass 107 and 109 and before averaging. The silver determination is performed in nitric media. Sample dilutions were performed as follows: samples were heated in a bath at a temperature of 30°C to avoid CTAB solidification. A 10 μL aliquot of sample was added to a polypropylene vial. On the aliquot was poured 10 mL of aqua regia saturated with NH_4Cl to dissolve both gold and silver.[224] Sample dilution was then

realized by the addition of diluted hydrochloric or nitric acid. Both hydrochloric acid and nitric acid were purified previously by distillation. The same protocol was repeated for standards except that stock standard solutions were not heated.

2.6 Hyper Rayleigh scattering

The hyper Rayleigh scattering (HRS) setup[225] is sketched in Figure 2.9. Briefly, it comprises a mode-locked Ti: sapphire laser tuned to 800 nm and delivering pulses of about 180 fs at a repetition rate of 80 MHz. The mean power was set at about 450mWat the sample level to avoid any heating or deterioration as checked by simple extinction spectroscopy of the sample cell before and after each measurement. The fundamental laser beam was focused with a 16 objective (NA 0.32) into a quartz cell with a 5 mm-long optical path (Q107 cell, Hellma). The intensity IHRS scattered at a right angle from the incident beam was collected with a lens and sent to a spectrometer coupled to a cooled CCD camera. Color filters were inserted to remove any unwanted harmonic light before the cell and fundamental light after the cell.

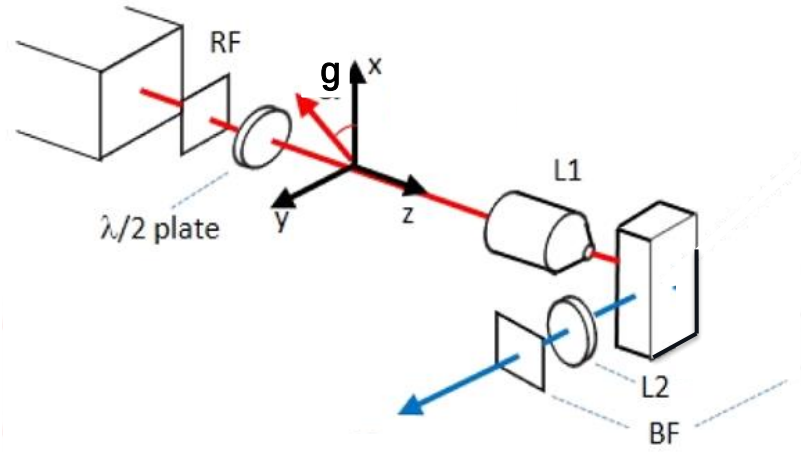

Figure 2.9 Diagram of the experimental setup. Adapted from Ref. 225.

The hyper Rayleigh scattering (HRS) experiment to determine the first hyperpolarizability of an NP consists of the measurement of the linear dependence of the HRS intensity with the number density of particles in the solution N and with the square of the fundamental intensity, I. Indeed, the HRS intensity is given by:

$$I_{HRS} = G[N_S\langle\beta_S^2\rangle + N\langle\beta^2\rangle]I^2 \exp(-\epsilon NL) \qquad (2\text{-}9)$$

where the average $\langle\cdot\rangle$ is taken over all orientations. G is an overall prefactor including all geometrical factors as well as absolute constants, I is the fundamental intensity, N

and β are the number density and the first hyperpolarizability of the NPs, while N_S and β_S are the same parameters for the solvent. ϵ is the molecular extinction coefficient due to the self-absorption of the HRS signal in the cell with optical path L. Note that, strictly speaking, $\epsilon L = 2\epsilon_\omega L_\omega + 2\epsilon_{2\omega} L_{2\omega}$, to account for extinction and optical path length at the fundamental ω and harmonic 2ω frequencies. The HRS intensity of the neat solvent provides the internal reference for the absolute determination of β. In order to achieve this absolute calibration, the spectrum around the HRS line is always performed to subtract any photoluminescence background that can lead to an overestimation of β. This subtraction procedure is valid since HRS and photoluminescence are uncorrelated processes. Note that in our case, we report first hyperpolarizabilities as $\beta = \sqrt{\langle \beta^2 \rangle}$ for vertically polarized fundamental and harmonic light.

The polarization-dependent HRS intensity can be written as:

$$I_{HRS}^{\Gamma} = a^{\Gamma}\, cos^4(\gamma) + \, b^{\Gamma}\, cos^2(\gamma) sin^2(\gamma) + c^{\Gamma}\, sin^4(\gamma) \qquad (2\text{-}10)$$

where γ is the angle of polarization of the input fundamental beam, Γ is the polarization of the harmonic (V or H for vertically and horizontally polarized light, respectively) and a^{Γ} , b^{Γ} and c^{Γ} are three real coefficients.

The polarization analysis yields two parameters: the depolarization ratio D and the retardation parameter ζ^{Γ}, defined as:

$$D = \frac{c^V}{a^V}, \qquad \zeta^V = \frac{b^V - a^V - c^V}{b^V}\,, \qquad \zeta^H = \frac{a^H - c^H}{a^H + c^H} \qquad (2\text{-}11)$$

D provides information on the origin of the HRS response through the tensor symmetry, whereas ζ^{Γ} quantifies the extent of retardation.

2.7 Surface-enhanced Raman scattering

Raman scattering measurements were performed in a Raman microscope (Witec UHTS 300, Germany) equipped with a 633 nm diode laser as an excitation source. The configuration involved a 600 grooves/mm diffraction grating and a front illuminated Peltier-cooled CCD camera (1650x200 pixels), and a 100× objective (N.A.=0.8). 10 µL of CV (10^{-6} M in ethanol) dropped cast on the sample after preparation (no cleaning procedure was involved). SERRS spectra and mappings were obtained with a laser power of 0.1 mW (on the sample) and an integration time of 400 ms. SERRS signals

are displayed after cosmic ray removal and background subtraction, using the WITio toolbox in MATLAB (https://gitlab.com/jtholmi/wit_io). To check the reproducibility, the measurements were repeated on at least 10 supercrystals for each sample (see Chapter 6).

2.8 Simulations

2.8.1 Boundary Element Method

The boundary element method (BEM) is a method for searching for approximate numerical solutions to boundary integral equations, which is a typical tool for analyzing boundary value issues.[226] The optical properties of plasmonic nanoparticles can be simulated using the BEM approach as implemented by the MNPBEM toolbox developed in the MATLAB environment.[227,228]

2.8.2 Monte Carlo computer simulations

Monte Carlo (MC) computer simulation is a type of simulation that relies on repeated random sampling and statistical analysis to compute the results. This simulation is immensely related to random experiments, i.e. experiments for which the specific outcome is not known in advance. In this situation, MC simulation can be considered as a methodical approach, so-called what-if analysis.[229]

The packing of NPs can be investigated by the crystal structure prediction method using variable box shape MC simulations introduced in Ref. 230. In this method, we performed Monte Carlo simulations of perfectly hard bipyramids in a small simulation box with a variable box shape in the isotension-isothermal ensemble. The number of particles in the simulation box is deliberately chosen to be small (on the order of a single unit cell), to ensure that the system can easily reach a compact structure. During the simulation, the pressure of the simulation box is gradually increased, followed by a final quench at the end at essentially infinite pressure (see Chapter 6).

3 Monitoring the growth of core-shell bimetallic nanoparticles

The results in this chapter were published in references **I** and **VI**:

I. **Lyu, J.**; Geertsen, V.; Hamon, C.; Constantin, D. Determining the Morphology and Concentration of Core–Shell Au/Ag Nanoparticles. *Nanoscale Adv.* **2020**, *2* (10), 4522–4528. https://doi.org/10.1039/D0NA00629G.

VI. Aliyah, K.; **Lyu, J.**; Goldmann, C.; Bizien, T.; Hamon, C.; Alloyeau, D.; Constantin, D. Real-Time *In Situ* Observations Reveal a Double Role for Ascorbic Acid in the Anisotropic Growth of Silver on Gold. *J. Phys. Chem. Lett.* **2020**, 2830–2837. https://doi.org/10.1021/acs.jpclett.0c00121.

3.1 Introduction

Synthesizing nanoparticles with carefully chosen properties (optical, magnetic, catalytical, etc.) is one of the main goals of materials science. These properties depend on the shape and composition of the particles, and measuring these parameters accurately is an essential prerequisite to developing a reliable formulation process. Noble metal nanoparticles are particularly interesting due to their optical properties, related to the presence of plasmon resonances (very sensitive to the particle shape) and due to the richness of synthesis methods that can yield a large variety of shapes and sizes, with very good yield and relatively low polydispersity. Bimetallic particles consisting of a gold core covered with a silver shell offer further control over the optical properties and exhibit lower dissipation in the visible range.[128,207,231–233]

Before any application, it is indispensable to determine the particle concentration, as well as their average morphology (size, shape, rounding) and their distribution. Ideally, these parameters should be determined by non-invasive techniques, directly applicable in the reaction medium and time-resolved. The typical example is UV-Vis-IR absorption spectroscopy (AS), but several groups have shown that small-angle X-ray scattering (SAXS) can also provide valuable information.[234–238] Although the presence of two constituents complicates the application of these methods to bimetallic objects, recent studies point the way towards a deeper understanding of their structure and evolution.[231,239] An important source of progress over the last decade has been the

improvement in synthesis protocols, yielding particle populations with better size and shape monodispersed, and allowing the extraction of more information using the various characterization techniques. In turn, this information can be used to further improve the synthesis protocols.

Depending on the gold core crystallinity, the silver shell will grow at different locations,[197] changing the overall morphology of the particle which results from a competition between the rate of atom deposition and NP faceting driven by possible preferential adsorption sites and surface diffusion, in other words, kinetics versus thermodynamics.[108,240] Experimentally, different NP morphologies can be obtained by varying the deposition rate onto the seeds via reaction parameters such as the pH, the temperature, and the nature and concentration of reductant and surfactant species.[130,131,207,233] The description of the synthetic pathways of anisotropic Au@Ag NPs has mostly relied on spectroscopy measurements and *ex situ* TEM.[241,242] Although this approach has greatly expanded the available library of particle shapes and compositions, time-resolved information on the growth mechanisms and reaction intermediates remains limited. Diffraction and spectroscopy techniques can be used to follow NPs formation in the growth medium, with high temporal resolution.[216,243–245] However, given their limited spatial resolution and the necessity to develop models to retrieve the NP morphology, these *in situ* approaches provide an indirect and incomplete overview of the nucleation and growth processes implied in wet-chemical synthesis. Over the past few years, liquid-cell transmission electron microscopy (LCTEM) has become a leading method for directly visualizing the dynamics of single nanostructures in their formation medium.[246,247] An important feature of this technique is that the electron dose rate can be used to control reaction kinetics because NP formation is generally driven by radiolysis processes.[123] This opportunity to control the growth rate and chemical environment of nanostructures has been exploited to reveal the growth mechanisms of various metallic and bimetallic NPs,[213,248–250] including core-shell nanostructures.[251–255] However, exploiting this *in situ* information in high-yield synthesis remains difficult because radiochemical effects are not involved in conventional protocols. Therefore, an important challenge is to reduce the gap between nanoscale *in situ* observations and bench-scale synthesis, by correlating LCTEM results with *in situ* techniques based on light-matter interactions, which probe large nanoparticles ensembles without radiolysis effects.

In this chapter, we first apply AS and SAXS to a series of samples where the particle morphology is modified systematically by changing a reaction parameter and validate the information by cross-checking the results and by comparing them with two other methods: TEM and ICP-MS which, require extracting the particles from their environment. More specifically, we synthesize core-shell Au@Ag nanoparticles by growing a silver shell on top of a spherical gold seed, for various values of the molar ratio K between silver precursor and gold. At low K, the shell is quasi-spherical (probably rhombicuboctahedral[239]), while at higher K, it becomes cubic. We measure the size and shape of the objects by SAXS and TEM and their concentration by SAXS, AS and ICP-MS and compare the results of the various techniques.

Then, we study the anisotropic growth of silver shells on preformed gold bipyramidal seeds. The seeds are injected into an aqueous growth solution containing silver salt ($AgNO_3$), a mild reducing agent (ascorbic acid, AA), and the ionic surfactant cetyltrimethylammonium chloride (CTAC). The formation of these bimetallic nanostructures was monitored in real-time by using multimodal and multiscale *in situ* measurements. LCTEM was exploited to follow the formation of single NPs and confirm the growth pathway inferred from using a combination of *in situ* SAXS and AS techniques on bulk solutions. In the different experiments, the growth rate differs by more than one order of magnitude, yet yields similar anisotropic nanoproducts, suggesting that the reaction is under thermodynamic control. Furthermore, we show that ascorbic acid is essential to obtaining anisotropic bimetallic NPs, not only as a source of electrons but also as a shape-directing agent.

3.2 Single gold nanoparticles

We first synthesized various single GNPs with different shapes for further use.

The synthesis protocols of GNPs were shown in Section 2.1. After synthesis, the optical properties of gold nanoparticles (GNPs) with different shapes were characterized by AS. Gold nanorods (GNRs), for instance, the longitudinal LSPR peak is at 695 nm, while the transverse LSPR peak is at 516 nm, see Figure 3.1a1. The shape of the GNRs can be observed directly by TEM, as shown in b1. The size distribution obtained from at least 200 particles in the TEM images is presented in c3. From the histogram, the length was estimated at L = 48.6 ± 2.5 nm (mean ± SD) and the width at W = 17.0 ± 4.5 nm, for an aspect ratio AR = L/W = 2.9 ± 0.4. The length and width of the gold

particles were measured using the particle analysis functions in Igor Pro. For the gold bipyramids (GBPs), the longitudinal LSPR peak is observed at 714 nm, while the transverse LSPR peak is at 512 nm and the gold concentration in the cuvette is 0.09 mM from the AS spectrum in a2. From the TEM images b2, the length of 47.4 ± 2.0 nm, the width of 17.5 ± 2.5 nm and the AR is 2.8 ± 0.3. In a3, the LSPR peak of gold spheres (GNSs) is observed at 522 nm. After TEM characterization b3, the diameter of 19.1 ± 1.0 nm was obtained by the same size measurement method. The diameter distribution of all NPs was fitted by Gaussian functions. We also synthesized gold nanotetrapods (GNTPs) with four sharp arms, however, GNTPs displayed poor stability at room temperature.[68] Fortunately, we found that coating with a thin silver layer can stop their reshaping and stabilizer their morphology. I will show you the details in the next chapter.

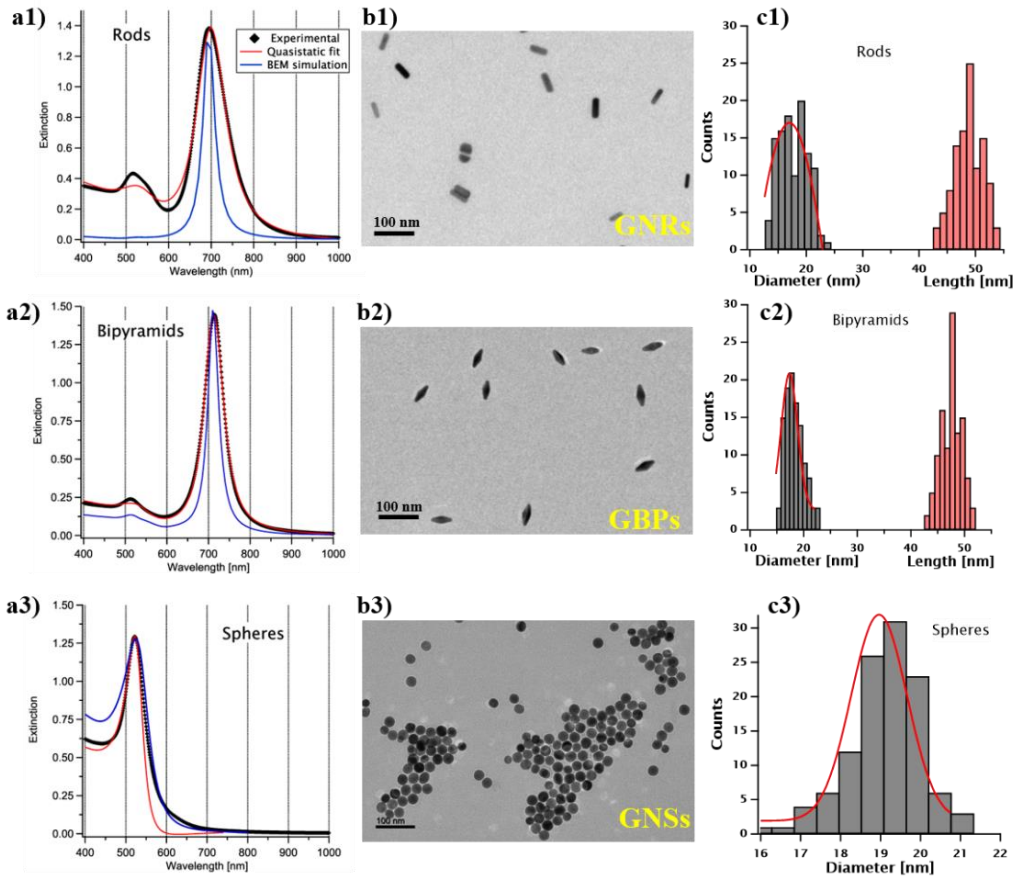

Figure 3.1 Characterization results of the different types of GNPs. a) AS spectra of GNPs colloid: a1) GNRs, a2) GBPs and a3) GNSs. Experimental data (diamonds), fits with a quasistatic analytical model (red lines) and BEM simulations (blue lines). b) TEM images and c) Size distributions of GNPs with different shapes. Fits the diameter distribution with Gaussian (red lines). Fits with a quasistatic analytical model and BEM simulations were done by Dr. Doru Constantin.

3.3 Determining the morphology and concentration of gold nanospheres@Ag nanoparticles

Accurately measuring the shape, structure and concentration of NPs is a crucial step towards understanding their formation and a prerequisite for any applications. While determining these parameters for single-metal NPs is by now rather routine, reliably characterizing bimetallic NPs is still a challenge. To deeper understand the structure and evolution of bimetallic NPs, isotropic GNSs first attracted our attention compared with other anisotropic GNPs. The silver shells are formed by epitaxial growth on the GNSs seeds.

The synthesis protocol of core-shell GNSs@Ag NPs was shown in Section 2.1.5. The silver-to-gold molar ratio K (Ag ions per Au atoms in the GNSs, at the beginning of the process) was varied between 0.1 and 8. For instance, in the case of K = 2, 50 µL of a 0.1 M $AgNO_3$ solution was injected in 10 mL GNSs suspension. After brief shaking, the solution was supplemented with 50 µL of a 0.4 M AA solution, shaken again and kept at 60°C for 3 h. The gold concentration keeps at 0.25 mM.

The particle shape evolved from spherical to cubic as silver coating increased (see Figure 3.4). To describe the particle geometry, we built two different models: sphere-in-sphere and sphere-in-cube (see Figure 3.2). The particles are described as GNSs with radius R centered within silver shells of thickness t, and hence with outer radius $R + t$ (sphere-in-sphere model), or within cubes of size a (sphere-in-cube model). In the latter situation, we define the thickness $t = \frac{a}{2} - R$. We denote by $K = \frac{\nu_{\mathrm{Ag}}}{\nu_{\mathrm{Au}}}$ the molar Ag/Au ratio for the individual particles. The corresponding volume ratio is given by fK, with $f = \frac{M_{Ag}}{M_{Au}}\frac{\rho_{Ag}}{\rho_{Ag}} = 1.008$. If K is known, t is given by:

$$t = R\left[(1 + fK)^{1/3} - 1\right] \tag{3-1}$$

for a sphere-in-sphere and by:

$$t = R\left[(1 + fK)^{1/3}\left(\frac{\pi}{6}\right)^{1/3} - 1\right], \text{for } fK > \left(\frac{6}{\pi} - 1\right) \tag{3-2}$$

for a sphere-in-cube. Note that, in Eq. (3-2), the sphere-in-cube model is only defined above a minimal Ag/Au ratio $K_{\min} = f^{-1}\left(\frac{6}{\pi} - 1\right) \approx 0.903$ below which the silver amount is not enough to form a complete cubic shell around the core sphere.

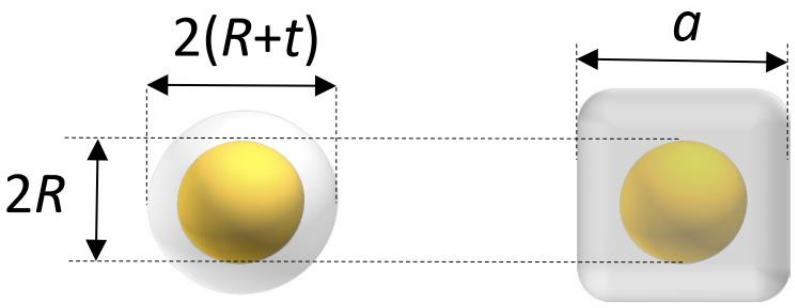

Figure 3.2 Diagram of the sphere-in-sphere (left) and sphere-in-cube (right).

3.3.1 AS spectra of gold nanospheres@Ag

After synthesis, each 150 μL suspension was diluted with 2250 μL 10 mM CATC, and the optical properties were first observed using AS. In Figure 3.3, as the ratio K (and hence the amount of silver) increases, the initial plasmon peak of gold (around 525 nm) flattens and is gradually replaced by a peak around 440 nm, characteristic of silver. At the same time, a dip at 320 nm and a peak at 350 nm becomes more and more marked, due to the interband transitions of silver.[256]

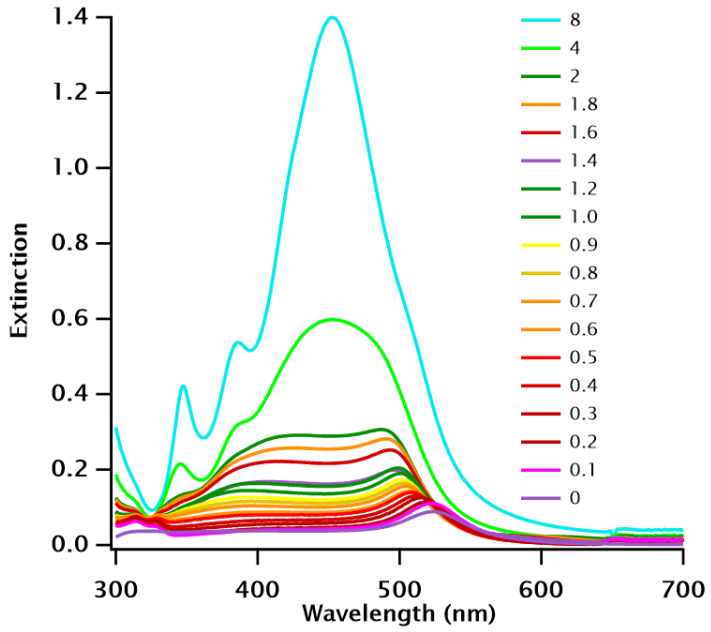

Figure 3.3 AS spectra of GNSs@Ag with variable Ag/Au molar ratio K.

3.3.2 Particle size and shape

3.3.2.1 TEM images

We performed TEM measurements on nine samples, with K = 0, 0.4, 0.7, 0.9, 1.2, 1.4, 2, 4, and 8. Additional TEM images are shown in Appendix Figure 8.1.

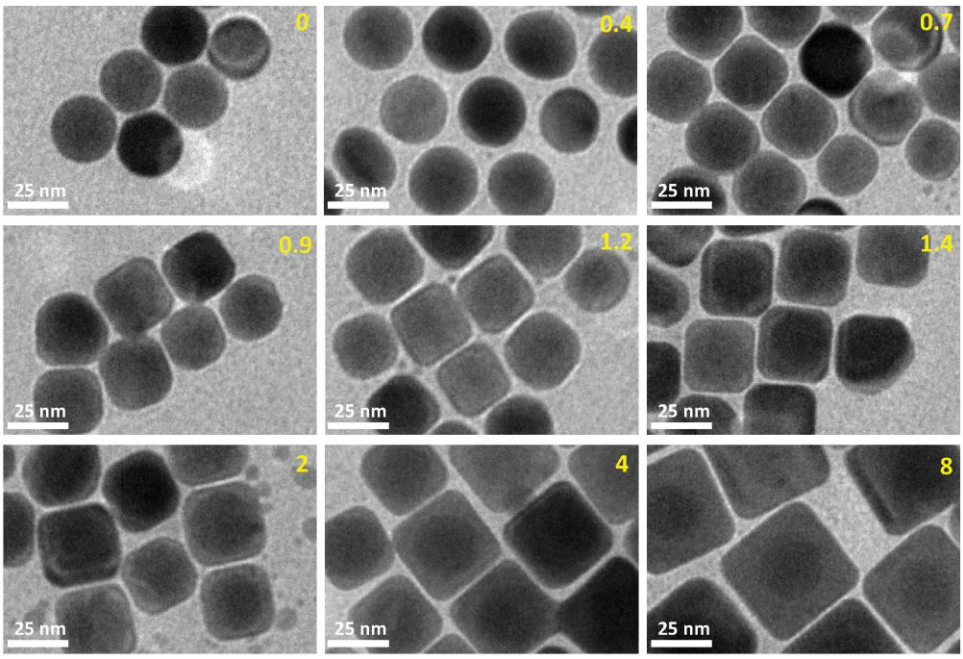

Figure 3.4 TEM images for different values of the molar ratio K. The K values are indicated in each panel.

The size of the gold core was extracted from the initial population, before the addition of silver (molar ratio K = 0), yielding a radius R_0 = 13.0 nm. The shell thickness for each $K > 0$ was obtained by subtracting R_0 from the mean equivalent particle radius $\langle R_K \rangle$ at that given K. The polydispersity is computed as the standard deviation of the radius distribution divided by its mean: $p_K = \frac{\sigma_K}{\langle R_K \rangle}$. These parameters are shown in Figure 3.5a.

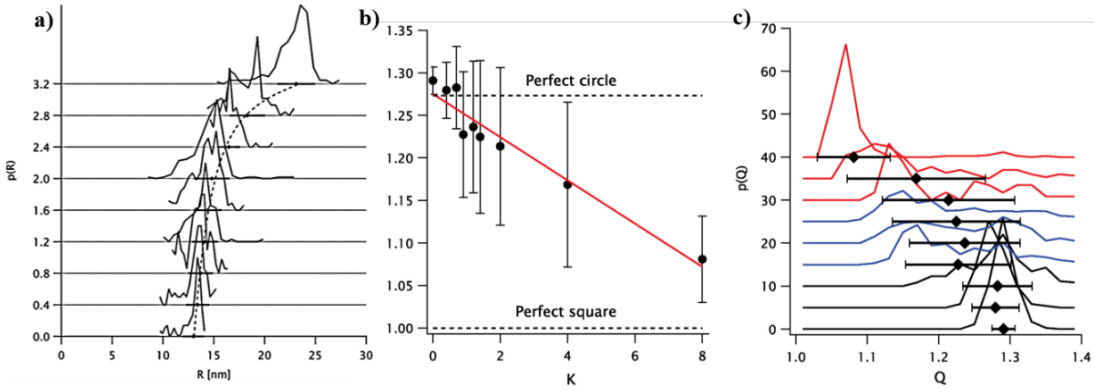

Figure 3.5 a) Particle radius histograms extracted from the TEM images. The mean and standard deviation (SD) are shown as diamonds and bars. For clarity, the curves are shifted upwards in steps of 0.4. The dashed line is a guide to the eye. Quadraticity parameter Q: b) average value $\langle Q \rangle$ as a function of K (mean and SD, solid dots and error bars) with the linear fit (solid line). The limiting values for a perfect circle and square are shown as dashed lines; c) histograms of Q for each K value (shifted vertically for clarity). The mean and SD from b) are shown under

each curve. Colors (black, blue and red) distinguish three types of curves. The molar Ag/Au ratios K are (from bottom to top): 0, 0.4, 0.7, 0.9, 1.2, 1.4, 2, 4, and 8. The calculation of Q was done in MATLAB by Dr. Cyrille Hamon.

The shape of the particles can be assessed using the quadraticity Q, defined as the ratio between the area of the smallest circumscribed square and that of the particle projection. This parameter is 1 for a perfect square, $\frac{4}{\pi}$ for a perfect circle and can be even larger for anisotropic or irregular shapes. The mean quadraticity $\langle Q \rangle$ is shown in Figure 3.5b. at first glance, it seems to decrease linearly with K, as shown by the fit. However, the large standard deviations call for a more refined analysis. To this end, we plot in the same figure (Figure 3.5c) the histograms of Q for each K value. We can separate three regimes, identified by line color: at low $K \leq 0.7$ (black line), the distributions are monomodal, relatively narrow and centered around the $\frac{4}{\pi}$ value corresponding to a perfect circle. Almost all particles are spherical. At intermediate K (blue line) the distributions are wide and possibly bimodal, with one spherical subpopulation and one with $Q \approx 1.15$. At high $K \geq 2$ (red line) the distributions are once again monomodal, with a decreasing mode but with a substantial contribution at higher Q. This contribution is almost absent for K = 8, as shown by the reduced standard deviation. The cubes become predominant at K = 2, so we can locate the shape transition between 1.4 and 2.

3.3.2.2 SAXS measurement

We recorded the azimuthally averaged scattered intensity $I(q)$ as a function of the scattering vector q for all samples in dilute solutions. The data is shown in Figure 3.6, along with fits using both sphere-in-sphere and sphere-in-cube models (Eq. (3-1) and (3-2), respectively). For coherence, the latter model was only used for molar Ag/Au ratios above $K_{\min} \approx 0.903$, attempts to fit curves at lower ratios yield unphysical results (cube sizes $a < 2R$). We fixed throughout the core radius R = 12.4 nm, the value obtained by fitting the data for $K = 0$.

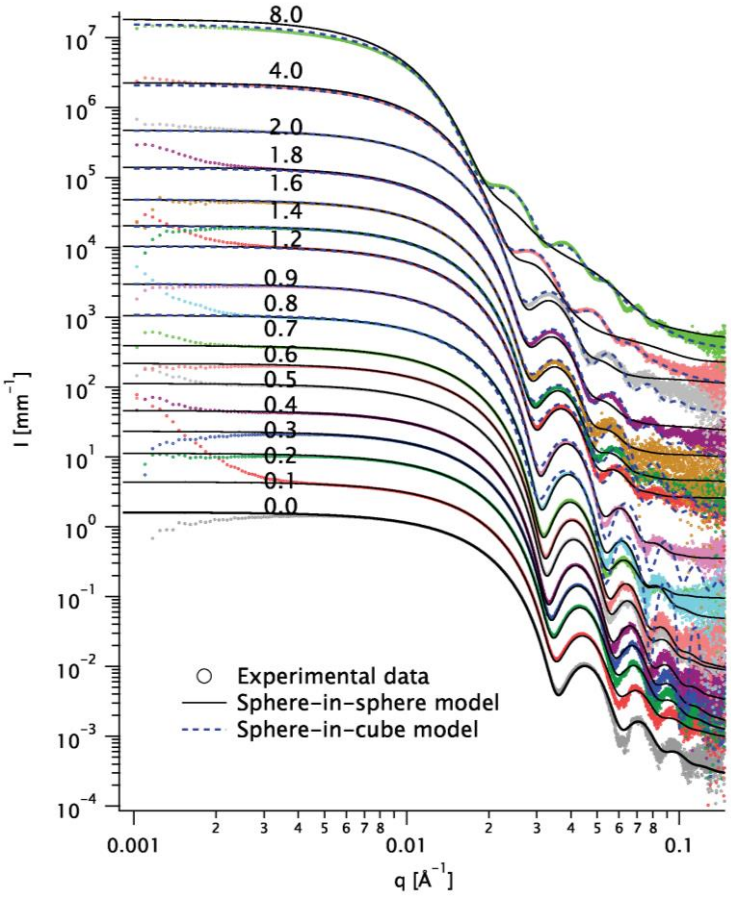

Figure 3.6 Scattered intensity I as a function of the scattering vector q for all solutions (dots, various colors). The spectra were shifted vertically for clarity. The molar Ag/Au ratio K is indicated above each curve. Fits with the sphere-in-sphere model (solid lines) and with the sphere-in-cube model (dashed lines) are displayed for each curve. The fits were done by Dr. Doru Constantin.

The goodness-of-fit function χ^2 divided by the number of experimental points N_{pts} is shown in Figure 3.7 for all the fits displayed in Figure 3.6. The fit quality is better for the sphere-in-sphere model below K = 1.4 and for the sphere-in-cube model above $K = 2$, in agreement with the visual inspection of Figure 3.6. The oscillations between 0.03 and 0.1 Å^{-1} are very revealing: they are deep for spheres and shallow for cubes and are very well described by the corresponding model at low and high K, respectively. In the intermediate range ($0.9 \leq K \leq 1.6$) both models are unsatisfactory due to the shape polydispersity illustrated in Figure 3.5.

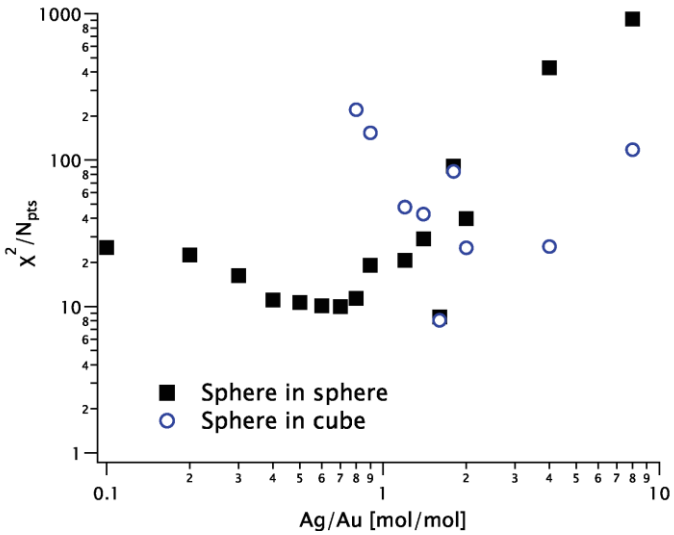

Figure 3.7 Goodness-of-fit function for the SAXS models in Figure 3.6, shown as solid squares (for the sphere-in-sphere model) and as open circles (for the sphere-in-cube model) as a function of the Ag/Au ratio K.

We then plot the thickness t extracted from the fits in Figure 3.6 (solid squares for sphere-in-sphere and open dots for sphere-in-cube) and the TEM values (diamonds). We also plot the thickness values predicted by Eq. (3-1) and (3-2) (solid and dashed line, respectively) assuming that the Ag/Au ratio for each particle is the experimental one K in the reaction medium (i.e. that all the Ag ions are used to form shells and that all particles have the same morphology). The SAXS models include a homothetical polydispersity, plotted in Figure 3.8b, alongside the TEM values. The latter is in good agreement with the sphere-in-sphere model up to K = 2 and with the sphere-in-cube model above this value.

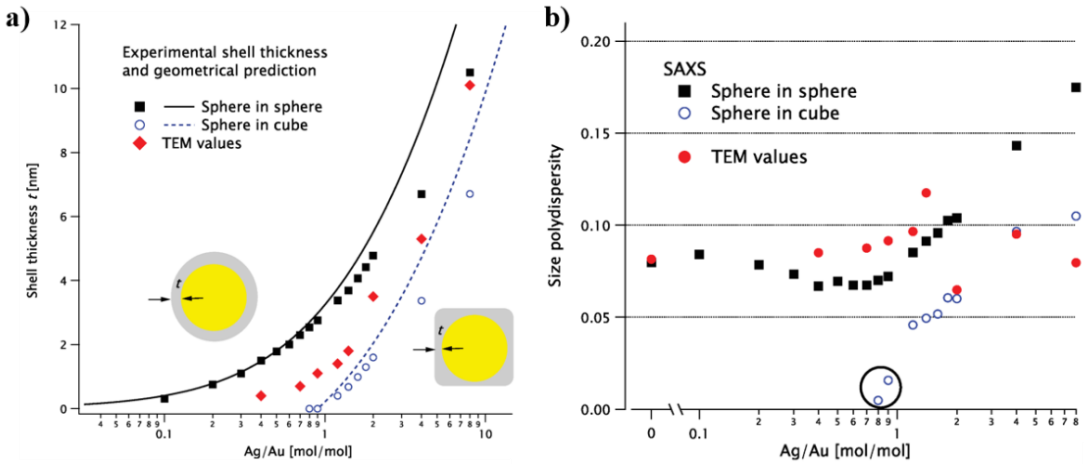

Figure 3.8 a) Shell thickness extracted from the fits in Figure 3.6 for the two models and corresponding geometrical predictions. The TEM values are shown as red diamonds. b)

Relative polydispersity extracted from the SAXS fits in Figure 3.6 for the two models (solid squares for sphere-in-sphere and open dots for sphere-in-cube). The circled points with abnormally low values (for K = 0.8 and 0.9) have very poor fit quality (see Figure 3.7). Relative polydispersity extracted from the TEM data (solid dots).

3.3.3 Silver-to-gold ratio

Using ICP-MS, we can determine the Ag/Au ratio within the particles. We plot it against their ratio in solution, K, see Figure 3.9. The diagonal line is the expected value if the reaction proceeded to completion and the two parameters are equal. The same line corresponds to the solid/dashed curve for the spherical/cubical shell model in Figure 3.8a. The experimental values follow K with considerable variability: their ratio fluctuates between 0.74 and 1.74. ICP-MS experiments were done by our collaborator Dr. Valérie Geertsen at CEA.

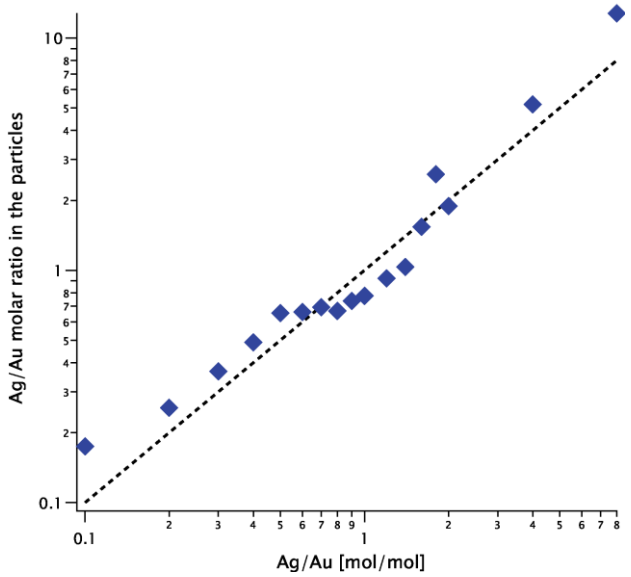

Figure 3.9 The Ag/Au ratio in the particles, measured by ICP-MS, versus the same ratio in solution, K (diamonds). The dashed line marks the expected values if all the silver is deposited onto the gold cores.

3.3.4 Particle concentration

The concentration of particles in solution is of course a very important parameter: it can be obtained from full-curve fitting of the AS[257] or SAXS[258] curves or, for homogeneous GNPs, in an easier manner from the near-UV extinction[209,259] or the integrated invariant, respectively.[243] ICP-MS gives access to the molar concentration of gold and silver separately (in different measurements). Each of these techniques uses a completely different principle. A full analysis of the SAXS data gives access to both the size and

the number density of the particles, while the other techniques only yield their product, i.e. the volume concentration. For bimetallic objects, no simple method exists, either in SAXS or AS, it is therefore necessary to model the entire experimental curve.

Since the scattered intensity $I(q)$ is measured in absolute units, it is directly proportional to the number density n. We plot (as solid squares) this parameter as a function of the molar ratio K for the sphere-in-sphere model (the results of the sphere-in-cube model are within 9% of these values), see Figure 3.10. The number density also appears in the model for the extinction spectra. We fit the experimental data with the sphere-in-sphere model, where only n and a constant background are adjustable parameters: the core radius R and the shell thickness t are fixed at the values obtained from the SAXS data using the same model. The results are plotted as open dots in Figure 3.10.

From the mass gold concentration, C_{Au} measured via ICP-MS we determine $n = \frac{C_{Au}}{\rho_{Au}} \frac{3}{4\pi R^3}$ (where R = 12.4 nm is the radius determined by SAXS) and plot it as diamonds in Figure 3.10. The SAXS values for n are more scattered than the AS ones and some points (circled in Figure 3.10) are very low. The ICP-MS results are close to the SAXS ones at low $K \leq 1$ and above the AS at $K \geq 2$.

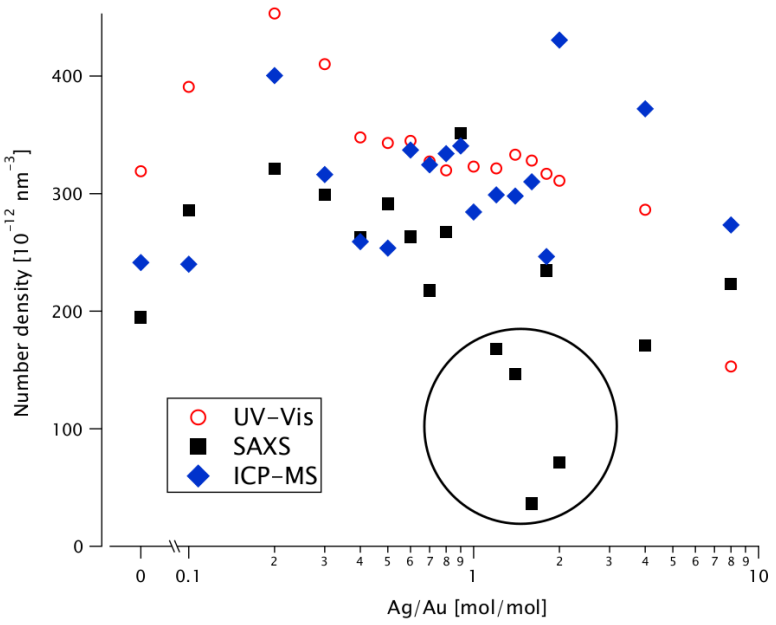

Figure 3.10 Number particle density n as a function of the Ag/Au ratio K, extracted from fitting the SAXS data in Figure 3.6 (solid black squares), from the AS data (open red dots) and ICP-MS (blue diamonds). Anomalously low SAXS values are circled. Data analysis was done by Dr. Doru Constantin.

3.3.5 Conclusions

The particle populations have excellent monodispersity p (between 5 and 10%) as measured by SAXS and TEM (see Figure 3.8b) and confirmed by the agreement between the calculated and predicted shell thickness (see Figure 3.8a). Analysis of the TEM images (see Figure 3.5) shows a transition between quasi-spherical and cubic shapes between K = 1.4 and 2, while the quality of the SAXS fits finds the transition at about K = 2: the two techniques are in very good agreement! The values for the particle concentration n obtained by three techniques are in good agreement (within 40% of their average), except for some low-value SAXS points. The systematic difference between the techniques is lower than the spread of values for each technique, highlighting the importance of careful sampling protocols: sample agitation to ensure homogeneity and avoid the appearance of concentration gradients, temperature control to prevent surfactant crystallization, weighing the aliquots rather than relying on pipetting volumes (which are not always accurate for surfactant solutions).

Among the four methods used, SAXS yields the most information about the particles: the size, polydispersity, shape and concentration are accurately determined, as shown by very good agreement with the other techniques. This result validates the use of SAXS for studying complex (bimetallic and aspherical) nano-objects, statically or during their growth. However, the particles must be reasonably monodispersed in order to take full advantage of this technique. Of course, scattering methods only yield indirect information and imaging techniques remain essential for identifying the particle shapes and choosing the appropriate model, so TEM should always be used as a complement.

3.4 Real-time *in situ* observations of the anisotropic growth of silver on gold bipyramids

Rational nanoparticle design is one of the main goals of materials science, but it can only be achieved via a thorough understanding of the growth process and the respective roles of the molecular species involved. We monitored the growth of long aspect ratio silver rods from gold pentatwinned seeds by three *in situ* techniques (SAXS, AS, and LCTEM). Understanding the mechanism of the anisotropic growth and the role of the composition can easily be applied to a wide variety of synthesis strategies.

3.4.1 Characterization of gold bipyramids@Ag

The synthesis protocol of GBPs@Ag nanoparticles was described in Section 2.1.5. We first synthesized GBPs@Ag with different silver-to-gold molar ratios K, the AS spectra are shown in Figure 3.11. As the ratio K increases, the initial longitudinal plasmon peak of the GBPs (around 754 nm) is first blue-shifted and then red-shifted. The reason for this phenomenon is the ellipsoid particles formed (see TEM images below) and the optical properties of silver are dominantly inducing a blue shift for a low silver ratio ($K \leq 0.8$). Then the size effect becomes more important, an increase in aspect ratio leads to a redshift for a high silver ratio. Peaks between 350 nm to 450 nm are due to the interband transitions of silver.[256] More interesting, the longitudinal LSPR peak of GBPs@Ag as $K = 8$ shifts to infrared range, so we can't observe it at 300 to 1200 nm, which can be proven by BEM simulation or observation of AS spectra using deuterated water to disperse particles.

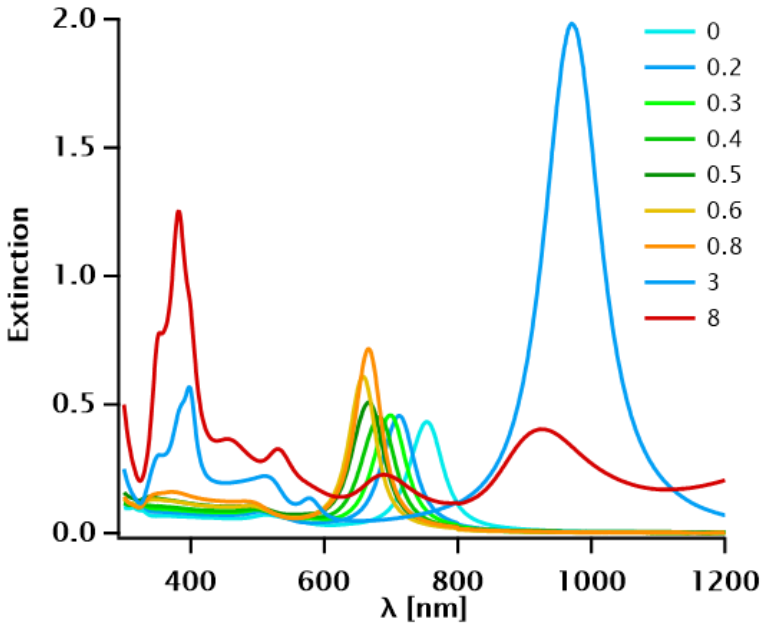

Figure 3.11 AS spectra of GBP@Ag with variable molar Ag/Au ratio K.

From standard TEM images (see Figure 3.12), we can observe that silver is first deposited onto the facets of the GBPs ($K \leq 0.6$), followed by a gradual shape rounding that yields ellipsoidal objects ($K = 0.8$) and finally anisotropic growth leading to long cylinders ($K > 0.8$). Note that the particle diameter changes very little, remaining essentially equal to that of the initial GBP. Additional TEM images are provided in Appendix Figure 8.2.

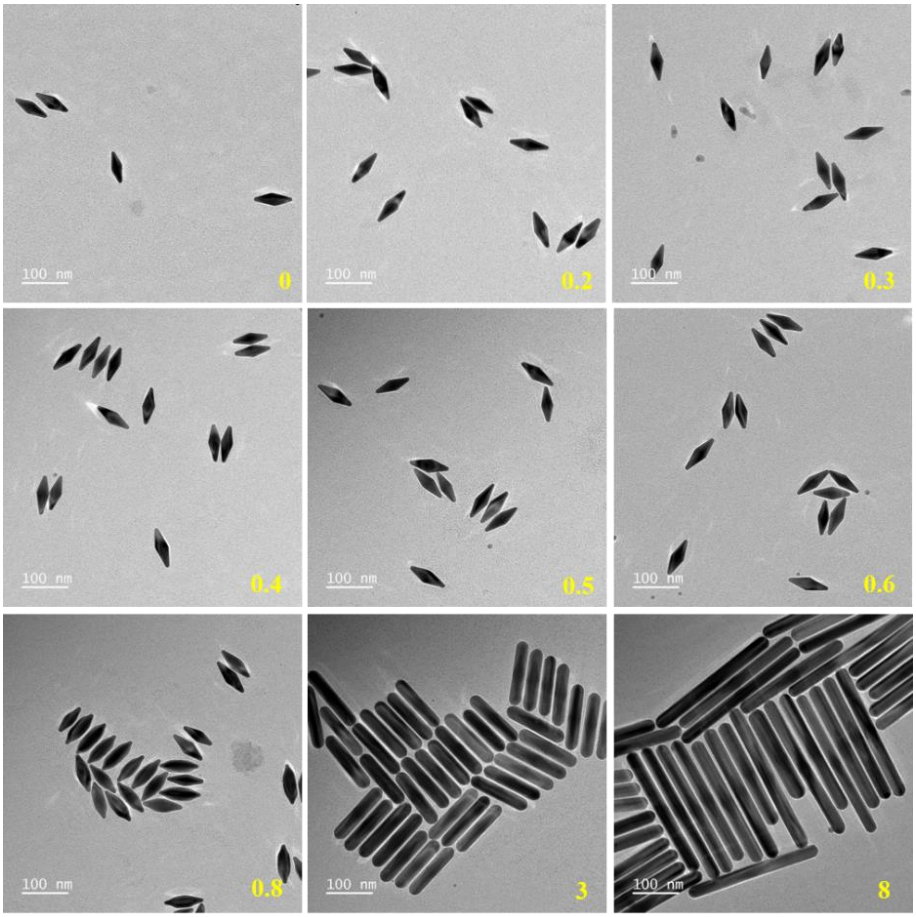

Figure 3.12 Standard TEM images for different values of the molar ratio K. The K values are indicated in each panel.

3.4.2 *In situ* observations of the anisotropic growth of silver on bipyramids

We then followed the growth of GBPs@Ag at K = 3 in real-time by AS and SAXS. GBP seeds exhibit a longitudinal LSPR centered at 752 nm. Upon silver overgrowth, the AS extinction spectra show a blue shift of this peak by 102 nm after 9 min and a red shift by 512 nm after 48 min, the time at which the system stops evolving (see Figure 3.13a). The blue and redshifts correspond to a decrease and increase in aspect ratio, respectively, consistent with the growth of the initial bipyramid into a short rod which then increases in length.

Corresponding SAXS measurements (Figure 3.13b) describe the evolution of the form factor with oscillations of increasing definition, indicating the formation of particles with a more homogeneous thickness, consistent with a shape transformation from a bipyramid to a rod. After about 38 min, the features no longer changed in the large q range ($q > 0.025$ Å^{-1}) while still evolving in the lower q range ($q < 0.025$ Å^{-1}),

indicating that the objects have a fixed width but an increasing length. The rod length can also be extracted directly from the SAXS curves,[260] but this method is unreliable for particles longer than the reciprocal of the minimum scattering vector. We use a more precise strategy, obtaining the aspect ratio AR of the particles from boundary element method (BEM) simulations of the experimental AS (Figure 3.13a). With W obtained from SAXS, L (Figure 3.13d) can be better estimated. A rigorous determination of $L(t)$ is essential for understanding the growth kinetics, especially in the case of very anisotropic particles. We model this parameter using a version of the Avrami equation,[261] with the distinction that, in our case, saturation occurs due to precursor exhaustion, not to the lack of free space, then yields the longitudinal growth rate of GBPs@Ag as 0.046 nm/s after fitting the experimental data. The fits were done by Dr. Cyrille Hamon.

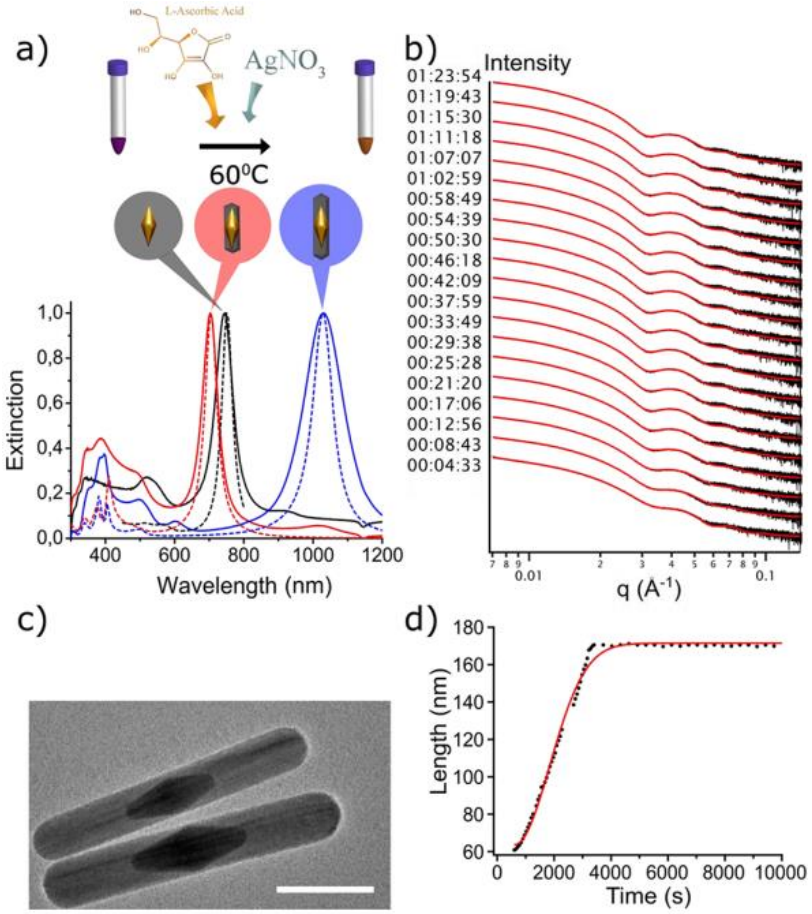

Figure 3.13 Presentation of the system and ensemble time-resolved measurement of GBPs@Ag rods. a) (Top) Scheme depicting the synthesis of GBPs@Ag rods and the shape transition from a bipyramid to a rod. (Bottom) Time-resolved AS of GBPs@Ag rods synthesis. For clarity, we show only three spectra, representing three important stages of the reaction: GBPs seeds (black), seeds completely covered in silver, yielding a short rod (red) and a long rod obtained as the

final result (blue). The dashed lines correspond to BEM models. b) Time-resolved SAXS curves (black) with fits (red) of diluted suspension of GBPs@Ag rods during their synthesis. Curves are shifted vertically for clarity. c) TEM image of GBPs@Ag rods obtained in *ex-situ* synthesis. The scale bar is 100 nm. d) Determination of the length of GBPs@Ag rods as a function of time (black dots) by the combined AS, SAXS, and BEM modeling approach and corresponding fit with the Avrami equation (red line). Data analysis was done by our intern Kinanti Aliyah and BEM simulation was done by Dr. Cyrille Hamon.

We also conducted LCTEM experiments in STEM-HAADF mode to distinguish gold and silver nanocrystals by their difference in Z-contrast. An identical reaction mixture to that studied above was confined in the liquid cell and investigated in ambient conditions. Although the reaction rate in bulk synthesis is rather slow at room temperature, bimetallic NPs were obtained within minutes in the irradiated area, confirming that silver reduction is speeded up by radiolysis. The image sequence in Figure 3.14a shows clearly the anisotropic deposition of silver on the bipyramidal template alongside the formation of faceted silver NPs that nucleate on the SiN membrane. As many silver-based crystal phases could form under the electron beam,[262] we exploited the STEM nanodiffraction technique[215] to confirm that the shells around the gold seeds and the faceted NPs are all made of metallic silver, with a face-centered cubic structure and a lattice parameter of 0.41 nm, see Figure 3.15.

Extracting contour plots of the GBPs@Ag nanostructure from the entire image series revealed the spatiotemporal evolution of the overgrowth reaction (Figure 3.14b). These contour plots were fitted with a superellipsoid model: $\left(\frac{r}{a}\right)^n + \left(\frac{z}{b}\right)^n = 1$, where $r^2 = x^2 + y^2$ is the radial distance, z is parallel to the long axis of the NP, and parameters $a = \frac{W}{2}$ and $b = \frac{L}{2}$ are the half-width and half-length, respectively (Figure 3.14c). It is well established in the literature that the rods have a pentagonal cross-section in the (x, y) plane, perpendicular to their long axis z. For simplicity, we assume this cross-section to be circular; growth in the direction normal to the image is taken as identical to that along the small axis of the object. The parameter n describes the "bluntness" of the particles: n = 1 describes a diamond, n = 2 an ellipse and then, as n increases, a less and less rounded rectangle. During the first 40 seconds, sizes a and b remain constant and only the bluntness varies, as the initial bipyramid "fills up" to yield a short rod. As illustrated in Figure 3.14a, this shape transformation goes through the deposition of silver from the common base of the GBP toward its two tips. This growth process explains the conservation of the 5-fold symmetry of the nanostructure, as the ⟨001⟩

edges forming the pentagonal base of the bipyramid generate the five {100} side facets of the nanorods (see Figure 3.16). Once the nanostructure reaches a rodlike shape, it starts elongating, whereas the increase in width does not exceed 1 nm. It should be noted that systematic discrepancies persist between the experimental particle shapes and the superellipsoid model, which fails to capture the high curvature at the tip of the particles.

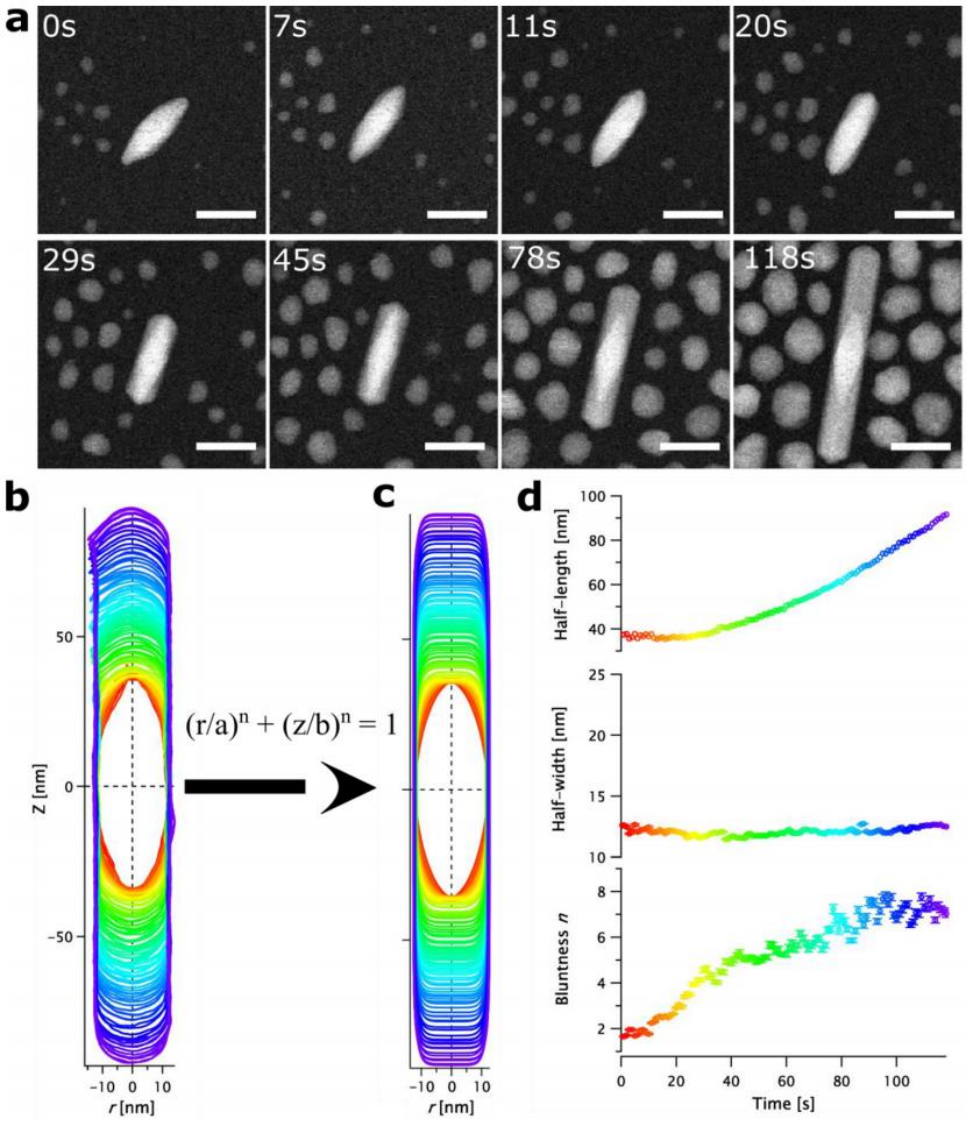

Figure 3.14 Time-resolved growth of GBPs@Ag rods by LCTEM. (a) Time-lapse STEM images showing the anisotropic deposition of silver on a gold bipyramid as well as homonucleation. The scale bar is 50 nm on all images. b) Contour plots of the GBPs@Ag rods were extracted every second from image analysis. c) Corresponding fit with a superellipsoid model. (d) Time dependence of length, width, and bluntness of the same GBPs@Ag rod as determined from the superellipsoid model. The color code of these parameters corresponds to that of the outlines in (b) and the fits in (c). The LCTEM experiment was done by Dr. Damien Alloyeau and the fit was done by Dr. Doru Constantin.

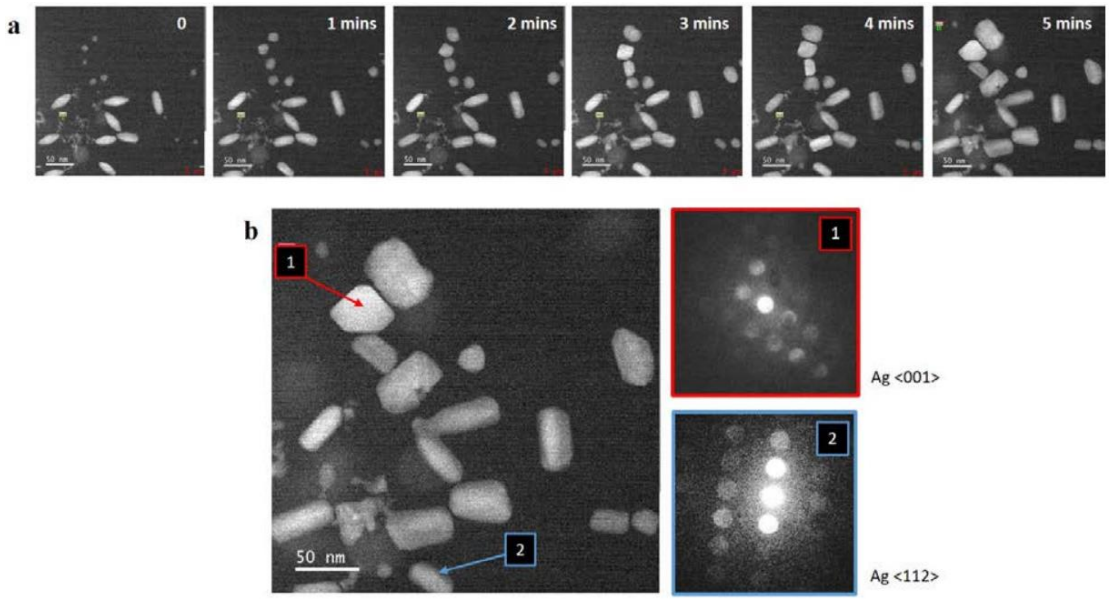

Figure 3.15 *In-situ* structural analysis of Ag and GBPs@Ag NPs. (a) Image series of a growth experiment performed without ascorbic acid. We observe the growth of facetted nanoparticles and isotropic shell on the GBPs. (b) STEM nanodiffraction analyses were performed after 5 min of growth on a facetted nanoparticle (diffraction 1) and the shell of a bimetallic nanostructure (diffraction 2). The positions of the STEM nanoprobe (convergence angle of 7.4 mrad) are selected directly on the STEM HAADF image (left) and the diffractions of individual nano-objects (right) are acquired on a CCD camera. The diffractions 1 and 2 correspond to the FCC structure of metallic silver oriented along the and directions, respectively. No other silver crystalline phase was observed in the reaction media.

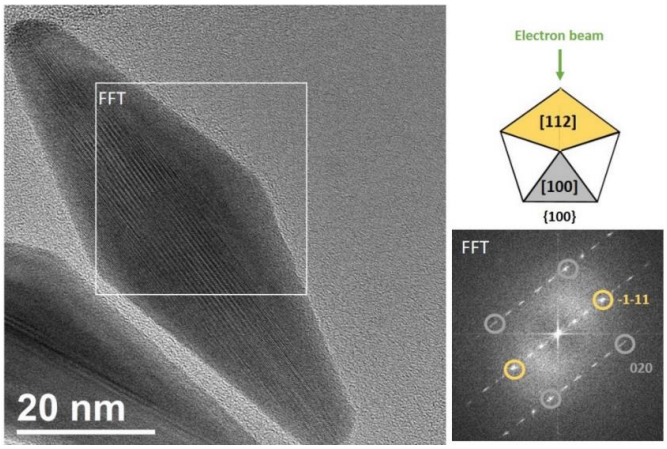

Figure 3.16 HRTEM image of a bipyramidal seed. The Fast Fourier Transform (FFT) corresponds to the superposition of two FCC crystals oriented along the ⟨100⟩ and ⟨112⟩ zone axes. Such atomic contrasts are characteristic of a pentatwinned nanostructure with one of its lateral {100} facets (or edge for bipyramids) perpendicular to the electron beam.

To provide a deeper understanding of this anisotropic growth mode, it is crucial to evaluate kinetic and thermodynamic effects on the shape of NPs. Interestingly, the growth rate of the GBPs@Ag was very different in our nanoscale and bulk-scale *in situ*

investigations. Indeed, the longitudinal growth rate deduced from AS and BEM simulations were 0.046 nm/s (Figure 3.13d). We further show that the growth rate of the GBPs@Ag rods can be varied between 0.0045 and 0.13 nm/s by performing the overgrowth reaction at other reaction temperatures and precursor concentrations (Figure 3.17a). In the LCTEM experiments, the longitudinal growth rate of the NPs varies from 0.54 to 1.25 nm/s (Figure 3.17b). The graph shows that the average growth rate does not increase with the dose rate. It is worth noting that the growth of silver is only observed in the irradiated area, but the reaction kinetics is not controllable with the electron beam. The radiolysis of water generates several radical and molecular species, including aqueous electrons and hydrogen radicals, which are two strong reducing agents. As demonstrated by many groups both experimentally and theoretically,[123,250,262] these radiolytic products can reduce metal precursors and activate the nucleation and growth of metallic nanoparticles within the liquid cell. Therefore, the much higher longitudinal growth rate observed in the liquid cell is very likely due to radiolysis boosting the silver atom supply. Surprisingly, the growth rate did not scale with the electron dose rate but seems rather dependent on the local availability of silver precursor feedstock. This absence of kinetic effects on the shape of the NPs indicates that the anisotropic growth along the ⟨110⟩ direction is governed by thermodynamic effects, most likely due to the passivation of the lateral {100} facets by capping ligands.

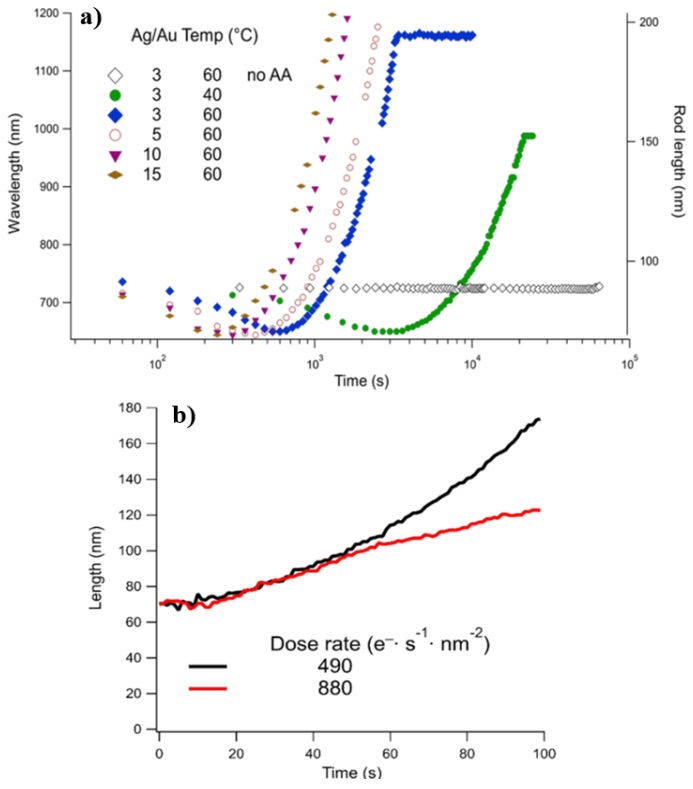

Figure 3.17 a) Investigation of the growth kinetics at other reaction temperatures and precursor concentrations. b) Evolution of the nanorod length observed by LCTEM as a function of time for two different electron dose rates (i.e. different magnification).

In LCTEM, metallic precursor reduction can be driven by radiolysis alone. We took advantage of this feature to conduct an overgrowth reaction without AA in the reaction medium and reveal the role of this chemical in the anisotropic growth process. Figure 3.18 shows that isotropic silver shells were obtained without AA, suggesting a dramatic modification of the growth pathway. The transformation of bipyramids into nanorods in the first stage of shell formation is similar to that of AA. However, the subsequent growth proceeds at a similar speed in the longitudinal and lateral directions (0.66 and 0.23 nm/s, respectively), suggesting an isotropic radial growth in three dimensions (Figure 3.14c). The dose rate range used in the experiments performed with and without ascorbic acid is the same. These *in situ* observations indicate that AA drives the anisotropic growth of silver on gold, but a direct correlation with batch synthesis was needed to support LCTEM results, in particular, to ensure that radiolysis effects, such as the possible transformation of AA, do not impact these directional growth processes. In order to confirm the role of AA in bulk experiments, halides had to be removed from the reaction medium due to their known role in stabilizing the {100} facets of silver.[128,263] This was challenging because the positively charged headgroups of the surfactant (i.e. CTA^+) are balanced with halides counterions (i.e. Cl^-). Fortunately, we successfully stabilized the GBPs with sodium polystyrene sulfonate (NaPSS)[264] and conducted the silver overgrowth reaction in an aqueous solution (Figure 3.19).

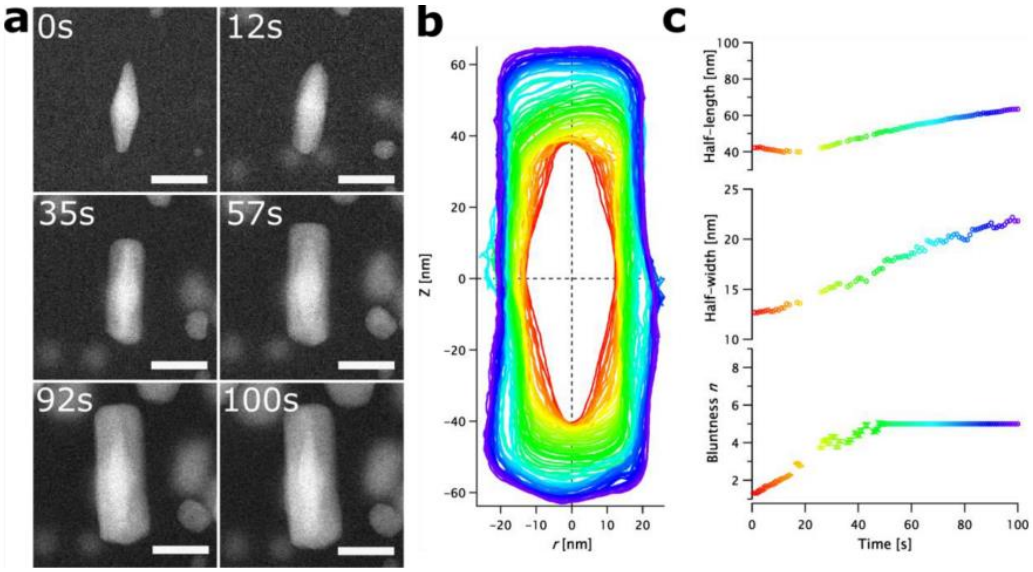

Figure 3.18 Time-resolved growth of GBPs@Ag rods by LCTEM without AA. a) Time-lapse STEM images showing the isotropic deposition of silver on a gold bipyramid as well as homonucleation. The scale bar is 50 nm on all images. b) Contour plots of the GBPs@Ag rods were extracted every second from image analysis. The contour plots were first extracted by image analysis and then fitted by a superellipsoid model. c) Graphs show the time dependence of length, width, and bluntness of the same GBPs@Ag rod as a function of time as determined from the superellipsoid model. The color code of these parameters corresponds to that of the outlines in b).

AA was substituted by hydroquinone (HQ), which was used previously as a weak reducing agent in the synthesis of gold nanorods[265] and we studied the influence of halides by means of supplementing the reaction medium with KCl aliquots. First, the reaction was conducted with 0.003 M of AA and varying the concentration of chlorine ions (i.e. trace amounts or 0.01 M). Remarkably, GBPs@Ag rods were obtained in the presence of chlorine ions and ascorbic acid, using NaPSS as a stabilizer (Figure 3.19e). Although silver deposition was observed without chlorine ions, the growth was not anisotropic in this case.

Second, the synthesis was performed in the same way by replacing AA with HQ but we did not observe the formation of GBPs@Ag rods, even by adding 0.4 M of HQ in the reaction medium (Figure 3.19f). Halide ions are known to play multiple roles in the synthesis of GBPs@Ag rods, such as modifying the silver redox potential, forming complexes with silver, capping the {100} facets and influencing the shape of the surfactant micelles.[263] Although our results tend to demonstrate that the nature of the surfactant is not relevant in directing the anisotropic growth of silver onto GBPs, we cannot neglect the other possible functions of chlorine ions in the synthesis. Overall, this set of experiments confirms that LCTEM results did not originate in radiolysis effects and confirm the key role of AA, in synergy with chlorine ions, as a shape-directing agent in the synthesis of GBPs@Ag rods.

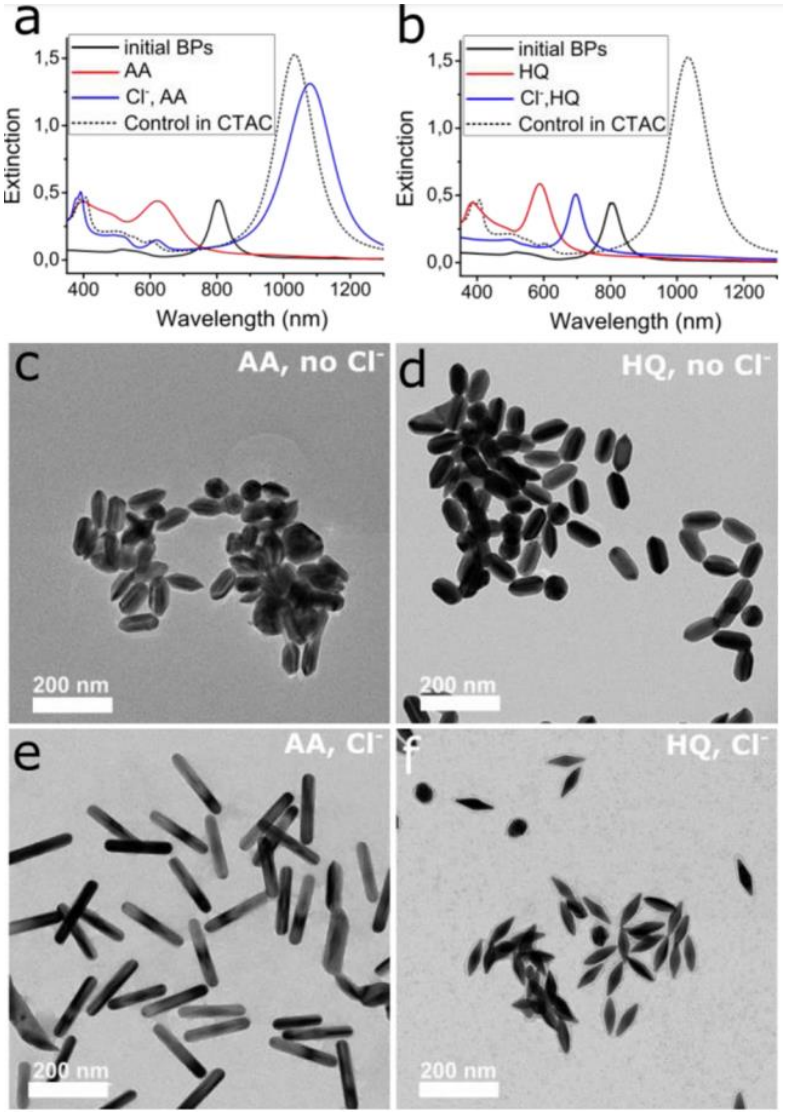

Figure 3.19 Bulk synthesis of GBPs@Ag rods using NaPSS as a stabilizer and various reaction conditions a), (b) AS of the GBPs@Ag rods obtained by using AA or hydroquinone (HQ) as reducing agent, respectively. Experiments are systematically conducted with (blue solid lines) and without (red solid lines) chlorine ions. References spectra of the GBPs (black solid line) and GBPs@Ag rods obtained in CTAC and AA (black dashed line) are displayed for comparison. (c)-(f) Corresponding TEM images.

3.4.3 Conclusions

In conclusion, our LCTEM investigations confirm the key role of AA in guiding silver-on-gold growth processes. Commonly described as a mild-reducing agent, we demonstrate here that AA, combined with halide ions, is also a shape-directing agent that favors the formation of nanorods by stopping crystal growth along with the ⟨001⟩ directions. This is an important result for future optimization and all applications already using those particles, such as sensing[266] and biomedical technologies[267].

More generally, the present work shows that such multimodal *in situ* studies provide a clearer image of the growth mechanisms of nanomaterials. First, corroborating large-scale and nanoscale investigations allow us to sidestep the inherent limitations and artifacts associated with each technique. Second, this approach allows determining whether crystal growth is under kinetic or thermodynamic control and finally it provides a way of identifying the individual role of chemicals in the growth mechanisms, helping our understanding of nanomaterial synthesis.

We should emphasize that our result differs from the work of Visaveliya and Köhler,[11] which describes the synthesis of Ag nanowire by a seedless approach, through the polyol process at 160°C, and it uses PVP as a stabilizer and shape-directing agent. These authors also conclude that AA is essential for the anisotropic growth of silver rods, but only consider the reducing role of AA in their study and ascribe to it a kinetic effect (due to an increase in reaction rate) on the formation of multitwinned particles, which then act as seeds.

In our work, we use preformed seeds and demonstrate that AA has a thermodynamic effect (by stabilizing the {100} facets). Our method can readily be extended to other chemicals that are believed to have a double role (e.g., both reducing and shape-directing agents). For instance, citric acid is widely used as a reducing agent, but it also appears to stabilize the {111} facets of Pd[268] and Au[269]. Experiments and density functional simulations[270] indicate that polyvinylpyrrolidone binds more strongly to the {100} than to the {111} facets of Ag crystals. Our strategy would allow decoupling of the two roles of these compounds and hence a thorough analysis of the growth process, as shown above for AA.

4 Reshaping kinetics of acicular nanoparticles and their nonlinear optical properties

The results in this chapter were published in references **IV** and **VII**:

IV. **Lyu, J**.; Rondepierre, F.; Jonin, C.; Brevet, P.-F.; Hamon, C.; Constantin, D. Shape-Controlled Second-Harmonic Scattering from Gold Nano-Tetrapods. *J. Phys. Chem. C*, **2022,** *126,* (23), 9831–9835. https://doi.org/10.1021/acs.jpcc.2c01867.

VII. **Lyu, J**.; Alloyeau, D.; Matthews, L.; Zinn, T.; Hamon, C.; Constantin, D. Reshaping Kinetics of Nano-Tetrapods. In preparation.

4.1 Introduction

Considerable force is required to deform macroscopic metal pieces. At the nanoscale, however, surface forces are enough to change the shape of nanoparticles (NPs).[271] That is why we can obtain remarkably regular NP populations, but also why some geometrical shapes are difficult to reach or maintain. Understanding and controlling (for instance, blocking) this shape remodeling process is of course very important for further use of NPs. Such reshaping can be understood in a comparison between Ostwald ripening and surface melting, while the former involves the dissolution of weakly bound surface atoms at areas with high convex curvature and re-deposition at concave areas (i.e. it strongly depends on the moieties present in solution), the latter originates from the heat-induced atom motion, the solution composition is irrelevant.[82] However, there is very little work on the dissolution/re-deposition process, which is dominant in solution at room temperature. A system where this process occurs spontaneously and reproducibly would be ideally suited for studying the phenomenon.

Acicular shapes are not thermodynamically stable, so they are obtained in fast processes and often reshape into spheroids over time.[272] Among acicular NPs, especially nanotetrapods (GNTPs)[68] are particularly interesting due to their well-defined and non-centrosymmetric structure. This feature distinguishes them from nanostars,[67] which have an uncontrolled surface distribution of short tips. Studying the evolution of these objects is a challenge due to their complex shape, which is difficult to characterize solely via indirect techniques such as small- or wide-angle X-ray scattering (SAXS or WAXS) or absorption spectroscopy (AS). Time-resolved visualization techniques such

as liquid-cell transmission electron microscopy (LCTEM) do exist, but only a few particles can be observed at a time and the electron beam can drastically modify the process. A comprehensive picture of the synthesis process can thus only emerge from a combination of several methods.

Another fundamental problem in nanoscale physics concerns the relation between the shape of NPs and their linear and nonlinear optical properties. As an example, in the nonlinear optical domain, second harmonic generation (SHG) from nanoscale objects with centrosymmetric shapes and composed of centrosymmetric materials (which is the case of all noble metals) can only result from retardation effects over the particle size and from surface imperfections, precluding large conversion efficiencies for particle sizes well below the wavelength. Here too, a non-centrosymmetric model system where the various aspects (size, shape, symmetry, surface state) can be tuned independently is needed to understand this effect and harness it in view of applications.

In this chapter, we follow in detail the evolution of the GNTPs reshaping as a function of temperature by a combination of techniques, namely time-resolved SAXS, AS, and LCTEM. Not only concern with the evolution of the GNTPs in solution, but we also monitor their reshaping in the dry state to reveal their reshaping mechanism. Moreover, we monitor the SHG properties of the solutions, as the non centro-symmetric distribution of the arms on the GNTP surface and their flattening during reshaping into centrosymmetric shapes has a dramatic effect on the optical properties of these objects. The SHG efficiency is also strongly affected by the surface properties, such as the density and nature of ligands.

4.2 Growth and reshaping of gold nanotetrapods

The synthesis protocol of gold nanotetrapods (GNTPs) was described in Section 2.1.4. Injected the seeds solution into the growth solution, we noted as time 0. Then inserted the mixture into a cuvette to monitor the optical properties of GNTPs by AS at room temperature. In Figure 4.1, the intensity of the plasma peak initially increases (from 0.5 min, aqua line) until it reaches its maximum after 6 min, we believe that the GNTP has been fully formed. There exhibit also two plasmon peaks like GNRs, one is transverse LSPR at 520 nm, and another is a longitudinal LSPR peak around 670 nm. However, the longitudinal LSPR peak blue-shifted gradually and evolved to one peak over time, which shows the GNTPs are not stable and will reshape to spherical GNPs.

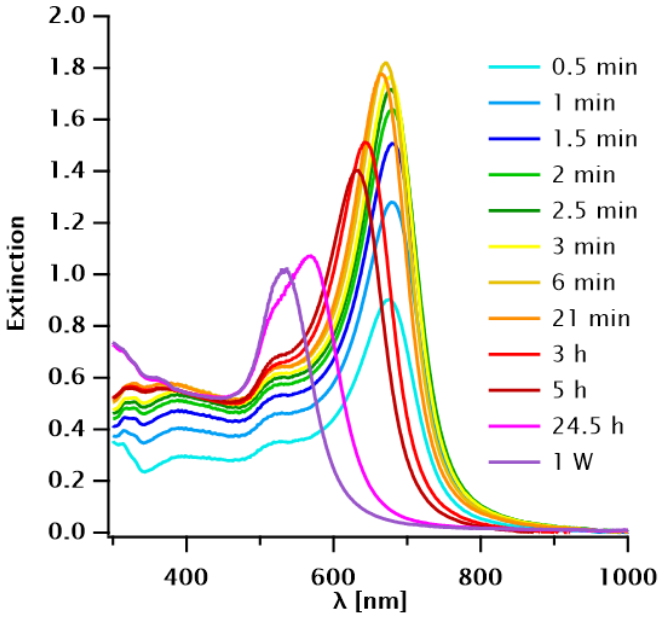

Figure 4.1 Time-resolved AS spectra of GNTPs at room temperature.

To understand better the reshaping mechanism of GNTPs, we controlled the reshaping process using several parameters, such as temperature, silver coating, presence/absence of solvent, and the type of solution such as the addition of iodine.

4.2.1 The role of temperature

We first followed the reshaping of GNTPs by AS at different temperatures, i.e. 9°C, 20.8°C, and 60°C. From the AS spectra, the reshaping process is faster at higher temperatures. For instance, GNTPs reshaped into spheroids in 1 h at 60°C, indicating the high temperature will speed up the reshaping process.

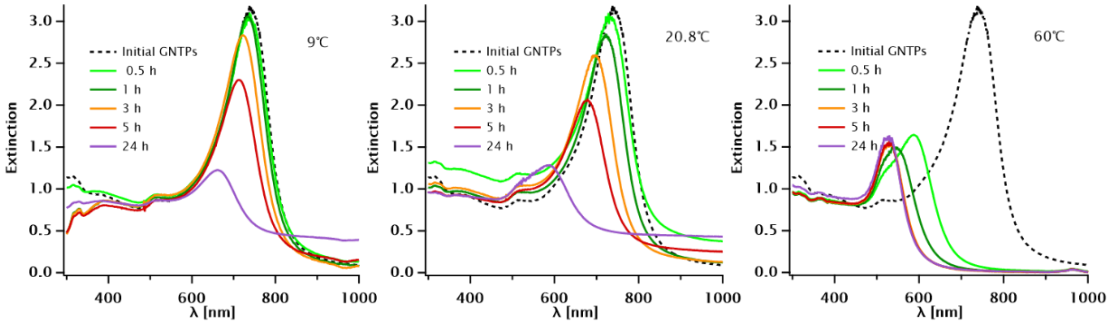

Figure 4.2 AS spectra of GNTPs reshaping over time at different temperatures.

The reshaping process was also monitored by a combined time-resolved AS, SAXS/WAXS and LCTEM under a temperature control setup at the ESRF synchrotron. The AS spectra of the GNTPs reshaping process at different temperatures are shown in

Figure 4.3, in which the interval time is 1 min. It is evident that the higher the temperature, the faster the reshaping rate. At 60°C, GNTPs reshaped completely into a spherical shape in almost an hour. We are treating the AS data using the singular value decomposition (SVD) method to extract the spectral signature of the relevant species and their time evolution and the data analysis of SAXS/WAXS is in progress.

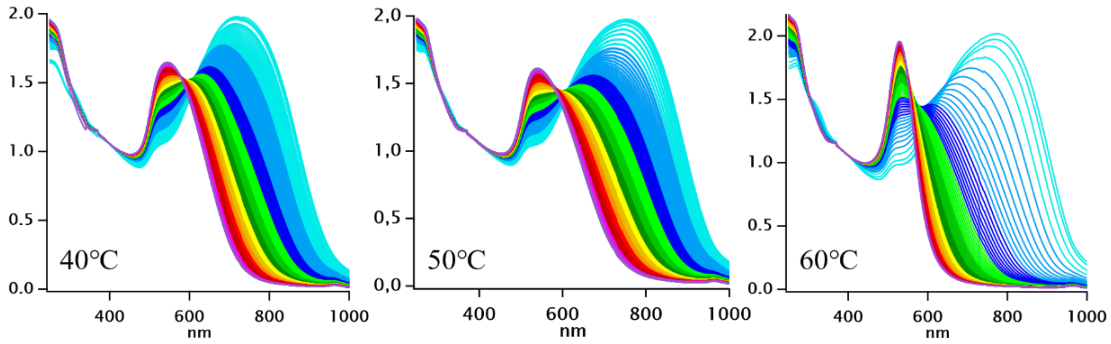

Figure 4.3 Time evolution AS spectra of GNTPs reshaping at different temperatures, i.e. 40°C, 50°C and 60°C, the time spacing is 1 min.

Due to the crystallization of CTAB during the synthesis of GNTPs, it is difficult to monitor the synthesis process by *in situ* LCTEM. We therefore tracked the reshaping of GNTPs pre-coated with a thin silver layer at 150°C. From the video, one GNTP we zoomed reshaped to spheres, supporting atom migration occurs at high temperatures. However, GNTPs without zoomed hardly evolve when we move the observation window, indicating the reshaping process is speeded up by radiolysis. After extracting the images from the video (see Figure 4.4), we can notice the shape revolution over time. Furthermore, we are now trying to treat more videos and draw the contour line of particles during the reshaping process, thereby obtaining the revolution of arm's length and core diameter of GNTPs and then helping us to understand deeply their reshaping kinetic.

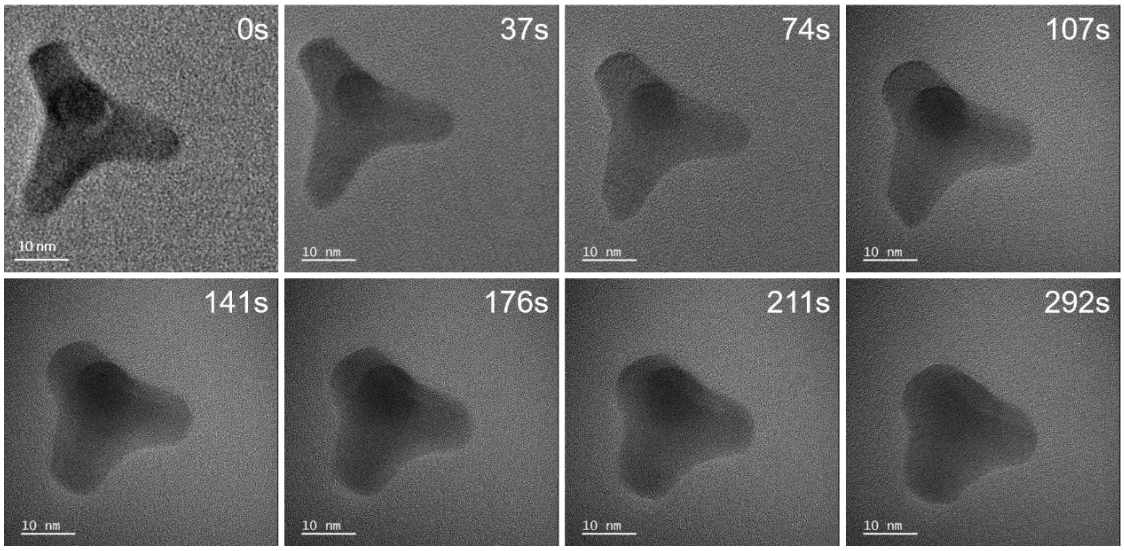

Figure 4.4 Time-resolved images of GNTPs reshaping extracted from LCTEM video.

4.2.2 Silver coating

With the experience of the core-shell bimetallic NPs synthesis, we expect to apply this strategy to quench the reshaping process and obtain objects with the same morphology to the greatest extent.

4.2.2.1 Stabilizing GNTPs with different Ag/Au molar ratios *K*

Firstly, the prepared GNTPs were coated with different Ag/Au molar ratios *K* (from 0.01 to 8). The optical properties and the morphology of GNTPs@Ag were obtained by AS and TEM separately. Note here that the silver coating is performed directly after the longitudinal plasma peak of GNTPs reaches the highest value.

Some of AS spectra were selected to be shown here, the GNTPs will still reshape to spherical when *K* is below 0.2, but the morphology of GNTP will be changed due to the overgrowth of silver when *K* is larger than 0.2. Therefore, a thin silver coating, *K* = 0.2, can efficiently block the reshaping of GNTPs and prevent the morphology from evolving.

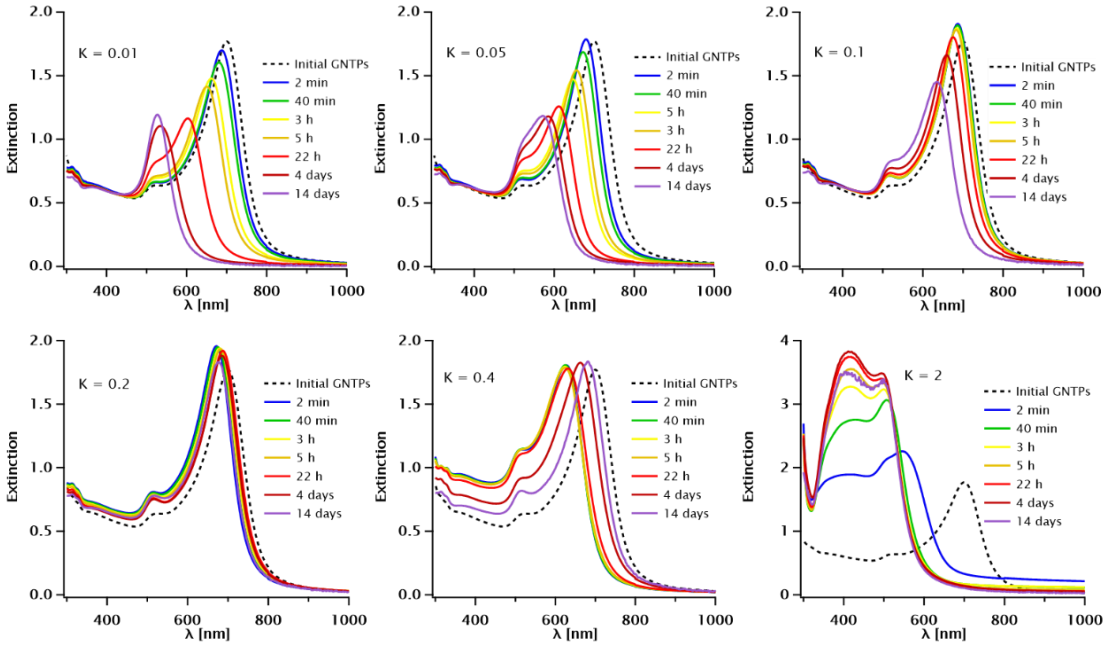

Figure 4.5 AS spectra of GNTPs coated with variable Ag/Au molar ratio K. The K values are indicated in each panel.

The reshaping is still slowly proceeding over time when K is below 0.2. It's difficult to capture the morphology of the particles, we thus took the TEM images of GNTPs coated with silver when K between 0.2 to 8. We can observe distinctly the GNTPs core and silver shell when K increases. Therefore, we used Ag/Au molar ratio K = 0.2 for the following experiments. Additional TEM images are shown in Appendix 8.2.1.

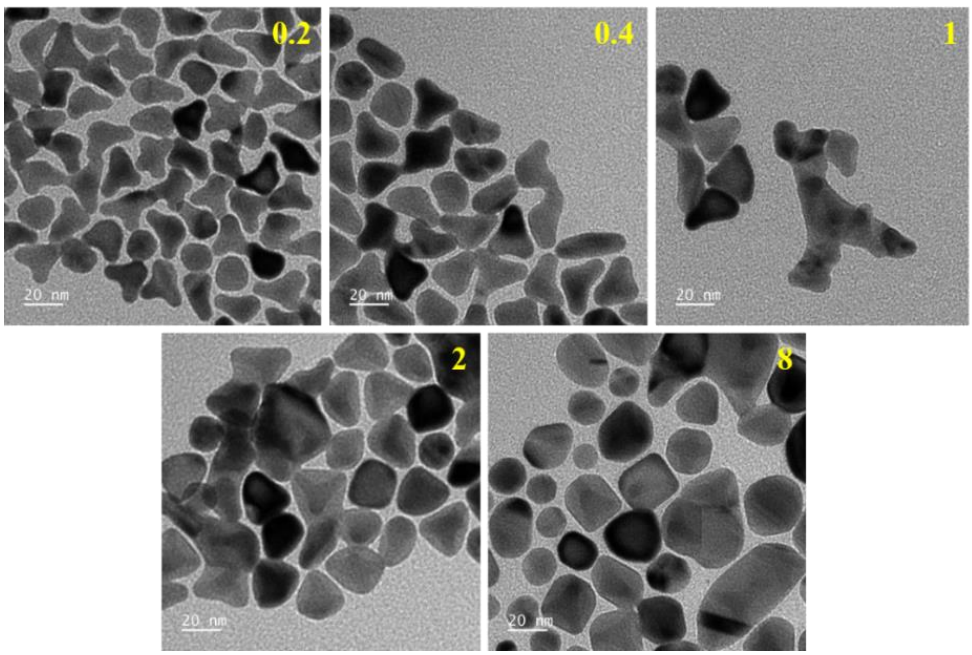

Figure 4.6 TEM images of GNTPs coated with variable Ag/Au molar ratio K. The K values are indicated in each panel.

Thus, any state during GNTPs growth and reshaping can also be blocked by a thin layer of silver. The AS spectrum in Figure 4.7 (left panel) is after the silver coating of the GNTPs in Figure 4.1. The SAXS spectra of the same samples are shown in the right panel, the oscillation peak significantly occurred between 0.03 and 0.1 A^{-1} indicating that spherical NPs formed after 1 week. In addition, several samples were then selected for TEM (Figure 4.8). GNTPs was fully generated 6 min after the addition of the seed solution and had the longest arm lengths. After that, GNTPs start to reshape, manifested by a blue shift of the plasma peak and a gradual decrease in arm length. The details are shown below.

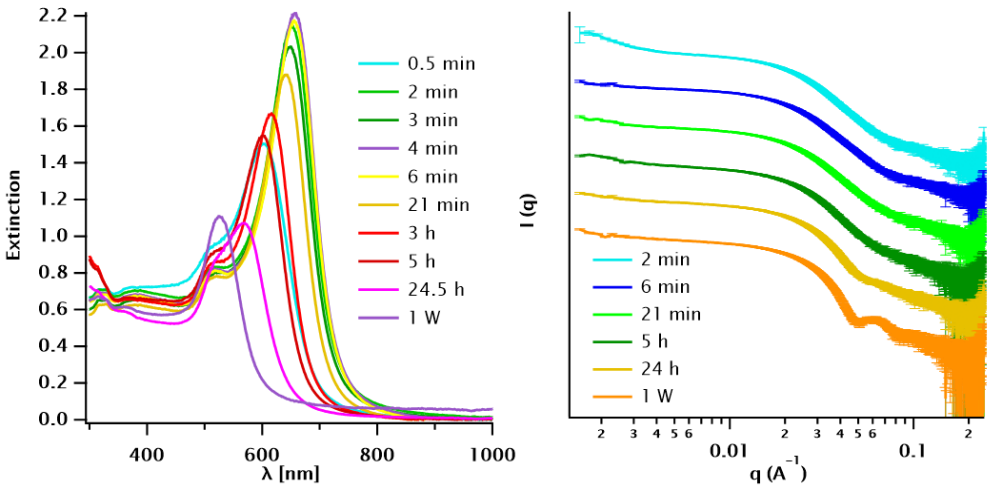

Figure 4.7 AS (left) and SAXS (right) spectra of GNTPs coated with silver over time.

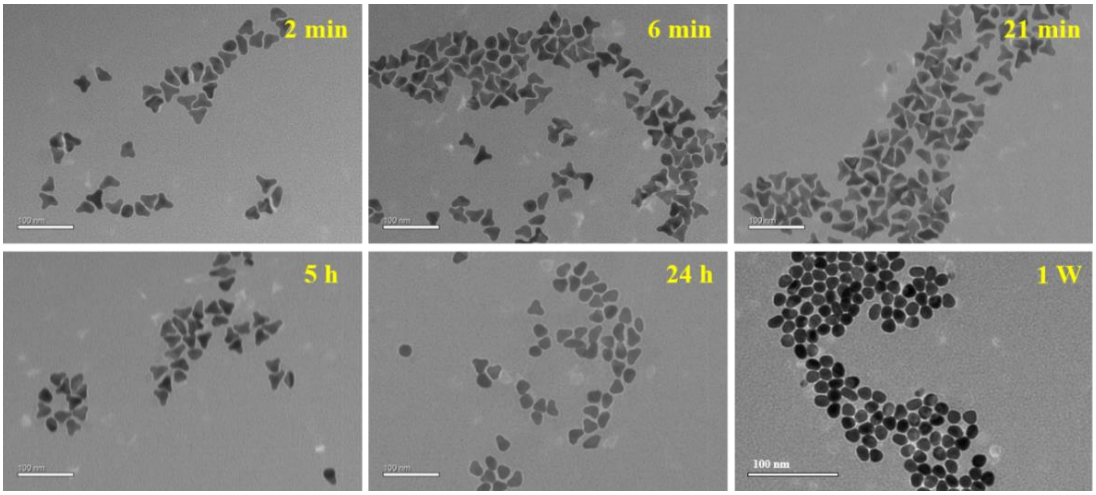

Figure 4.8 TEM images of GNTPs coated with silver at different times.

The size distribution of particles is shown in Table 4-1, the details of measurements are provided in Section 2.3.1.1 and Appendix 8.2.2.

Table 4-1 Particle sizes extracted from the TEM images (mean ± SD): arm length L and core diameter $2R$ for the GNTPs.

Sample	L (nm)	$2R$ (nm)
GNTPs-2 min	13.2 ± 2.5	15.8± 1.2
GNTPs-6 min	13.7 ± 2.0	15.4± 0.8
GNTPs-21 min	12.6 ± 2.4	16.2 ± 1.2
GNTPs-5 h	10.7 ± 2.0	16.9 ± 1.2
GNTPs-24 h	7.7 ± 2.1	18.6 ± 2.1
GNTPs-1 W	0	22.4 ± 2.1

4.2.3 Presence/absence of solvent

We are not only concerned with the evolution of the GNTPs in the solution but also studied their reshaping in the dry state, for two main reasons: i) this process can serve as a reference and a source of complementary information for the solution kinetics, and ii) the possibility of preserving the tetrapodal shape or, conversely, of inducing the transition at will, makes these objects very attractive for applications. Specifically, 10 µL of GNPs droplets were deposited immediately on the glass coverslip and carbon grid for AS and TEM measurements over time respectively, once GNTPs formed completely. Of particular note is that these two samples have to be dried under a vacuum as soon as possible until in the dry state to avoid the influence of the solvent in the droplets. The rest of the suspension were extracted into aliquot and then stabilised with silver at different times. Their properties were monitored over time with AS and TEM. Time 0 coresponds to the time at which the seeds solution is injected into the growth solution. The general procedure is shown in Figure 4.9.

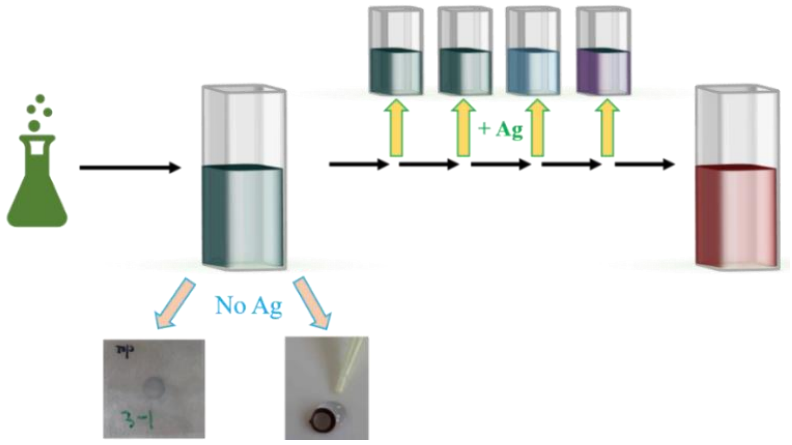

Figure 4.9 Scheme of monitoring GNTPs reshaping process in the solution and the dry state.

As described above, the plasmon peak blue shift and lead to a strong color shift of the colloidal suspensions, from deep blue-green to red. The TEM images of GNTPs obtained after various reshaping times are shown in Figure 4.10C, various arm lengths L and core diameter $2R$ are shown in Table 4-2.

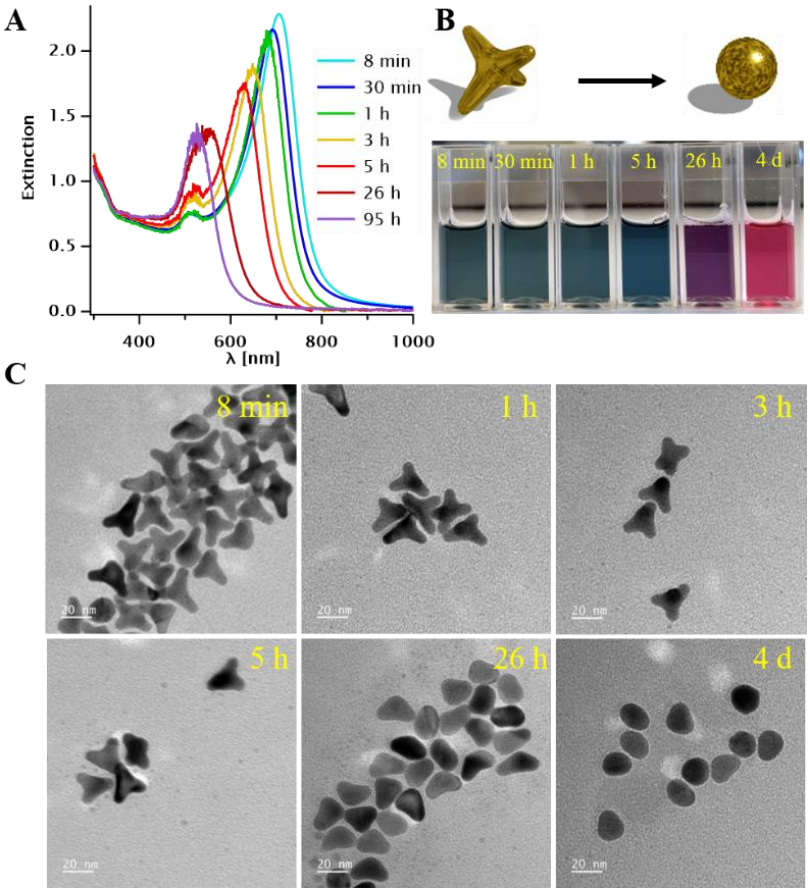

Figure 4.10 Time-resolved AS spectra (A) and photograph (B) of GNTPs suspensions. (C) Corresponding TEM images.

Table 4-2 Particle sizes of GNTPs in the solution extracted from the TEM images (mean ± SD): arm length L and core diameter $2R$ for the GNTPs.

Sample	L (nm)	$2R$ (nm)
GNTPs-8 min	10.1 ± 3.1	9.1± 0.8
GNTPs-1 h	9.3 ± 2.8	9.4± 0.7
GNTPs-3 h	7.9 ± 2.5	9.6 ± 1.6
GNTPs-5 h	7.4 ± 2.6	10.0 ± 0.6
GNTPs-26 h	4.8 ± 2.1	10.4 ± 0.6
GNTPs-4 d	0	16.8 ± 2.4

It took around 30 min to make sure the GNTPs were in the dry state under vacuum, after that, the particles deposited on the coverslip were monitored by time-resolved AS, see Figure 4.11A. The plasmon peak blue shift obviously but still exhibits two peaks until 111h later (around 5 days), demonstrating the GNTPs reshaping process occurred in the dry state but the reshaping process is slower than in suspension. From the TEM images (see Figure 4.11B), one could still observe definitely the arm of GNTPs two months later. Various arm lengths L and core diameter $2R$ are shown in Table 4-3.

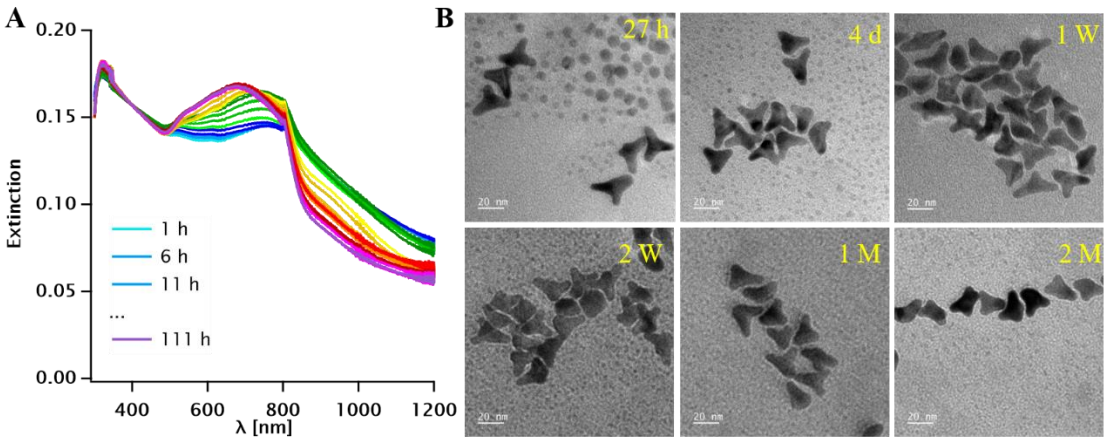

Figure 4.11 (A) Time-resolved AS spectra of GNTPs deposited on a glass coverslip. (B) TEM images of GNTPs deposited on the carbon grid.

Table 4-3 Particle sizes of GNTPs in the dry state extracted from the TEM images (mean ± SD): arm length L and core diameter $2R$ for the GNTPs.

Sample	L (nm)	$2R$ (nm)
GNTPs-27 h	10.1 ± 3.1	9.1± 0.8
GNTPs-4 d	9.3 ± 2.8	9.4± 0.7
GNTPs-1 W	7.9 ± 2.5	9.6 ± 1.6
GNTPs-2 W	7.4 ± 2.6	10.0 ± 0.6
GNTPs-1 M	4.8 ± 2.1	10.4 ± 0.6
GNTPs-2 M	0	16.8 ± 2.4

The dimensions of GNTPs obtained after various reshaping times in the different states are shown in Figure 4.12. We can conclude that reshaping of GNTPs occurs both in the solution and dry state, but the reshaping rate is relatively slow in the dry state. Atom migration plays a key in the reshaping process in the dry state, while atom migration and dissolution/redeposition are both mechanisms that are at play in the solution.

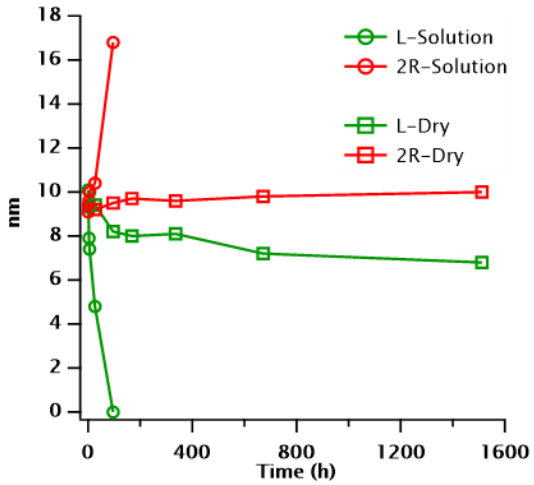

Figure 4.12: The dimensions of GNTPs obtained after various reshaping times in the different states.

4.2.4 The addition of iodine

The reshaping of GNTPs was apparent in the solution, we then carried out the experiments where Au^0 concentration was fixed at 0.25 mM and CTAB concentration was at 12.8 mM, and 0.01 mM KI was added in the other one. As shown in Figure 4.13, the reshaping rate drastically increase when iodide was added, which is in agreement with the previous works of Liz-Marzán et al.[82] The reason is that they can also adsorb (displacing bromide) and then coordinate and solubilize the weakly bound gold atoms, which will re-deposit onto more favorable sites, thus driving the reshaping. This experiment indicates that the shape deformation is indeed related to the solutes in the solution, confirming the Ostwald ripening occurred, which usually refers to a dissolution and redeposition process. Meanwhile, confirmed the iodide ions' stronger coordination affinity to gold.[82]

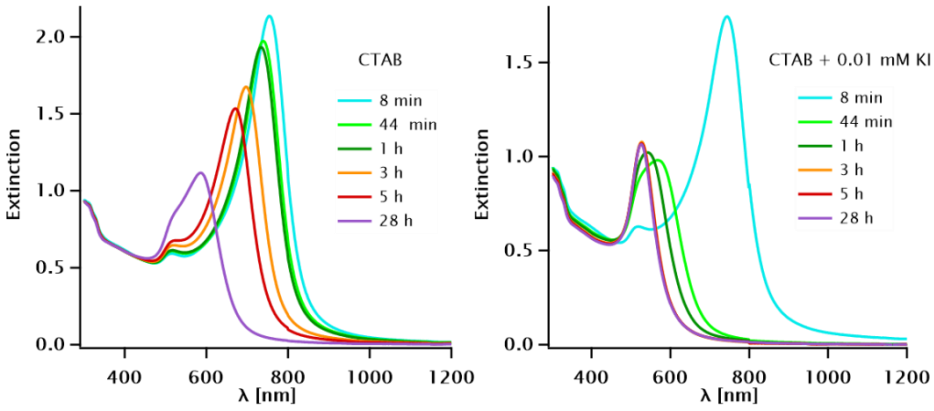

Figure 4.13 AS spectra of GNTPs dispersed in the different solutions: CTAB (left) and CTAB + KI (right).

4.2.5 Stability of gold nanotetrapods

The stability of GNTPs after being coated with a thin layer of silver at different temperatures was investigated by AS and SAXS. From AS, the plasmon peak didn't evolve showing the GNTPs are very stable at room temperature for at least 2 months and still keep well at 60℃, which is very critical for our following experiments.

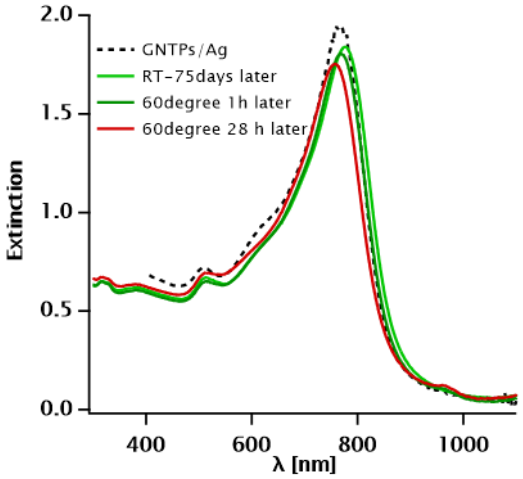

Figure 4.14 AS spectra of GNTPs coated with silver at different temperatures. The black dashed line is the initial GNTPs coated with silver as a reference.

The SAXS spectra were shown in Figure 4.15, without silver on the left panel, the number of the oscillation peaks increase in 1h and shift to lower *q* indicating the spherical formed, but after being coated with silver, the oscillation peak didn't change proving the GNTPs coated with silver are stable at 70℃.

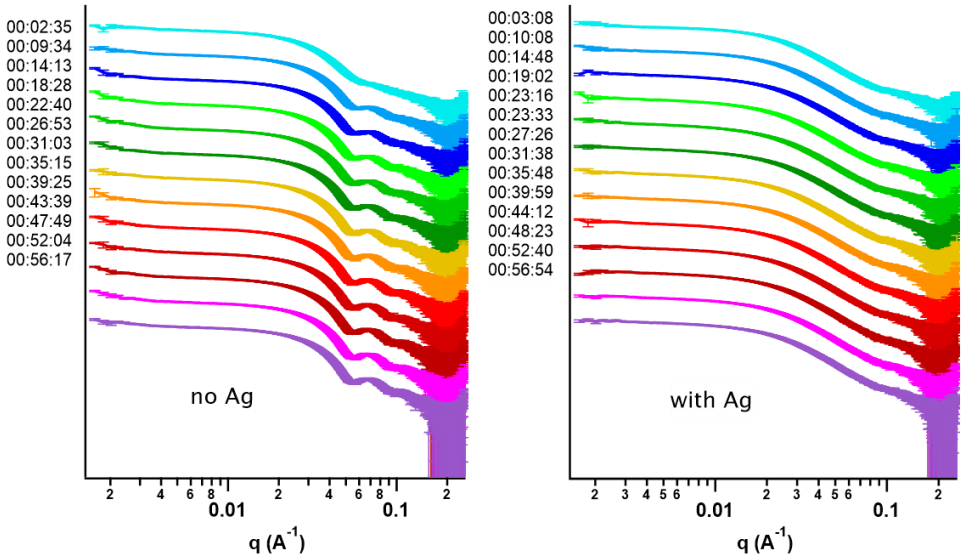

Figure 4.15 Time evolution SAXS spectra of GNTPs coated without (left) and with (right) silver at 70℃.

4.2.6 Seeds volume tunability

Like ordinary seed-mediated methods, we can also tune the morphology of GNTPs via adjusting the content of seeds. By decreasing the seed solution without changing other experimental parameters, the intensity of the longitudinal plasmon peak decreases, and a new third plasmon peak occurs at the middle wavelength. From the TEM images, the polydispersity GNTPs with longer arm lengths while few complete four arms were obtained at lower seeds content. These results explain the existence of other plasmon peaks in the AS spectra and illustrate that reducing continually the volume of the seeds to obtain the GNPs with longer and sharper arm lengths is not the ideal GNTPs.

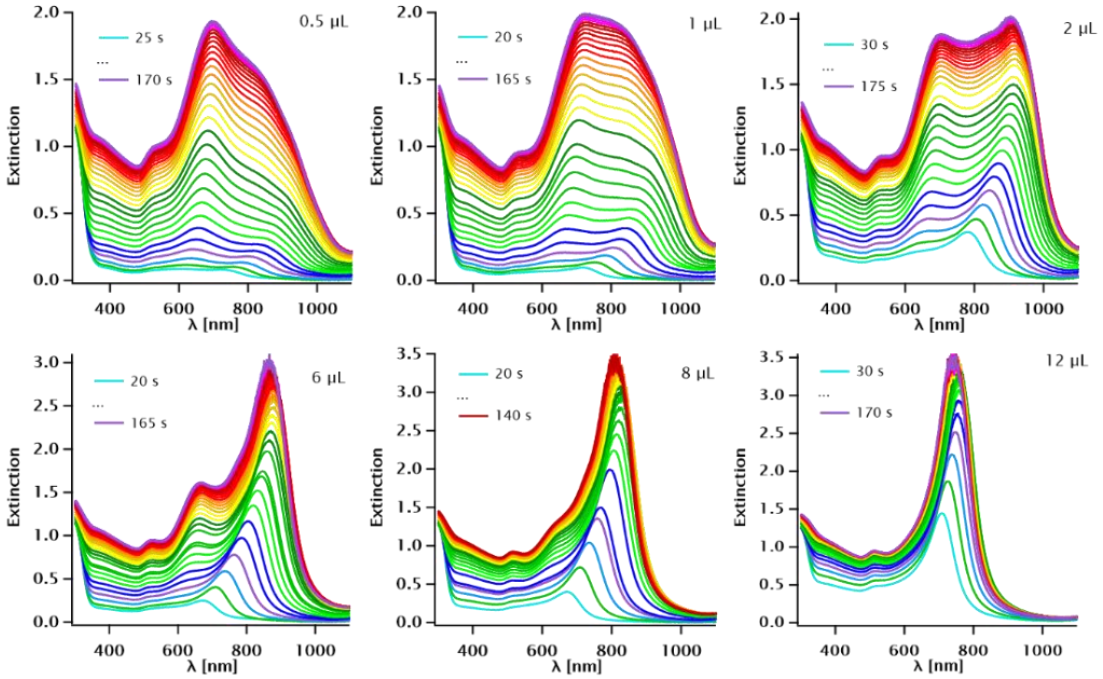

Figure 4.16 AS spectra of GNTPs synthesized with different seed volumes.

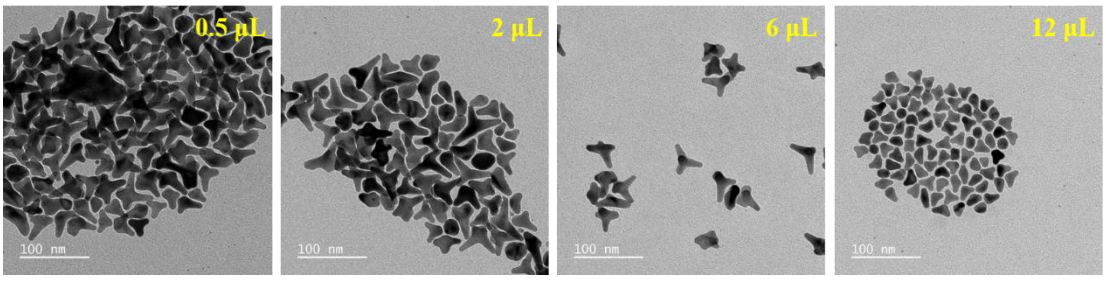

Figure 4.17 TEM images of GNTPs synthesized with different seed volumes.

4.2.7 Conclusions

This reshaping process of GNTPs is related strongly to the temperatures, presence/absence of a solvent, and the addition of Iodine. In detail, as the higher temperatures, the fast reshaping process. Also, reshaping of GNTPs occurs in the dry state as well suggesting an atom migration mechanism, but the kinetic is much slower than one in solution. In addition, the reshaping rate drastically increased when iodide was added, indicating that the shape deformation is indeed related to the various solutes, confirming the dissolution and redeposition mechanism.

One interesting thing is that the reshaping process can be blocked with a thin silver layer at a different stage (Ag/Au=0.2). Using this way, the morphology of GNTPs can be well stabilized to the greatest extent, thereby also preventing the evolution of optical properties. Moreover, the GNTPs coated with silver are very stable for 2 months as well as at 70℃.

In end, we also give general recommendations for the synthesis of GNTPs. Different from the common seed-mediated method, the regulation of seed content cannot precisely adjust the morphology of GNTPs, while some particles with other morphologies will appear.

4.3 Nonlinear optical properties: shape-controlled second-harmonic scattering from gold nanotetrapods

In the search for efficient building blocks for nonlinear metamaterials, plasmonic NPs have received considerable attention. Their quadratic nonlinear optical properties result from a complex interplay between the nature of the bulk material, the object shape, surface defects and retardation effects. This versatility can be used to tailor the properties of the resulting material. However, despite extensive investigation, separating and controlling these contributions is still a challenge. In this section, we explore the second harmonic scattering response from colloidal GNPs with tetrahedral symmetry. The material itself is centrosymmetric but not the shape, conferring to the first hyperpolarizability an almost purely octupolar symmetry. By reshaping the nanoparticles into spheres, we show that their nonlinear response is controlled by morphology. These results open the way for new kinds of nonlinear plasmonic platforms and imaging probes.

4.3.1 Gold nanotetrapods reshaping and stabilizing

After GNTP formation, the solution was diluted by an appropriate amount of 10 mM CTAC solution in order to bring the Au^0 concentration to 0.25 mM and then put in a water bath at 60°C to induce fast reshaping. Several mL was extracted at different times. We then injected 10 mM $AgNO_3$, 40 mM AA, and 0.2 M NaOH sequentially into the GNTPs solution to block the reshaping. We lightly shook the solutions up and down after each injection.

We applied a thin silver layer at an Ag/Au molar ratio of 0.2 at different times after particle formation, obtaining nano-objects with the same morphology and total volume, but various arm lengths L and core diameters $2R$, as shown in Figure 4.18a-e. Gold nanospheres (GNSs) were also covered with silver (Ag/Au= 0.2), an operation that does not change the morphology of the particles (see Figure 4.18f). All particles were dispersed in an aqueous solution of 10 mM cetyltrimethylammonium chloride (CTAC), at an Au^0 concentration of 0.17 mM (GNTPs) or 0.22 mM (GNSs). Their dimensions are given in Table 4-4 and their AS spectra are displayed in Figure 4.18g, along with boundary element method (BEM) simulations.

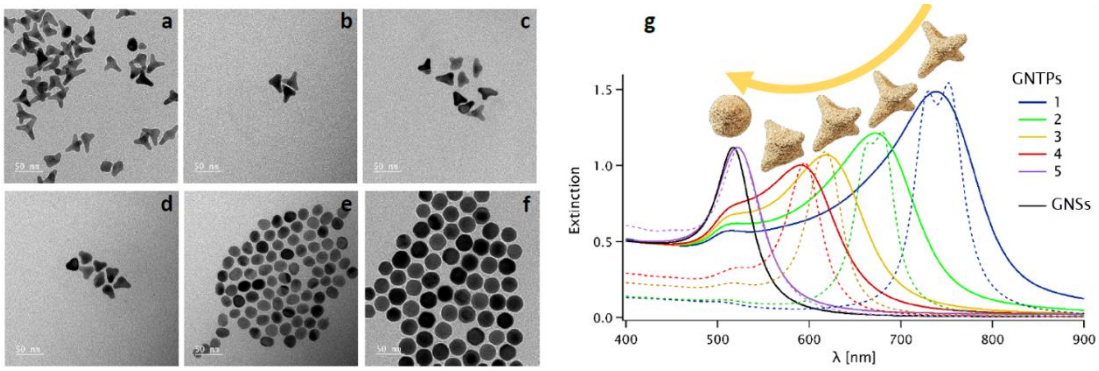

Figure 4.18 a) TEM images of (a-e) GNTPs obtained after various reshaping times: 3 min, 18 min, 33 min, 48 min and 12 h, (f) GNSs, and (g) AS spectra of particle suspensions, renormalized to the extinction of 0.5 at λ = 400 nm (solid lines) and spectra of the model shapes, simulated using BEM (dashed lines). The GNTPs are represented above each curve, and BEM simulations were done by Dr. Doru Constantin.

Table 4-4 Particle sizes extracted from the TEM images (mean $\pm$ SD): arm length L and core diameter $2R$ for the GNTPs, diameter $2R$ for the GNSs. Simulation parameters: BEM simulations were done using the TEM values for $2R$ and the slightly higher values L_{BEM} for the arm length in order to yield a good agreement between the fits and the data in Figure 4.18g. HRS parameters: first hyperpolarizability β, depolarization ratio D and retardation parameter ζ^V (see the text below for details).

Sample	Age	L (nm)	$2R$ (nm)	L_{BEM} (nm)	β (10^{-25} esu)	D	ζ^V
GNTPs-1	3 min	17.1 ± 2.3	15.2 ± 1	19	6.04 ± 0.06	0.61 ± 0.01	0.01 ±0.002
GNTPs-2	18 min	11.1 ± 2.6	15.8 ± 0.8	13	2.56 ± 0.03	0.52 ± 0.02	$(4 \pm 0.5)10^{-3}$
GNTPs-3	33 min	8.7 ± 2.3	16.6 ± 0.8	9.5	1.42 ± 0.11	0.48 ± 0.01	0.13 ±0.01
GNTPs-4	48 min	6.3 ± 2.2	17.0 ± 0.6	7.5	1.3 ± 0.09	0.38 ± 0.01	0.11 ± 0.01
GNTPs-5	12 h	0	19.6 ± 1.2	0	1.5 ±0.17	0.20 ± 0.01	0.08 ± 0.01
GNSs	-	-	28.1 ± 2.1	-	0.56 ± 0.05	0.27 ± 0.01	0.33 ± 0.06

4.3.2 Second-harmonic scattering

The linear polarization of the fundamental beam was controlled with a half-wave plate, defining the angle γ with respect to the laboratory vertical direction. The polarization angle Γ of the harmonic light was selected with a linear polarizer placed either vertically ($\Gamma = 0$) or horizontally ($\Gamma = \pi/2$), denoted in the following by V and H, respectively. For the two Γ positions, we measured $I^{\Gamma}_{HRS}(\gamma)$ over a complete 2π range, see Figure 4.19A. The concentration dependence of $I^{\Gamma}_{HRS}(\gamma = 0)$ normalized to the solvent signal yielded the first hyperpolarizability β in absolute esu units using water as the reference while the dependence of the signal intensity on the polarization angle (Figure 4.19B) yielded the depolarization ratio D and the retardation parameter ζ^V. All these quantities are given in Table 1 for each sample.

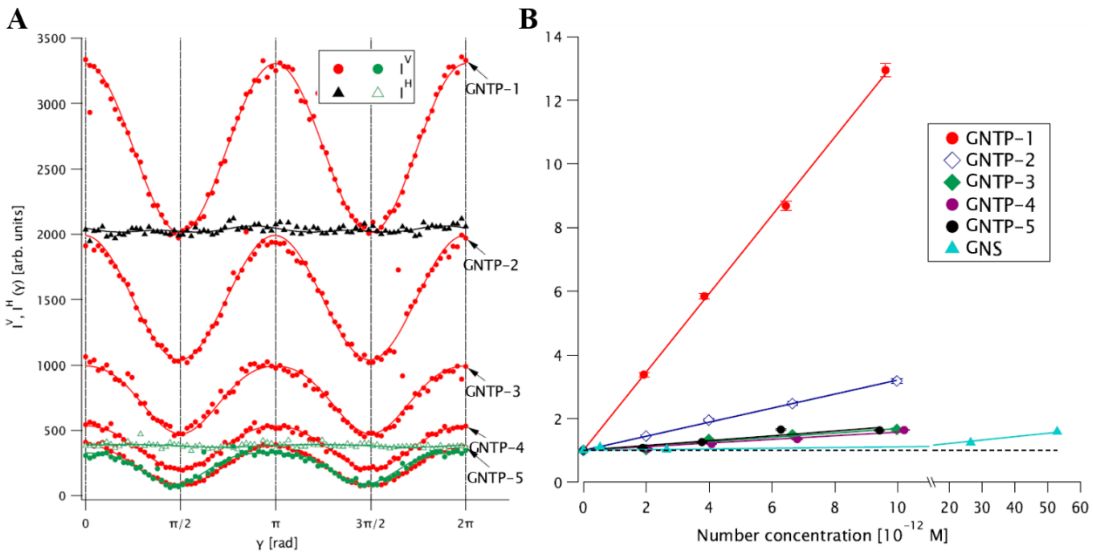

Figure 4.19 (A) Polarization-resolved HRS intensity $I^{\Gamma}_{HRS}(\gamma)$,with $\Gamma = V, H$ for the GNTP samples (red and black symbols) and the GNS (green symbols) and fits with Eq. (2-10) (solid

lines). I_H is only shown for GNTP-1 and GNS. (B) HRS intensity $I_{HRS}(N)$ for all the samples discussed in the text (symbols) and linear fits (lines). Note the split x axis for the GNS data.

The first hyperpolarizability β (solid dots in Figure 4.20) decreases markedly as the GNTPs reshape. The initial GNTPs (sample GNTP-1) have a hyperpolarizability β over 10 times higher than that of the reference nanospheres (sample GNS), although their volume is three times lower! For the more symmetric shapes (GNTP-3 to 5) β reaches a plateau of the order of 10^{-25} esu that we attribute to surface defects (leading to effective asphericity).

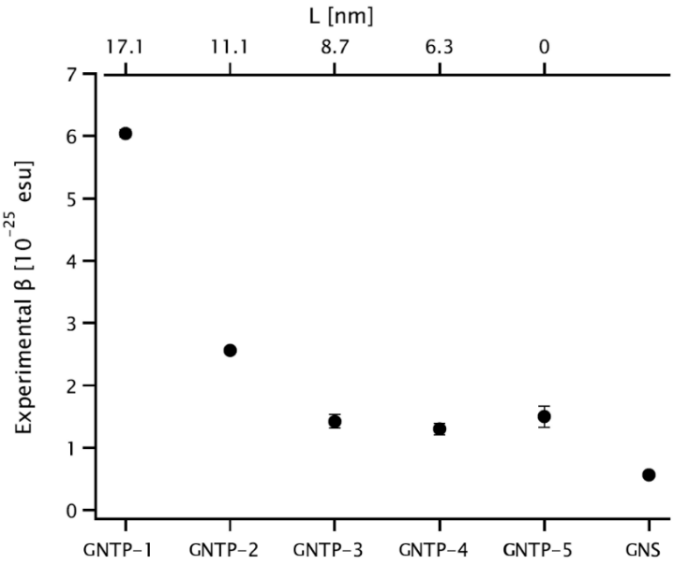

Figure 4.20 Left axis: first hyperpolarizability β for all the samples, identified on the bottom axis (solid black dots). Error bars are smaller than the symbol size. For GNTPs, the arm length L is given on the top axis.

More information can be gleaned from the polarization dependence of $I_{HRS}^{\Gamma}(\gamma)$. The depolarization ratio D (Figure 4.21, left) is initially rather high (D = 0.61), indicating a harmonic response with almost purely three-dimensional octupolar symmetry (D_{oct} = 2/3), as expected from the shape of the GNTPs. This parameter decreases along the reshaping process, spanning the range from D_{oct} to D_{dip} = 1/9 for purely dipolar symmetry. The retardation parameter ζ^V (Figure 4.21, right) remains low for all samples, as expected for objects much smaller than the wavelength. For spheres (GNS), where the shape is perfectly centrosymmetric and the surface free from defects, the only source of SHG is retardation, hence a high ζ^V value. This contribution is however ineffective at small sizes and therefore the hyperpolarizability is small. The determination of a depolarization ratio D is, in this context, a measure of the distribution

of the defects at the nanoparticle surface, since it is indefinite for a pure retardation contribution (D being the ratio of two vanishing intensities). The experimental value, markedly different from the pure dipolar 1/9 theoretical value, indicates a rather general defect distribution over the entire surface.

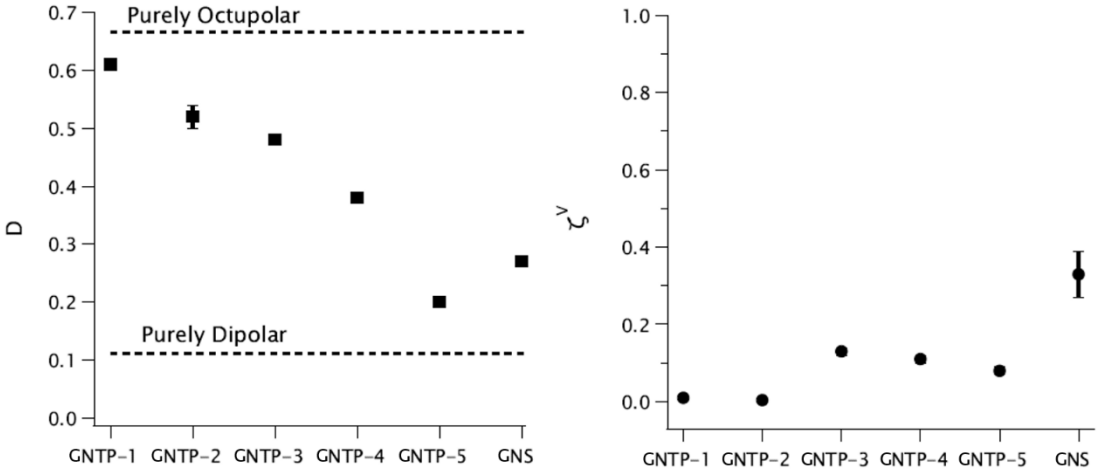

Figure 4.21 Depolarization ratio D (left) and retardation parameter ζ^V (right) for all the samples.

4.3.3 Conclusions

Gold nanotetrapods exhibit strong SHG, essentially due to their shape (and hence with the same octupolar symmetry as the objects themselves) and which decreases as they reshape into spheres, reaching a plateau, the origin of which is driven by the surface defects. Initially, retardation is weak and the SHG response is dominated by the shape non-centrosymmetry. As the GNTPs evolve into spheres, this source weakens and is complemented with an origin due to retardation.

The arm length (and hence the extinction spectrum) of the GNTPs can be tuned over a wide range, which is very interesting in view of applications. For instance, one could place either the maximum value (peak) or the steepest slope of the longitudinal plasmon band at the excitation frequency for maximum efficacy or sensitivity, respectively. The presence of two plasmon bands opens the way toward doubly resonant systems,[273] where the fundamental and harmonic frequencies coincide with the longitudinal and transverse bands, respectively.

Possible applications to nonlinear imaging can also be envisioned, since the SHG signal is spectrally sharp and coherent, in contrast with two-photon luminescence, for instance. These advantages have already prompted the use of ferroelectric materials (e.g. $BaTiO_3$)

as microscopy probes.[274,275] Gold nanoparticles have the added benefit of very versatile surface chemistry, making them adaptable to practically all relevant media (biological or otherwise).

5 Assembling gold nanoparticles into one-dimensional chains

The results in this chapter were published in references **II** and **V**:

II. **Lyu, J.**; Alloyeau, D.; Hamon, C.; Constantin, D. Two-Step Assembly Kinetics of Gold Nanoparticles. *J. Mater. Chem. C* **2021**, *9* (5), 1730–1739. https://doi.org/10.1039/D0TC05076H.

V. Li, X.; **Lyu, J.**; Goldmann, C.; Kociak, M.; Constantin, D.; Hamon, C. Plasmonic Oligomers with Tunable Conductive Nanojunctions. *J. Phys. Chem. Lett.* **2019**, *10* (22), 7093–7099. https://doi.org/10.1021/acs.jpclett.9b03185.

5.1 Introduction

One-dimensional nanoparticle chains (also called "plasmonic polymers"[276]) exhibit fascinating optical properties, such as multiple surface plasmon resonance peaks and the generation of a strong electromagnetic field at the interparticle gaps, as "hot spots", which are very different from those of the isolated objects.[277] Gold nanoparticles (GNPs) are easily assembled into compact structures, e.g. by Van der Waals or depletion forces, but it is much more difficult to obtain open or elongated patterns. End-to-end assembly into long chains is of particular interest,[139] since the longitudinal plasmon peak of the aggregate can be red-shifted over a very wide wavelength range, depending on the number of NPs in the chain and on the tip-to-tip distance. However, by increasing further the number of particles in the chain, the plasmon band red-shift to a finite value due to the so-called "infinite chain limit effect".[278,279]

Plasmonic polymers have been obtained by wet chemical approaches,[280] including but not limited to molecular recognition[146,281–285] or solvophobic interaction[286,287] or mediated by templates.[288] In many cases, the self-assembly reaction progresses until flocculation and can be difficult to handle. In this respect, it is crucial to control the assembly process and stabilize a preferred configuration with defined optical properties. This requires the ability to controllably manipulate the reaction rate, which can be achieved by an external stimulus. A light-controlled synthetic procedure has been demonstrated, but this technique necessitates a femtosecond laser tuned to the plasmon frequencies of the NPs.[289–291] Benchtop methods relying on purely chemical strategies

have been developed to prevent the growth of larger structures such as a molecular competitor[289,292] (e.g. addition of an excess of mono-thiol to compete a dithiolated linker mediated assembly) or through encapsulating the oligomers.[293,294] In these cases, the surface of the oligomers, as well as the particle junctions, are passivated by strongly bound ligands, which may impede further use. This shortcoming can be avoided by a simpler strategy, which involves adding salt to a particle suspension in various solvents, such as DMF,[295] ethanol[296] or a DMF-water mixture.[167] In a recent study, sulfate ions were used to self-assemble gold nanorods into chains in water. They think the end-to-end assembly is attributed to the localized association of sulfate with exposed ammonium head groups of CTAB at the GNRs tip and the assembly kinetics follows the second-order after analyzing the plasmon band of extinction spectra.[76]

After assembly, the region of "hot spots" generated has led to many applications (ranging from biosensing to metamaterial design) that strongly depend on the detailed geometry of the metal surfaces.[297] Therefore, controlling the shape and chemical nature of the "hot spots" in colloidal plasmonic nanosystems has a very wide range of applications. For instance, one can tailor plasmon coupling by bridging NPs together with molecular junctions whose conductivity can be switched at will.[298,299] Controlled melting of adjacent NPs has been performed at the single-particle level by an electron beam to connect gold nanospheres into solid networks featuring low-energy plasmon modes.[300] Colloidal approaches include welding NP assemblies using ultrafast laser pulses.[289,290] In another example, conductive connections were engineered by controlling the sintering of GNP dimers within a silica shell.[301] Another group has controlled the silver thickness at the junction of asymmetric dimers linked with DNA.[302] Although some colloidal-based strategies have been demonstrated, engineering plasmonic assemblies with tunable conductive junctions remains challenging. Current methods rely on the controlled fusing or melting of NP assemblies but do not allow control over the metallic nature of the nanojunction. Moreover, most studies have focused on dimers rather than on larger objects, which are however more interesting for the directional control of light.

We therefore followed the protocol to prepare GNPs chains using sulfate ions. In the present work, various types of surfactant-stabilized GNPs (spheres, rods and bipyramids) were self-assembled into chains. The self-assembly process can be stopped at any stage by adding an excess surfactant to the reaction mixture. We investigated the

reaction kinetics by AS and SAXS and found a two-step mechanism: (1) an initial fast aggregation process (detected by SAXS), in which particles are loosely bound and (2) a slow self-assembly step whereby the particles come into intimate contact. During this step, the AS spectrum of the GNPs changes, and we analyzed it quantitatively by singular value decomposition (SVD) method to extract the time-dependent fraction of monomers and chains as well as the short-scale structure of the latter. The chain's size and structure were also studied by ex-situ and liquid-cell transmission electron microscopy (TEM and LCTEM, respectively). We also could characterize this interaction between NPs by LCTEM and explore the stability of chains by dialysis experiments.

After obtaining the stable chains of GBPs, we deposit a metal of choice at the hot spots' location in chains via the seed-mediated growth procedure. We focused on silver due to its notable plasmonic and photocatalytic properties, respectively. AS and electron energy loss spectroscopy (EELS) were used to describe the evolution of the collective plasmonic response of the nanostructures. Upon bridging the NPs, we observed a strong variation of the optical properties, which can be tuned by the nature of the metallic junction.

5.2 Assembly procedure

Various types of GNPs comprising spheres, rods, and bipyramids were assembled into one-dimensional chains using sulfate ions as initiators. It is worth mentioning that the low concentration of CTAB is the key to the assembly reaction. Typically, 5.7 µL of the stock GNPs suspension (at 88 mM Au and 1.8 mM CTAB) were injected into a polystyrene cuvette, then add 10.2 µL of 1.8 mM CTAB and 16.1 µL water in sequence, and then 1968 µL 1mM $MgSO_4$, the scheme is shown in Figure 5.1. The final CTAB concentration is just 14.3 µM. Note that the order of mixing is important: premixing the CTAB and $MgSO_4$ solutions before adding them to the stock GNP suspension often leads to rapid (a few second) precipitations of the particles, revealed by a grayish color of the solution. The detailed information on well-dispersed NPs is shown in Section 3.2. At any time of the process, 26.5 µL of a 0.756 M CTAC or CTAB solution can be added to the mixture to quench the assembly. A reminder that the amount of CTAB is crucial to the reaction but the CTAB solution is easy to crystallize at low temperature, so be sure to prevent the crystallization of CTAB before assembly.

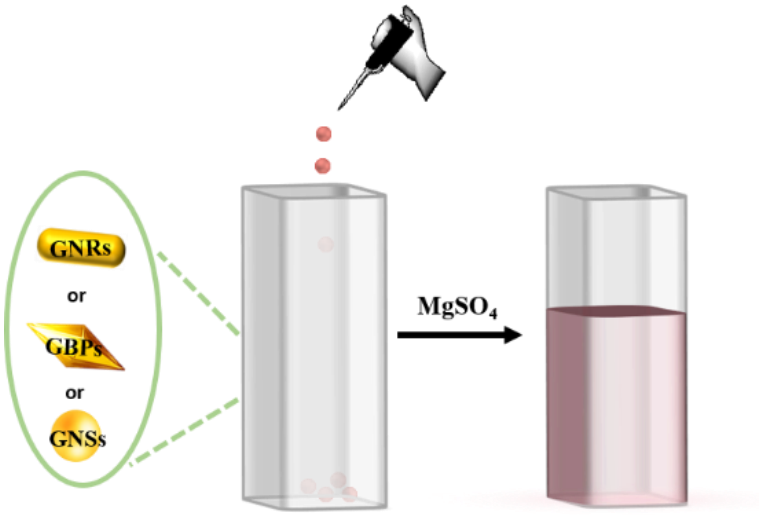

Figure 5.1 Scheme of assembling various GNPs into chains.

In general, we monitored the assembly process by time-resolved AS. The mixture solution was prepared in a 2 mL polystyrene cuvette and inserted within 30 seconds into the instrument to start recording. The spectrum was taken every 30 min.

5.3 Stop and stabilizer the assembly reaction

The assembly process was stopped by the addition of 10 mM CTAC at 0 h, 5 h, and 20 h. For instance, assembly of GNRs and GBPs with 0.25 mM Au^0, 14.3 µM CTAB and 1 mM $MgSO_4$, the evolution of the plasmon band is the same trend as the assembly of GNRs and GBPs (see Figure 5.2). The transverse plasmon peak around 510 nm did not change noticeably, but the longitudinal plasmon band decreased in intensity and new red-shifted broad bands appeared compared with the AS of initial isolated GNPs. This evolution is an indication of particle assembly in a tip-to-tip configuration,[161,303] which we confirmed by our TEM images shown later. After 14 days, the extinction spectra of the suspensions did not evolve (dashed line). This experiment shows that the assembly process can be controlled by excess surfactant and stabilized chains with defined optical properties, which is also fundamental for our further characterizations and applications.

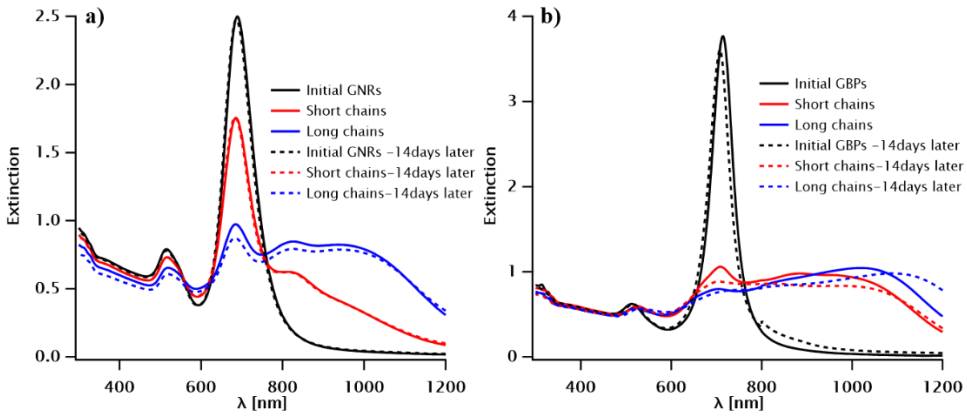

Figure 5.2 Stopping and stabilizing the assembly process of GNRs (a) and GBPs (b) by adding excess CTAC. AS of various plasmon polymers just after stopping (solid line) and the same dispersions after 14 days (dashed line). 0.25 mM Au^0, 14.3 μM CTAB and 1 mM $MgSO_4$ were used for assembly.

5.4 Following the kinetics by TEM

We present TEM images taken at the beginning (0 h) and the end (20 h) of the assembly process for the three-particle shapes in Figure 5.3. In the right column, we zoom in on individual chains. We can observe the beautiful chains with tip-to-tip configurations from the images.

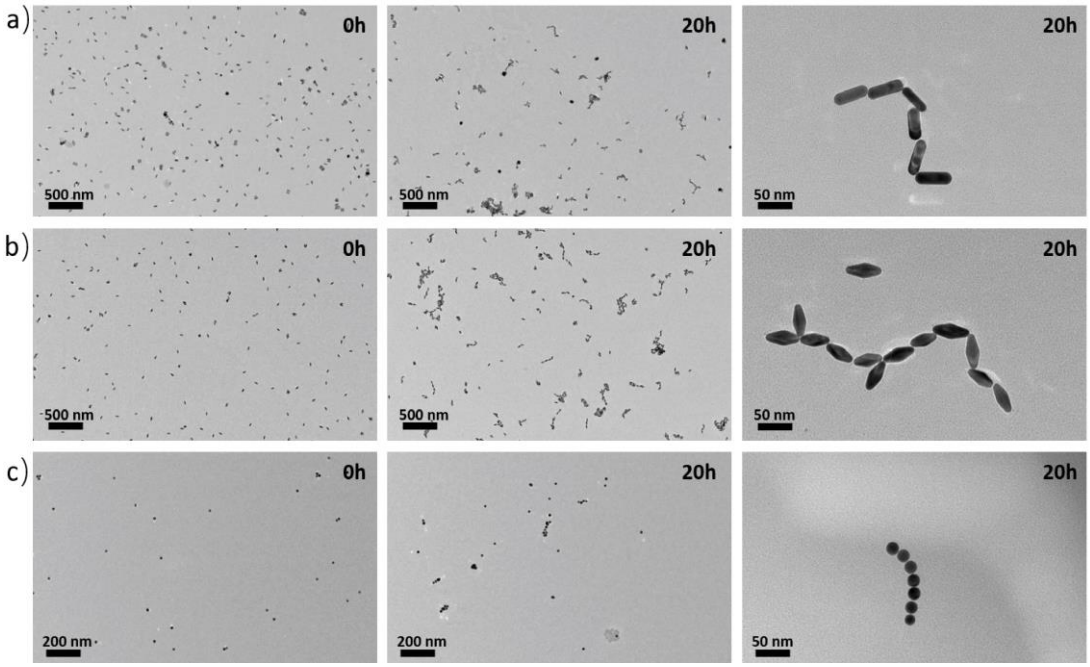

Figure 5.3 TEM images of the assembly state at 0 h and 20 h. (a) GNRs, (b) GBPs and (c) GNSs. The rightmost panel shows individual chains under higher magnification.

5.5 The role of experimental parameters

The concentration of reactant (in our case, the initially isolated GNPs) C_{Au} or Au^0 is a very important parameter, and its influence on the kinetics can reveal the reaction mechanism. The presence of sulfate ions is necessary for the formation of chains, and the content of CTAB is also a crucial factor for tip-to-tip chains formation. Therefore, to understand the assembly mechanism, we adjusted these reaction parameters through the controlled variable method.

5.5.1 The role of gold concentration and the reaction order

Firstly, we assembly the GNRs with varied gold concentrations (C_{Au} or Au^0) from 0.0163 to 0.3 mM, while fixed at 14.3 μM CTAB and 1 mM $MgSO_4$. A part of the AS data is shown in Figure 5.4, taking the spectrum of assembly at 0.0163 mM Au^0 as an example, the transverse plasmon peak did not change noticeably, but the longitudinal plasmon band decreased in intensity and new red-shifted broad bands appeared compared with the AS of initial isolated GNRs.

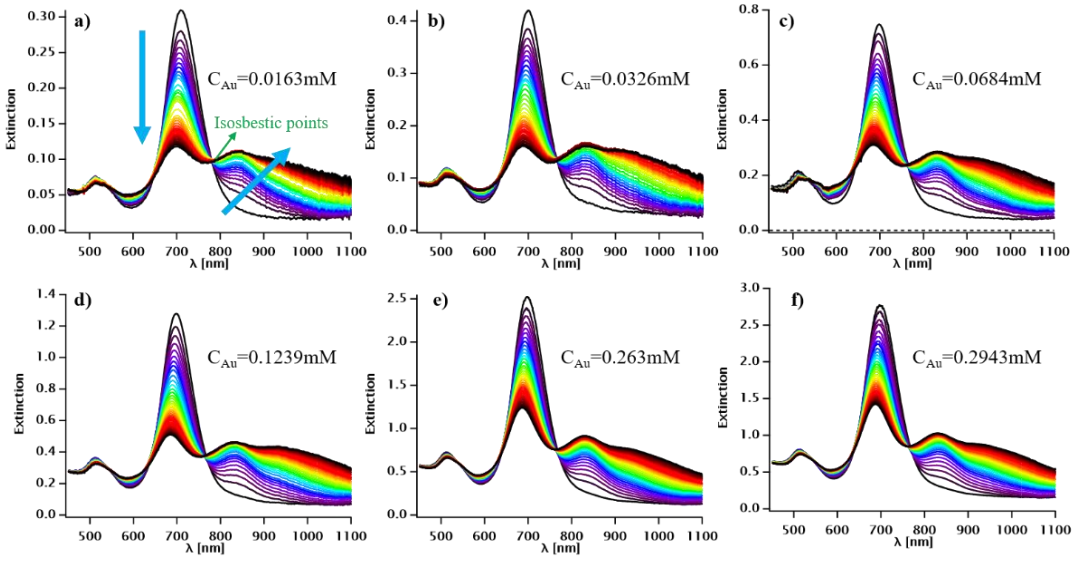

Figure 5.4 AS spectra of GNRs assembly as a function of C_{Au} in the presence of 1.0 mM $MgSO_4$ and 14.3 μM CTAB. The C_{Au} values are indicated in each panel.

We then treated all the AS data using SVD method to extract the spectral signature of the relevant species and their time evolution. In the AS, the assembly reaction is a limited process within 20 hours of monitoring relative to the general chemical reaction kinetic. The details of general and limited reaction kinetics and the SVD method are provided in Appendix 8.3. To obtain the yield η and understand the assembly reaction order, we fitted the time coefficient of the isolated particle concentration $\boldsymbol{C}_1(t)$ with an exponential function (first-order kinetic) and a reciprocal function respectively

(second-order kinetic), see Figure 5.5. Due to $\boldsymbol{C_1}(0) = 1$ is the time-dependent normalized concentrations of isolated particles at $t = 0$, the first-order kinetic Eq. (8-8) can be written as an exponential function:

$$C_1(t) = \eta\, e^{-\mathrm{kt}} + (1 - \eta) \tag{5-1}$$

and the second-order kinetic Eq. (8-11) can be written as a reciprocal function:

$$C_1(t) = \frac{\eta}{\eta + \eta\, kt} + (1 - \eta) \tag{5-2}$$

where the yield η is

$$\eta = 1 - [A]_{\mathrm{final}} \tag{5-3}$$

Each function has two free parameters: the yield η (constrained to the [0,1] interval), and the rate constant k. The fits are shown in Figure 5.5 for various C_{Au} values and the corresponding goodness-of-fit parameter χ^2 is displayed in Figure 5.6. Below C_{Au} = 0.15 mM, the exponential model is better than the reciprocal one, while above 0.25 mM the quality fit is indistinguishable. We conclude that the data is better described by first-order kinetics.

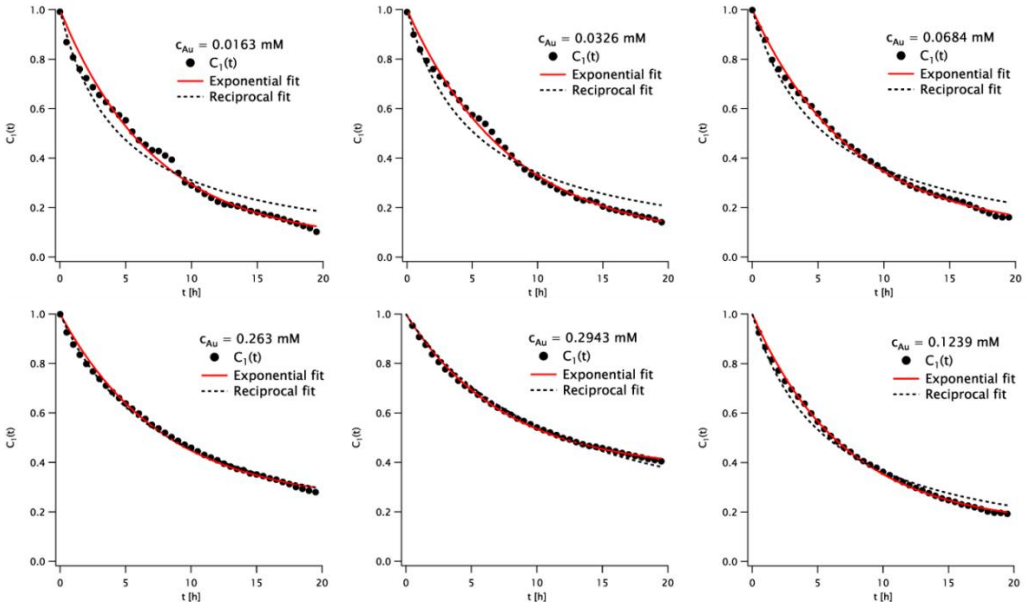

Figure 5.5 Fit of the time coefficient of the isolated particle concentration $\boldsymbol{C_1}(t)$ with an exponential (solid red line) and a reciprocal (black dashed line) function. The C_{Au} values are indicated in each panel.

Therefore, the time-dependent normalized concentrations of final aggregates $\boldsymbol{C_2}(t)$ is:

$$C_2(t) = 1 - C_1(t) = \eta\left(1 - e^{-\mathrm{kt}}\right) \tag{5-4}$$

the yield $\eta \sim \eta_2 = C_2(\infty)$ is the particle fraction that belongs to the aggregates (defined as objects characterized by $\boldsymbol{S}_2(\lambda)$ at the end of the process.

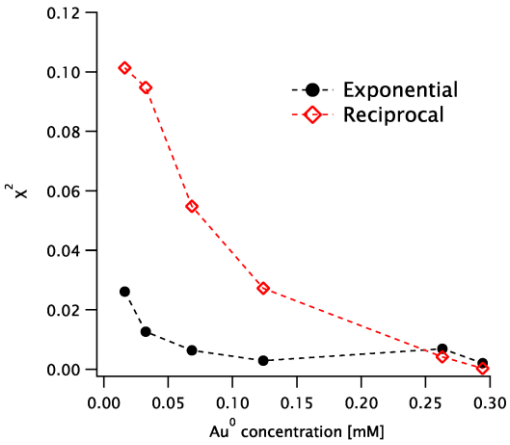

Figure 5.6 Goodness-of-fit values χ^2 corresponding to the fits in Figure 5.5.

After that, I took one of the SVD results of GNRs assembly at 0.263 mM C_{Au} for an example (see Figure 5.7). $\boldsymbol{S}_1(\lambda)$ is slightly different from the first experimental spectrum (red open dots) because we only took K = 2. The yield η is 72% and the rate constant is 0.13 h^{-1} after fitting $\boldsymbol{C}_2(t)$ with exponential function Eq. (5-4). From Figure 5.7c, we see that the first two singular values are greater than the other, which also proves that there are only two components that contributed significantly to the experimental spectra.

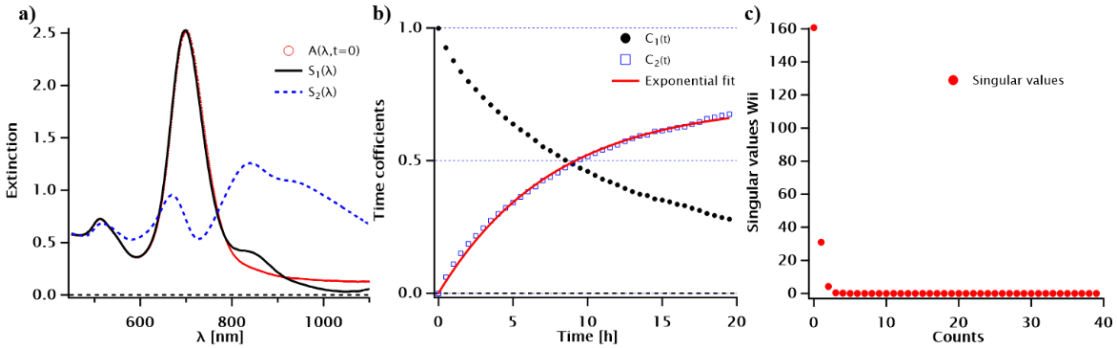

Figure 5.7 a) SVD-extracted spectra of the first and second species, $\boldsymbol{S}_1(\lambda)$ and $\boldsymbol{S}_2(\lambda)$. b) Time coefficients $\boldsymbol{C}_1(t)$ and $\boldsymbol{C}_2(t)$ of the identified species with an exponential fit (red solid line). c) Singular values W_{ii}.

The values of the yield and rate constant for GNRs assembly as a function of C_{Au} in the presence of 1.0 mM $MgSO_4$ and 14.3 μM CTAB are shown in Figure 5.8. The yield

decreased with C_{Au} by about 30% over the studied range, while the rate constant was virtually unchanged, supporting our conclusion that the reaction is apparently first-order in the gold concentration.

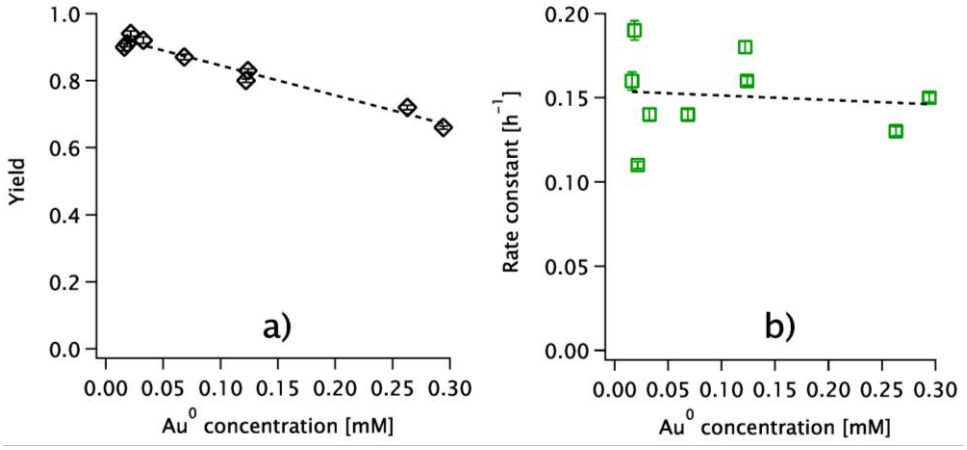

Figure 5.8 a) Yield and b) reaction rate constant for GNRs assembly as a function of C_{Au} in the presence of 1.0 mM $MgSO_4$ and 14.3 μM CTAB. Dashed lines are linear fits to the data.

5.5.2 The role of sulfate

We studied the kinetics for three different $MgSO_4$ concentrations at 0.25 mM Au^0 and 14.3 μM CTAB, the AS data is shown in Figure 5.9.

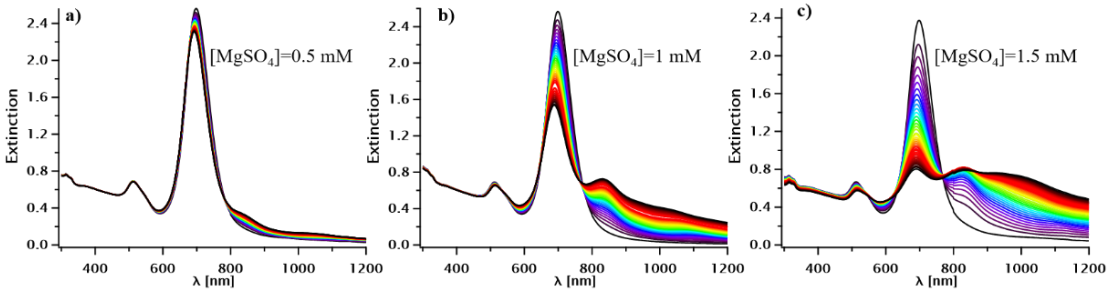

Figure 5.9 AS of GNRs assembly as a function of the $MgSO_4$ concentration for C_{Au} = 0.25 mM in the presence of 14.3 μM CTAB. The sulfate values are indicated in each panel.

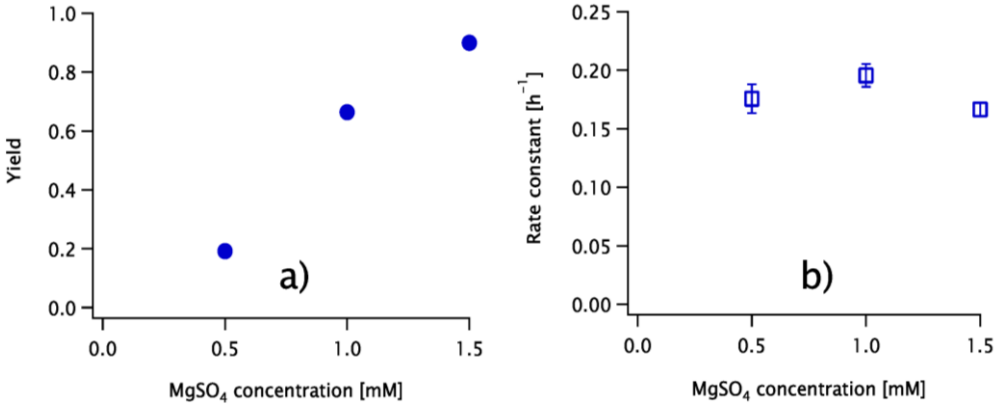

Figure 5.10 a) Yield and b) reaction rate constant for GNRs assembly as a function of the $MgSO_4$ concentration for C_{Au} = 0.25 mM in the presence of 14.3 μM CTAB.

After SVD, the values of the yield η and rate constant k are shown in Figure 5.10. The yield was roughly linear in the $MgSO_4$ concentration, which did not affect the rate.

5.5.3 The role of surfactant

The density of CTAB on the particle surface is different due to the different curvatures of the particle surface. Therefore, we assembled three types of GNPs comprising spheres, rods, and bipyramids by adjusting the concentration of CTAB in the presence of 1 mM $MgSO_4$. The C_{Au} was fixed at 0.25 mM.

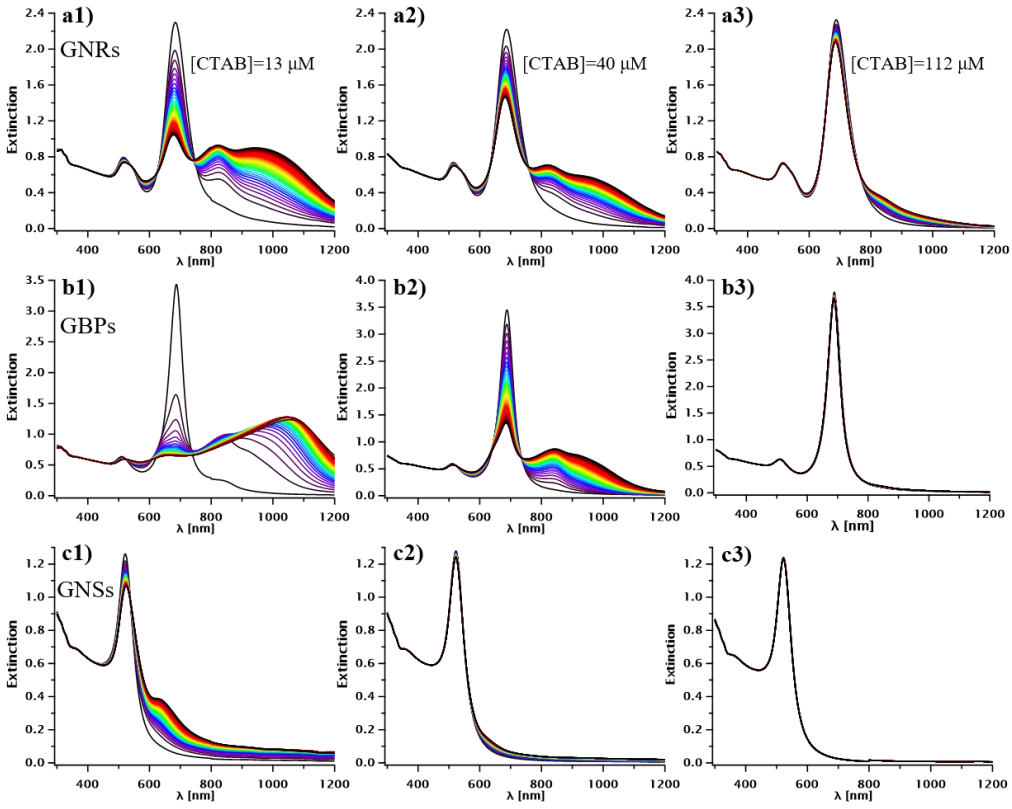

Figure 5.11 AS of GNPs assembly as a function of the CTAB concentration for C_{Au} = 0.25 mM in the presence of 1 mM $MgSO_4$. a) GNRs, b) GBPs and c) GNSs. The concentrations of CTAB are indicated in each panel.

Some of AS data are shown in Figure 5.11. For all particle shapes, new absorbance bands appeared in the spectra and red-shifted with respect to the initial ones, indicating the formation of close contacts between particles. In the case of spheres, the plasmon band centered at 525 nm decreased slightly, while a moderately intense band appeared at 700 nm. In contrast, the spectra of rods and bipyramids varied significantly under

otherwise similar experimental conditions. Their transverse band around 510 nm did not change noticeably, but the longitudinal plasmon band decreased in intensity and a new red-shifted broad band appeared.

Both the yield $\boldsymbol{C}_2(\infty)$ and the reaction rate constant k are shown in Figure 5.12 as a function of the CTAB concentration in the presence of 1 mM $MgSO_4$. From these results, it is clear that the self-assembly yield increases as the CTAB concentration decreases. This experiment confirms that sulfate ions mediate the self-assembly of GNPs but also highlights the role of surfactant concentration in this process. Decreasing the CTAB concentration in solution well below the CMC (1 mM) ultimately leads to disruption of the bilayer at the surface of the NPs, weakening their electrostatic repulsion and rendering their surface accessible for conjugation with sulfate moieties. Moreover, the CTAB density is lower at the tips of anisotropic NPs due to the higher local curvature compared to the lateral facets.[304] As discussed below, there is not enough place between the particle tips for two surfactant bilayers.

Our explanation entails that various particle shapes, with different curvatures, should evolve differently. This is indeed the case, as one can see in Figure 5.12, the yield increased with the curvature (from spheres to rods to bipyramids). As expected, the reaction rate constant of nanorods was higher than that of spheres, but that of bipyramids showed a significantly different trend, decreasing steeply with the CTAB concentration. This might indicate a different mechanistic pathway, which requires further study to elucidate.

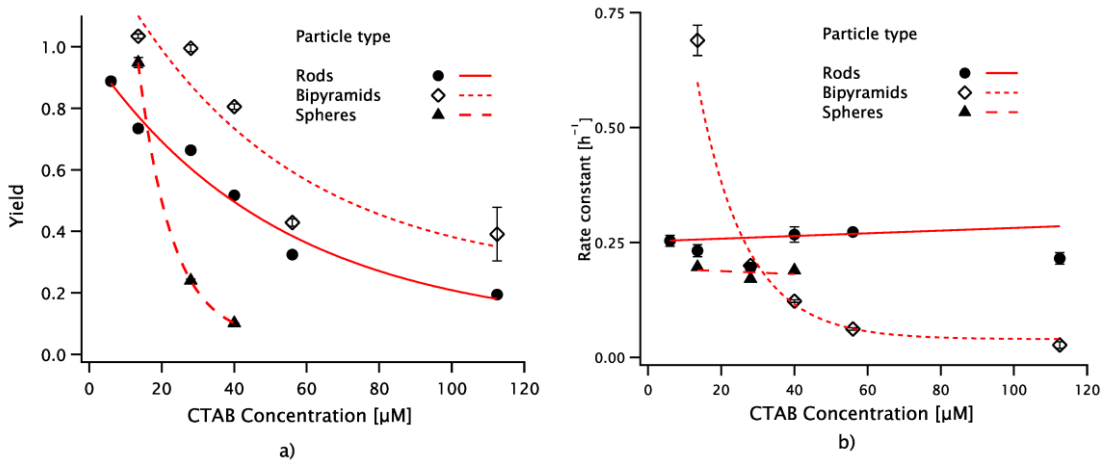

Figure 5.12 a) Yield and b) reaction rate constant for particle assembly as a function of the CTAB concentration for C_{Au} = 0.25 mM in the presence of 1 mM $MgSO_4$. The symbols correspond to different particle shapes. The lines are guides to the eye.

5.6 Two-step assembly process

Taking the assembly nanorods as an example, we followed the assembly reaction process at high and low CTAB concentrations in the presence and absence of sulfate solution by in-situ AS and SAXS. Here, the gold concentration was fixed at 0.25 mM. For AS, the mixture solution was prepared in a 2 mL polystyrene cuvette and inserted within 30 seconds in the instrument to start recording. The spectrum was taken every 30 min. For SAXS, we filled the mixture solutions into round glass capillaries, with an outer diameter of 1.2 mm and 10 micron-thick walls, purchased from WJM-Glas (Berlin, Germany), and placed them vertically in a motorized and temperature-controlled holder. Preliminary data treatment (angular averaging and normalization) was done using the software Foxtrot developed at the beamline and yielded the intensity as a function of the scattering vector $I(q)$ in absolute units. Specially, we determined the (isotropically averaged) form factor $P(q)$ of the particles by measuring a well-dispersed solution and obtained an approximate structure factor as $S(q) = I(q)/P(q)$.

5.6.1 First Step: fast aggregation due to surfactant dilution

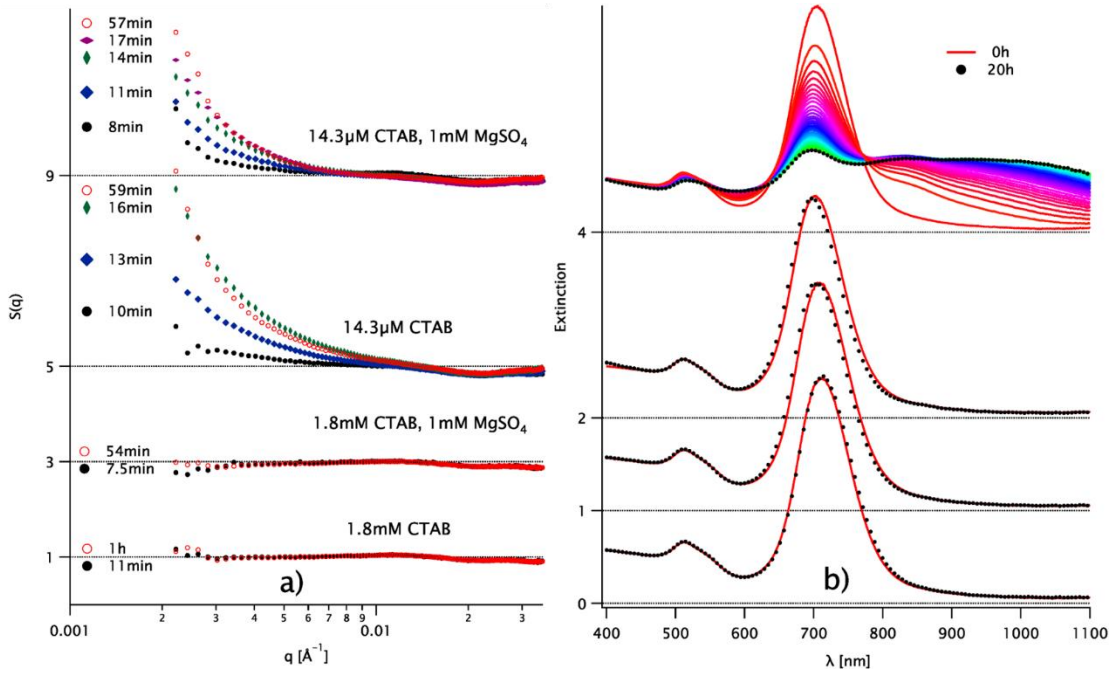

Figure 5.13 a) SAXS structure factors of nanorods at CTAB and $MgSO_4$ concentrations indicated on top of the curves, for various times after preparation (different colors and markers). b) Extinction spectra for the solutions in a) immediately after preparation and after 20 h. For the solution at 14.3 μM CTAB and 1.0 mM $MgSO_4$, intermediate spectra (taken every 30 min.)

are also shown. Curves shifted vertically for clarity: SAXS and corresponding AS data for the same solution are at the same level.

As shown in Figure 5.13a, at high CTAB concentration, the structure factor $S(q)$ remained flat, indicating well-dispersed particles. At low CTAB concentration, 8 to 10 min after preparation there was already an increase in $S(q)$ at low q, signs that the particles aggregated. The aggregation process continued until about 20 min and then there was no change until the end of the experiments (1 h). Note that the presence of $MgSO_4$ did not affect the SAXS results. We can conclude that the first step of the assembly process is fast aggregation due to the reduction in surfactant concentration.

5.6.2 Second step: slow assembly due to the presence of sulfate

The AS data (Figure 5.13b) at high CTAB concentration showed no change over 20 h, confirming good particle dispersion as well. Although no AS change occurred at low CTAB concentration and in the absence of $MgSO_4$, the SAXS data clearly shows the particles were aggregated. It is only when both conditions (low CTAB and presence of $MgSO_4$) are met that the assembly occurred, as seen by the gradual changes in the spectrum. To get more insight into the structure of the assemblies, we performed a longer (20 h) time-resolved SAXS study (see Figure 5.14) for a sample in appropriate conditions (0.22 mM Au^0, 1.0 mM $MgSO_4$ and 28 µM CTAB). At this point, we find that the change in AS only occurs in the second step. Therefore, the influence of the various parameters on assembly is in fact contained in this step. Also, we emphasize that the first-order assembly kinetics only applies to the second step of the process. Presumably, the rapid first step is collective in nature so we would expect it to have higher-order kinetics, but we could not test this hypothesis with the techniques we used.

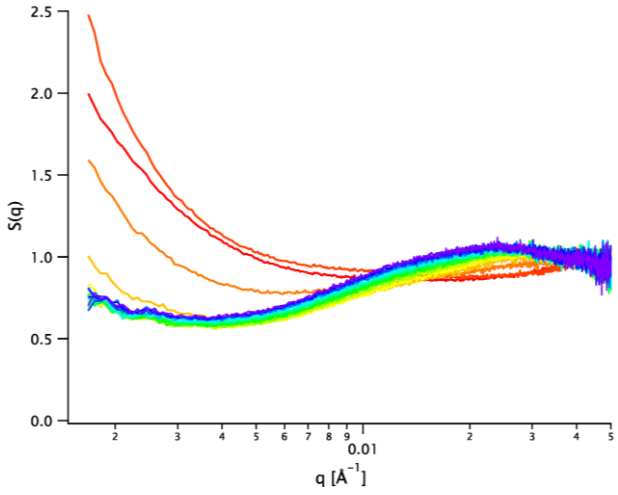

Figure 5.14 Assembly kinetics for GNRs with 1.0 mM $MgSO_4$ and 28 μM CTAB. SAXS curves were acquired at 30 min intervals and color-coded from red to violet.

5.7 Properties of the final state

5.7.1 Chain spectra and modeling

One major advantage of the SVD technique is that it yields the spectra $\boldsymbol{S}_2(\lambda)$ of the final assemblies using a minimal number of assumptions. These spectra contain information on the inner structure of the assemblies, in particular on the contact configuration (tip-to-tip, side-to-side, etc.) and the interparticle distance at contact. Aided by BEM simulations, we then can describe these spectra with different contributions.

5.7.1.1 Plasmon coupling simulations

As we mentioned earlier, the changes in AS spectra of the particles are attributed to the coupling of the plasmon modes. This coupling is extremely sensitive to the reciprocal position and orientation of the objects, as shown in Figure 5.15. All simulations are performed using the MNPBEM toolbox.[227] The dielectric constant for gold is that given by Johnson and Christy[55] (with no finite-size correction) and the host medium is water. We report the extinction efficiency Q_{ext}, defined as the ratio of the extinction cross-section C_{ext} to the geometrical cross-section of the particle. All coupling simulations were done by Dr. Doru Constantin.

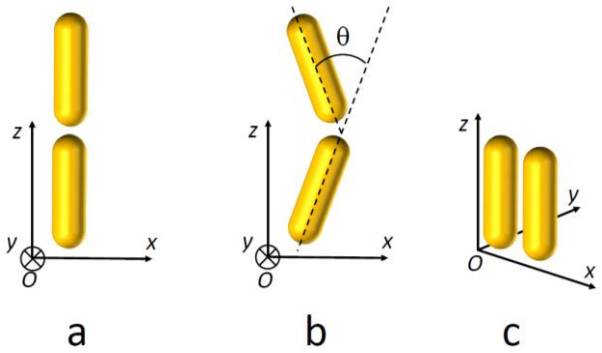

Figure 5.15 System geometry for the plasmon coupling simulations, in a) tip-to-tip b) tilted and c) side-to-side configuration of a particle dimer.

Both the GNRs and the GBPs are anisotropic, so the simulations of anisotropic GNRs assembly and isotropic GNSs assembly are taken as examples.

(1) Plasmon coupling simulations of GNRs assembly

- Tip-to-tip assembly

It is well-known that tip-to-tip assembly of nanorods leads to a red shift of their longitudinal plasmon resonance.[305] In this section we quantify the shift as a function of separation distance and number of particles in the chain for the nanorod morphology used in our experiments (AR = 2.9). In Figure 5.16, the extinction spectrum depends not only on the distance between particles but also on the number of particles. We then plotted the position of the longitudinal peak (LSPR) as a function of the surface separation d for dimer to hexamer and fits with the Hill equation. Empirically, we find that the dependence of the peak maximum on the interparticle separation $\lambda_{\max}(d)$ is much better described by the Hill equation:[306]

$$\lambda_{\max}(d) = \lambda_{\max}(\infty) + \frac{\lambda_{\max}(0) - \lambda_{\max}(\infty)}{1 + \left(\frac{d}{d_{\text{half}}}\right)^{\alpha}} \qquad (5\text{-}5)$$

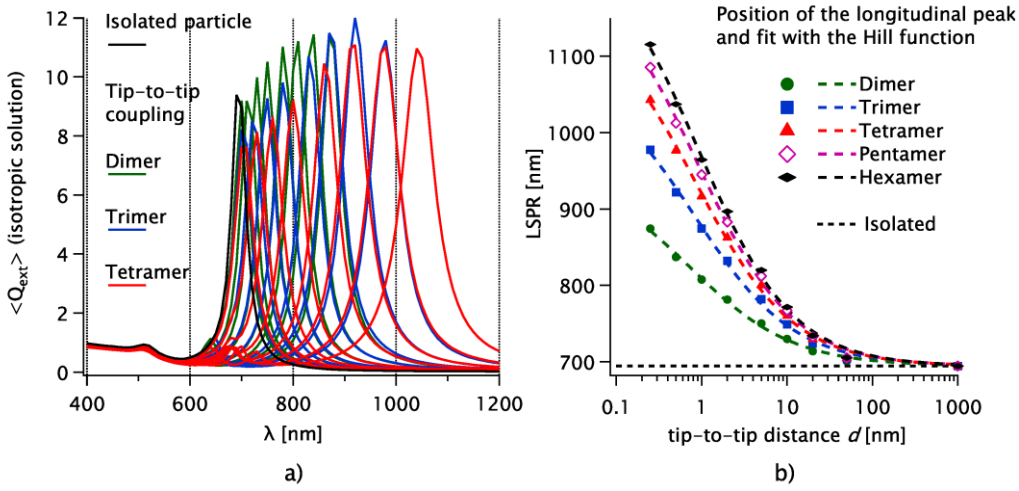

Figure 5.16 a) Simulated extinction spectra for an isolated gold spherocylinder with $AR = \frac{L}{D} =$ 2.9 (black line) and for a tip-to-tip dimer, trimer and tetramer of such objects with a minimal surface separation d varying from 0.25 to 50 nm (green, blue and red line, respectively). b) Position of the longitudinal peak (LSPR) as a function of the surface separation d for dimer to hexamer (symbols) and fits with the Hill equation.

- Side-to-side assembly

We also quantify the shift as a function of separation distance for a side-to-side dimer (see Figure 5.17), the blue-shifted from the longitudinal band of the isolated nanorods is attributed to side-to-side assembly.

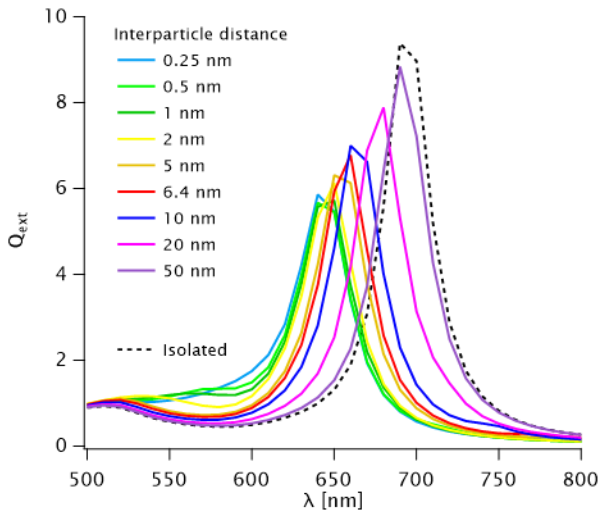

Figure 5.17 Simulated extinction spectra for a side-to-side dimer with a minimal surface separation d varying from 0.25 to 50 nm. The isotropic average is shown as a solid black line.

- Tilt effect

Aside from the tip-to-tip and side-to-side configurations, the particles can of course be tilted, with an angle θ between 0 and π. We simulated a dimer with a constant minimal surface separation d = 2 nm, for different tilt angles θ (see Figure 5.18). As already shown in the literature,[303] the spectra have two well-defined peaks, corresponding to the bonding and anti-bonding plasmon modes (observed in the tip-to-tip and side-to-side configurations, respectively) with varying amplitudes. Thus, particle tilt changes the relative amplitude of these modes in the final spectrum but not their position so it is not relevant for our discussion.

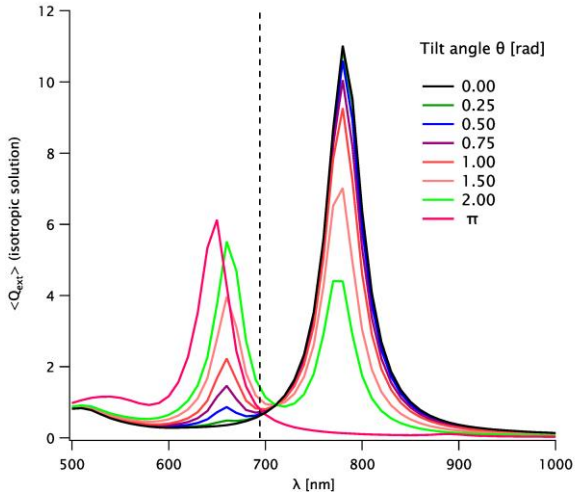

Figure 5.18 Simulated extinction spectra for a dimer, with a minimal surface separation d = 2 nm, for different tilt angles indicated on the graph (different colors). The position of the longitudinal peak for the isolated particle is shown as a dashed line.

(2) Plasmon coupling simulations of GNSs assembly

As for the GNSs assembly, we plotted the position of the plasmonic peak as a function of the surface separation d for dimer to hexamer (symbols) as well.

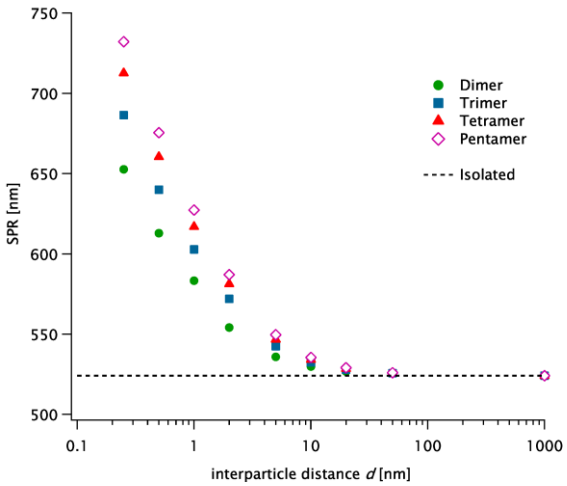

Figure 5.19 Position of the coupled peak as a function of the surface separation d between spheres for dimer to pentamer chains.

5.7.1.2 Chain spectra of final state

(1) GNRs chains

After the SVD technique, the spectra $\boldsymbol{S}_2(\lambda)$ of the final GNRs assemblies are shown in Figure 5.20 for various CTAB concentrations. These spectra can be described in terms of four contributions aided by BEM simulations.

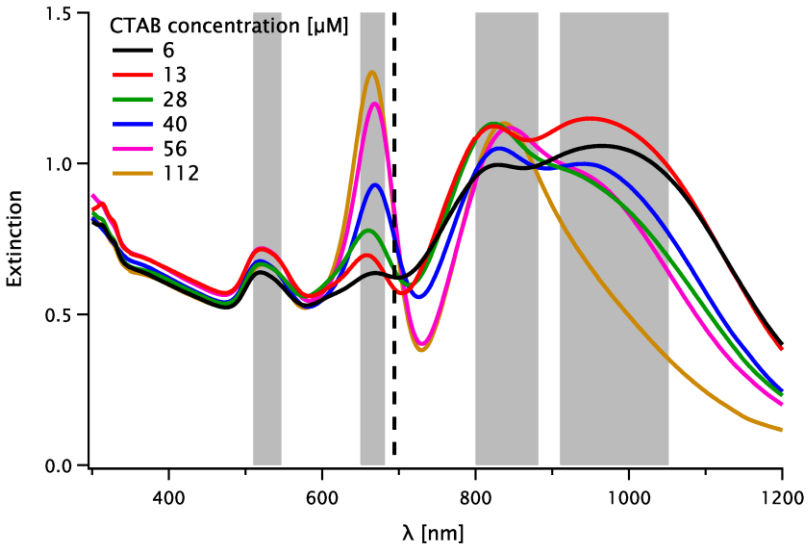

Figure 5.20 Extinction spectra $\boldsymbol{S}_2(\lambda)$ of the nanorod aggregates, for various CTAB concentrations (different colors). The position of the longitudinal peak for the isolated particle is shown as a dashed line. Relevant plasmon bands are marked by gray shading.

- The transverse band (500-520 nm) is not modified with respect to that of the isolated nanorods.
- A narrow peak around 660 nm, slightly blue-shifted from the longitudinal band of the isolated nanorods is a signature of side-to-side assembly (often observed in the TEM images); from the amplitude of this shift, we infer that the interparticle distance was between 6 and 10 nm, enough to accommodate two CTAB layers, with a thickness of 3.2 nm.[307] The amplitude of this peak increased with the CTAB concentration.
- Two wide and superposed modes, centered around 850 and 950 nm, respectively. Both are significantly red-shifted with respect to the longitudinal band of the isolated nanorods, marking the presence of even more anisotropic objects. We assign them to tip-to-tip chain assemblies (very frequently observed in the TEM images). The red shift depends on the number of particles in the chains, but also, very sensitively, on the tip-to-tip distance (Figure 5.16). Even for hexamers, reaching such a large shift requires close contact, below 3.5 nm for the first peak and below 1.5 nm for the second. Allowing for possible systematic errors in the BEM simulations at very short distances, we can however conclude that a vast majority of the contacts are “intimate”, with at most one intervening bilayer for the first one and practically no surfactant for the second. This conclusion is supported by the fact that the amplitude of the second mode decreases with increasing CTAB concentration in solution (presumably also leading to more surfactant being present on the NP surfaces).

(2) GBPs chains

Similar to GNRs assembly, we can also describe four different contributions to GBPs chains. The transverse band (500-520 nm) is not modified with respect to that of the isolated bipyramids. A narrow peak around 682 nm, slightly blue-shifted from the longitudinal band of the isolated bipyramids is a signature of side-to-side assembly. Two wide and superposed modes, centered around 836 and 1000 nm, respectively. we

can also conclude that the first one has at most one intervening bilayer and practically no surfactant for the second.

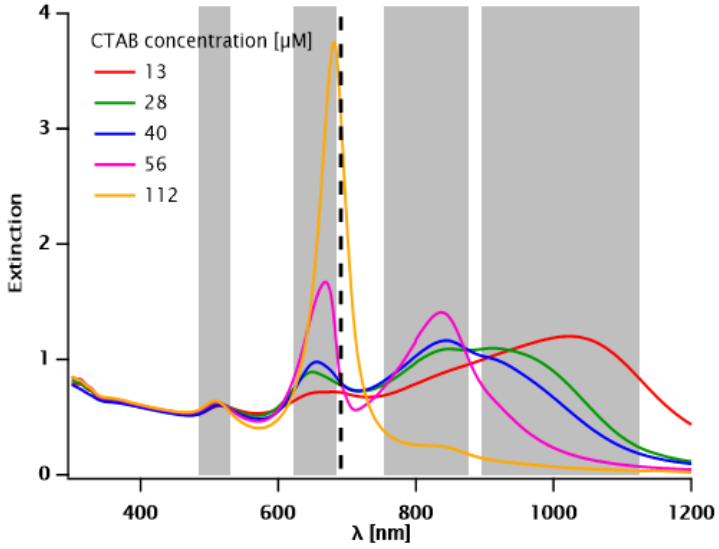

Figure 5.21 Extinction spectra $\boldsymbol{S}_2(\lambda)$ of the GBPs aggregates, for various CTAB concentrations (different colors). The position of the longitudinal peak for the isolated particle is shown as a dashed line. Relevant plasmon bands are marked by gray shading.

(3) GNSs chains

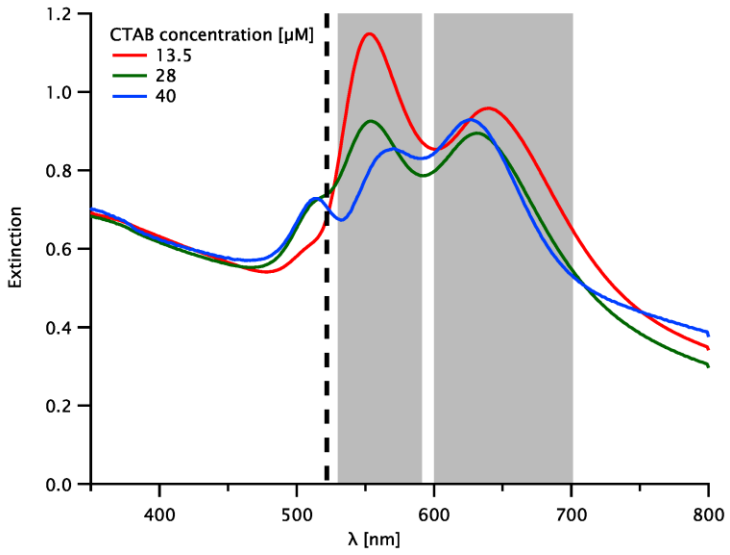

Figure 5.22 Extinction spectra $\boldsymbol{S}_2(\lambda)$ of the coupled modes of sphere assemblies, for various CTAB concentrations (different colors). The position of the plasmon peak for the isolated particle is shown as a dashed line. Relevant plasmon bands are marked by gray shading.

For sphere assemblies, we performed an analysis similar to that done for rods, but for clarity, we consider the spectra $\boldsymbol{S}_2(\lambda)$ of the coupled modes, before applying the "mixing matrix" **M** as discussed above to yield the physical spectra $\boldsymbol{S}_2'(\lambda)$ of the

chains. This data is shown in Figure 5.22, like rods, exhibit two bands (shaded in gray) red-shifted with respect to the peak of the isolated particles (dashed line) by about 35 and 130 nm. There may be a slightly blue-shifted band (by less than 10 nm), but its amplitude is very low.

Based on MNPBEM simulations of sphere chains with varying particle numbers and spacing (Figure 5.19) we conclude that the red-shifted bands correspond to an interparticle distance d of above 2 nm (consistent with one bilayer thickness) and below 0.5 nm (less than one monolayer), with the same interpretation as for nanorods.

5.7.2 Chain statistics from TEM

The time-resolved AS measurements yield the assembly rate $\boldsymbol{C}_2(t)$, but the method is indirect, so we confirm it by direct inspection of the individual objects. We have seen that the kinetics can be controlled by adjusting the surfactant concentration. In addition, we have shown that the reaction can be arrested by increasing the CTAB concentration up to the millimolar range. After supplementing the dispersion with 10 mM CTAC, the optical properties did not significantly change over one month, demonstrating the stabilization of the assemblies.

We used TEM to check for one system (bipyramids in 1 mM $MgSO_4$) the aggregation state at the beginning of the process (0 h) and after 5 and 20 hours. Some images are shown in Figure 5.3. Aside from the number of particles in aggregates of various sizes, we are also interested in the relative position of the particles so we sort the interparticle contacts into tip-to-tip, tip-to-side and side-to-side. From Figure 5.23, we extract $\boldsymbol{C}_2(t)$ = 0.19, 0.57 and 0.69 at t = 0, 5 h and 20 h, respectively, in good agreement with the AS data. The tip-to-tip configuration is the most, about 48%.

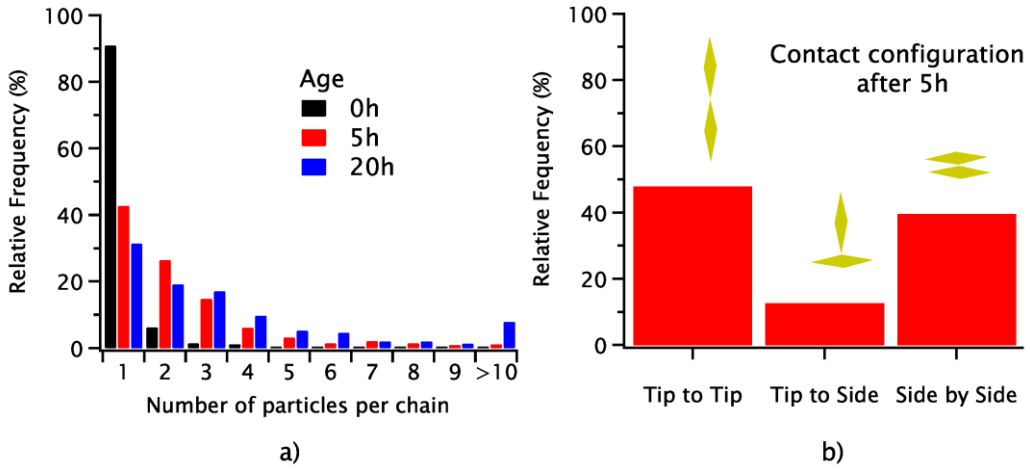

Figure 5.23 a) Statistics of the aggregate size measured by TEM for three different times (0 h, 5 h and 20 h) after the beginning of the process. Each count represents one object (isolated particle or aggregate) and we analyzed at least 400 objects each time. b) Statistics of the contact distribution after 5 hours. Each count represents one contact and we analyzed 625 contacts.

The Carothers equation predicts a degree of polymerization $\overline{X}_n(t) = \frac{1}{1-p}$, where p is the fraction of reactant conversion: $\frac{1-[A]_{final}}{1} = 1 - C_1(t) = C_2(t)$ in our experiment, i.e. values of 1.2, 2.3 and 3.2 after 0, 5 and 20 h, in excellent agreement with the experimental TEM results: 1.1, 2.3 and 3.3. Therefore, the second step of the assembly seems to follow a step-growth mechanism (both monomers and oligomers can self-assemble[308]), albeit with apparent first-order kinetics, unlike for organic polymers, for which the kinetics is generally second or higher order.[309] This unusual behavior is probably due to the rapid aggregation in the first step, which already brings the particles close together.

5.7.3 Particle interaction

5.7.3.1 Dialysis tests

We assembled GNR chains at C_{Au} = 0.125 mM in 14.3 µM CTAB with 1 mM $MgSO_4$. After 20 h, we stopped the assembly process by adding CTAC to a final 10 mM concentration. We then inserted 2 mL of chain solution in a dialysis bag (MWCO 10K, at width: 32 mm, Spectrum Laboratories, Inc., CA, USA), sealed the ends with clips and placed it in 1 L of an aqueous solution with the same surfactant concentration (10 mM CTAC and 14.3 µM CTAB). We also prepared a reference sample in the same conditions but without $MgSO_4$.We renewed the dialysis solution twice a day. After 1 week, we retrieved the chain solution and reference sample from their dialysis bags. AS spectra were measured immediately after preparation (0 h), after 20 h and after dialysis.

From the AS, the intensity of LSPR of chains solution changed from 0.72 to 0.41, and the intensity of LSPR of the reference sample changed from 1.42 to 0.91. The decrease in intensity is due to the change in the concentration of the solution in the dialysis bag under the effect of osmotic pressure. Therefore, the assemblies are very stable under dialysis.

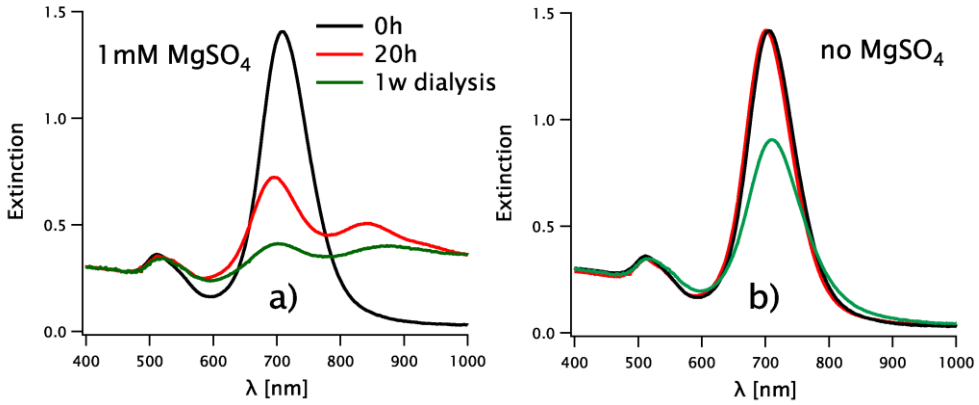

Figure 5.24 AS results for dialyzed samples: a) with 1 mM $MgSO_4$ and b) without $MgSO_4$. In both panels, we show the initial spectrum (black), the one after 20 h of reaction (red) and the one after a subsequent 1W dialysis (green).

5.7.3.2 LCTEM experiments

Direct information on the interparticle distance can be obtained by TEM. In conventional TEM the particles are deposited on a substrate and dried, so there is no guarantee that this distance is preserved. We therefore used LCTEM to characterize the particles. Specifically, 10 µL of a colloidal suspension of GBPs assemblies (2.5 mM Au^0, 28 µM CTAB) dispersed a CTAC aqueous solution (10 mM), was encapsulated in the liquid-cell by using the conventional loading process. Throughout the experiment, the assemblies were attached to the membrane by injecting water to reduce the surfactant concentration, the flow rate was 5 µL/min. LCTEM experiments could be conducted thanks to a collaboration with Dr. Damien Alloyeau at Université de Paris.

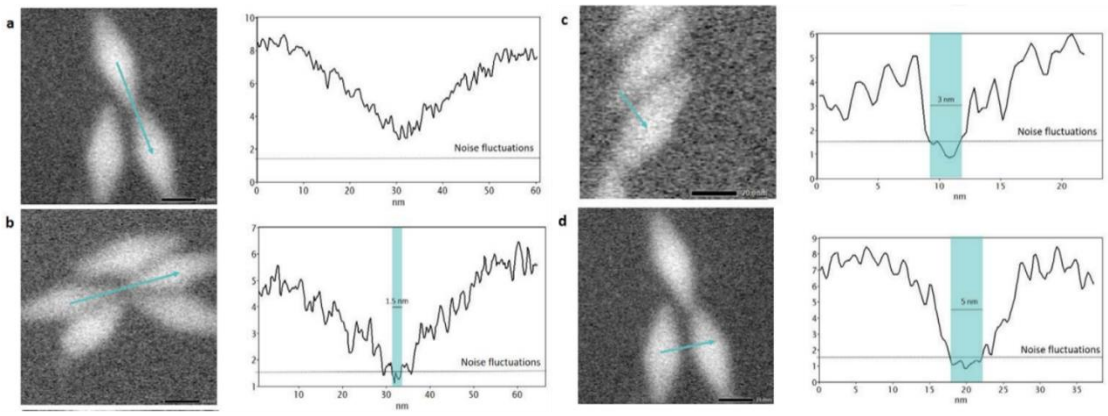

Figure 5.25 Measurements of tip to tip (a, b) and side to side (c, d) distances between gold bipyramids in water. (Left) LCTEM images were extracted from videos acquired with a frame rate of 25 images per second. (Right) The signal-to-noise ratio profile was measured along the arrows seen on the image. The gap between the nanoparticles is indicated in blue on the profile. It corresponds to the area where the signal-to-noise ratio goes below the noise fluctuations

measured in the image areas where there are no nanoparticles (< 1.5). Video analysis was done by Dr. Damien Alloyeau.

We first measured the tip-to-tip and side-to-side distances between bipyramids in assemblies. Most of the time, the tip-to-tip distances were undetectable (Figure 5.25a). In our high frame rate imaging conditions, the resolution obtained on GNPs is around 1 nm, suggesting that the tip-to-tip distance is below this value. Occasionally, we could detect tip-to-tip distances between 1 and 2 nm (Figure 5.25b). The side-to-side distances can always be measured and vary between 2 and 5 nm (Figure 5.25c and d). These values are in rough agreement with the values inferred from the AS data for nanorods.

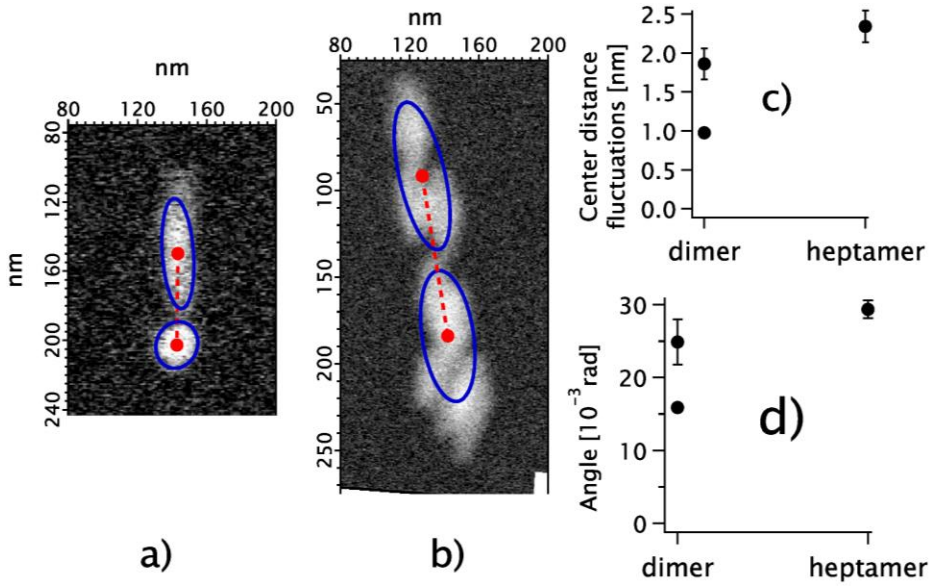

Figure 5.26 LCTEM images: (a) bipyramid-sphere dimer and (b) heptamer. The particle outlines used to define the center of mass of the single particles or groups of particles on each side of the analyzed connection point are shown as blue solid lines. The center-to-center segments are shown as dashed red lines. Analysis: standard deviation of fluctuation amplitudes for (c) the center-to-center distance and (d) the interparticle angle. Image analysis was done by Dr. Doru Constantin.

Using time-resolved LCTEM imaging we also could characterize this interaction by analyzing the positional and orientational fluctuations of objects in an assembly. We studied a bipyramid-sphere dimer (see Figure 5.26a) and a heptamer of bipyramids (Figure 5.26b). For the former, we extracted from the images the center-to-center distance and the tilt of the bipyramid with respect to the center line; for the latter, we used the distance between the centers of the upper part, consisting of three particles, and the lower one, consisting of four particles, and the angle between the long axis of these objects. It should be noted that these objects were attached to the membrane of

the observation cell at the upper extremity (dimer) or the lower one (heptamer) but were otherwise free to swing around these points.

We obtained 120 usable frames for the dimer and 202 for the heptamer. The histograms of the distances and angles were fitted with a Gaussian function: $exp\left(\frac{x-x_0}{\sigma}\right)^2$ yielding the standard deviation σ and the associated uncertainty, represented in (Figure 5.26c and d) as dots and error bars. For the dimer, we also have a shorter segment (23 images) and we extract s as the standard deviation (point shown without error bars).

The interparticle distance varied by about 2 nm. Surprisingly, the angle only fluctuates by about 25 mrad (about 1.5°), so the interaction is also extremely directional. We emphasize that we do not analyze the absolute distance, but rather its fluctuations. Configuration changes within the two-particle groups would increase the fluctuation amplitude, so the values in Figure 5.26c are upper boundaries for the amplitude of fluctuations in contact distance.

5.8 Metal deposition at the GBPs chains' junction

We produced colloidally stable assemblies of gold bipyramids (GBPs) and then grew metallic patches at the NP junctions. Typically, 1 mL of stabilized GBPs oligomers (0.25 mM Au^0, 10 mM CTAC) was supplemented with 5 µL of 10 mM metallic precursor ($AgNO_3$, K_2PdCl_6, H_2PtCl_6) and 5 µL of 40 mM AA solution. This corresponds to a molar ratio between the metallic precursor and gold of 0.2. The molar ratio between the AA and metallic precursor was fixed to 4 in all experiments. After mixing, the reaction vials were kept at 60°C for 1 h. After synthesis, connected oligomers were purified from the excess reactant by at least one centrifugation step (1500rpm, 30 min) and pellet redispersion in a solution of 1 mM CTAC at a final gold concentration of 0.25 mM in all samples.

We stopped the GBPs assembly process at 5 h and 20 h by adding CTAC, then deposited with Ag, Pd, Pt. From AS (Figure 5.27), we can observe a clear evolution of the optical properties after the deposition of metal. In the case of Pd- and Pt-oligomers, the LSPR bands significantly broaden due to the interband transitions in palladium and platinum (Figure 5.27B, C).[310] In contrast to palladium and platinum, silver deposition displays a sharp plasmonic response in the visible-IR spectral range that is preserved when deposited on gold. In the case of silver, the LSPR band of the isolated particles at

696 nm shifts towards lower energies due to the deposition of Ag thin Ag layers.[311] The plasmon band of the oligomers shifts out of the visible range after connecting the NPs. We performed electrodynamical simulation by the boundary element method (BEM) using the MNPBEM17 toolbox,[227] and the LSPR of continuous oligomers of different lengths was shifted systematically beyond 1200 nm. This suggests that the LSPR of the Ag-oligomers was shifted outside of the experimentally accessible spectral range.

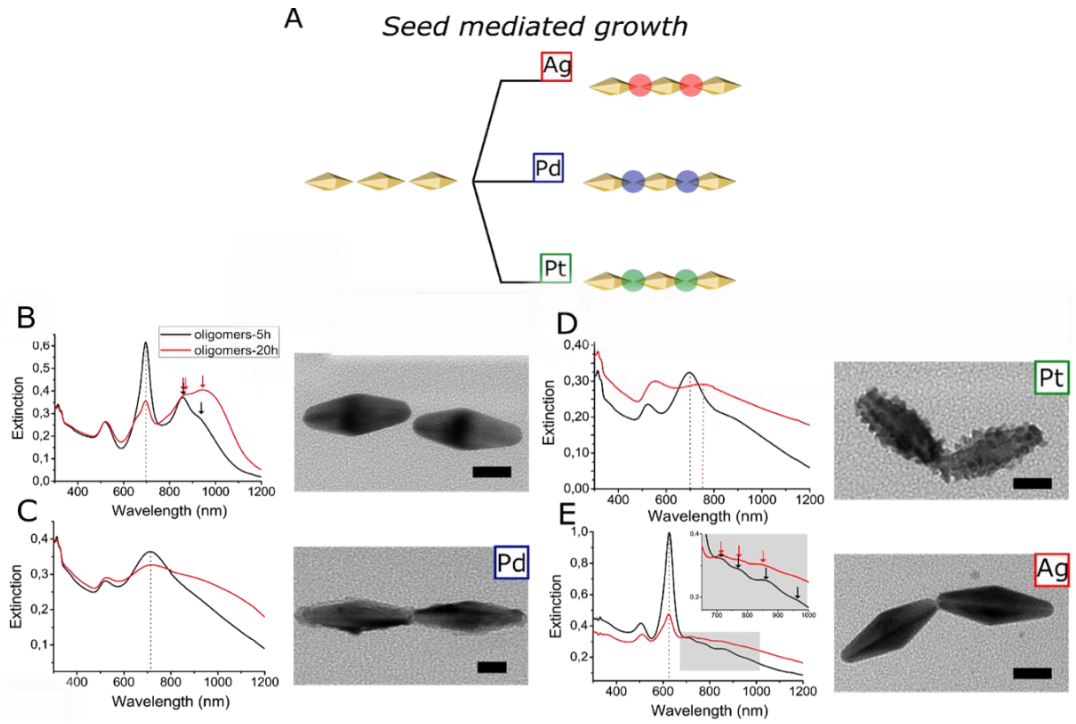

Figure 5.27 Tunable conductive nanojunctions in plasmonic oligomers engineered by seed-mediated growth. A) Scheme highlighting the versatility of the seed-mediated growth approach to engineer tunable metallic nanojunctions. B) AS of two oligomer suspensions in which the self-assembly process was frozen after 5 h and 20 h. TEM images of corresponding particles dimer. C-E) AS and TEM image of the dimer of the same suspensions in B) after growing nanojunctions of silver, palladium and platinum respectively. The scale bar is 20 nm on all images.

We also used scanning transmission electron microscopy electron energy loss spectroscopy (STEM-EELS) to study in more detail the collective plasmonic properties of such structures at the single-particle level. For example, the silver deposition, we can observe the plasmon modes and the plasmon band of the assemblies shifts to mid-infrared and lower energy position in Figure 5.28. We think the large spectral shift due to the transition from capacitive to conductive coupling, which allows charge transfer between neighboring NPs. STEM-EELS experiments were done by our collaborations Dr. Xiaoyan Li and Dr. Mathieu Kociak at LPS.

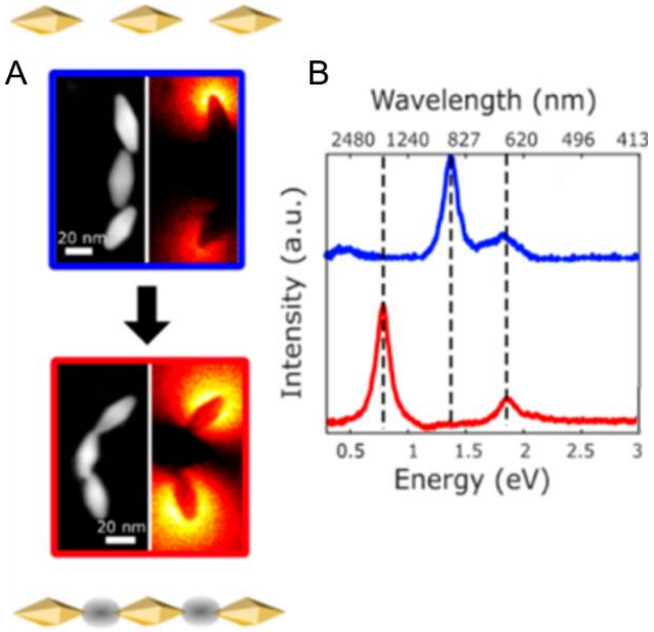

Figure 5.28 (A) STEM high-angle annular dark-field (HAADF) images and (B) EELS spectra of oligomers (upper) and Ag-oligomers (bottom).

5.9 Conclusions

The assembly process of GNPs is driven by reducing the CTAB concentration well below the CMC: immediately (a few minutes, at most) after this step large objects are present in the solution, as revealed by the small-angle increase in the static SAXS data (Figure 5.13). At this point, the AS is still unchanged, because the interparticle distances are above a few nm, presumably imposed by the surfactant bilayers coating them. The chains, if present, do not have a well-defined spacing (we observe no peaks in the SAXS data).

The self-assembly process can be stopped at any stage by adding an excess surfactant to the reaction mixture. Various oligomers with defined optical properties have been stabilized for a long period of time (at least 15 days) in this way. The assemblies are very stable under dialysis, and the interaction of the interparticle is quite strong from LCTEM.

The assembly can be simply described as the conversion from the initial species (isolated particles) to the final one (chains), but with apparent first-order kinetics. This conclusion holds very well for rods and spheres, but not for bipyramids, where the evolution is more complicated, both in terms of the number of species involved and of the time evolution.

The final objects exhibit both tip-to-tip and side-to-side assembly. While the side-to-side distance is large enough to accommodate two surfactant bilayers, as expected for CTAB-covered objects merely coming into contact, the tip-to-tip distance is much smaller, so the surfactant must have been expelled from the interspace, leaving either one bilayer or essentially no surfactant. The interparticle distance is relatively well defined, with a peak in the SAXS structure factor.

The rate-limiting step of the reaction could be related to surfactant expulsion. This is supported by the apparently first-order character of the reaction, which is in apparent contradiction with an aggregation process, where the initial particles must first encounter each other, leading to (at least) second-order kinetics. To understand it, we must keep in mind that the AS spectra only change when the particles are in close proximity: the particles in the same population (described by $\boldsymbol{S}_1(\lambda)$) may very well be together in a loose clump; it is only when they get together and form chains that their spectrum shifts to $\boldsymbol{S}_2(\lambda)$. While the aggregation step is controlled by the CTAB concentration, the sulfate ions are involved in the formation of tip-to-tip contacts, in agreement with the conclusion of Abtahi et al.[76] As to the kinetics, we show that it is apparently first-order, as opposed to the second-order behavior found by these authors.

We posit that such a two-step evolution, which can only be uncovered by combining AS with a structural technique (e.g. SAXS), may very well occur in other processes exhibiting apparent first-order kinetics, for instance when gold NPs assemble due to the induction of an electric dipole at their surface.[166]

Finally, we can tune the plasmon band shift towards the mid-infrared window and precise design of the "hot spots" in NP assemblies by engineering conductive junctions using various metals. Catalysts such as palladium and platinum can also be deposited at the "hot spots". Although the plasmonic response is damped, such a configuration is ideal for photocatalysis because hot charge carriers would be generated in the vicinity of the catalyst.[312] Similarly, our method could be applied to deposit semiconductor materials at the hot spots' location to form double Schottky barriers. Overall, this benchtop method is simple and scalable and yields high-aspect-ratio nanostructures with optical properties that can be tailored across a very wide spectral range, from the visible to the mid-infrared region. We believe that this work provides a leap forward

for all plasmonic applications that can benefit from the precise design of the “hot spots” in plasmonic polymers.

6 Assembling gold bipyramids into three-dimensional supercrystals

The results in this chapter were published in reference **III:**

III. **Lyu, J**.; Chaâbani, W.; Modin, E.; Chuvilin, A.; Bizien, T.; Smallenburg, F.; Impéror-Clerc, M.; Constantin, D.; Hamon, C. Double-Lattice Packing of Pentagonal Gold Bipyramids in Supercrystals with Triclinic Symmetry. *Adv. Mater.* **2022**, 2200883. https://doi.org/10.1002/adma.202200883.

6.1 Introduction

Since Greek antiquity, scientists have been fascinated by the way identical bodies pack together in regular assemblies. Determining their optimal packing, i.e. the one with the highest possible volume fraction is still a challenging task, even for bodies with simple geometrical shapes like convex polyhedra or polygons in the plane. Recently, this quest for optimal packing has been fueled by the design of nanoparticles with increased structural complexity, which typically self-assemble into dense colloidal supercrystals. However, the vast majority of these efforts have focused on isometric particles (with a similar size along with the three space directions)[195,313–318] and elongated shapes have received much less attention.[157,196,319]

Fivefold symmetry is ubiquitous, from human-made architecture to floral symmetries.[320] In two dimensions, pentagonal packing is a long-standing issue and a rich mathematical topic, started by the early work of Johannes Kepler.[321] Tiling the plane with pentagons can be achieved either with non-regular pentagons in 15 different ways[322] or combination with other polygonal shapes, giving rise to the fascinating aperiodic Penrose tilings.[323,324] The optimal packing of regular pentagons is a periodic lattice with a packing fraction around 0.92 called the “pentagonal ice ray”.[325,326] First reported in China as a decorative pattern,[327] it consists of two vertical columns of pentagons pointing in opposite directions and stacked along their edges.[325,326] Since the two orientations of pentagons form two sublattices that are related to each other via an inversion center, this results in a double-lattice packing.[328] This organization has also been observed in numerical simulations of hard pentagons.[329]

Fivefold symmetry is regularly encountered in the shape of gold nanoparticles (GNPs), as a result of crystal twinning during particle synthesis. For instance, gold bipyramids consist of two pentagonal pyramids base-stacked together.[197,330] Pentatwinned gold bipyramids (GBPs) were first obtained as a byproduct in gold nanorod synthesis,[331] but since then high-yield synthesis has been achieved by seed-mediated growth.[111,332] The self-assembly of pentagonal bipyramids has been studied within monolayers,[185,198] but their self-assembly into 3D supercrystals has not yet been elucidated. In contrast to many other elongated particles, the cross-section of a pentagonal bipyramid is not constant along the symmetry axis, and hence their packing in 3D space does not reduce to its 2D counterpart.[157,196,319] Allowing the section to vary along the length increases the complexity of the problem, as demonstrated by the case of ellipsoids.[333] For ellipsoids, the unit cell of the densest lattice contains a motif of two inequivalent particles having two different orientations.[334] Although the stacking of ellipsoid-like particles such as bipyramids, prolate spheroids and bicones has been investigated numerically,[314,333–336] there is to date no experimental evidence on the three-dimensional packing of elongated particles with varying cross-sections. This may be due to their relative experimental scarcity: notable exceptions are hematite NPs[337] and ellipsoidal microparticles,[338,339] but crystallization also requires a high size and shape homogeneity of the particle ensemble,[340] which was difficult to achieve until about fifteen years ago. Furthermore, investigating the structure of the supercrystals by electron microscopy in real space is challenging, as the electrons typically interact too strongly with the nanoparticles to penetrate the bulk of supercrystals and reveal their three-dimensional order.

In this work, we obtain long-range supercrystals of pentagonal GBPs with a packing fraction of 0.835. Their structure is a double-lattice packing, where all bipyramids are arranged parallel to each other but have two different in-plane orientations of the pentagonal cross-section. This double lattice generalizes the optimal packing of regular pentagons in the plane, the “pentagonal ice ray”, in the sense that the two orientations of the pentagonal GBPs are related to each other by an inversion center. Synchrotron-based small-angle X-ray scattering (SAXS) and focused ion beam-scanning electron microscopy (FIB-SEM) tomography analysis reveal a two-particle unit cell with triclinic symmetry. Monte Carlo (MC) computer simulations show that this arrangement corresponds to the densest possible packing. The crystalline order of the

GBPs supercrystals results in a facet-dependent optical response, which is demonstrated by surface-enhanced Raman scattering (SERS) spectroscopy.

6.2 Assembly procedure of the supercrystals

GBPs supercrystals were formed via evaporation-induced self-assembly of a sessile droplet, the scheme is shown in Figure 6.1. Coverslips and Si wafer were used as substrates and treated firstly by UV/Ozone (ProCleaner) for at least 1 h before deposition. Typically, a 10 μL GBPs suspension (64 mM in Au^0 and 2.5 mM CTAC) dropped cast on a substrate and dried in a sealed petri dish for about 48 h.

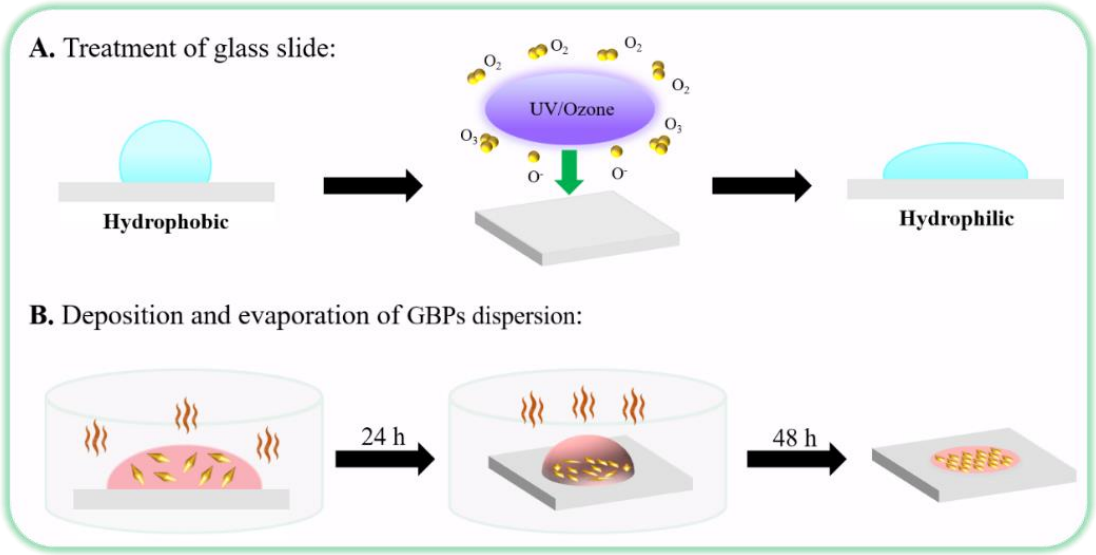

Figure 6.1 Schematic representation of the GBPs assembly process.

6.3 Optimization of the conditions for bipyramids supercrystals

6.3.1 Varied morphologies of bipyramids

Four batches of pentatwinned GBPs were prepared by adjusting the volume of seeds during the synthesis (i.e. 5000 μL, 2000 μL, 1000 μL and 100 μL). The samples are denoted by GBPs_i where "i" indicates the batch number. The AS and corresponding representative TEM images of the four batches of GBPs dispersions are shown in Figure 6.2.

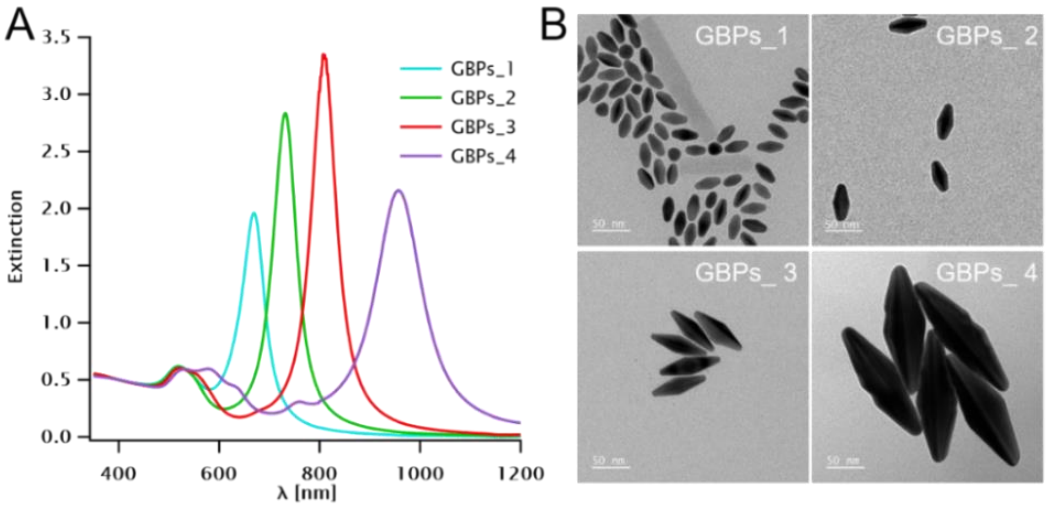

Figure 6.2 Characterization of the GBPs. A) AS of the four batches of GBPs dispersions and (B) corresponding representative TEM images. The scale bar is 50 nm on all images.

From TEM images, these GBPs with high yields show truncated structures. Interestingly, when large amounts of seeds were injected, it was possible to grow small rice-like structures with no sharp edges presenting a longitudinal surface plasmon resonance below 700 nm. In contrast, in the case of lower amounts, the LSPR was clearly shifted to the NIR with intense and sharp resonances in the 800 to 1000 nm range. It is well established that LSPR varies with the aspect ratio of GBPs, while truncation and the aspect ratio are actually linked to each other. LSPR varies by varying the truncation of GBPs, in other words, the sharpness of the tips has been illustrated by S. Parola et al.[332] Enlightened by their works, we gave the details of measurements from TEM images. As shown in Figure 6.3, where L' represents the overall length of the non-truncated object, L is the length of the truncated GBPs, D expresses the central diameter and d is the tip diameter. Thus, the truncation t can be easily calculated using the ratio of the tip diameter d and the central diameter D of GBPs. These notations are used in Table 6-1 . Each GBPs batch we synthesized was uniform in size, as shown by a relative standard deviation of the length and width below 8%.

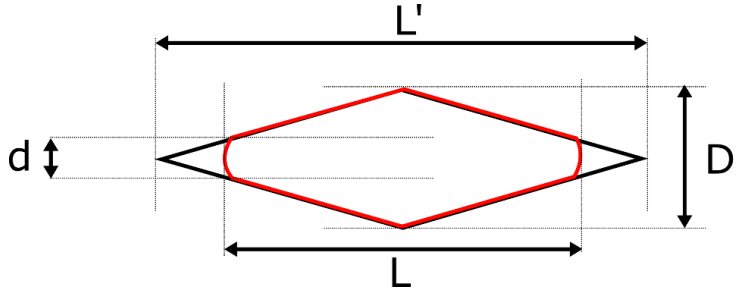

Figure 6.3 Schematic representation of a truncated bipyramid (red) superimposed on a non-truncated bipyramid (black) and corresponding dimensions. Adapted from Ref. 332.

Table 6-1 Dimensions of the nanoparticles determined by TEM image analysis over at least 100 particles. Vseeds indicate the volume of seeds injected in the growth solution as a mean to tune the size of the GBPs.

Sample	**Vseed (µL)**	**L (nm)**	**D (nm)**	**d (nm)**	**L' (nm)**	**L'/D**	**L/D**	**t=d/D**
GBPs_1	5000	32.6 ± 2.5	16.4 ± 0.8	10.4 ± 0.9	89.1	5.43	1.99	0.634
GBPs_2	2000	47.0 ± 3.2	21.5 ± 0.9	11.8 ± 1.1	104.2	4.85	2.19	0.549
GBPs_3	1000	75.3 ± 3.6	25.2 ± 1.5	9.7 ± 1.1	122.4	4.86	2.99	0.385
GBPs_4	100	159.0 ± 7.0	55.7 ± 3.4	26.0 ± 2.5	298.2	5.35	2.85	0.467

Self-assembly supercrystals of these four batches of GBPs were conducted by the slow evaporation (over 48 h) of a sessile droplet and their nanostructurations were probed by SAXS at SWING. As shown in Figure 6.4, supercrystals obtained from GBPs_3 and GBPs_4 showed well-defined Bragg peaks, indicating the crystallization of the GBPs. Although the experimental conditions were identical, GBPs_1 and GBPs__2 did not crystallize, suggesting that the detailed morphology of the GBPs was important for obtaining supercrystals. Indeed, the aspect ratio (ratio between the length and width) and the truncation of the GBPs varied from batch to batch. Smaller GBPs (i.e. GBPs_1 and GBPs_2) were less anisotropic and more truncated compared to larger GBPs (i.e. GBPs_3 and GBPs_4). Although no quantitative measurements are provided, GBPs_1 and GBPs_2 are likely more rounded than GBPs_3, suggesting that well faceted NPs are important for regular self-assembly. While the shape of GBP_4 deviated from a bipyramid by featuring grooves, resulting in another nanostructuration than GBPs_3. Since this work is focused on the self-assembly of plasmonic bipyramids with pentagonal cross-sections, only GBPs_3 was selected in the following experiments.

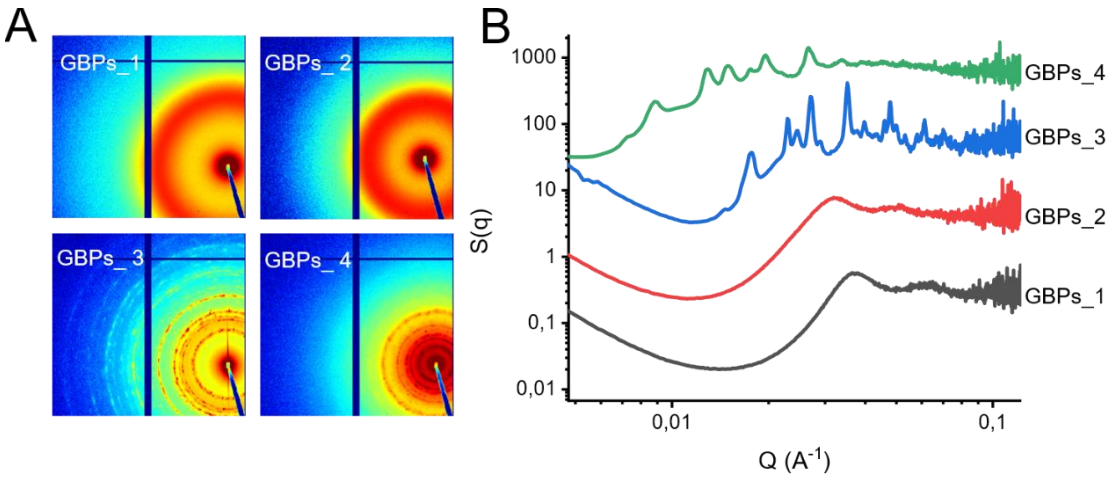

Figure 6.4 Effect of the bipyramid shape on the long-range order. A) Representative 2D SAXS images of supercrystals obtained from the four batches of GBPs and B) corresponding structure factor. These measurements were performed at SWING. The experiments were performed with 2.5 mM CTAC and 64 mM Au^0.

6.3.2 Tunable concentrations of surfactant and gold

We then optimized the assembly's formation by screening the varied concentrations of surfactant (i.e. hexadecyltrimethylammonium chloride (CTAC)) and gold. Three concentrations of surfactant (i.e. 1 mM, 2.5 mM, 10 mM) and three concentrations of gold (i.e. 8 mM, 64 mM, 128 mM) were investigated combinatorically. Their nanostructurations were probed by SAXS at both LPS and SWING (see Figure 6.5 and Figure 6.6). Interestingly, the macroscale deposition was more homogeneous with increasing surfactant concentration, as shown by the sample images taken after solvent evaporation. Assemblies obtained with 1 mM CTAC did not crystallize, as shown by the absence of Bragg spots on the 2D SAXS images (Figure 6.5A and Figure 6.6). In contrast, nanostructuration was clearly visible in SAXS for samples obtained with 2.5 mM and 10 mM CTAC, suggesting an influence of depletion forces during the drying process. At 2.5 mM CTAC, the assemblies exhibited Bragg spots, indicating the presence of a few oriented supercrystals within the footprint of the X-ray beam (300×500µm²) (Figure 6.6). At 10 mM CTAC, rings rather than discrete spots were obtained indicating that the supercrystals size was smaller than the one obtained at 2.5 mM CTAC. Results show that not only does the detailed morphology of the GBPs matter (anisotropy, truncation of the tips) but also that the surfactant concentration has to be tuned carefully to obtain supercrystals.

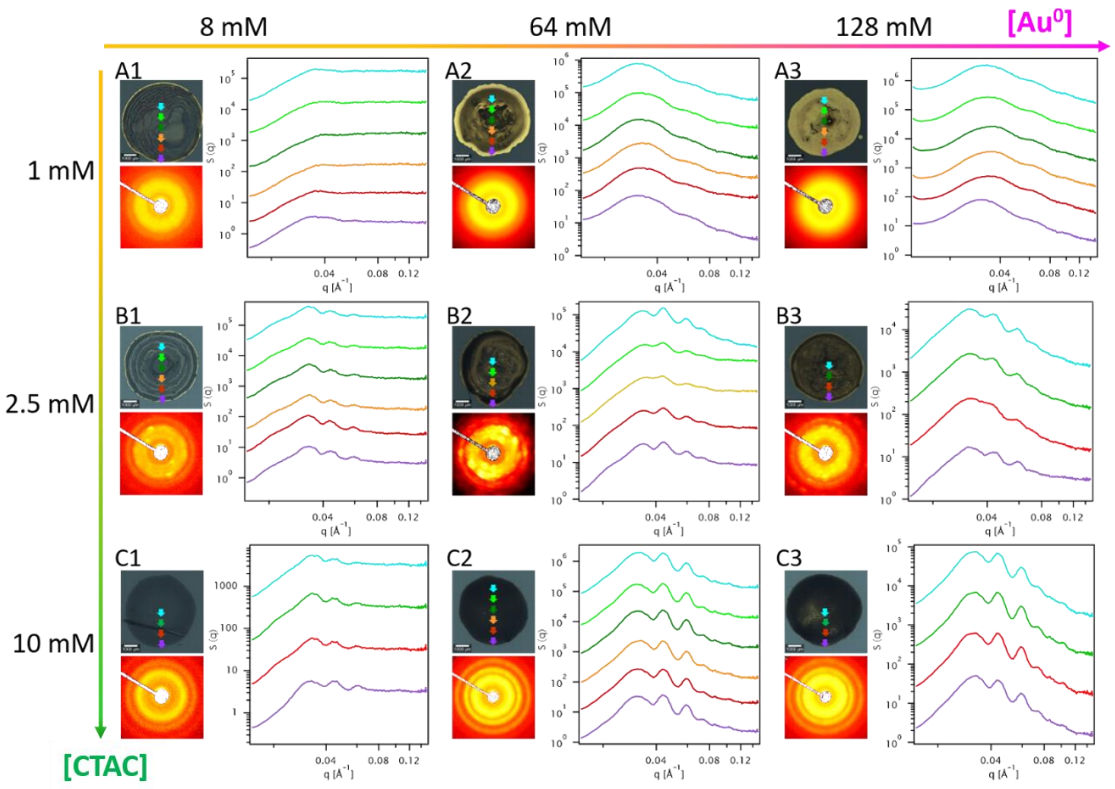

Figure 6.5 Spatially resolved SAXS on GBPs thin films obtained at varying concentrations of CTAC and Au^0**.** The detailed concentrations are shown in the panel. Insets show photographs of the deposit, with the scale bar being 1 mm in all images. Beam positions corresponding to the SAXS measurement are marked on the image, with the same color code as for the SAXS curves. These measurements were performed on GBPs_3 at LPS.

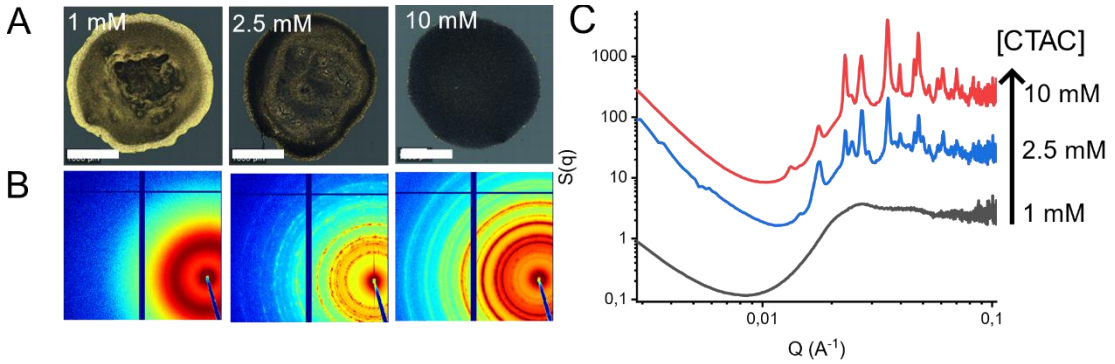

Figure 6.6 Evaporation-induced self-assembly of GBPs at different CTAC concentrations. Three concentrations of CTAC were investigated: 1 mM, 2.5 mM and 10 mM. A) Optical microscopy image of the sample after evaporation of the solvent. The scale bar is 2 mm. B) Representative 2D SAXS image of the samples shown in A). SAXS images are displayed on a logarithmic intensity scale. C) Corresponding structure factors. These measurements were performed on GBPs_3 with 64 mM Au^0 and measured at SWING.

6.4 Double-lattice packing with triclinic symmetry

6.4.1 Combined SAXS and SEM measurements

Measurements by optical microscopy and SAXS alone are not sufficient to reveal the structure of the supercrystal, we thus supplemented the characterization by SEM. The combined optical microscopy, SAXS and SEM analysis of a sample comprising GBPs supercrystals are shown in Figure 6.7. Low-magnification optical microscopy images show numerous supercrystals, a few micrometers in size and with the same rhomboidal shape, scattered randomly on the substrate (see Figure 6.7A-C). 2D SAXS image (Figure 6.7D) and the structure factor $S(q)$ (Figure 6.7H) are exhibited here again to combine these results together. In which the structure factor $S(q)$ is the ratio between the intensity scattered by the supercrystal and the one for isolated GBPs. As shown in Figure 6.7H, the Bragg peak positions are in agreement with a triclinic lattice. To confirm the lattice symmetry, GBPs supercrystals were investigated by SEM. Analysis of the surface of the supercrystal revealed that all GBPs are oriented in the same direction and parallel to the substrate (Figure 6.7F). Further investigation of the internal structure was carried on by FIB-SEM tomography, allowing the 3D rendering of a portion of the supercrystal.[341,342] 2D analysis of the images allowed identifying the lattice vectors of the triclinic unit cell (Figure 6.7F-G). 3D analysis of the supercrystal revealed that all layers were identical and were stacked in an ABA fashion, with a relative offset along the $2\mathbf{c} + \mathbf{a}$ triclinic lattice direction. From the SEM image analysis, we confirmed that the supercrystal belongs to the triclinic symmetry, in agreement with the SAXS indexing of the Bragg peaks. Additional SEM images of the sample (in 2D and 3D) are provided in Appendix 8.4.1. The FIB-SEM tomography characterization could be conducted thanks to our collaborations with Dr. Evgeny Modin and Dr. Andrey Chuvilin at Electron Microscopy Laboratory and Basque Foundation of Science, Spain.

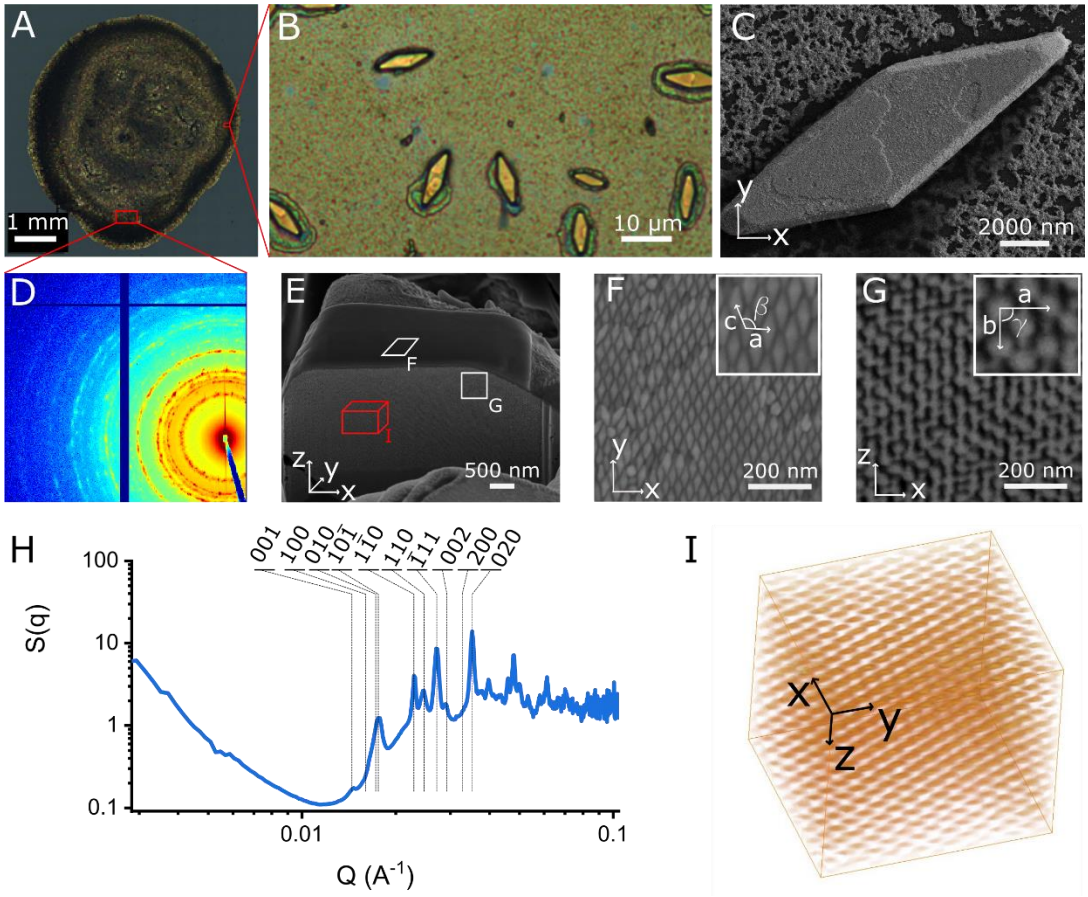

Figure 6.7 Multiscale characterization of pentagonal gold bipyramid supercrystals obtained by evaporation-induced self-assembly. A-B) Optical microscopy image of rhomboidal supercrystals at different magnifications. C) SEM micrograph of a rhomboidal supercrystal. D) Representative 2D SAXS image, displayed on a logarithmic intensity scale. E-G) SEM micrographs of a GBP supercrystal viewed at different magnification and different orientations. In E), the supercrystal was sliced by FIB to reveal the NPs' organization from the top (F) and the side (G). The insets in F, G) show the lattice parameters a, b, c, β, γ of the triclinic unit cell. H) SAXS data with experimental structure factor, $S(q)$. Vertical lines indicate the expected positions of some Bragg peaks of the triclinic lattice. I) Three-dimensional reconstruction of a portion of the supercrystal. In SAXS and SEM, 64 mM in Au^0 and 16 mM in Au^0 were used for the preparation of the sample, respectively. A fixed concentration of CTAC of 2.5 mM was used in all cases.

6.4.2 Monte Carlo computer simulations

We next performed Monte Carlo (MC) computer simulations to investigate the effect of the detailed morphology of the GBPs on the lattice symmetry. In particular, we use a crystal structure prediction technique based on MC simulations of small numbers of particles in a simulation box with a variable shape.[230] Here, we make the assumption that the interactions between the bipyramids are dominated by the hard cores, and neglect other possible interactions due to e.g. charges, Van der Waals attractions, or

ligands. Note that since the bipyramids used in this work are large compared to the size of the CTAC ligands, we do not expect the ligands to modify the effective shape of the nanoparticles. Hence, our model consists of perfectly hard truncated bipyramids, with a varying number of vertices on the polygonal base: n = 3, 4, 5, 6, 7, 10, 12 and 20. For each particle shape, we simulate on the order of 300 compression runs, in which a small variable unit cell containing between 2 and 6 particles is compressed slowly under gradually increasing pressure. After compression, we examine the final structures and calculate their packing fractions. In practice, structures that are commonly found using this method tend to be good candidates for entropically favored phases in the system, and the densest-packed phase is expected to be the stable phase at sufficiently high packing fractions.[230,343] Note that the anisotropy and the truncation of the object corresponded to the ones obtained experimentally and, if these parameters were varied, the simulation outcome would change, especially if the anisotropy decreased significantly. We show the results of the simulations in histograms of the number of observations of predicted structures as a function of packing fraction, together with two snapshots of the corresponding densest structure (Figure 6.8A-B). Interestingly, five recurrent structures were found for n = 5, but only one for both n = 4 and n = 6 and at most three for the other shapes. For n = 4 and n = 6, the packing fraction of the predicted structure was about 0.94 and 0.87 respectively. For n = 5, the packing fraction of the recurrent structures varied between 0.69 and 0.83, the structure as highest packing fraction 0.83 is shown in Figure 6.8, other three major structures are displayed in Figure 6.9. In Figure 6.8C, we plotted the packing fraction of the densest recurrent structure as a function of n. For n < 10, results show an odd-even effect of the number of sides on the packing density: bipyramids with an odd number of vertices yield less dense structures. We attribute this to the non-centrosymmetry of the odd shapes, imposing lattices with two NPs in the unit cell in a double-lattice configuration,[328] whereas those of centrosymmetric nanoparticles (i.e. with even n) have only one NP in the unit cell (Figure 6.8B). Pentagons do not tile the plane, inducing the emergence of more open lattice polymorphs compared to the other shapes. For n < 10, the packing fraction of the densest structure evolves significantly with n (i.e. between 0.83 and 0.92), whereas for $n \geq 10$, it converges towards 0.84. It is noteworthy that, although these NPs are faceted, for large n the problem converges to the closest packing of perfectly rounded truncated bicones. In this limit ($n \to \infty$), the densest phase has a packing

fraction of approximately 0.84, but the second densest (and quite frequently occurring) structure, with a packing fraction of 0.77, corresponds to an ellipsoid packing (the densest to date), in which the particles are stacked in alternating layers with differing orientations.[334] Our results point towards an even denser packing than previously reported for ellipsoids due to the noncircular cross-section of the objects. Overall, two regimes for the structuration of faceted bipyramids were identified, depending on n: a "faceted" regime for $n < 10$ and a "smooth" regime for $n \geq 10$. Among these different shapes, bipyramids with $n = 5$ exhibit a particularly rich variety of observed structures and low maximum packing, confirming the specificity of the pentagonal cross-section. Monte Carlo computer simulations could be conducted thanks to our collaboration with Dr. Frank Smallenburg at LPS.

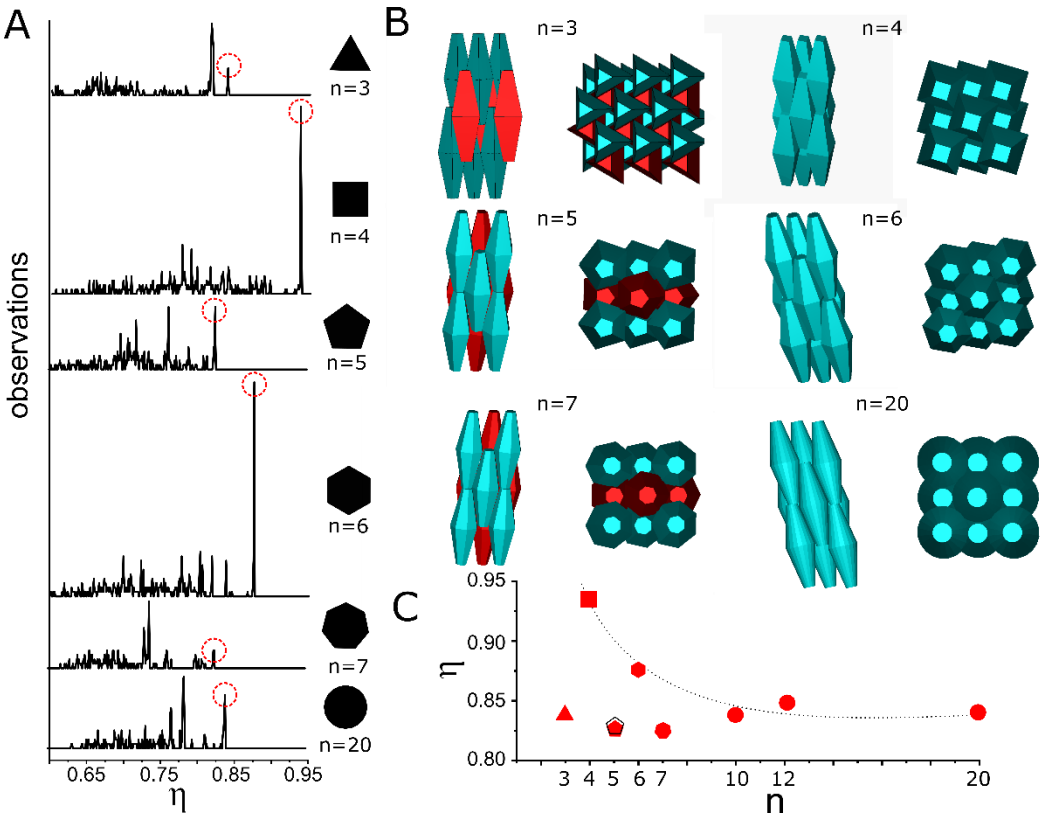

Figure 6.8 Monte-Carlo computer simulation of the packing of truncated bipyramids with varying cross-sections. A) Histograms of the packing fraction of predicted phases for n-sided bipyramids with, $n = 3$, $n = 4$, $n = 5$, $n = 6$, $n = 7$ and $n = 20$. B) Representation along with two directions of the predicted phase with the highest packing fraction, for each shape, corresponding to the phase highlighted by a red dotted circle in (A). For odd n values, two colors (blue and red) are used as the unit cell is composed of two particles with different orientations. C) Graph representing the packing fraction of the densest phase for each bipyramidal shape as a function of n. The packing fraction determined experimentally (for $n = 5$) is added as an open black pentagon for comparison.

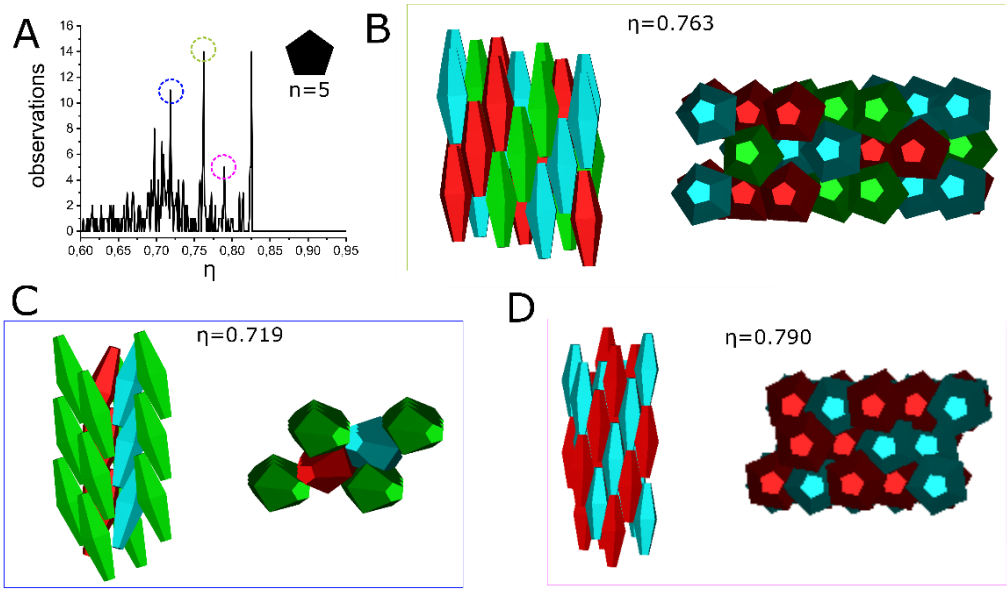

Figure 6.9 Monte-Carlo computer simulation of the packing of truncated bipyramids with a pentagonal cross-section. A) Histogram of the packing fraction of predicted phases of pentagonal bipyramids. B-D) Representation along with two directions of predicted phases at a certain packing fraction, corresponding to the phase highlighted by a colored dotted circle in (A). Two or three colors are used when the unit cell is composed of two or three particles respectively.

6.4.3 Comparison of simulations and experimental characterizations

We then compared the simulation results with the experimental analysis in real space (SEM) and reciprocal space (SAXS), see Figure 6.10. Among the five predicted structures for pentagonal bipyramids, the densest one matched the lattice determined experimentally. In agreement with the simulations, we find a double-lattice arrangement, where all pentagonal bipyramids are parallel to each other but have two different orientations colored in blue and red in Figure 6.8 and Figure 6.10. The periodic arrangement is a triclinic lattice with two particles in the unit cell with each type of orientation (Figure 6.10A-B). The two-particle orientations are related by an inversion center, so their pentagonal cross-sections are turned by an angle of $\frac{2\pi}{10} = 36°$ (Figure 6.10B). The whole structure can be decomposed into two identical lattices, each one containing all particles with the same orientation (blue or red). The space group is $P\bar{1}$, with the inversion center located in-between the centers of the two particles in the unit cell, in agreement with the SAXS model. Note that the long axis of the bipyramids is along a direction close to $\mathbf{a} + \mathbf{2c}$. The structure can also be decomposed in alternate layers with the two orientations (ABA stack), as can be seen from the projection of the

structure onto the (**a**, **b**) plane displaying pentagons with the two orientations (Figure 6.10D). We conclude that the supercrystals are oriented along the **c** and **c** − **a** vectors of the triclinic lattice, by superimposing the model lattice composed of a few NPs on an SEM image of one supercrystal (Figure 6.10E).

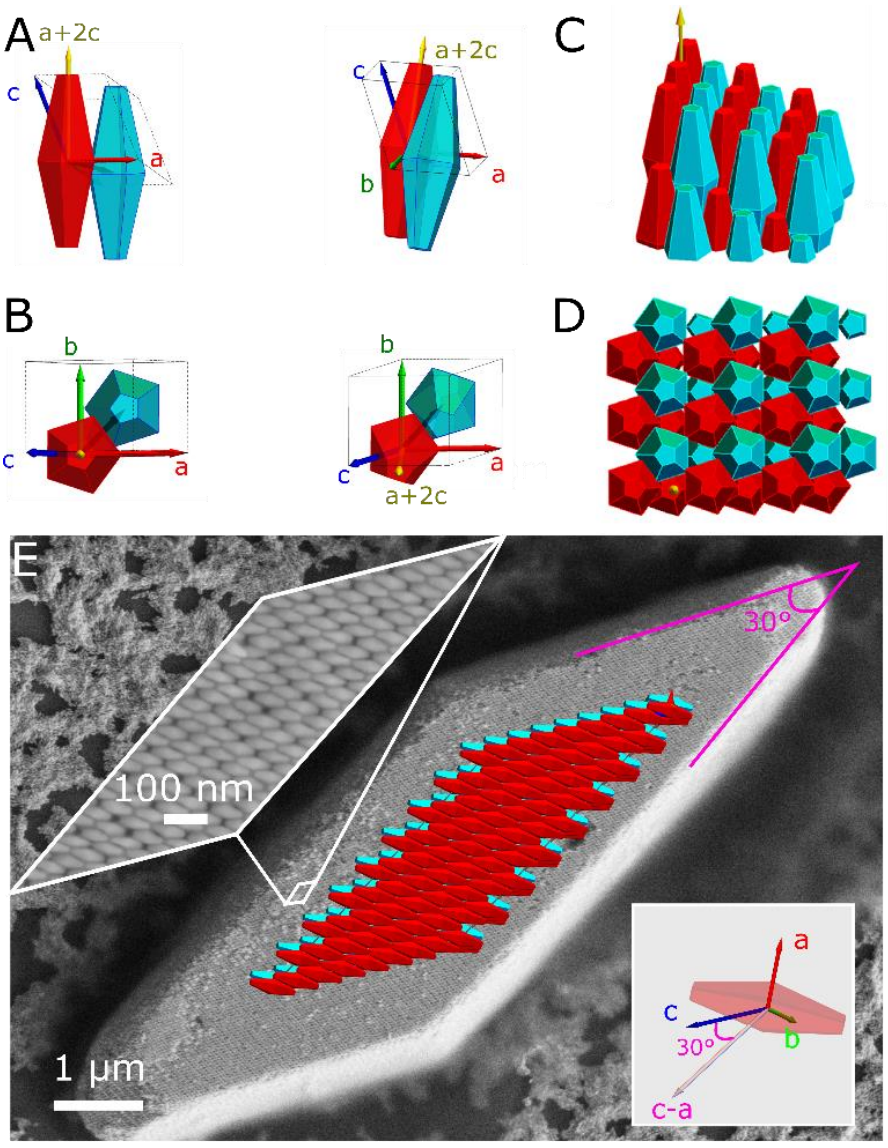

Figure 6.10 Comparison between the model and the experiment**.** A-B) P unit cell predicted numerically, composed of two bipyramids drawn in red and blue. C) View of the lattice in which the cut is orthogonal to the [1,0,2] direction. D) Projection of the packing along with the [1,0,2] direction (i.e. the longitudinal axis of the bipyramids). E) SEM image of a rhomboidal supercrystal, with superimposed model: both exhibit an angle of 30° at their tips. On top of the supercrystal, the (010) facet forms a rhomboid. The inset at the top shows a magnified SEM image of the supercrystal surface in the (010) facet where the bipyramids are lying flat. The inset at the bottom shows the unit cell of the model-oriented along the **c** and **c** − **a** vectors of the triclinic lattice. 16 mM in Au^0 and 2.5 mM of CTAC were used for sample preparation.

We could now give the 3D reconstruction of our supercrystals in Figure 6.11. In addition, we found it's possible to generate rhomboidal supercrystals a few microns in size at 16 mM Au^0, whereas at 64 mM Au^0 and 400 mM Au^0, a thin film was obtained. The 2D SAXS image of the supercrystals at 400 mM Au^0 is shown in Figure 6.12, by indexing the Bragg spots with the appropriate Miller indices corresponding to the triclinic lattice in the software SingleCrystal, we can indicate the crystal symmetry is still triclinic. Combined with the simulation and experiments, the two-particle unit cell in triclinic can be demonstrated in Figure 6.13, we then can also obtain the hkl indices and peak positions of the supercrystals in Figure 6.7H (see Table 6-2) in the software CrystalMaker.

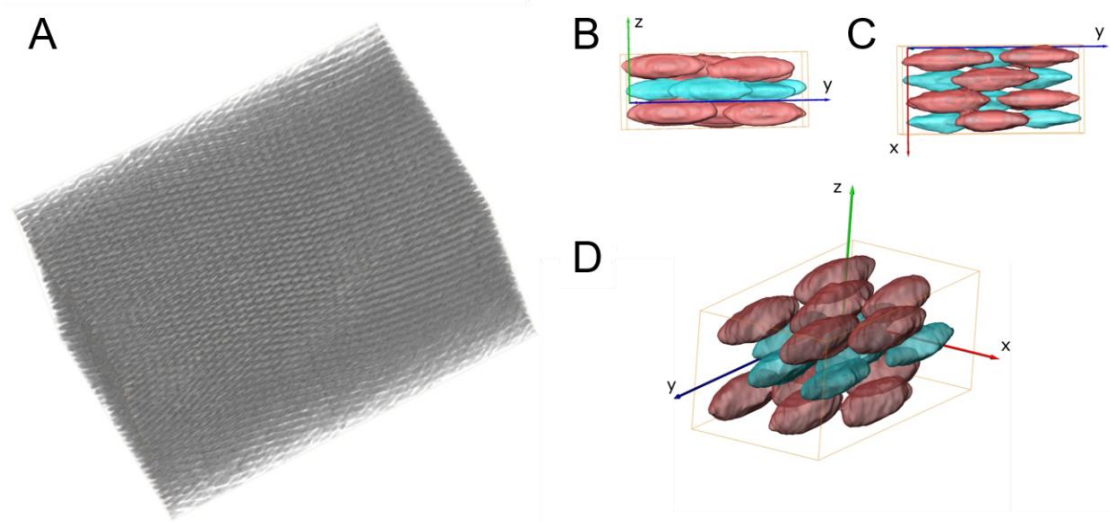

Figure 6.11 A) Three-dimensional reconstruction of a large portion of the supercrystal and B) a small portion of a supercrystal, obtained by FIB-SEM tomography and viewed along different orientations. These experiments were performed with GBPs_3 with 2.5 mM CTAC and 64 mM Au^0. The three arrows represent the Cartesian coordinates.

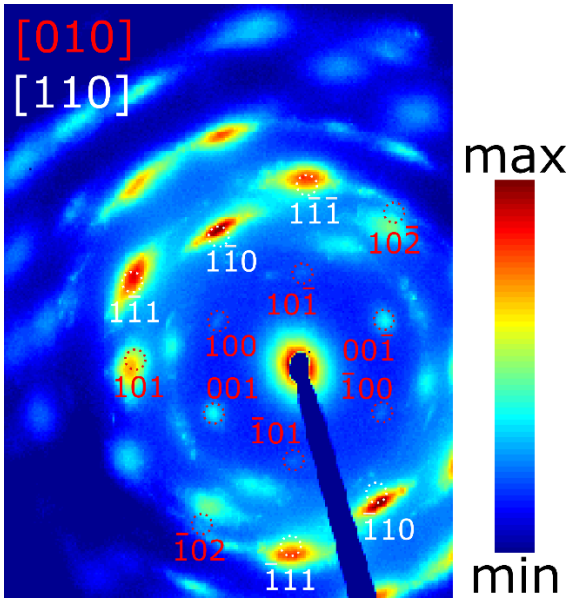

Figure 6.12 2D SAXS image (on a logarithmic intensity scale) of a few supercrystals in which Miller indices corresponding to the triclinic lattice are indicated on some Bragg spots. Two colors (red and white) are used for the indexation of two supercrystals with different orientations defined by the corresponding zone axis [UVW]. A few Bragg spots were obtained on the 2D SAXS images, indicating the formation of a few oriented supercrystals. By indexing the Bragg spots with the appropriate Miller indices, the supercrystals were found to be mainly oriented along the [110] and [010] directions, which corresponds to the orientation of the supercrystal displayed in Figure 6.10E. 400 mM in Au^0 and 2.5 mM of CTAC were used for the preparation of the sample.

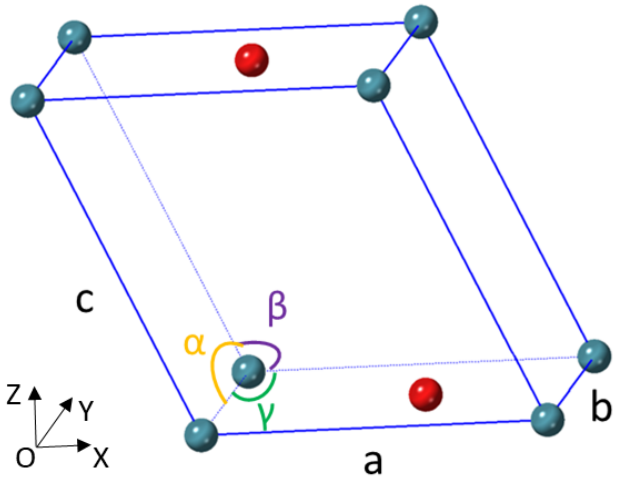

Figure 6.13 Representation of the triclinic unit cell used to index the peaks in Figure 6.7H. Using the positions of the observed diffraction peaks (see Table hereafter), a refinement of the triclinic cell was performed. We assume that the angle γ is equal to 90°, as per the numerical simulations of the structure. Accordingly, we take vector **a** along OX and vector **b** along OY, where OXYZ is an orthogonal basis. The refinement yields: a = 41.35 nm {ax, ay, az}={41.35,0,0}; b = 37.24 nm {bx, by, bz}={0,37.24,0}; c = 47.74 nm {cx, cy, cz}={-

15.54,-12.35,43.42}; α = 104.99°; β = 109°; γ = 90°. The volume of the unit cell is 66861.33 nm^3.

Since there are two bipyramids per unit cell, the packing fraction (η) can be determined as follow:

$$\eta = \frac{2V_{bipyramid}}{V_{unit\ cell}} \tag{6-1}$$

$V_{bipyramid}$ could be determined as follow:

$$V_{bipyramid} = 2 \times \frac{1}{3} \times \left[\left(\left(\frac{5}{2} r_L^2 \times sin\frac{2\pi}{5}\right) \times \frac{L'}{2}\right) - \left(\left(\frac{5}{2} r_s^2 \times sin\frac{2\pi}{5}\right) \times \left(\frac{L'}{2} - \frac{L}{2}\right)\right)\right] = \frac{5}{3} L'\, r_L^2 \times \sin\frac{2\pi}{5} \times (1-t)^3 \tag{6-2}$$

where r_L is the radius at the base of the bipyramid and r_s is the radius of the pyramid at one tip, the relationship between both quantities is $r_s = r_L \times t$. Other quantities such as L, t and $L'$are defined in Figure 6.3 and Table 6-1. The radius r_L is defined as follow:

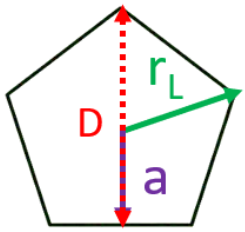

Figure 6.14 Definition of the width D, of the radius r_L and of the apothem a of the pyramid base.

Therefore, r_L can be determined from the TEM images using the following relation:

$$D = a + r_L = r_L \times cos\left(\frac{\pi}{5}\right) + r_L \tag{6-3}$$

To the particle width determined via TEM we toad the thickness of a CTAC bilayer, which is about 3.2 nm.[307,344] The experimental packing fraction was thus determined to be 0.835, in excellent agreement with the one determined from the MC computer simulations (0.83), see Figure 6.8.

Table 6-2 Attribution of the hkl indices for the peaks observed in Figure 6.7H and comparison of the peak position with the ones expected from the model corresponding to the unit cell. The model (q_{cal}) was determined in the software CrystalMaker.

h	k	l	d(hkl) (nm)	q_{exp} (nm^{-1})	q_{cal} (nm^{-1})	Delta=q_{exp}-q_{cal}
0	0	1	43.41501	0.1465	0.1447	0.0018
1	0	0	38.93043	0.1642	0.1614	0.0028
0	1	0	35.81765	0.1755	0.1754	0.0001
1	0	-1	35.54431	0.1780	0.1768	0.0012
0	1	-1	32.30918	-	0.1945	-
1	-1	0	27.66104	0.2286	0.2271	0.0015
1	1	-1	27.20377	-	0.231	-
1	1	0	25.22465	0.2447	0.2491	-0.0044
1	0	1	25.08483	0.2501	0.2505	-0.0004
0	1	1	24.52863	-	0.2561	-
-1	1	1	23.63118	0.2696	0.2659	0.0037
1	-1	1	23.03705	-	0.2727	-
1	0	-2	22.44895	0.2860	0.2799	0.0061
0	0	2	21.70751	0.2891	0.2894	-0.0003
1	1	-2	21.35897	-	0.2942	-
0	1	-2	21.33206	-	0.2945	-
2	0	-1	20.53203	-	0.306	-
2	0	0	19.46522	0.3271	0.3228	0.0043
1	1	1	18.72163	0.3334	0.3356	-0.0022
0	2	-1	18.42917	-	0.3409	-
2	1	-1	18.06513	-	0.3478	-
0	2	0	17.90883	0.35169	0.3508	0.0004

So far, the agreement between the model and the experiments is very good, as shown by the identical orientation of the particles at the nanoscale and a similar angle of 30° between the micrometer-sized rhombohedra tips and the angle defined by the **c** and **c** − **a** vectors of the unit cell. The lattice parameters of the triclinic unit cell were found to be a = 41.35 nm; b = 37.24 nm; c = 47.74 nm; α = 105°; β = 109°; γ = 90° (Figure 6.13). The experimental packing fraction was determined as 0.835, in excellent

agreement with the one determined from the MC computer simulations (0.83). The triclinic pinacoidal lattice ($P\bar{1}$) defines a low-symmetry architecture of low symmetry with only the center inversion as symmetry operation.[345] To the best of our knowledge, this is the first experimental realization of the shape-directed self-assembly of a triclinic supercrystal.[346]

6.5 Facet-dependent SERS experiments

The optical properties of the supercrystals were finally investigated by SERS, allowing the detection of the spectral fingerprint of a probe molecule in contact with the plasmonic surface.[86,347] As an analyte, we used crystal violet (CV), which is resonant with the laser frequency, resulting in surface-enhanced resonance Raman scattering (SERRS). This analysis was performed on a faceted supercrystal (Figure 6.15A-B). The SERRS signal intensity was uniform on each facet due to the periodic arrangement of the nanoparticles (Figure 6.15C). Moreover, the average signal is found to be facet-dependent, with the $(1\bar{2}1)$ facets displaying the highest SERRS intensity (Figure 6.15D). This phenomenon can be ascribed to the varying local arrangement of the NPs on the different facets, directly affecting electromagnetic hotspots formation at the interparticle gaps.[86,347] The orientation of the longitudinal axis of the bipyramids with respect to the surface plays a key role. When the longitudinal axis of the bipyramids is parallel to the surface facet (i.e. the (010) one), the Raman enhancement is small (201 CPS) whereas a much higher enhancement (560 CPS) is observed when the bipyramids point outwards (i.e. the $(1\bar{2}1)$ facet) (Figure 6.15).[35,159] Additional SERS characterizations of the supercrystals are provided in Appendix 8.4.1. In contrast, similarly mapping SERRS intensity on gold nanosphere (GNSs) supercrystals resulted in a uniform response (Figure 6.16). Here we show facet-dependent SERS properties that originate from the anisotropy of the GBPs, opening an avenue for tailored SERS performances using supercrystals with spiky and smooth facets displaying respectively high and low SERS efficiency. SERS measurements were done by my colleague Dr. Wajdi Chaâbani at LPS.

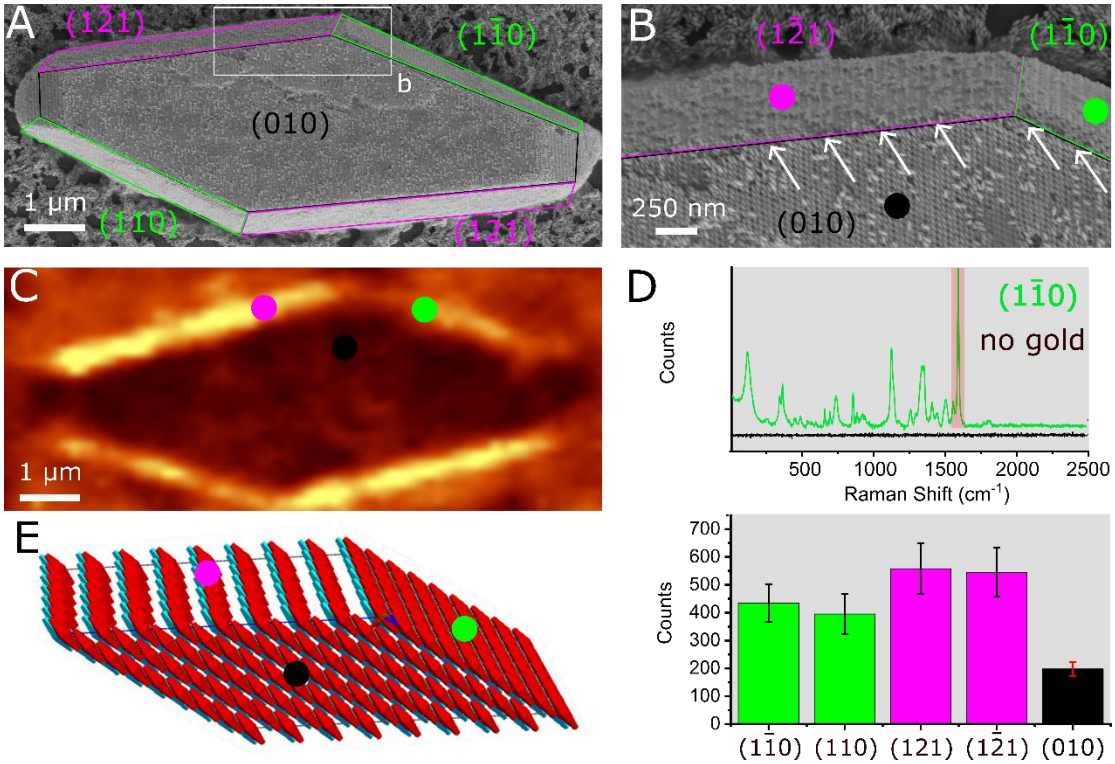

Figure 6.15 Facet-dependent surface-enhanced resonance Raman scattering on a gold bipyramid supercrystal. A-B) SEM micrographs of a GBP supercrystal viewed at different magnification. The largest facet (010) is surrounded by lateral facets. The surface facets of the supercrystal, $(1\bar{2}1)$, $(1\bar{1}0)$ and (010), are outlined with pink, green and black frames respectively. C) SERRS image obtained by mapping the SERRS intensity of the crystal violet vibrational peak over 1618-1632 cm^{-1}. D) (top) representative SERRS spectrum of crystal violet measured on the $(1\bar{1}0)$ facet (green) and Raman spectrum of CV measured without gold in the same experimental conditions (black). The red-shaded area indicates the spectral range integrated for generating the SERRS images in (C). (bottom) histogram of the mean SERRS intensity at 1620 cm^{-1} on the different facets, with the error bars indicating the standard deviation on each facet. The concentration of CV in the solution was 10^{-6} M, the acquisition time was 100 ms, and the laser power at the sample was ≈ 0.1 mW, at an excitation wavelength of 633 nm. E) Model of the triclinic lattice for the supercrystal. The (010) facet is constructed with the edge vectors **c** and $\mathbf{c} - \mathbf{a}$ of the unit cell. The GBPs are lying flat onto the (010) facet and they are pointing outwards of the $(1\bar{2}1)$ facet.

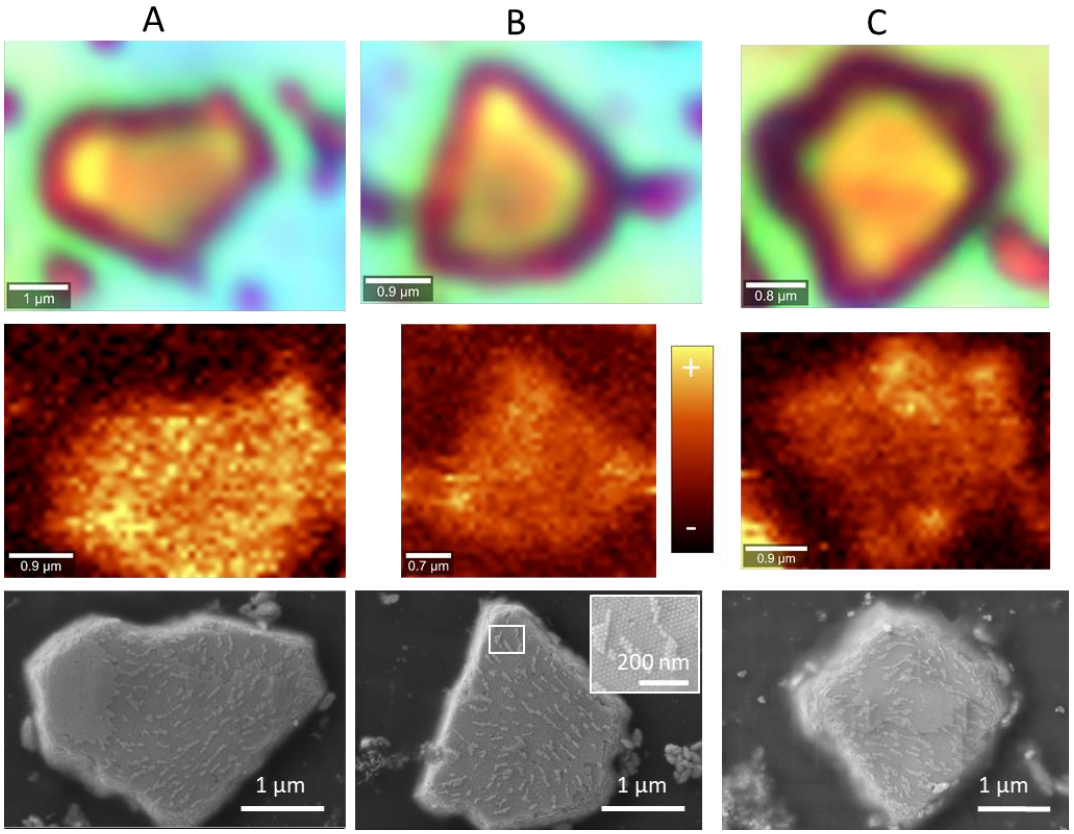

Figure 6.16 Combined spectroscopic and structural characterization on supercrystal composed of spherical NPs. A-C) Characterization of three supercrystals composed of nanospheres. Each supercrystal is characterized by optical microscopy (top), corresponding SERRS image obtained by mapping the SERRS intensity of the crystal violet vibrational peak over 1618-1632 cm^{-1} (middle), corresponding SEM micrograph (bottom). For SERRS, the concentration of CV solution was 10^{-6} M, acquisition time was 100 ms, and laser power at the sample was ≈ 0.01 mW, at an excitation wavelength of 633 nm. 16 mM in Au^0 and 2.5 mM of CTAC were used for the preparation of the sample. Contrary to the GBPs supercrystals, the SERRS image shows a uniform signal due to the isotropy of the NPs.

6.6 Conclusions

This work shows that fivefold symmetry and anisotropy can be combined to crystallize complex nano-objects into triclinic pinacoidal supercrystals. Pentagonal gold bipyramids pack into crystals with two particles per unit cell, corresponding to the densest packing predicted by Monte Carlo (MC) computer simulations. Further simulations show how the cross-section influences the arrangement (symmetry and packing fraction) of the particles, beyond pentagonal bipyramids. Objects with an odd-sided base are non-centrosymmetric but the two-particle unit cell retrieves inversion symmetry, explaining the double-lattice arrangement. Surprisingly, their packing fraction is lower than that of even-sided particles. The double-lattice packing

generalizes the optimal packing of regular pentagons in the plane, the “pentagonal ice ray” in a non-trivial manner (as can be seen in Figure 6.10D), since the section of the bipyramids is not constant along their long axis. This gold bipyramid supercrystal has a facet-dependent optical response, with spiky and smooth facets displaying respectively high and low SERS efficiency. Its low-symmetry triclinic structure is also useful for metamaterials applications and fundamental studies of self-assembly processes.

7 Conclusions and perspectives

7.1 Conclusions

On the whole, the research work elaborated in this thesis dealt with various aspects regarding synthetic control of nanoparticle's size, shape, and composition, as well as the design of self-assembled nanostructures with promising applications such as surface-enhanced Raman scattering.

Various types of plasmonic NPs were synthesized via seed-mediated growth throughout our entire work, comprising gold spheres (GNSs), gold nanorods (GNRs), gold bipyramids (GBPs), gold nanotetrapods (GNTPs) and core-shell GNPs@Ag. All the NPs with tunable size and shape were characterized by UV-Vis-NIR absorption spectroscopy (AS) and transmission electron microscopy (TEM).

Core-shell NPs were demonstrated in Chapter 3, we studied the morphology evolution and concentration of GNSs@Ag bimetallic NPs using four complementary techniques: TEM, AS, small-angle X-ray scattering (SAXS) and inductively coupled plasma mass spectrometry (ICP-MS) in Section 3.3. We then monitored the anisotropic growth of silver shells on preformed gold bipyramidal seeds by three *in situ* techniques (SAXS, AS and liquid-cell TEM) in Section 3.4. In addition, we revealed that ascorbic acid (AA) has a thermodynamic effect (by stabilizing the {100} facets) and plays a double role (e.g., both reducing and shape-directing agent) in the presence of CTAC.

In Chapter 4, we revealed the reshaping mechanism of GNTPs by the way of demonstrating the reshaping kinetics as well as controlling their stability with a thin silver layer. This reshaping of GNTPs is related strongly to the temperatures, presence/absence of solvent, and the addition of iodine. In detail, the reshaping process is faster at higher temperatures, and the reshaping of GNTPs also occurs in the dry state suggesting atom migration, but the kinetics is much slower than in solution. In addition, the reshaping rate drastically increased when iodide was added, indicating that the shape deformation is indeed related to the various solutes, confirming the dissolution and redeposition mechanism. The reshaping can be blocked with a thin silver layer (Ag/Au=0.2): GNTPs coated with silver are very stable for 2 months at room temperature as well as at 60°C-70°C for at least 1 day. We also showed that the GNTPs exhibit strong SHG, essentially due to their shape and which decreases as they reshape

into spheres, reaching a plateau, the origin of which is driven by the surface defects. Initially, retardation is weak and the SHG response is dominated by the shape non-centrosymmetry. As the GNTPs evolve into spheres, this source weakens and is complemented with an origin due to retardation.

In Chapter 5, several types of surfactant-stabilized GNPs (i.e. GNSs, GNRs and GBPs) were self-assembled into one-dimensional chains using sulfate ions. We showed that such a two-step evolution can only be uncovered by combining AS with a structural technique (e.g. SAXS). The assembly can be simply described as the conversion from the initial species (isolated particles) to the final one (chains), but with apparent first-order kinetics by analysis of AS with a single value decomposition (SVD) method. This conclusion holds very well for rods and spheres, but not for bipyramids, where the evolution is more complicated. Moreover, the self-assembly process can be stopped at any stage by adding an excess surfactant to the reaction mixture. Various oligomers with defined optical properties were stabilized for a long period of time (at least 15 days) in this way. The assemblies are very stable under dialysis, and the interaction of the interparticle is quite strong, as seen in LCTEM. Finally, the “hot spots” in plasmonic polymers could be precisely targeted and a second metal deposited at their location.

In Chapter 6, we obtained long-range three-dimensional supercrystals of pentagonal GBPs and revealed that the structure is a triclinic arrangement. GBPs pack into crystals with two particles per unit cell, as shown via a combination of several characterization techniques: SAXS and focused ion beam-scanning electron microscopy (FIB-SEM) tomography analysis, in agreement with the Monte Carlo (MC) computer simulations. The crystalline order of the GBPs supercrystals results in a facet-dependent optical response, which is demonstrated by SERS spectroscopy.

All in all, in these four years, I am proficient in the synthesis and purification of various high-yield NPs. In addition, using several combinations of techniques such as AS, TEM, SAXS, etc to monitor the nanoparticle growth. With the experience of core-shell NPs synthesis, we found the reshaping of gold nanotetrapods can be blocked with a thin Ag layer. We also found a two-step assembly kinetics of gold NPs into one-dimensional chains in combination with the SAXS and the SVD treatment of AS data and built a double-lattice packing of pentagonal gold bipyramids in supercrystal with triclinic symmetry. All these experiences are the strong foundation for my follow-up scientific

research in particle synthesis, self-assembly as well as characterization techniques, and data analysis in the future.

7.2 Perspectives

Optimizing architecture design for a broad range of plasmonic applications is encouraging. The assembly of core-shell NPs into supercrytals is still fascinating, due to the variation of cross-sections. We have known the optical properties and morphology of gold bipyramid@Ag can be tuned by adjusting the Ag/Au ratio. Based on the triclinic lattice of single GBPs supercrystal and the hexagonal symmetry of long rods supercrystals, we are interested in probing the structure evolution of core-shell GBPs@Ag supercrystals and exploring the utilization in the SERS.

Furthermore, we are building upon the findings of triclinic symmetry of pentagonal bipyramids to explore the self-assembly of other NPs of interest with five-fold symmetry. Decahedra can be seen as bipyramids with shorter aspect ratios, we have preliminarily assembled five gold decahedrons of different sizes. The preliminary SAXS results show that flatter decahedra self-assemble into ordered structures showing that faceting is also a very important parameter in the self-assembly process. Therefore, revealing their packing structure by other techniques such as 3D FIB-SEM tomography analysis as well as simulations is our following research plan.

A great majority of supercrystals are formed by the deposition of NPs on substrates, which can indeed limit their wide application. Therefore, we are looking forward to developing a method for supercrystals that can be easily retrieved, for instance, using a non-stick but very cheap Teflon as a substrate, or using a levitation method.

We are also assembling various gold NPs in confinement to build a long-range crystal, this work has collaborated with my colleague Dr. Wajdi Chaâbani.

In the future, I expect to synthesize other metal NPs (Cu, Ni, Co…) with different morphologies, monitor their growth via various techniques, and self-assembly of NPs into a long-range crystal to fabricate the application devices, such as sensing, catalyst…etc.)

8 Appendix

8.1 Synthesis of core-shell bimetallic nanoparticles

8.1.1 Additional TEM images of gold nanospheres@Ag

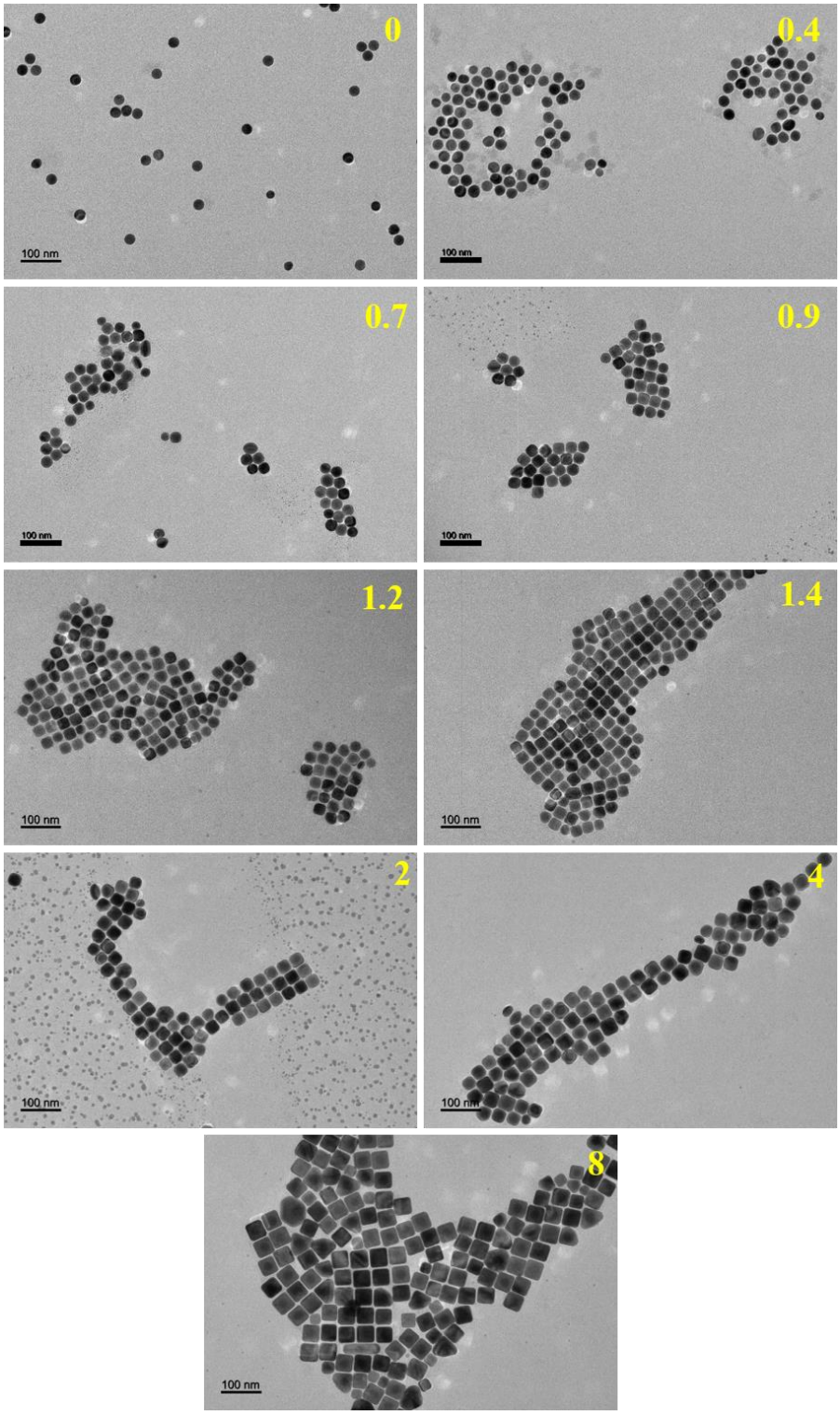

Figure 8.1 TEM images of GNS@Ag for K = 0 through 8 at low magnification. The K values are indicated in each panel.

8.1.2 Additional TEM images of gold bipyramids@Ag

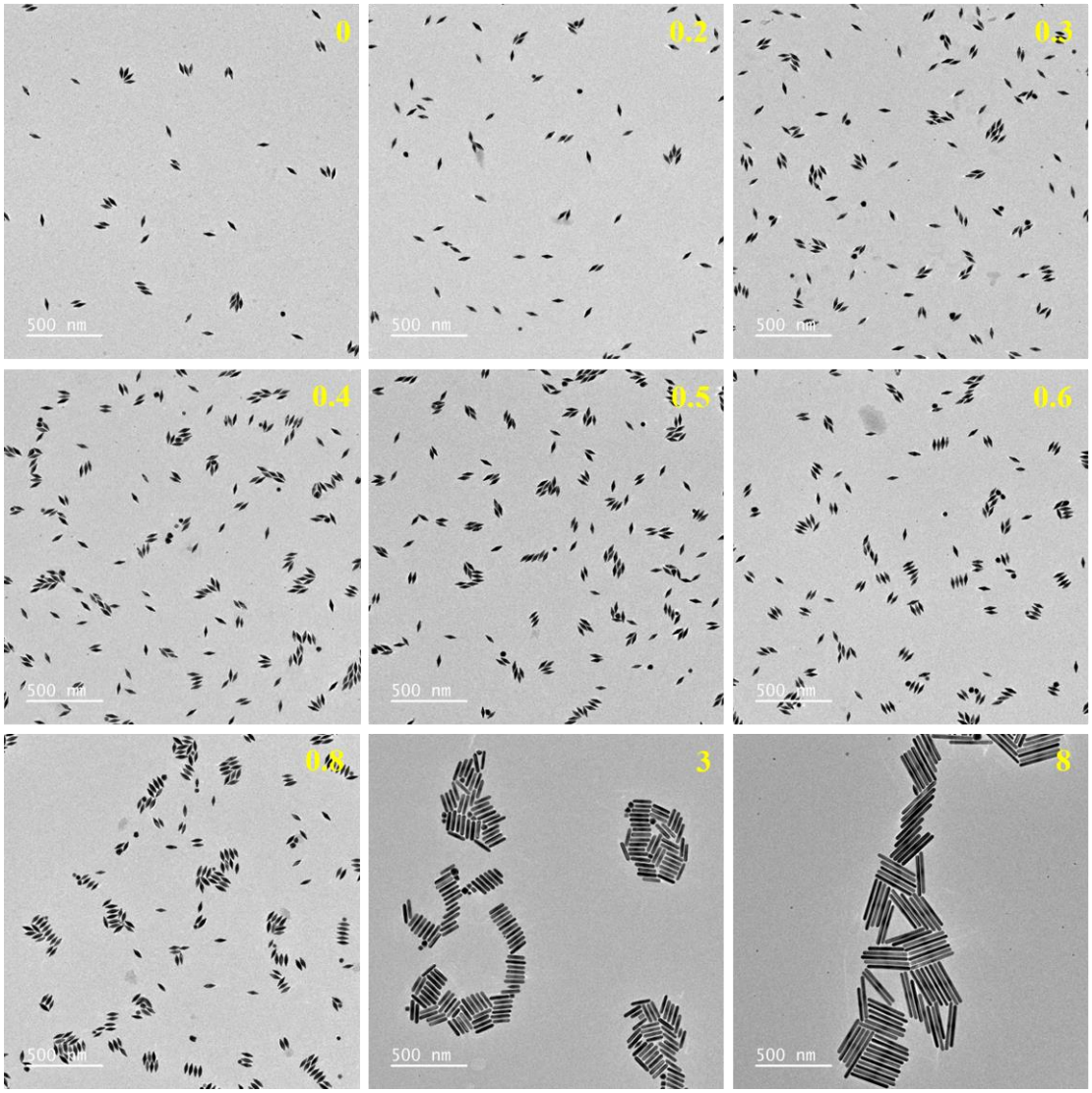

Figure 8.2TEM images of GBPs@Ag for K = 0 through 8 at low magnification. The K values are indicated in each panel.

8.2 Reshaping kinetics of acicular nanoparticles and their nonlinear optical properties

8.2.1 Additional TEM images of gold nanotetrapods stabilized with different Ag/Au molar ratios K

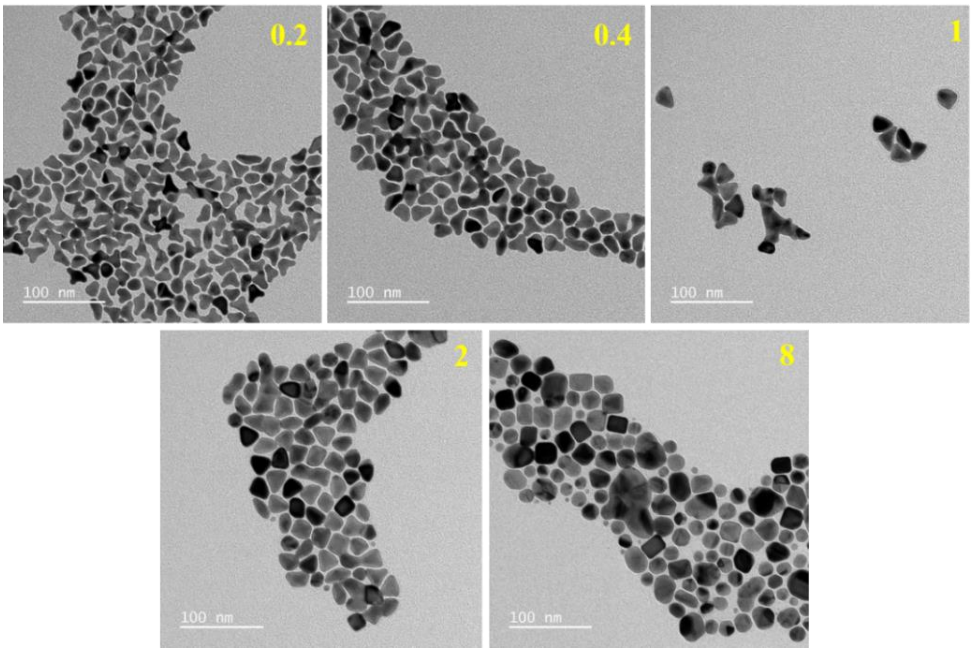

Figure 8.3 TEM images of GNTPs for K = 0 through 8 at low magnification. The K values are indicated in each panel.

8.2.2 Additional TEM images of gold nanotetrapods stabilized with silver at different times

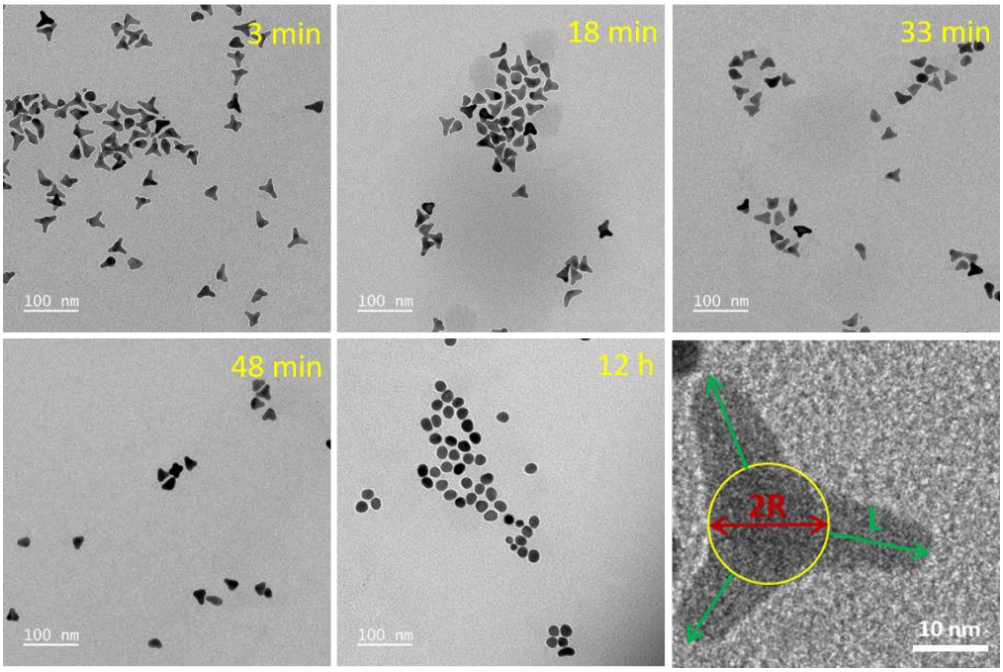

Figure 8.4 TEM images of GNTPs obtained after various reshaping times at 60°C and construction used to determine manually the core diameter $2R$ and the arm length L, illustrated using an GNTP-1 particle.

8.3 Assembling gold nanoparticles into one-dimensional chains

8.3.1 Reaction kinetics

During the assembly process, the plasmon band red-shift to a finite value due to the infinite chain limit effect and the intensity changes weakly. Therefore, it is difficult for us to continue to monitor the evolution of the plasma band in the AS. I will call this type of reaction is limited reaction to facilitate the subsequent discussion. Studying the kinetics of such reactions based on the general chemical kinetics is essential for understanding the assembly process of GNPs.

8.3.1.1 General chemical kinetics

To give a simple example, suppose that the reactant is only A and the product is B. The rate of A is the slope of variation of concentration $\frac{d[A]}{dt}$. The kinetics of the ideal reaction are[348]:

Zero-order law:

$$v = -\frac{d[A]}{dt} = k \tag{8-1}$$

which means the reaction rate is independent of the concentration of the reactant. After integration, we can get

$$[A]_t = [A]_0 - kt \tag{8-2}$$

First-order law:

$$v = -\frac{d[A]}{dt} = k[A] \tag{8-3}$$

After the same integration, the final solution can be gotten:

$$ln[A] = ln[A]_0 - kt \quad , \quad [A]_t = [A]_0 e^{-kt} \tag{8-4}$$

Second-order law:

$$v = -\frac{d[A]}{dt} = k[A]^2 \tag{8-5}$$

the solution is

$$\frac{1}{[A]_t} = \frac{1}{[A]_0} + kt \quad , \quad [A]_t = \frac{[A]_0}{1 + kt[A]_0} \tag{8-6}$$

8.3.1.2 Limited reaction kinetics

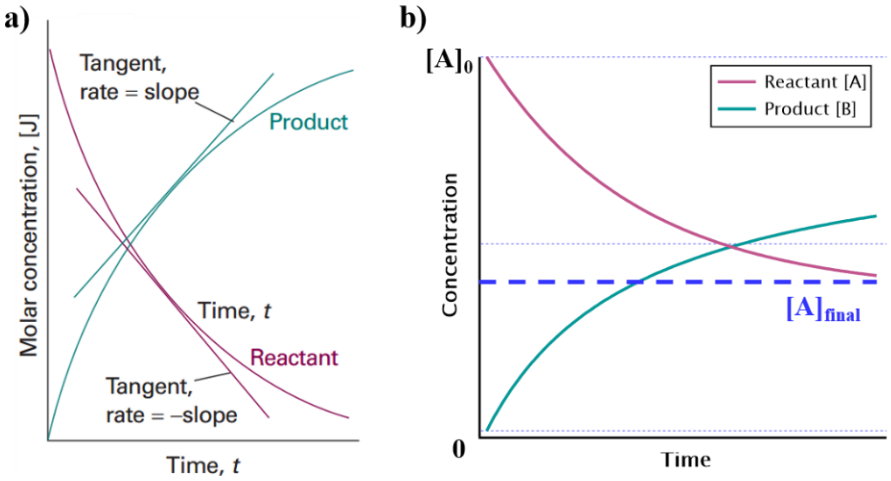

Figure 8.5 (a) The definition of the rate as the slope of the tangent drawn to the curve shows the variation of concentration with time for the general chemical reactions. (b) The approach of reactant's concentration decreases to a finite value for a reaction A to B. Adapted from Ref. 348.

When a reaction is limited, the concentration of reactant A will decrease from $[A]_0$ to a finite value marked as $[A]_{\text{final}}$ instead of arriving at 0 (see Figure 8.5b), and changes weakly afterward. In this case, if this reaction follows the first-order law, then its reaction rate is

$$v = -\frac{d[A]}{dt} = k([A] - [A]_{\text{final}}) \tag{8-7}$$

the solution can be known:

$$[A] = ([A]_0 - [A]_{\text{final}})\, e^{-kt} + [A]_{\text{final}} \tag{8-8}$$

If this reaction is a second-order reaction, the rate of the reaction is

$$v = -\frac{d[A]}{dt} = k([A] - [A]_{\text{final}})^2 \tag{8-9}$$

then we can get the solution as well,

$$\frac{1}{[A] - [A]_{\text{final}}} = \frac{1}{[A]_0 - [A]_{\text{final}}} + kt \tag{8-10}$$

or

$$[A] = \frac{1}{\frac{1}{[A]_0 - [A]_{\text{final}}} + kt} + [A]_{\text{final}} \tag{8-11}$$

Finally, the yield η can be known:

$$\eta = \frac{[A]_0 - [A]_{\text{final}}}{[A]_0} = 1 - \frac{[A]_{\text{final}}}{[A]_0} \tag{8-12}$$

8.3.2 Singular value decomposition

As shown in all the above reaction kinetics equations, studying the assembly kinetics of GNPs requires us to indicate the initial concentration $[A]_0$ and the finite concentration $[A]_{\text{final}}$ of the reactants A. Therefore, how to extract effective information from the numerous AS data and describing all the data are the key to understanding our assembly kinetics.

Singular value decomposition (SVD) is a factorization of a real or complex matrix $\boldsymbol{A}$ that generalizes the eigendecomposition of a square normal matrix to any $M \times N$ matrix via an extension of the polar decomposition. The matrix $\boldsymbol{A}$ can be expressed as[349]:

$$A = U\, W\, V^{\mathrm{T}} \tag{8-13}$$

Where $\boldsymbol{U}$ is $M \times M$ orthogonal matrix and $\boldsymbol{V}^{\mathrm{T}}$, the conjugate transpose of $\boldsymbol{V}$, is $N \times N$ orthogonal matrix, $\boldsymbol{W}$ is an $M \times N$ diagonal matrix with non-negative elements $W_{\mathrm{ii}} \geq 0$, known as singular values. A common practice is to arrange the singular values from large to small, which is $W_{\mathrm{ii}} \geq \mathbf{W}_{\mathrm{jj}}$ for $i \geq j$. In this way, one can obtain a very good approximation to $\boldsymbol{A}$ by truncating $\boldsymbol{W}$ to keep only the K largest singular values:

$$A \approx A_{\mathrm{K}} = U\, W_{\mathrm{K}}\, V^{\mathrm{T}} \tag{8-14}$$

In other words, we can use K important components to describe all the matrix data.

In our experiments, the experimental AS data $A(\lambda, t)$measured as a function of the wavelength λ and the time t can be organized as an $M \times N$ matrix $\boldsymbol{A}$ with M wavelength values and N time points, such that A_{ij} is the value for λ_{I} at t_{j}, where $t_1 = 0$ and $t_{\mathrm{n}} = t_{\text{final}}$ (the beginning and the end of the kinetics, respectively). Using SVD, the matrix $\boldsymbol{A}$ can be factorized into $A = U\, W\, V^{\mathrm{T}}$, the columns of $\boldsymbol{U}$ can be seen as basis vectors that, when multiplied by the time-dependent coefficients in $\boldsymbol{V}$ and weighted by the singular values, yield back the experimental absorbance spectra.

We keep K largest singular values, the $\boldsymbol{W}_{\mathrm{k}}$ is obtained from $\boldsymbol{W}$ by setting $W_{\mathrm{ii}} = 0$ for $i > K$, which means only K species contribute to the absorbance over the duration of the process. The signal of each species, $\boldsymbol{S}_{\mathrm{i}}(\lambda)$, $i = 1, 2, \dots, K$ can be accurately described as a linear combination of the first K columns of $\boldsymbol{U}$ (which form $\boldsymbol{U}_{\mathrm{K}}$), but the combination coefficients are a priori unknown and must be constrained by physical considerations. Explicitly, the signal matrix $\boldsymbol{S}$ given by $S_{\mathrm{ij}} = S_{\mathrm{i}}(\lambda_{\mathrm{j}})$ is related to the truncated $\boldsymbol{A}_{\mathrm{K}}$ via a generalized "rotation" matrix $\boldsymbol{R}$: $S = U\, W_{\mathrm{K}}\, R$, so we can rewrite Eq.(8-14) by inserting the identity $1 = R\, R^{-1}$:

$$A_{\mathrm{k}} = U_{\mathrm{K}}\, W_{\mathrm{K}}\, R\, R^{-1} V_{\mathrm{K}}{}^{\mathrm{T}} = S\, C^{\mathrm{T}} \tag{8-15}$$

with $\boldsymbol{C}^{\mathrm{T}}$ the time coefficient matrix. $\boldsymbol{A}_{\mathrm{K}}$ is of size $M \times N$, $\boldsymbol{U}_{\mathrm{K}}$ and $\boldsymbol{S}$ are $M \times K$, $\boldsymbol{W}_{\mathrm{K}}$, $\boldsymbol{R}$ and $\boldsymbol{R}^{-1}$are $K \times K$ while $\boldsymbol{V}_{\mathrm{K}}^{\mathrm{T}}$ and $\boldsymbol{C}^{\mathbf{T}}$ are $K \times N$.

Guided by the presence of isosbestic points (where the signal remained constant in time) from the AS (see Figure 5.4a) during the process of assembly, we infer that only two components contributed significantly to the experimental spectra.[350] We can describe the data very well using only $K = 2$ components, which is easily explained by the conversion between the initial population (isolated particles) and the final aggregates. This interpretation imposes a strict condition on the matrix $\boldsymbol{R}$, namely that one of the basis spectra $\boldsymbol{S}_1$ is simply the first column of $\boldsymbol{U}_{\mathrm{K}}$ (since only the first species is present in the beginning. The second species does not contribute at the beginning of assembly, so $\boldsymbol{C}_1(0) = 1$ and $\boldsymbol{C}_2(0) = 0$. More precisely,

$$C_{\mathrm{i1}}^{\mathrm{T}} = \left[R^{-1} V_{\mathrm{K}}^{\mathrm{T}}\right]_{\mathrm{i1}} = (1,0,0,0, \dots, 0)^{\mathrm{T}} \tag{8-16}$$

The second condition is that the amount of gold is constant during the assembly process. It is well known that the extinction of gold nanoparticle solutions at a wavelength $\lambda_{\mathrm{norm}} \approx 400\ nm$ is relatively independent of the shape, size and aggregation state of the gold nanoparticles[204], so we can normalize the second and subsequent components such that $\boldsymbol{S}_{\mathrm{i}}(\lambda_{\mathrm{norm}}) = \boldsymbol{S}_1(\lambda_{\mathrm{norm}})$.

As we mentioned before, the final relation stems $\boldsymbol{S}_2$ is free of any contribution from $\boldsymbol{S}_1$, we therefore adjust $\boldsymbol{R}$ by hand that $\boldsymbol{S}_2$ has no peak at the position of the LSPR of the initially isolated particles for GNRs and GBPs. This is the last condition to define the matrix $\boldsymbol{R}$.

When a beam of polarized incident light interacts with GNPs, the transverse plasmon peak of GNRs and GBPs is not sensitive before and after assembly, the new peak is contributed by the change of longitudinal peak (see Figure 1.10). But the situation is more complicated for spheres because the isolated objects have three equivalent space directions, so the final spectrum is $S_1 = \frac{1}{3} 3 S_{\mathrm{iso}}$, while those assembled into chains are described by $S_2 = \frac{1}{3}\left(2S_{\mathrm{iso}} + S_{\mathrm{coupl}}\right)$, where S_{coupl} is the (red-shifted) coupled plasmon resonance excited when the incident polarization is along the chain. Applying here the final relation used for rods and bipyramids yields a spectrum matrix $\boldsymbol{S}$ containing the two distinct modes S_{iso} and S_{coupl}.

Separating the different modes is crucial to understanding the kinetics of the assembly process. We must “remix" the modes in the proportions defined above, by inserting into Eq.(8-15) the matrix $\boldsymbol{M}$ to yield:

$$A = S\, M\, M^{-1} C^{\mathrm{T}} = S' C'^{\mathrm{T}} \tag{8-17}$$

The resulting $\boldsymbol{S}'$now contains the desired $\boldsymbol{S}'_1$ and $\boldsymbol{S}'_2$, while $\boldsymbol{C}'^{\mathrm{T}}$ holds the corresponding time coefficients, the matrix $\boldsymbol{M}$ is:

$$M = \begin{bmatrix} 1 & {}^{2}/_{3} \\ 0 & {}^{1}/_{3} \end{bmatrix} \tag{8-18}$$

8.4 Assembling gold bipyramids into three-dimensional supercrystals

8.4.1 Additional SEM images of bipyramids supercrsystals

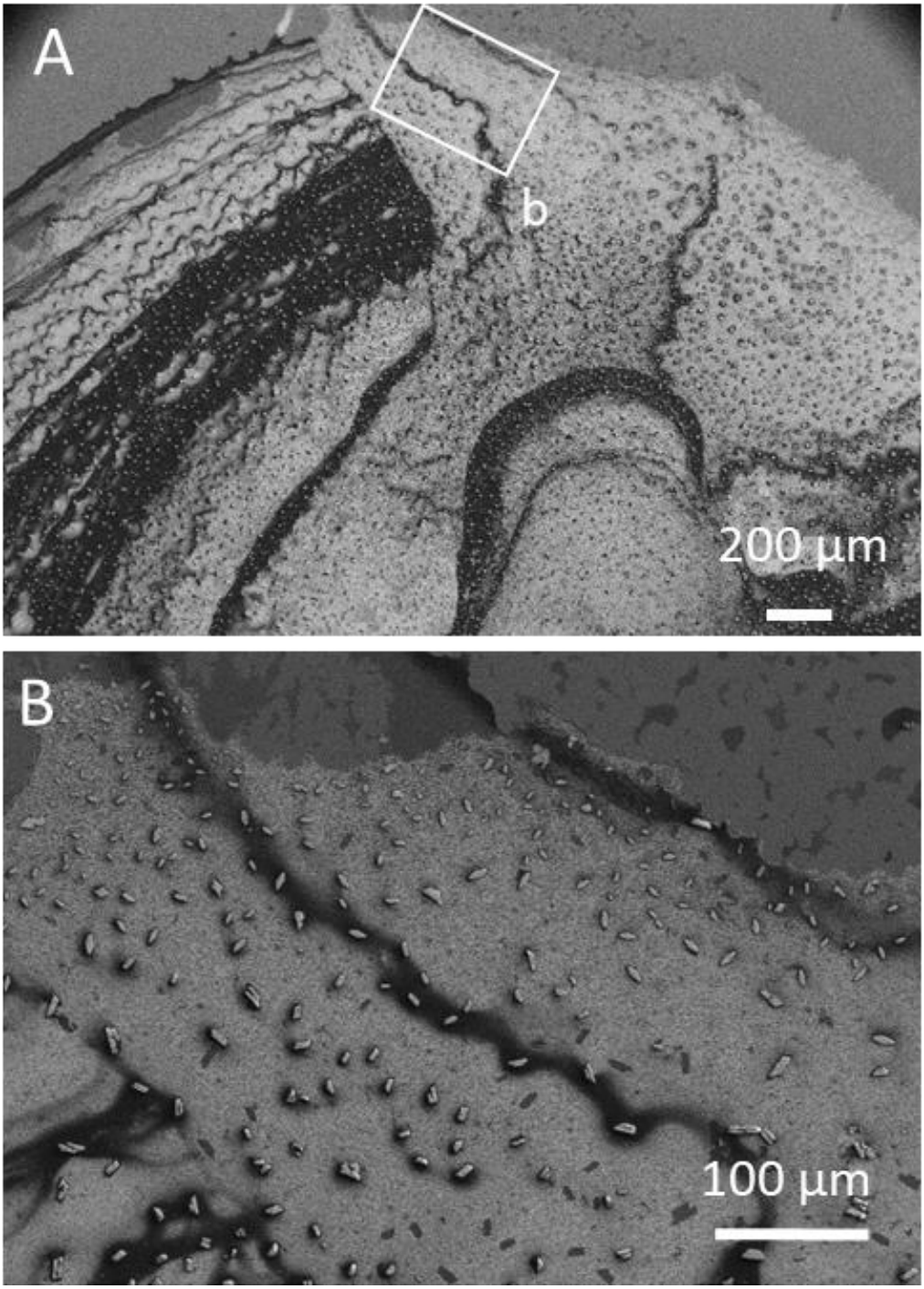

Figure 8.6 SEM images at low magnifications show the uniform formation of gold bipyramid supercrystals on the substrate obtained by drop-casting. These experiments were performed with GBPs_3 with 2.5 mM CTAC and 16 mM Au^0.

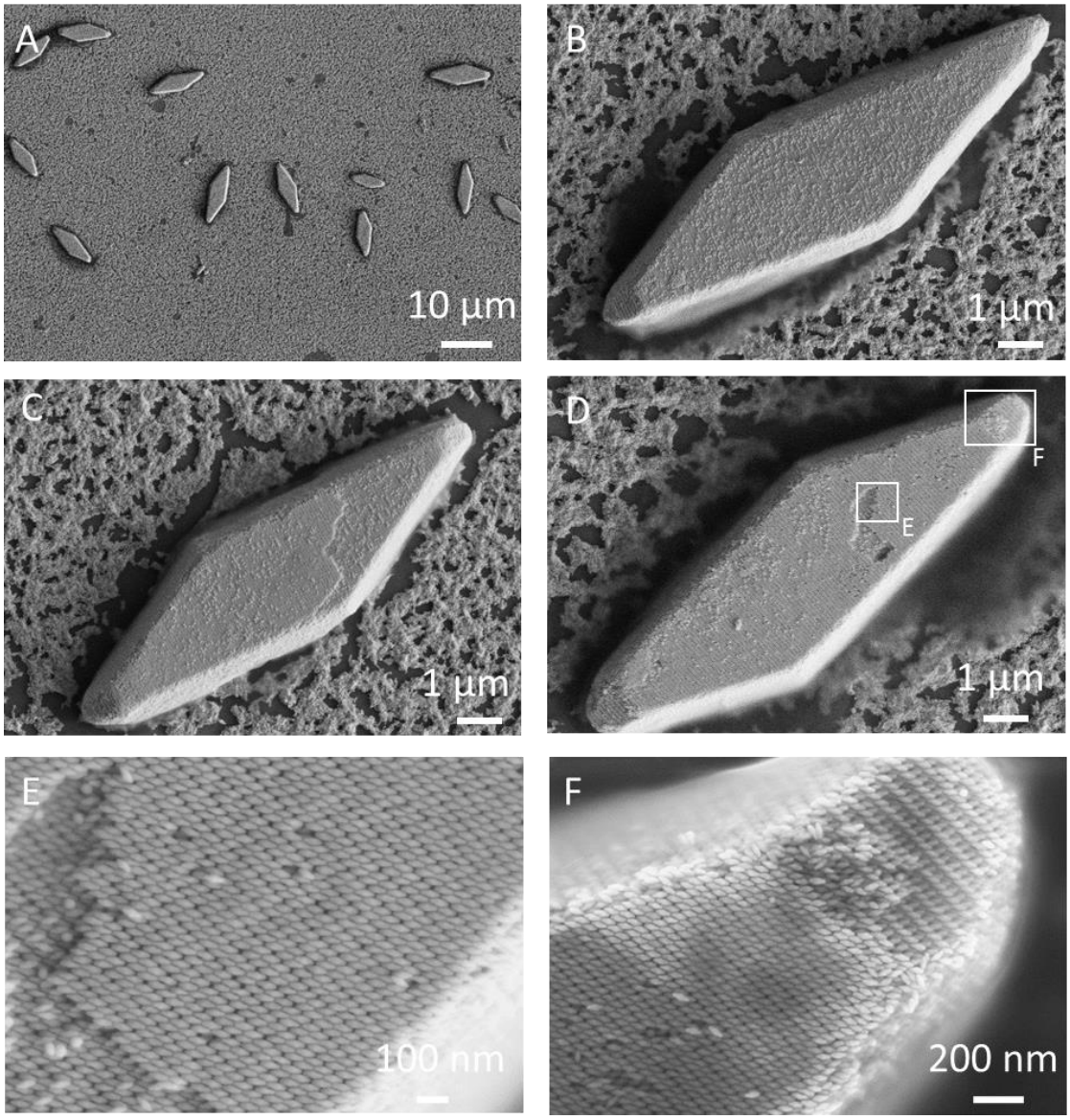

Figure 8.7 SEM images at different magnifications showing rhombohedral supercrystal on the substrate obtained by drop-casting. These experiments were performed with GBPs_3 with 2.5 mM CTAC and 16 mM Au^0.

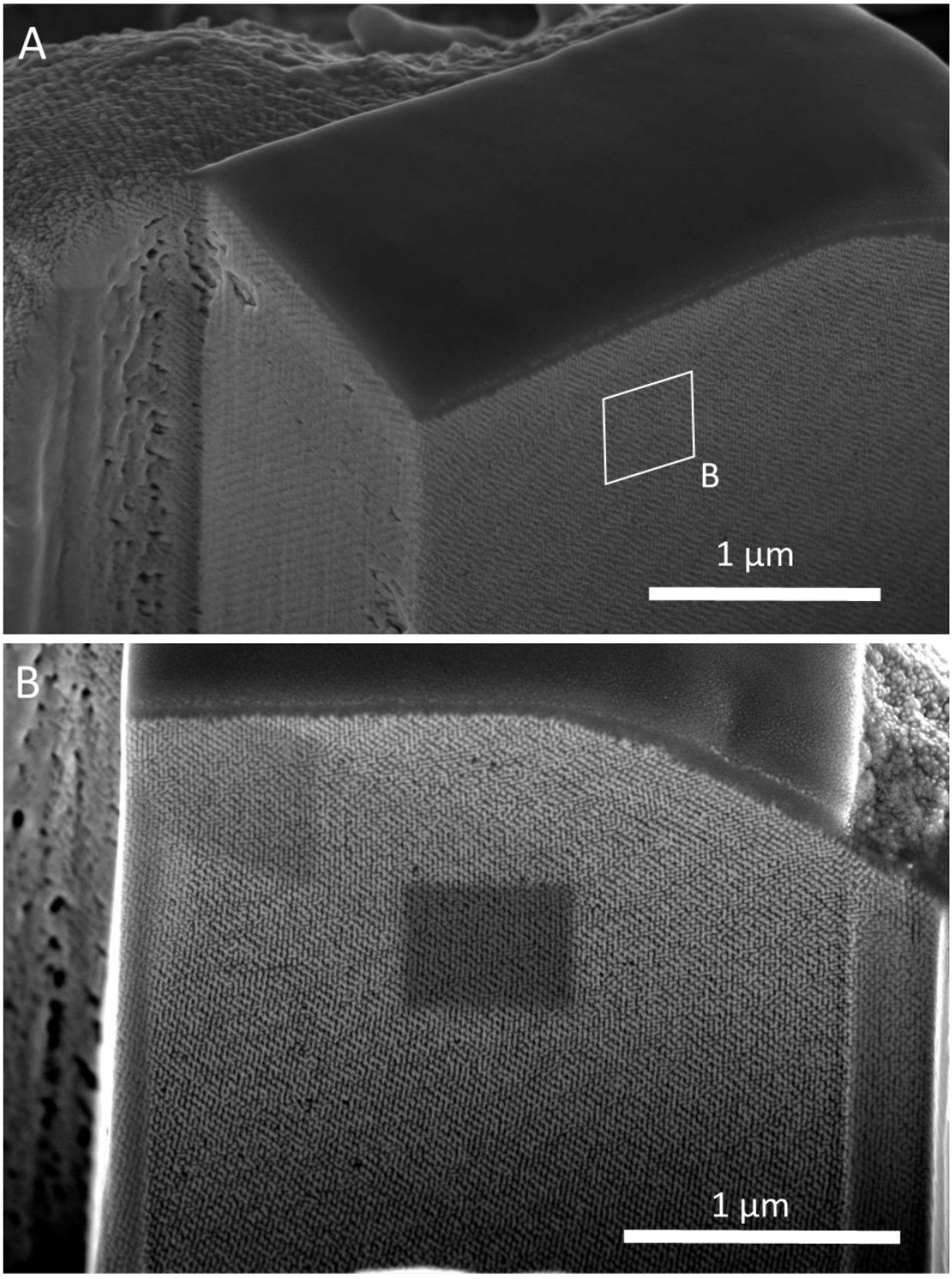

Figure 8.8 SEM images on a gold bipyramid supercrystal "slice" after FIB cutting. These experiments were performed with GBPs_3 with 2.5 mM CTAC and 64 mM Au^0.

8.4.2 Additional SERS characterization of gold bipyramids supercrystals

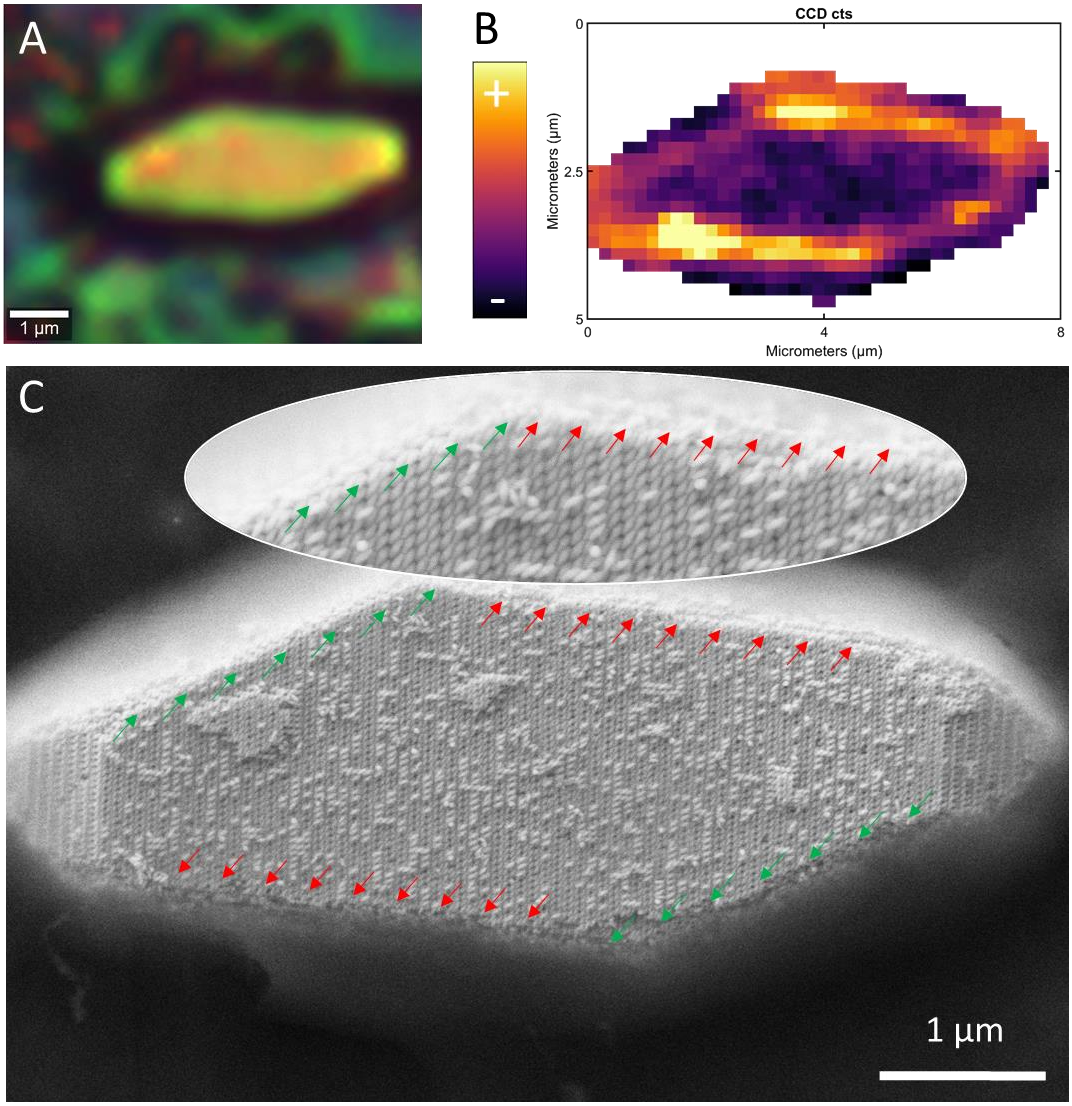

Figure 8.9 Combined spectroscopic and structural characterization of the supercrystal. A) Optical microscopy image and B) corresponding SERRS image obtained by mapping the SERRS intensity of the crystal violet vibrational peak over 1618-1632 cm^{-1}. The concentration of CV solution was 10^{-6} M, acquisition time was 100 ms, and laser power at the sample was ≈ 0.01 mW, at an excitation wavelength of 633 nm. C) SEM micrograph of a GBPs supercrystal viewed at different magnification. The arrows show the orientation of the bipyramids with the red arrows indicating the spiky facets whereas the green arrows indicate the smooth ones displaying high and low SERRS efficiency, respectively.

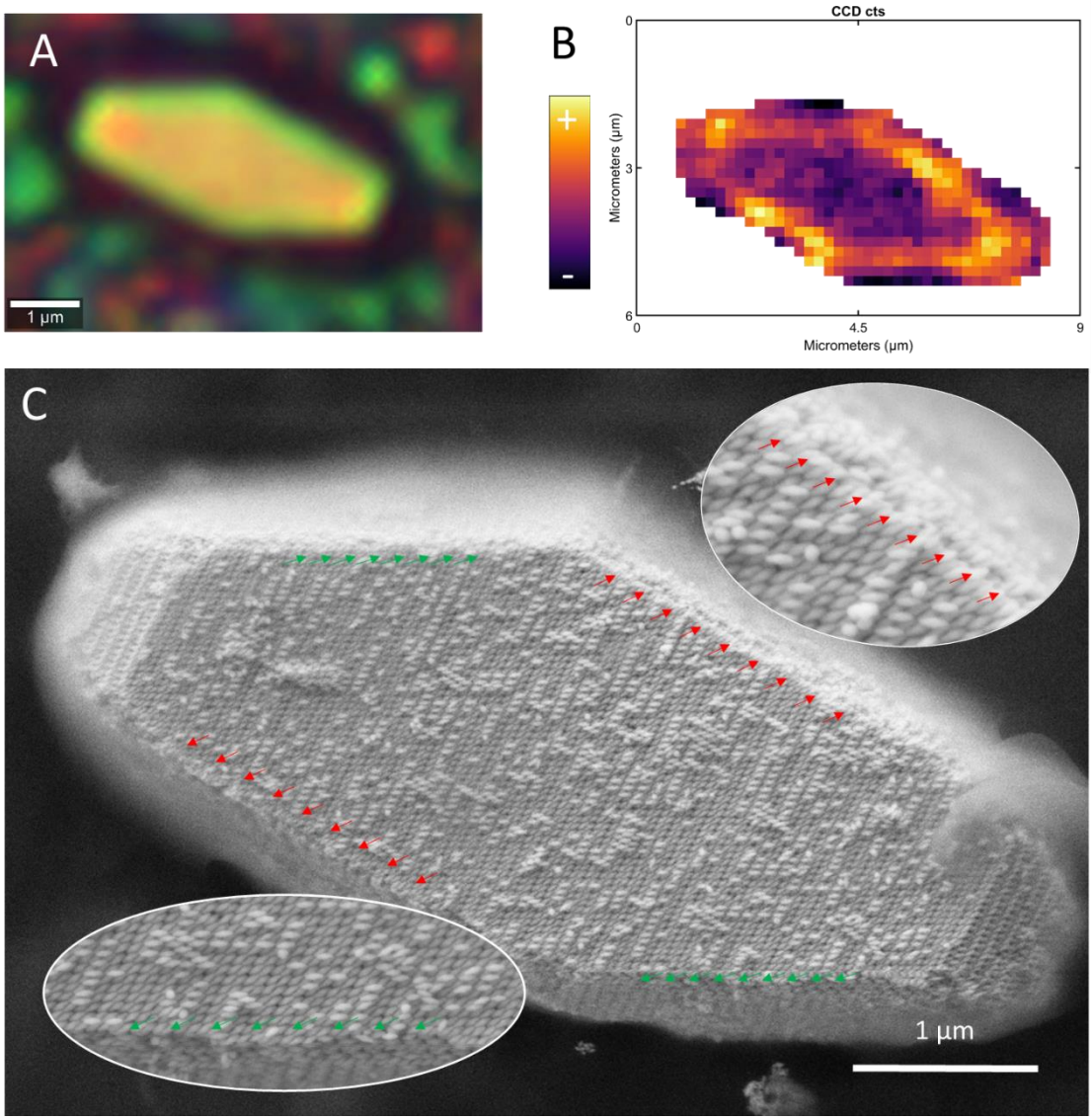

Figure 8.10 Combined spectroscopic and structural characterization of the supercrystal. A) Optical microscopy image and B) corresponding SERRS image obtained by mapping the SERRS intensity of the crystal violet vibrational peak over 1618-1632 cm^{-1}. The concentration of CV solution was 10^{-6} M, acquisition time was 100 ms, and laser power at the sample was ≈ 0.01 mW, at an excitation wavelength of 633 nm. C) SEM micrograph of a GBPs supercrystal viewed at different magnification. The arrows show the orientation of the bipyramids with the red arrows indicating the spiky facets whereas the green arrows indicate the smooth ones displaying high and low SERRS efficiency, respectively.

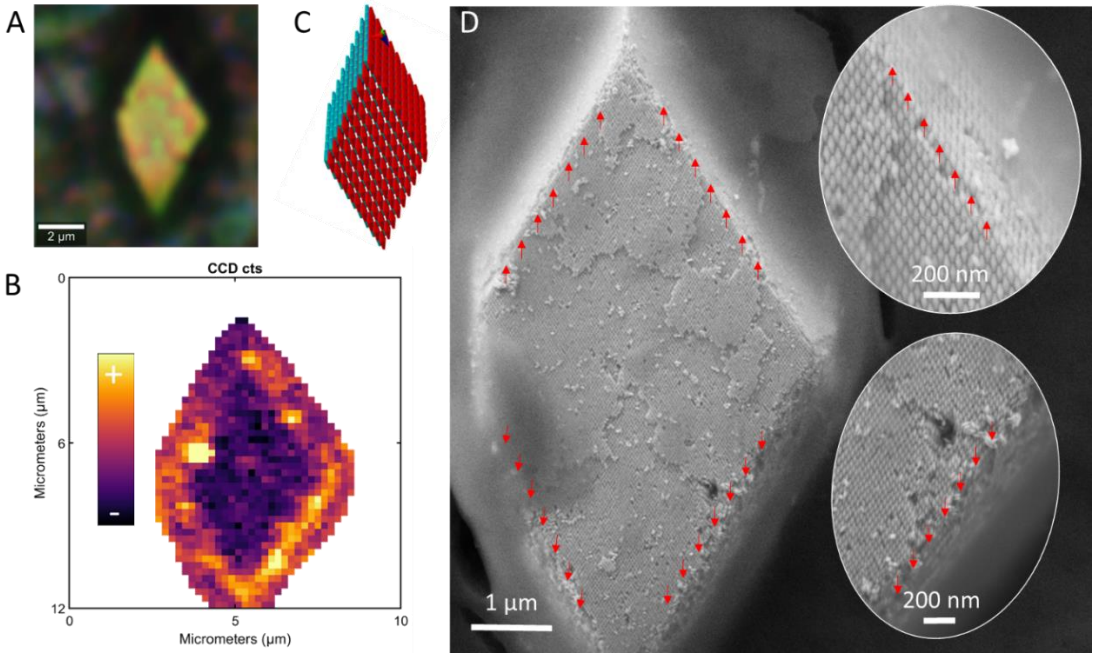

Figure 8.11 Combined spectroscopic and structural characterization of the supercrystal. A) Optical microscopy image and B) corresponding SERRS image obtained by mapping the SERRS intensity of the crystal violet vibrational peak over 1618-1632 cm^{-1}. The concentration of CV solution was 10^{-6} M, acquisition time was 100 ms, and laser power at the sample was ≈ 0.01 mW, at an excitation wavelength of 633 nm. C) Model of the triclinic lattice oriented along the $\boldsymbol{c}$ and $\boldsymbol{a} + \boldsymbol{c}$ vectors of the unit cell. D) SEM micrograph of a GBPs supercrystal viewed at different magnification. The arrows show the orientation of the bipyramids which is identical along to the four lateral facets and displays similar SERRS efficiency.

List of Figures

List of Tables

Bibliography

(1) Hornyak, G. L.; Tibbals, H. F.; Dutta, J.; Moore, J. J. *Introduction to Nanoscience and Nanotechnology*, 1st ed.; CRC Press, 2008.

(2) Corbett, J.; McKeown, P. A.; Peggs, G. N.; Whatmore, R. Nanotechnology: International Developments and Emerging Products. *CIRP Annals* **2000**, *49*, 523–545.

(3) *Outputs from EPSRC Physics Grand Challenge Surveys-EPSRC Pioneering Research and Skills*; 2011.

(4) Feynman, R. P. There's Plenty of Room at the Bottom. *Eng. Sci.* **1960**, *23*, 22–36.

(5) Norio, T. On the Basic Concept of 'Nano-Technology'. *Proceedings of the International Conference on Production Engineering* **1974**, 18–23.

(6) Drexler, K. E. Molecular Engineering: An Approach to the Development of General Capabilities for Molecular Manipulation. *Proceedings of the National Academy of Sciences* **1981**, *78*, 5275–5278.

(7) Ramsden, J. *Nanotechnology: An Introduction*; Micro and nano technologies series; William Andrew/Elsevier: Oxford ; Waltham, MA, 2011.

(8) Korvink, J. G.; Greiner, A. *Semiconductors for Micro- and Nanotechnology: An Introduction for Engineers*, 1st ed.; Wiley, 2002.

(9) *National Nanotechnology Initiative Strategic Plan*; National Science and Technology Council Committee on Technology (CoT) Subcommittee on Nanoscale Science, Engineering, and Technology (NSET), 2011.

(10) Scarabelli, L. Rational synthesis and self-assembly of anisotropic plasmonic nanoparticles. http://purl.org/dc/dcmitype/Text, Universidade de Vigo, 2016.

(11) Visaveliya, N.; Köhler, J. M. A Self-Seeding Synthesis of Ag Microrods of Tuned Aspect Ratio: Ascorbic Acid Plays a Key Role. *Nanotechnology* **2013**, *24*, 345604.

(12) Peng, Z. A.; Peng, X. Mechanisms of the Shape Evolution of CdSe Nanocrystals. *J. Am. Chem. Soc.* **2001**, *123*, 1389–1395.

(13) Haddon, R. C. Carbon Nanotubes. *Acc. Chem. Res.* **2002**, *35*, 997–997.

(14) Buffat, Ph.; Borel, J.-P. Size Effect on the Melting Temperature of Gold Particles. *Phys. Rev. A* **1976**, *13*, 2287–2298.

(15) Cao, J.; Sun, T.; Grattan, K. T. V. Gold Nanorod-Based Localized Surface Plasmon Resonance Biosensors: A Review. *Sens. Actuators B Chem.* **2014**, *195*, 332–351.

(16) Scarabelli, L.; Sánchez-Iglesias, A.; Pérez-Juste, J.; Liz-Marzán, L. M. A "Tips and Tricks" Practical Guide to the Synthesis of Gold Nanorods. *J. Phys. Chem. Lett.* **2015**, *6*, 4270–4279.

(17) Ward, C. J.; Tronndorf, R.; Eustes, A. S.; Auad, M. L.; Davis, E. W. Seed-Mediated Growth of Gold Nanorods: Limits of Length to Diameter Ratio Control. *J. Nanomater.* **2014**, *2014*, 1–7.

(18) Wasserman, H. J.; Vermaak, J. S. On the Determination of a Lattice Contraction in Very Small Silver Particles. *Surf. Sci.* **1970**, *22*, 164–172.

(19) Goldstein, A. N.; Echer, C. M.; Alivisatos, A. P. Melting in Semiconductor Nanocrystals. *Science* **1992**, *256*, 1425–1427.

(20) De Aberasturi, D. J.; Serrano-Montes, A. B.; Liz-Marzán, L. M. Modern Applications of Plasmonic Nanoparticles: From Energy to Health. *Adv. Opt. Mater.* **2015**, *3*, 602–617.

(21) Chen, H.; Shao, L.; Li, Q.; Wang, J. Gold Nanorods and Their Plasmonic Properties. *Chem. Soc. Rev.* **2013**, *42*, 2679–2724.
(22) Lohse, S. E.; Murphy, C. J. Applications of Colloidal Inorganic Nanoparticles: From Medicine to Energy. *J. Am. Chem. Soc.* **2012**, *134*, 15607–15620.
(23) Li, N.; Zhao, P.; Astruc, D. Anisotropic Gold Nanoparticles: Synthesis, Properties, Applications, and Toxicity. *Angew. Chem. Int. Ed.* **2014**, *53* (7), 1756–1789.
(24) Liz-Marzán, L. M. *Colloidal Synthesis of Plasmonic Nanometals*, 1st ed.; Jenny Stanford Publishing, 2020.
(25) Teo, B. K.; Sun, X. H. From Top-Down to Bottom-Up to Hybrid Nanotechnologies: Road to Nanodevices. *J Clust Sci* **2006**, *17*, 529–540.
(26) Ochekpe, N. A.; Olorunfemi, P. O.; Ngwuluka, N. C. Nanotechnology and Drug Delivery Part 1: Background and Applications. *Trop. J. Pharm Res* **2009**, *8*, 265–274.
(27) Xia, Y.; Whitesides, G. M. Soft Lithography. *Annu. Rev. Mater. Sci.* **1998**, *28*, 153–184.
(28) Moore, G. E. Cramming More Components onto Integrated Circuits. *Electronics* **1965**, *38*, 114.
(29) We're not prepared for the end of Moore's Law https://www.technologyreview.com/2020/02/24/905789/were-not-prepared-for-the-end-of-moores-law/ (accessed Feb 23, 2022).
(30) *Moore's Law 40th Anniversary with Gordon Moore*; https://www.youtube.com/watch?v=MH6jUSjpr-Q, 2007.
(31) Mike, G. What is Moore's Law? https://www.synopsys.com/glossary/what-is-moores-law.html (accessed Feb 23, 2022).
(32) Van Manen, H.-J.; Auletta, T.; Dordi, B.; Schönherr, H.; Vancso, G. J.; Van Veggel, Frank. C. J. M.; Reinhoudt, David. N. Non-Covalent Chemistry on Surface-Confined, Isolated Dendrimers. *Adv. Funct. Mater.* **2002**, *12*, 811–818.
(33) Iqbal, P.; Preece, J. A.; Mendes, P. M. Nanotechnology: The "Top-Down" and "Bottom-Up" Approaches. In *Supramolecular Chemistry: From Molecules to Nanomaterials*; Gale, P. A., Steed, J. W., Eds.; John Wiley & Sons, Ltd: Chichester, UK, 2012; pp 1–14.
(34) Anderson, P. W. More Is Different. *Science* **1972**, *177*, 393–396.
(35) Reguera, J.; Langer, J.; Jiménez de Aberasturi, D.; Liz-Marzán, L. M. Anisotropic Metal Nanoparticles for Surface Enhanced Raman Scattering. *Chem. Soc. Rev.* **2017**, *46*, 3866–3885.
(36) Aberasturi, D. J. D.; Hamon, C.; Liz-Marzán, L. M. Chemical Synthesis of Plasmonic Nanoparticles. In *World Scientific Series in Nanoscience and Nanotechnology*; World Scientific, 2017; Vol. 4, pp 439–473.
(37) Ian, F.; Nigel, M.; Margaret, S.; Catherine, H. The Lycurgus Cup-A Roman Nanotechnology. *Gold Bull.* **2007**, *40*, 270–277.
(38) Hunt, L. B. The True Story of Purple of Cassius: The Birth of Gold-Based Glass and Enamel Colours. *Gold Bull.* **1976**, *9*, 134–139.
(39) Thompson, D. Michael Faraday's Recognition of Ruby Gold: The Birth of Modern Nanotechnology. *Gold Bull.* **2007**, *40*, 267–269.
(40) Tweney, R. D. Discovering Discovery: How Faraday Found the First Metallic Colloid. *Perspect Sci.* **2006**, *14*, 97–121.
(41) Michael, F. Experimental Relations of Gold (and Other Metals) to Light. *Phil. Trans. R. Soc.* **1857**, *147*, 145–181.

(42) Kelly, K. L.; Coronado, E.; Zhao, L. L.; Schatz, G. C. The Optical Properties of Metal Nanoparticles: The Influence of Size, Shape, and Dielectric Environment. *J. Phys. Chem. B* **2003**, *107*, 668–677.
(43) Hirst, L. S. *Fundamentals of Soft Matter Science*, 1st ed.; CRC Press, 2012.
(44) Willets, K. A.; Van Duyne, R. P. Localized Surface Plasmon Resonance Spectroscopy and Sensing. *Annu. Rev. Phys. Chem.* **2007**, *58*, 267–297.
(45) Amendola, V.; Pilot, R.; Frasconi, M.; Maragò, O. M.; Iatì, M. A. Surface Plasmon Resonance in Gold Nanoparticles: A Review. *J. Phys.: Condens. Matter* **2017**, *29*, 203002.
(46) Maier, S. A. *Plasmonics: Fundamentals and Applications*; Springer US: New York, NY, 2007.
(47) Kociak, M.; Stéphan, O. Mapping Plasmons at the Nanometer Scale in an Electron Microscope. *Chem. Soc. Rev.* **2014**, *43*, 3865–3883.
(48) Ashcroft, N. W.; Mermin, N. D. *Solid State Physics*; Holt, Rinehart and Winston: New York, 1976.
(49) Blaber, M. G.; Arnold, M. D.; Ford, M. J. A Review of the Optical Properties of Alloys and Intermetallics for Plasmonics. *J. Phys.: Condens. Matter* **2010**, *22*, 143201.
(50) Arnold, M. D.; Blaber, M. G. Optical Performance and Metallic Absorption in Nanoplasmonic Systems. *Opt. Express* **2009**, *17*, 3835–3847.
(51) Afrooz, A. R. M. N.; Sivalapalan, S. T.; Murphy, C. J.; Hussain, S. M.; Schlager, J. J.; Saleh, N. B. Spheres vs. Rods: The Shape of Gold Nanoparticles Influences Aggregation and Deposition Behavior. *Chemosphere* **2013**, *91*, 93–98.
(52) Eustis, S.; El-Sayed, M. A. Determination of the Aspect Ratio Statistical Distribution of Gold Nanorods in Solution from a Theoretical Fit of the Observed Inhomogeneously Broadened Longitudinal Plasmon Resonance Absorption Spectrum. *J. Appl. Phys.* **2006**, *100*, 044324.
(53) Perezjuste, J.; Pastorizasantos, I.; Lizmarzan, L.; Mulvaney, P. Gold Nanorods: Synthesis, Characterization and Applications. *Coord. Chem. Rev.* **2005**, *249*, 1870–1901.
(54) Sosa, I. O.; Noguez, C.; Barrera, R. G. Optical Properties of Metal Nanoparticles with Arbitrary Shapes. *J. Phys. Chem. B* **2003**, *107*, 6269–6275.
(55) Johnson, P. B.; Christy, R. W. Optical Constants of the Noble Metals. *Phys. Rev. B* **1972**, *6*, 4370–4379.
(56) Amendola, V. Surface Plasmon Resonance of Silver and Gold Nanoparticles in the Proximity of Graphene Studied Using the Discrete Dipole Approximation Method. *Phys. Chem. Chem. Phys.* **2016**, *18*, 2230–2241.
(57) Xia, Y.; Xiong, Y.; Lim, B.; Skrabalak, S. E. Shape-Controlled Synthesis of Metal Nanocrystals: Simple Chemistry Meets Complex Physics? *Angew. Chem. Int. Ed.* **2009**, *48*, 60–103.
(58) Jana, N. R.; Gearheart, L.; Murphy, C. J. Wet Chemical Synthesis of Silver Nanorods and Nanowires of Controllable Aspect Ratio. *Chem. Commun.* **2001**, 617–618.
(59) Sau, T. K.; Murphy, C. J. Seeded High Yield Synthesis of Short Au Nanorods in Aqueous Solution. *Langmuir* **2004**, *20*, 6414–6420.
(60) Gao, J.; Bender, C. M.; Murphy, C. J. Dependence of the Gold Nanorod Aspect Ratio on the Nature of the Directing Surfactant in Aqueous Solution. *Langmuir* **2003**, *19*, 9065–9070.

(61) Jana, N. R.; Gearheart, L.; Murphy, C. J. Seed-Mediated Growth Approach for Shape-Controlled Synthesis of Spheroidal and Rod-like Gold Nanoparticles Using a Surfactant Template. *Adv. Mater.* **2001**, *13*, 1389–1393.
(62) Link, S.; El-Sayed, M. A. Size and Temperature Dependence of the Plasmon Absorption of Colloidal Gold Nanoparticles. *J. Phys. Chem. B* **1999**, *103*, 4212–4217.
(63) Cai, J.; Raghavan, V.; Bai, Y. J.; Zhou, M. H.; Liu, X. L.; Liao, C. Y.; Ma, P.; Shi, L.; Dockery, P.; Keogh, I.; Fan, H. M.; Olivo, M. Controllable Synthesis of Tetrapod Gold Nanocrystals with Precisely Tunable Near-Infrared Plasmon Resonance towards Highly Efficient Surface Enhanced Raman Spectroscopy Bioimaging. *J. Mater. Chem. B* **2015**, *3*, 7377–7385.
(64) Xie, J.; Zhang, Q.; Lee, J. Y.; Wang, D. I. C. The Synthesis of SERS-Active Gold Nanoflower Tags for *In Vivo* Applications. *ACS Nano* **2008**, *2*, 2473–2480.
(65) Webb, J. A.; Erwin, W. R.; Zarick, H. F.; Aufrecht, J.; Manning, H. W.; Lang, M. J.; Pint, C. L.; Bardhan, R. Geometry-Dependent Plasmonic Tunability and Photothermal Characteristics of Multibranched Gold Nanoantennas. *J. Phys. Chem. C* **2014**, *118*, 3696–3707.
(66) Allgeyer, E. S.; Pongan, A.; Browne, M.; Mason, M. D. Optical Signal Comparison of Single Fluorescent Molecules and Raman Active Gold Nanostars. *Nano Lett.* **2009**, *9*, 3816–3819.
(67) Senthil Kumar, P.; Pastoriza-Santos, I.; Rodríguez-González, B.; Javier García de Abajo, F.; Liz-Marzán, L. M. High-Yield Synthesis and Optical Response of Gold Nanostars. *Nanotechnology* **2008**, *19*, 015606.
(68) Chang, Y.-X.; Zhang, N.-N.; Xing, Y.-C.; Zhang, Q.; Oh, A.; Gao, H.-M.; Zhu, Y.; Baik, H.; Kim, B.; Yang, Y.; Chang, W.-S.; Sun, T.; Zhang, J.; Lu, Z.-Y.; Lee, K.; Link, S.; Liu, K. Gold Nanotetrapods with Unique Topological Structure and Ultranarrow Plasmonic Band as Multifunctional Therapeutic Agents. *J. Phys. Chem. Lett.* **2019**, *10*, 4505–4510.
(69) Lu, L.; Burkey, G.; Halaciuga, I.; Goia, D. V. Core-Shell Gold/Silver Nanoparticles: Synthesis and Optical Properties. *J. Colloid Interface Sci.* **2013**, *392*, 90–95.
(70) Tsuji, M.; Miyamae, N.; Lim, S.; Kimura, K.; Zhang, X.; Hikino, S.; Nishio, M. Crystal Structures and Growth Mechanisms of Au@Ag Core-Shell Nanoparticles Prepared by the Microwave-Polyol Method. *Cryst. Growth Des.* **2006**, *6* (8), 1801–1807.
(71) Bhattacharjee, G.; Bhattacharya, M.; Roy, A.; Senapati, D.; Satpati, B. Core-Shell Gold@Silver Nanorods of Varying Length for High Surface-Enhanced Raman Scattering Enhancement. *ACS Appl. Nano Mater.* **2018**, *1*, 5589–5600.
(72) Hamon, C.; Goldmann, C.; Constantin, D. Controlling the Symmetry of Supercrystals Formed by Plasmonic Core-Shell Nanorods with Tunable Cross-Section. *Nanoscale* **2018**, *10*, 18362–18369.
(73) Zohar, N.; Chuntonov, L.; Haran, G. The Simplest Plasmonic Molecules: Metal Nanoparticle Dimers and Trimers. *J. Photochem. Photobiol. C: Photochem. Rev.* **2014**, *21*, 26–39.
(74) Ghosh, S. K.; Pal, T. Interparticle Coupling Effect on the Surface Plasmon Resonance of Gold Nanoparticles: From Theory to Applications. *Chem. Rev.* **2007**, *107*, 4797–4862.
(75) Dolinnyi, A. I. Nanometric Rulers Based on Plasmon Coupling in Pairs of Gold Nanoparticles. *J. Phys. Chem. C* **2015**, *119*, 4990–5001.

(76) Abtahi, S. M. H.; Burrows, N. D.; Idesis, F. A.; Murphy, C. J.; Saleh, N. B.; Vikesland, P. J. Sulfate-Mediated End-to-End Assembly of Gold Nanorods. *Langmuir* **2017**, *33*, 1486–1495.
(77) NanoComposix. Gold Nanoparticles: Optical Properties https://nanocomposix.com/pages/gold-nanoparticles-optical-properties (accessed May 4, 2020).
(78) Bao, Y.; Zhao, B.; Tang, X.; Hou, D.; Cai, J.; Tang, S.; Liu, J.; Wang, F.; Cui, T. Tuning Surface Plasmon Resonance by the Plastic Deformation of Au Nanoparticles within a Diamond Anvil Cell. *Appl. Phys. Lett.* **2015**, *107*, 201909.
(79) Zou, R.; Zhang, Q.; Zhao, Q.; Peng, F.; Wang, H.; Yu, H.; Yang, J. Thermal Stability of Gold Nanorods in an Aqueous Solution. *Colloids Surf, A Physicochem Eng Asp* **2010**, *372*, 177–181.
(80) Petrova, H.; Perez Juste, J.; Pastoriza-Santos, I.; Hartland, G. V.; Liz-Marzán, L. M.; Mulvaney, P. On the Temperature Stability of Gold Nanorods: Comparison between Thermal and Ultrafast Laser-Induced Heating. *Phys. Chem. Chem. Phys.* **2006**, *8*, 814–821.
(81) Chandra, K.; Kumar, V.; Werner, S. E.; Odom, T. W. Separation of Stabilized MOPS Gold Nanostars by Density Gradient Centrifugation. *ACS Omega* **2017**, *2*, 4878–4884.
(82) Rodríguez-Lorenzo, L.; Romo-Herrera, J. M.; Pérez-Juste, J.; Alvarez-Puebla, R. A.; Liz-Marzán, L. M. Reshaping and LSPR Tuning of Au Nanostars in the Presence of CTAB. *J. Mater. Chem.* **2011**, *21*, 11544–11549.
(83) Katrin, K. Surface-Enhanced Raman Scattering. *Phys. Today* **2007**, *60*, 40–46.
(84) Wang, Y.; Yan, B.; Chen, L. SERS Tags: Novel Optical Nanoprobes for Bioanalysis. *Chem. Rev.* **2013**, *113*, 1391–1428.
(85) Fleischmann, M.; Hendra, P. J.; Mcquillan, A. J. Raman Spectra of Pyridzne Adsorbed at a Silver Electrode. *Chem. Phys. Lett.* **1974**, *26*, 163–166.
(86) Schlücker, S. Surface-Enhanced Raman Spectroscopy: Concepts and Chemical Applications. *Angew. Chem. Int. Ed.* **2014**, *53*, 4756–4795.
(87) Yang, Y.; Shi, J.; Tanaka, T.; Nogami, M. Self-Assembled Silver Nanochains for Surface-Enhanced Raman Scattering. *Langmuir* **2007**, *23*, 12042–12047.
(88) Alvarez-Puebla, R. A.; Agarwal, A.; Manna, P.; Khanal, B. P.; Aldeanueva-Potel, P.; Carbo-Argibay, E.; Pazos-Perez, N.; Vigderman, L.; Zubarev, E. R.; Kotov, N. A.; Liz-Marzán, L. M. Gold Nanorods 3D-Supercrystals as Surface Enhanced Raman Scattering Spectroscopy Substrates for the Rapid Detection of Scrambled Prions. *Proc. Natl. Acad. Sci. USA* **2011**, *108*, 8157–8161.
(89) Lee, A.; Andrade, G. F. S.; Ahmed, A.; Souza, M. L.; Coombs, N.; Tumarkin, E.; Liu, K.; Gordon, R.; Brolo, A. G.; Kumacheva, E. Probing Dynamic Generation of Hot-Spots in Self-Assembled Chains of Gold Nanorods by Surface-Enhanced Raman Scattering. *J. Am. Chem. Soc.* **2011**, *133*, 7563–7570.
(90) Pardehkhorram, R.; Bonaccorsi, S.; Zhu, H.; Gonçales, V. R.; Wu, Y.; Liu, J.; Lee, N. A.; Tilley, R. D.; Gooding, J. J. Intrinsic and Well-Defined Second Generation Hot Spots in Gold Nanobipyramids *versus* Gold Nanorods. *Chem. Commun.* **2019**, *55*, 7707–7710.
(91) Louis, C.; Pluchery, O. *Gold Nanoparticles for Physics, Chemistry and Biology*; Imperial College Press ; Distributed by World Scientific Pub. Co: London : Singapore ; Hackensack, NJ, 2012.

(92) Turkevich, J.; Stevenson, P. C.; Hillier, J. A Study of the Nucleation and Growth Processes in the Synthesis of Colloidal Gold. *Discuss. Faraday Soc.* **1951**, *11*, 55–75.
(93) Frens, G. Controlled Nucleation for the Regulation of the Particle Size in Monodisperse Gold Suspensions. *Nat. Phys. Sci.* **1973**, *241*, 20–22.
(94) Brust, M.; Walker, M.; Bethell, D.; Schiffrin, D. J.; Whyman, R. Synthesis of Thiol-Derivatised Gold Nanoparticles in a Two-Phase Liquid-Liquid System. *J. Chem. Soc., Chem. Commun.* **1994**, 801–802.
(95) Seo, D.; Park, J. C.; Song, H. Polyhedral Gold Nanocrystals with O_h Symmetry: From Octahedra to Cubes. *J. Am. Chem. Soc.* **2006**, *128*, 14863–14870.
(96) Pastoriza-Santos, I.; Liz-Marzán, L. M. Formation of PVP-Protected Metal Nanoparticles in DMF. *Langmuir* **2002**, *18*, 2888–2894.
(97) Jana, N. R.; Gearheart, L.; Murphy, C. J. Seeding Growth for Size Control of 5-40 Nm Diameter Gold Nanoparticles. *Langmuir* **2001**, *17*, 6782–6786.
(98) Personick, M. L.; Mirkin, C. A. Making Sense of the Mayhem behind Shape Control in the Synthesis of Gold Nanoparticles. *J. Am. Chem. Soc.* **2013**, *135*, 18238–18247.
(99) Tartaj, P.; Morales, M. a del P.; Veintemillas-Verdaguer, S.; Gonz lez-Carre o, T.; Serna, C. J. The Preparation of Magnetic Nanoparticles for Applications in Biomedicine. *J. Phys. D: Appl. Phys.* **2003**, *36*, R182–R197.
(100) LaMer, V. K.; Dinegar, R. H. Theory, Production and Mechanism of Formation of Monodispersed Hydrosols. *J. Am. Chem. Soc.* **1950**, *72*, 4847–4854.
(101) Den Ouden, C. J. J.; Thompson, R. W. Analysis of the Formation of Monodisperse Populations by Homogeneous Nucleation. *J. Colloid Interface Sci.* **1991**, *143*, 77–84.
(102) Sugimoto, T.; Matijević, E. Formation of Uniform Spherical Magnetite Particles by Crystallization from Ferrous Hydroxide Gels. *J. Colloid Interface Sci.* **1980**, *74*, 227–243.
(103) Tao, A.; Kim, F.; Hess, C.; Goldberger, J.; He, R.; Sun, Y.; Xia, Y.; Yang, P. Langmuir-Blodgett Silver Nanowire Monolayers for Molecular Sensing Using Surface-Enhanced Raman Spectroscopy. *Nano Lett.* **2003**, *3*, 1229–1233.
(104) Murphy, C. J.; Sau, T. K.; Gole, A. M.; Orendorff, C. J.; Gao, J.; Gou, L.; Hunyadi, S. E.; Li, T. Anisotropic Metal Nanoparticles: Synthesis, Assembly, and Optical Applications. *J. Phys. Chem. B* **2005**, *109*, 13857–13870.
(105) Compton, O. C.; Osterloh, F. E. Evolution of Size and Shape in the Colloidal Crystallization of Gold Nanoparticles. *J. Am. Chem. Soc.* **2007**, *129*, 7793–7798.
(106) Xiong, Y.; Xia, Y. Shape-Controlled Synthesis of Metal Nanostructures: The Case of Palladium. *Adv. Mater.* **2007**, *19*, 3385–3391.
(107) Lu, X.; Rycenga, M.; Skrabalak, S. E.; Wiley, B.; Xia, Y. Chemical Synthesis of Novel Plasmonic Nanoparticles. *Annu. Rev. Phys. Chem.* **2009**, *60*, 167–192.
(108) Xia, Y.; Xia, X.; Peng, H.-C. Shape-Controlled Synthesis of Colloidal Metal Nanocrystals: Thermodynamic versus Kinetic Products. *J. Am. Chem. Soc.* **2015**, *137*, 7947–7966.
(109) Xiong, Y.; Cai, H.; Wiley, B. J.; Wang, J.; Kim, M. J.; Xia, Y. Synthesis and Mechanistic Study of Palladium Nanobars and Nanorods. *J. Am. Chem. Soc.* **2007**, *129*, 3665–3675.
(110) Xiong, Y.; Cai, H.; Yin, Y.; Xia, Y. Synthesis and Characterization of Fivefold Twinned Nanorods and Right Bipyramids of Palladium. *Chem. Phys. Lett.* **2007**, *440*, 273–278.

(111) Sánchez-Iglesias, A.; Winckelmans, N.; Altantzis, T.; Bals, S.; Grzelczak, M.; Liz-Marzán, L. M. High-Yield Seeded Growth of Monodisperse Pentatwinned Gold Nanoparticles through Thermally Induced Seed Twinning. *J. Am. Chem. Soc.* **2017**, *139*, 107–110.
(112) Xiong, Y.; McLellan, J. M.; Chen, J.; Yin, Y.; Li, Z.-Y.; Xia, Y. Kinetically Controlled Synthesis of Triangular and Hexagonal Nanoplates of Palladium and Their SPR/SERS Properties. *J. Am. Chem. Soc.* **2005**, *127*, 17118–17127.
(113) Scarabelli, L.; Grzelczak, M.; Liz-Marzán, L. M. Tuning Gold Nanorod Synthesis through Prereduction with Salicylic Acid. *Chem. Mater.* **2013**, *25*, 4232–4238.
(114) Carbó-Argibay, E.; Rodríguez-González, B.; Pastoriza-Santos, I.; Pérez-Juste, J.; Liz-Marzán, L. M. Growth of Pentatwinned Gold Nanorods into Truncated Decahedra. *Nanoscale* **2010**, *2*, 2377–2383.
(115) Khan, Z.; Singh, T.; Hussain, J. I.; Hashmi, A. A. Au(III)-CTAB Reduction by Ascorbic Acid: Preparation and Characterization of Gold Nanoparticles. *Colloids Surf. B: Biointerfaces* **2013**, *104*, 11–17.
(116) Zümreoglu-Karan, B. A Rationale on the Role of Intermediate Au(III)-Vitamin C Complexation in the Production of Gold Nanoparticles. *J. Nanopart Res.* **2009**, *11*, 1099–1105.
(117) Tu, Y.-J.; Njus, D.; Schlegel, H. B. A Theoretical Study of Ascorbic Acid Oxidation and $\mathbf{HOO}^{\cdot}/\mathbf{O}_2^{\cdot-}$ Radical Scavenging. *Org. Biomol. Chem.* **2017**, *15*, 4417–4431.
(118) Gramlich, G.; Zhang, J.; Nau, W. M. Increased Antioxidant Reactivity of Vitamin C at Low PH in Model Membranes. *J. Am. Chem. Soc.* **2002**, *124*, 11252–11253.
(119) Langille, M. R.; Personick, M. L.; Zhang, J.; Mirkin, C. A. Defining Rules for the Shape Evolution of Gold Nanoparticles. *J. Am. Chem. Soc.* **2012**, *134* (35), 14542–14554.
(120) Rodríguez-Fernández, J.; Pérez-Juste, J.; Mulvaney, P.; Liz-Marzán, L. M. Spatially-Directed Oxidation of Gold Nanoparticles by Au(III)-CTAB Complexes. *J. Phys. Chem. B* **2005**, *109*, 14257–14261.
(121) Brown, L. S.; Holme, T. A. *Chemistry for Engineering Students*, 2nd ed.; Brooks/Cole Cengage Learning: Belmont, Calif, 2011.
(122) Magnussen, O. M. Ordered Anion Adlayers on Metal Electrode Surfaces. *Chem. Rev.* **2002**, *102*, 679–726.
(123) Woehl, T. J.; Abellan, P. Defining the Radiation Chemistry during Liquid Cell Electron Microscopy to Enable Visualization of Nanomaterial Growth and Degradation Dynamics. *J. Microsc.* **2017**, *265*, 135–147.
(124) Personick, M. L.; Langille, M. R.; Zhang, J.; Mirkin, C. A. Shape Control of Gold Nanoparticles by Silver Underpotential Deposition. *Nano Lett.* **2011**, *11*, 3394–3398.
(125) Carbó-Argibay, E.; Rodríguez-González, B.; Gómez-Graña, S.; Guerrero-Martínez, A.; Pastoriza-Santos, I.; Pérez-Juste, J.; Liz-Marzán, L. M. The Crystalline Structure of Gold Nanorods Revisited: Evidence for Higher-Index Lateral Facets. *Angew. Chem. Int. Ed.* **2010**, *49*, 9397–9400.
(126) Lee, J.; Oh, I.; Hwang, S.; Kwak, J. Scanning Tunneling Microscopy Investigation of Silver Deposition upon Au(111) in the Presence of Chloride. *Langmuir* **2002**, *18*, 8025–8032.

(127) Aberasturi, D. J. D.; Hamon, C.; Liz-Marzán, L. M. Chemical Synthesis of Plasmonic Nanoparticles. In *World Scientific Series in Nanoscience and Nanotechnology*; World Scientific, 2017; Vol. 4, pp 439–473.
(128) Gómez-Graña, S.; Goris, B.; Altantzis, T.; Fernández-López, C.; Carbó-Argibay, E.; Guerrero-Martínez, A.; Almora-Barrios, N.; López, N.; Pastoriza-Santos, I.; Pérez-Juste, J.; Bals, S.; Van Tendeloo, G.; Liz-Marzán, L. M. Au@Ag Nanoparticles: Halides Stabilize {100} Facets. *J. Phys. Chem. Lett.* **2013**, *4*, 2209–2216.
(129) Bhattacharjee, G.; Majumder, S.; Senapati, D.; Banerjee, S.; Satpati, B. Core-Shell Gold@silver Hollow Nanocubes for Higher SERS Enhancement and Non-Enzymatic Biosensor. *Mater. Chem. Phys.* **2020**, *239*, 122113.
(130) Mayer, M.; Scarabelli, L.; March, K.; Altantzis, T.; Tebbe, M.; Kociak, M.; Bals, S.; García de Abajo, F. J.; Fery, A.; Liz-Marzán, L. M. Controlled Living Nanowire Growth: Precise Control over the Morphology and Optical Properties of AgAuAg Bimetallic Nanowires. *Nano Lett.* **2015**, *15*, 5427–5437.
(131) Zhuo, X.; Zhu, X.; Li, Q.; Yang, Z.; Wang, J. Gold Nanobipyramid-Directed Growth of Length-Variable Silver Nanorods with Multipolar Plasmon Resonances. *ACS Nano* **2015**, *9*, 7523–7535.
(132) Li, W.; Kanyo, I.; Kuo, C.-H.; Thanneeru, S.; He, J. PH-Programmable Self-Assembly of Plasmonic Nanoparticles: Hydrophobic Interaction versus Electrostatic Repulsion. *Nanoscale* **2015**, *7*, 956–964.
(133) Chen, Y.; Fu, J.; Ng, K. C.; Tang, Y.; Cheng, W. Free-Standing Polymer-Nanoparticle Superlattice Sheets Self-Assembled at the Air-Liquid Interface. *Cryst. Growth Des.* **2011**, *11*, 4742–4746.
(134) Lin, S.; Lin, X.; Han, S.; Zhao, H.; Hasi, W.; Wang, L. Highly Monodisperse Au@Ag Nanospheres: Synthesis by Controlled Etching Route and Size-Dependent SERS Performance of Their Surperlattices. *Nanotechnology* **2019**, *30*, 215601.
(135) Nie, Z.; Petukhova, A.; Kumacheva, E. Properties and Emerging Applications of Self-Assembled Structures Made from Inorganic Nanoparticles. *Nat. Nanotechnol.* **2010**, *5*, 15–25.
(136) Self-Assembly-Wikipedia https://en.wikipedia.org/wiki/Self-assembly (accessed Jan 13, 2022).
(137) Whitesides, G. M.; Grzybowski, B. Self-Assembly at All Scales. *Science* **2002**, *295*, 2418–2421.
(138) Grzelczak, M.; Vermant, J.; Furst, E. M.; Liz-Marzán, L. M. Directed Self-Assembly of Nanoparticles. *ACS Nano* **2010**, *4*, 3591–3605.
(139) Chen, L.; Su, B.; Jiang, L. Recent Advances in One-Dimensional Assembly of Nanoparticles. *Chem. Soc. Rev.* **2018**, *48*, 8–21.
(140) Sánchez-Iglesias, A.; Grzelczak, M.; Altantzis, T.; Goris, B.; Pérez-Juste, J.; Bals, S.; Van Tendeloo, G.; Donaldson, S. H.; Chmelka, B. F.; Israelachvili, J. N.; Liz-Marzán, L. M. Hydrophobic Interactions Modulate Self-Assembly of Nanoparticles. *ACS Nano* **2012**, *6*, 11059–11065.
(141) Grzybowski, B. A. Charged Nanoparticles Crystallizing and Controlling Crystallization: From Coatings to Nanoparticle Surfactants to Chemical Amplifiers. *CrystEngComm* **2014**, *16*, 9368–9380.
(142) Baranov, D.; Fiore, A.; van Huis, M.; Giannini, C.; Falqui, A.; Lafont, U.; Zandbergen, H.; Zanella, M.; Cingolani, R.; Manna, L. Assembly of Colloidal Semiconductor Nanorods in Solution by Depletion Attraction. *Nano Lett.* **2010**, *10*, 743–749.

(143) Carroll, J. B.; Frankamp, B. L.; Rotello, V. M. Self-Assembly of Gold Nanoparticles through Tandem Hydrogen Bonding and Polyoligosilsequioxane (POSS)-POSS Recognition Processes. *Chem. Commun.* **2002**, *17*, 1892–1893.
(144) Huo, Q.; Worden, J. G. Monofunctional Gold Nanoparticles: Synthesis and Applications. *J. Nanopart. Res.* **2007**, *9*, 1013–1025.
(145) Jones, M. R.; Macfarlane, R. J.; Lee, B.; Zhang, J.; Young, K. L.; Senesi, A. J.; Mirkin, C. A. DNA-Nanoparticle Superlattices Formed from Anisotropic Building Blocks. *Nat. Mater.* **2010**, *9*, 913–917.
(146) Wang, L.; Zhu, Y.; Xu, L.; Chen, W.; Kuang, H.; Liu, L.; Agarwal, A.; Xu, C.; Kotov, N. A. Side-by-Side and End-to-End Gold Nanorod Assemblies for Environmental Toxin Sensing. *Angew. Chem. Int. Ed.* **2010**, *49*, 5472–5475.
(147) Salant, A.; Amitay-Sadovsky, E.; Banin, U. Directed Self-Assembly of Gold-Tipped CdSe Nanorods. *J. Am. Chem. Soc.* **2006**, *128*, 10006–10007.
(148) Sharma, N.; Top, A.; Kiick, K. L.; Pochan, D. J. One-Dimensional Gold Nanoparticle Arrays by Electrostatically Directed Organization Using Polypeptide Self-Assembly. *Angew. Chem. Int. Ed.* **2009**, *48*, 7078–7082.
(149) Hu, Y.; He, L.; Yin, Y. Magnetically Responsive Photonic Nanochains. *Angew. Chem. Int. Ed.* **2011**, *123*, 3831–3834.
(150) Bai, J.; Huang, S.; Wang, L.; Chen, Y.; Huang, Y. Fluid Assisted Assembly of One-Dimensional Nanoparticle Array inside Inorganic Nanotubes. *J. Mater. Chem.* **2009**, *19*, 921–923.
(151) Dong, D.; Fu, R.; Shi, Q.; Cheng, W. Self-Assembly and Characterization of 2D Plasmene Nanosheets. *Nat. Protoc.* **2019**, *14*, 2691–2706.
(152) Reichhelm, A.; Haubold, D.; Eychmüller, A. Ligand Versatility in Supercrystal Formation. *Adv. Funct. Mater.* **2017**, *27*, 1700361.
(153) Deng, K.; Luo, Z.; Tan, L.; Quan, Z. Self-Assembly of Anisotropic Nanoparticles into Functional Superstructures. *Chem. Soc. Rev.* **2020**, *49*, 6002–6038.
(154) Li, R.; Bian, K.; Wang, Y.; Xu, H.; Hollingsworth, J. A.; Hanrath, T.; Fang, J.; Wang, Z. An Obtuse Rhombohedral Superlattice Assembled by Pt Nanocubes. *Nano Lett.* **2015**, *15*, 6254–6260.
(155) Klinkova, A.; Choueiri, R. M.; Kumacheva, E. Self-Assembled Plasmonic Nanostructures. *Chem. Soc. Rev.* **2014**, *43*, 3976–3991.
(156) Rycenga, M.; Camargo, P. H. C.; Xia, Y. Template-Assisted Self-Assembly: A Versatile Approach to Complex Micro- and Nanostructures. *Soft Matter* **2009**, *5*, 1129–1136.
(157) Scarabelli, L.; Hamon, C.; Liz-Marzán, L. M. Design and Fabrication of Plasmonic Nanomaterials Based on Gold Nanorod Supercrystals. *Chem. Mater.* **2017**, *29*, 15–25.
(158) Su, B.; Wu, Y.; Tang, Y.; Chen, Y.; Cheng, W.; Jiang, L. Free-Standing 1D Assemblies of Plasmonic Nanoparticles. *Adv. Mater.* **2013**, *25*, 3968–3972.
(159) Liu, M.; Guyot-Sionnest, P.; Lee, T.-W.; Gray, S. K. Optical Properties of Rodlike and Bipyramidal Gold Nanoparticles from Three-Dimensional Computations. *Phys. Rev. B* **2007**, *76*, 235428.
(160) Jain, P. K.; Eustis, S.; El-Sayed, M. A. Plasmon Coupling in Nanorod Assemblies: Optical Absorption, Discrete Dipole Approximation Simulation, and Exciton-Coupling Model. *J. Phys. Chem. B* **2006**, *110*, 18243–18253.
(161) Funston, A. M.; Novo, C.; Davis, T. J.; Mulvaney, P. Plasmon Coupling of Gold Nanorods at Short Distances and in Different Geometries. *Nano Lett.* **2009**, *9*, 1651–1658.

(162) Zhong, L.; Zhou, X.; Bao, S.; Shi, Y.; Wang, Y.; Hong, S.; Huang, Y.; Wang, X.; Xie, Z.; Zhang, Q. Rational Design and SERS Properties of Side-by-Side, End-to-End and End-to-Side Assemblies of Au Nanorods. *J. Mater. Chem.* **2011**, *21*, 14448.
(163) Liu, S.; Tok, J. B.-H.; Locklin, J.; Bao, Z. Assembly and Alignment of Metallic Nanorods on Surfaces with Patterned Wettability. *Small* **2006**, *2*, 1448–1453.
(164) Wang, K.; Jin, S.-M.; Xu, J.; Liang, R.; Shezad, K.; Xue, Z.; Xie, X.; Lee, E.; Zhu, J. Electric-Field-Assisted Assembly of Polymer-Tethered Gold Nanorods in Cylindrical Nanopores. *ACS Nano* **2016**, *10*, 4954–4960.
(165) Wang, Y.; Li, Y. F.; Wang, J.; Sang, Y.; Huang, C. Z. End-to-End Assembly of Gold Nanorods by Means of Oligonucleotide-Mercury(II) Molecular Recognition. *Chem. Commun.* **2010**, *46*, 1332–1334.
(166) Li, M.; Johnson, S.; Guo, H.; Dujardin, E.; Mann, S. A Generalized Mechanism for Ligand-Induced Dipolar Assembly of Plasmonic Gold Nanoparticle Chain Networks. *Adv. Funct. Mater.* **2011**, *21*, 851–859.
(167) Liu, K.; Resetco, C.; Kumacheva, E. Salt-Mediated Kinetics of the Self-Assembly of Gold Nanorods End-Tethered with Polymer Ligands. *Nanoscale* **2012**, *4*, 6574–6580.
(168) Kawabe, Y.; Yoshikawa, T.; Chida, T.; Tada, K.; Kawamoto, M.; Fujihara, T.; Sassa, T.; Tsutsumi, N. Absorption Spectrum Analysis Based on Singular Value Decomposition for Photoisomerization and Photodegradation in Organic Dyes; Toulouse, France, 2015; p 96520V.
(169) Shrager, R. I. Chemical Transitions Measured by Spectra and Resolved Using Singular Value Decomposition. *Chemometr. Intell. Lab. Syst.* **1986**, *1*, 59–70.
(170) Elgeti, M.; Ritter, E.; Bartl, F. J. New Insights into Light-Induced Deactivation of Active Rhodopsin by SVD and Global Analysis of Time-Resolved UV/Vis- and FTIR-Data. *Z. Phys. Chem.* **2008**, *222*, 1117–1129.
(171) Si, K. J.; Sikdar, D.; Chen, Y.; Eftekhari, F.; Xu, Z.; Tang, Y.; Xiong, W.; Guo, P.; Zhang, S.; Lu, Y.; Bao, Q.; Zhu, W.; Premaratne, M.; Cheng, W. Giant Plasmene Nanosheets, Nanoribbons, and Origami. *ACS Nano* **2014**, *8*, 11086–11093.
(172) Cargnello, M.; Johnston-Peck, A. C.; Diroll, B. T.; Wong, E.; Datta, B.; Damodhar, D.; Doan-Nguyen, V. V. T.; Herzing, A. A.; Kagan, C. R.; Murray, C. B. Substitutional Doping in Nanocrystal Superlattices. *Nature* **2015**, *524*, 450–453.
(173) Courty, A.; Mermet, A.; Albouy, P. A.; Duval, E.; Pileni, M. P. Vibrational Coherence of Self-Organized Silver Nanocrystals in f.c.c. Supra-Crystals. *Nat. Mater.* **2005**, *4*, 395–398.
(174) Mueggenburg, K. E.; Lin, X.-M.; Goldsmith, R. H.; Jaeger, H. M. Elastic Membranes of Close-Packed Nanoparticle Arrays. *Nat. Mater.* **2007**, *6*, 656–660.
(175) Dong, A.; Chen, J.; Vora, P. M.; Kikkawa, J. M.; Murray, C. B. Binary Nanocrystal Superlattice Membranes Self-Assembled at the Liquid-Air Interface. *Nature* **2010**, *466*, 474–477.
(176) Ng, K. C.; Udagedara, I. B.; Rukhlenko, I. D.; Chen, Y.; Tang, Y.; Premaratne, M.; Cheng, W. Free-Standing Plasmonic-Nanorod Superlattice Sheets. *ACS Nano* **2012**, *6*, 925–934.
(177) Desireddy, A.; Joshi, C. P.; Sestak, M.; Little, S.; Kumar, S.; Podraza, N. J.; Marsillac, S.; Collins, R. W.; Bigioni, T. P. Wafer-Scale Self-Assembled Plasmonic Thin Films. *Thin Solid Films* **2011**, *519*, 6077–6084.

(178) Cheng, W.; Campolongo, M. J.; Cha, J. J.; Tan, S. J.; Umbach, C. C.; Muller, D. A.; Luo, D. Free-Standing Nanoparticle Superlattice Sheets Controlled by DNA. *Nat. Mater.* **2009**, *8*, 519–525.
(179) Tao, A.; Sinsermsuksakul, P.; Yang, P. Tunable Plasmonic Lattices of Silver Nanocrystals. *Nature Nanotech.* **2007**, *2*, 435–440.
(180) Srivastava, S.; Nykypanchuk, D.; Fukuto, M.; Halverson, J. D.; Tkachenko, A. V.; Yager, K. G.; Gang, O. Two-Dimensional DNA-Programmable Assembly of Nanoparticles at Liquid Interfaces. *J. Am. Chem. Soc.* **2014**, *136*, 8323–8332.
(181) Zhang, H.; Wang, W.; Mallapragada, S.; Travesset, A.; Vaknin, D. Macroscopic and Tunable Nanoparticle Superlattices. *Nanoscale* **2017**, *9*, 164–171.
(182) Reincke, F.; Hickey, S. G.; Kegel, W. K.; Vanmaekelbergh, D. Spontaneous Assembly of a Monolayer of Charged Gold Nanocrystals at the Water/Oil Interface. *Angew. Chem. Int. Ed.* **2004**, *43*, 458–462.
(183) Shi, Q.; Sikdar, D.; Fu, R.; Si, K. J.; Dong, D.; Liu, Y.; Premaratne, M.; Cheng, W. 2D Binary Plasmonic Nanoassemblies with Semiconductor n/p-Doping-Like Properties. *Adv. Mater.* **2018**, *30*, 1801118.
(184) Si, K. J.; Sikdar, D.; Yap, L. W.; Foo, J. K. K.; Guo, P.; Shi, Q.; Premaratne, M.; Cheng, W. Dual-Coded Plasmene Nanosheets as Next-Generation Anticounterfeit Security Labels. *Adv. Opt. Mater.* **2015**, *3*, 1710–1717.
(185) Shi, Q.; Si, K. J.; Sikdar, D.; Yap, L. W.; Premaratne, M.; Cheng, W. Two-Dimensional Bipyramid Plasmonic Nanoparticle Liquid Crystalline Superstructure with Four Distinct Orientational Packing Orders. *ACS Nano* **2016**, *10*, 967–976.
(186) Dong, D.; Yap, L. W.; Smilgies, D. M.; Si, K. J.; Shi, Q.; Cheng, W. Two-Dimensional Gold Trisoctahedron Nanoparticle Superlattice Sheets: Self-Assembly, Characterization and Immunosensing Applications. *Nanoscale* **2018**, *10*, 5065–5071.
(187) Choi, J. J.; Bealing, C. R.; Bian, K.; Hughes, K. J.; Zhang, W.; Smilgies, D.-M.; Hennig, R. G.; Engstrom, J. R.; Hanrath, T. Controlling Nanocrystal Superlattice Symmetry and Shape-Anisotropic Interactions through Variable Ligand Surface Coverage. *J. Am. Chem. Soc.* **2011**, *133*, 3131–3138.
(188) Young, K. L.; Jones, M. R.; Zhang, J.; Macfarlane, R. J.; Esquivel-Sirvent, R.; Nap, R. J.; Wu, J.; Schatz, G. C.; Lee, B.; Mirkin, C. A. Assembly of Reconfigurable One-Dimensional Colloidal Superlattices Due to a Synergy of Fundamental Nanoscale Forces. *Proc. Natl. Acad. Sci. USA* **2012**, *109*, 2240–2245.
(189) Gurunatha, Kargal. L.; Marvi, S.; Arya, G.; Tao, A. R. Computationally Guided Assembly of Oriented Nanocubes by Modulating Grafted Polymer-Surface Interactions. *Nano Lett.* **2015**, *15*, 7377–7382.
(190) Wang, Z.; Bian, K.; Nagaoka, Y.; Fan, H.; Cao, Y. C. Regulating Multiple Variables To Understand the Nucleation and Growth and Transformation of PbS Nanocrystal Superlattices. *J. Am. Chem. Soc.* **2017**, *139*, 14476–14482.
(191) Bodnarchuk, M. I.; Kovalenko, M. V.; Pichler, S.; Fritz-Popovski, G.; Hesser, G.; Heiss, W. Large-Area Ordered Superlattices from Magnetic Wüstite/Cobalt Ferrite Core/Shell Nanocrystals by Doctor Blade Casting. *ACS Nano* **2010**, *4*, 423–431.
(192) Liang, Y.; Xie, Y.; Chen, D.; Guo, C.; Hou, S.; Wen, T.; Yang, F.; Deng, K.; Wu, X.; Smalyukh, I. I.; Liu, Q. Symmetry Control of Nanorod Superlattice Driven by a Governing Force. *Nat Commun* **2017**, *8*, 1410.

(193) Paik, T.; Ko, D.-K.; Gordon, T. R.; Doan-Nguyen, V.; Murray, C. B. Studies of Liquid Crystalline Self-Assembly of GdF_3 Nanoplates by In-Plane, Out-of-Plane SAXS. *ACS Nano* **2011**, *5*, 8322–8330.
(194) Ji, F.; Zhong, Q.; Chen, J.; Chen, L.; Hu, H.; Liu, Q.; Yang, P.; Yu, J.; Jiang, L.; Xu, Y.; Gross, E.; Zhang, Q. High-Yield Synthesis of Au@Ag Right Bipyramids and Self-Assembly into Four-Leaf-Clover-like Structures. *Part. Part. Syst. Charact.* **2018**, *35*, 1700114.
(195) Gong, J.; Newman, R. S.; Engel, M.; Zhao, M.; Bian, F.; Glotzer, S. C.; Tang, Z. Shape-Dependent Ordering of Gold Nanocrystals into Large-Scale Superlattices. *Nat. Commun.* **2017**, *8*, 14038.
(196) Frenkel, D. Order through Entropy. *Nat. Mater.* **2015**, *14*, 9–12.
(197) Xia, Y.; Gilroy, K. D.; Peng, H.-C.; Xia, X. Seed-Mediated Growth of Colloidal Metal Nanocrystals. *Angew. Chem. Int. Ed.* **2017**, *56*, 60–95.
(198) Ming, T.; Kou, X.; Chen, H.; Wang, T.; Tam, H.-L.; Cheah, K.-W.; Chen, J.-Y.; Wang, J. Ordered Gold Nanostructure Assemblies Formed By Droplet Evaporation. *Angew. Chem. Int. Ed.* **2008**, *47*, 9685–9690.
(199) Dreaden, E. C.; Alkilany, A. M.; Huang, X.; Murphy, C. J.; El-Sayed, M. A. The Golden Age: Gold Nanoparticles for Biomedicine. *Chem. Soc. Rev.* **2012**, *41*, 2740–2779.
(200) Lohse, S. E.; Murphy, C. J. The Quest for Shape Control: A History of Gold Nanorod Synthesis. *Chem. Mater.* **2013**, *25*, 1250–1261.
(201) Grzelczak, M.; Pérez-Juste, J.; Mulvaney, P.; Liz-Marzán, L. M. Shape Control in Gold Nanoparticle Synthesis. *Chem. Soc. Rev.* **2008**, *37*, 1783–1791.
(202) Murphy, C. J.; Thompson, L. B.; Alkilany, A. M.; Sisco, P. N.; Boulos, S. P.; Sivapalan, S. T.; Yang, J. A.; Chernak, D. J.; Huang, J. The Many Faces of Gold Nanorods. *J. Phys. Chem. Lett.* **2010**, *1*, 2867–2875.
(203) Chanana, M.; Liz-Marzán, L. M. Coating Matters: The Influence of Coating Materials on the Optical Properties of Gold Nanoparticles. *Nanophotonics* **2012**, *1*, 199–220.
(204) Ye, X.; Jin, L.; Caglayan, H.; Chen, J.; Xing, G.; Zheng, C.; Doan-Nguyen, V.; Kang, Y.; Engheta, N.; Kagan, C. R.; Murray, C. B. Improved Size-Tunable Synthesis of Monodisperse Gold Nanorods through the Use of Aromatic Additives. *ACS Nano* **2012**, *6*, 2804–2817.
(205) Lee, J.-H.; Gibson, K. J.; Chen, G.; Weizmann, Y. Bipyramid-Templated Synthesis of Monodisperse Anisotropic Gold Nanocrystals. *Nat. Commun.* **2015**, *6*, 7571.
(206) Hanske, C.; González-Rubio, G.; Hamon, C.; Formentín, P.; Modin, E.; Chuvilin, A.; Guerrero-Martínez, A.; Marsal, L. F.; Liz-Marzán, L. M. Large-Scale Plasmonic Pyramidal Supercrystals via Templated Self-Assembly of Monodisperse Gold Nanospheres. *J. Phys. Chem. C* **2017**, *121*, 10899–10906.
(207) Park, K.; Drummy, L. F.; Vaia, R. A. Ag Shell Morphology on Au Nanorod Core: Role of Ag Precursor Complex. *J. Mater. Chem.* **2011**, *21*, 15608–15618.
(208) Haidar, I.; Day, A.; Decorse, P.; Lau-Truong, S.; Chevillot-Biraud, A.; Aubard, J.; Félidj, N.; Boubekeur-Lecaque, L. Tailoring the Shape of Anisotropic Core-Shell Au-Ag Nanoparticles in Dimethyl Sulfoxide. *Chem. Mater.* **2019**, *31*, 2741–2749.
(209) Hendel, T.; Wuithschick, M.; Kettemann, F.; Birnbaum, A.; Rademann, K.; Polte, J. In Situ Determination of Colloidal Gold Concentrations with UV-Vis Spectroscopy: Limitations and Perspectives. *Anal. Chem.* **2014**, *86*, 11115–11124.

(210) Egerton, R. F. Electron Energy-Loss Spectroscopy in the TEM. *Rep. Prog. Phys.* **2009**, *72*, 016502.
(211) Kröger, R.; Bilton, M.; Scullion, M.; Roncal-Herrero, T.; Verch, A. Microscopy & Microtechniques. 3.
(212) Tubus, B. *Schematic View of STEM Mode-By Black Tubus - File:STEM Fig.Tif, CC BY-SA 4.0, Https://Commons.Wikimedia.Org/w/Index.Php?Curid=73810330*; 2017.
(213) Alloyeau, D.; Dachraoui, W.; Javed, Y.; Belkahla, H.; Wang, G.; Lecoq, H.; Ammar, S.; Ersen, O.; Wisnet, A.; Gazeau, F.; Ricolleau, C. Unravelling Kinetic and Thermodynamic Effects on the Growth of Gold Nanoplates by Liquid Transmission Electron Microscopy. *Nano Lett.* **2015**, *15*, 2574–2581.
(214) Piffoux, M.; Ahmad, N.; Nelayah, J.; Wilhelm, C.; Silva, A.; Gazeau, F.; Alloyeau, D. Monitoring the Dynamics of Cell-Derived Extracellular Vesicles at the Nanoscale by Liquid-Cell Transmission Electron Microscopy. *Nanoscale* **2018**, *10*, 1234–1244.
(215) Khelfa, A.; Byun, C.; Nelayah, J.; Wang, G.; Ricolleau, C.; Alloyeau, D. Structural Analysis of Single Nanoparticles in Liquid by Low-Dose STEM Nanodiffraction. *Micron* **2019**, *116*, 30–35.
(216) Li, T.; Senesi, A. J.; Lee, B. Small Angle X-Ray Scattering for Nanoparticle Research. *Chem. Rev.* **2016**, *116*, 11128–11180.
(217) Boldon, L.; Laliberte, F.; Liu, L. Review of the Fundamental Theories behind Small Angle X-Ray Scattering, Molecular Dynamics Simulations, and Relevant Integrated Application. *Nano Rev.* **2015**, *6*, 25661.
(218) Barré, L. Contribution of Small-Angle X-Ray and Neutron Scattering (SAXS and SANS) to the Characterization of Natural Nanomaterials. In *X-ray and Neutron Techniques for Nanomaterials Characterization*; Springer, Berlin, Heidelberg, 2016; pp 665–716.
(219) Oleg Gang. *Small Angle X-Ray Scattering (SAXS) from Bulks and Surfaces.*; BNL Online Course 2020: Advanced Synchrotron and Electron Techniques and Applications.; https://www.youtube.com/watch?v=Ys626SamlfA, 2020.
(220) What is measured in a Small Angle X-ray Scattering (SAXS) ? http://iramis.cea.fr/en/Phocea/Vie_des_labos/Ast/ast_sstechnique.php?id_ast=1065 (accessed Apr 27, 2020).
(221) Kline, S. R. Reduction and Analysis of SANS and USANS Data Using IGOR Pro. *J. Appl. Cryst.* **2006**, *39*, 895–900.
(222) Ilavsky, J. *Nika* : Software for Two-Dimensional Data Reduction. *J. Appl. Crystallogr.* **2012**, *45*, 324–328.
(223) Merrifield, R. C.; Stephan, C.; Lead, J. R. Single-Particle Inductively Coupled Plasma Mass Spectroscopy Analysis of Size and Number Concentration in Mixtures of Monometallic and Bimetallic (Core-Shell) Nanoparticles. *Talanta* **2017**, *162*, 130–134.
(224) Pollard, W. B. XIV.—The Action of Aqua Regia on Gold-Silver Alloys in the Presence of Ammonium Salts. *J. Chem. Soc., Trans.* **1920**, *117*, 99–103.
(225) Duboisset, J.; Brevet, P.-F. Second-Harmonic Scattering-Defined Topological Classes for Nano-Objects. *J. Phys. Chem. C* **2019**, *123*, 25303–25308.
(226) Costabel, M. Principles of Boundary Element Methods. *Comput. Phys. Rep.* **1987**, *6*, 243–274.
(227) Hohenester, U.; Trügler, A. MNPBEM-A Matlab Toolbox for the Simulation of Plasmonic Nanoparticles. *Comput. Phys. Commun.* **2012**, *183*, 370–381.

(228) Waxenegger, J.; Trügler, A.; Hohenester, U. Plasmonics Simulations with the MNPBEM Toolbox: Consideration of Substrates and Layer Structures. *Comput. Phys. Commun.* **2015**, *193*, 138–150.
(229) Raychaudhuri, S. Introduction to Monte Carlo Simulation. In *2008 Winter Simulation Conference*; IEEE: Miami, FL, USA, 2008; pp 91–100.
(230) Filion, L.; Marechal, M.; van Oorschot, B.; Pelt, D.; Smallenburg, F.; Dijkstra, M. Efficient Method for Predicting Crystal Structures at Finite Temperature: Variable Box Shape Simulations. *Phys. Rev. Lett.* **2009**, *103*, 188302.
(231) Tebbe, M.; Kuttner, C.; Mayer, M.; Maennel, M.; Pazos-Perez, N.; König, T. A. F.; Fery, A. Silver-Overgrowth-Induced Changes in Intrinsic Optical Properties of Gold Nanorods: From Noninvasive Monitoring of Growth Kinetics to Tailoring Internal Mirror Charges. *J. Phys. Chem. C* **2015**, *119*, 9513–9523.
(232) Ma, Y.; Li, W.; Cho, E. C.; Li, Z.; Yu, T.; Zeng, J.; Xie, Z.; Xia, Y. Au@Ag Core-Shell Nanocubes with Finely Tuned and Well-Controlled Sizes, Shell Thicknesses, and Optical Properties. *ACS Nano* **2010**, *4*, 6725–6734.
(233) Okuno, Y.; Nishioka, K.; Kiya, A.; Nakashima, N.; Ishibashi, A.; Niidome, Y. Uniform and Controllable Preparation of Au-Ag Core-Shell Nanorods Using Anisotropic Silver Shell Formation on Gold Nanorods. *Nanoscale* **2010**, *2*, 1489–1493.
(234) Bentrup, U. Combining in Situ Characterization Methods in One Set-up: Looking with More Eyes into the Intricate Chemistry of the Synthesis and Working of Heterogeneous Catalysts. *Chem. Soc. Rev.* **2010**, *39*, 4718–4730.
(235) Sciortino, L.; Giannici, F.; Martorana, A.; Ruggirello, A. M.; Liveri, V. T.; Portale, G.; Casaletto, M. P.; Longo, A. Structural Characterization of Surfactant-Coated Bimetallic Cobalt/Nickel Nanoclusters by XPS, EXAFS, WAXS, and SAXS. *J. Phys. Chem. C* **2011**, *115*, 6360–6366.
(236) Lehoux, A.; Ramos, L.; Beaunier, P.; Uribe, D. B.; Dieudonné, P.; Audonnet, F.; Etcheberry, A.; José-Yacaman, M.; Remita, H. Tuning the Porosity of Bimetallic Nanostructures by a Soft Templating Approach. *Adv. Funct. Mater.* **2012**, *22*, 4900–4908.
(237) Garcia, P. R. A. F.; Prymak, O.; Grasmik, V.; Pappert, K.; Wlysses, W.; Otubo, L.; Epple, M.; Oliveira, C. L. P. An in Situ SAXS Investigation of the Formation of Silver Nanoparticles and Bimetallic Silver-Gold Nanoparticles in Controlled Wet-Chemical Reduction Synthesis. *Nanoscale Adv.* **2020**, *2*, 225–238.
(238) Alayoglu, S.; Zavalij, P.; Eichhorn, B.; Wang, Q.; Frenkel, A. I.; Chupas, P. Structural and Architectural Evaluation of Bimetallic Nanoparticles: A Case Study of Pt-Ru Core-Shell and Alloy Nanoparticles. *ACS Nano* **2009**, *3*, 3127–3137.
(239) Steiner, A. M.; Mayer, M.; Schletz, D.; Wolf, D.; Formanek, P.; Hübner, R.; Dulle, M.; Förster, S.; Koenig, T. A. F.; Fery, A. Silver Particles with Rhombicuboctahedral Shape and Effectively Isotropic Interactions with Light. *Chem. Mater.* **2019**, *31*, 2822–2827.
(240) Polte, J. Fundamental Growth Principles of Colloidal Metal Nanoparticles – a New Perspective. *CrystEngComm* **2015**, *17*, 6809–6830.
(241) Gilroy, K. D.; Ruditskiy, A.; Peng, H.-C.; Qin, D.; Xia, Y. Bimetallic Nanocrystals: Syntheses, Properties, and Applications. *Chem. Rev.* **2016**, *116*, 10414–10472.

(242) Huo, D.; Kim, M. J.; Lyu, Z.; Shi, Y.; Wiley, B. J.; Xia, Y. One-Dimensional Metal Nanostructures: From Colloidal Syntheses to Applications. *Chem. Rev.* **2019**, *119*, 8972–9073.
(243) Abécassis, B.; Testard, F.; Spalla, O.; Barboux, P. Probing in Situ the Nucleation and Growth of Gold Nanoparticles by Small-Angle X-Ray Scattering. *Nano Lett.* **2007**, *7*, 1723–1727.
(244) Polte, J.; Ahner, T. T.; Delissen, F.; Sokolov, S.; Emmerling, F.; Thünemann, A. F.; Kraehnert, R. Mechanism of Gold Nanoparticle Formation in the Classical Citrate Synthesis Method Derived from Coupled In Situ XANES and SAXS Evaluation. *J. Am. Chem. Soc.* **2010**, *132*, 1296–1301.
(245) Ranasinghe, J. C.; Dikkumbura, A. S.; Hamal, P.; Chen, M.; Khoury, R. A.; Smith, H. T.; Lopata, K.; Haber, L. H. Monitoring the Growth Dynamics of Colloidal Gold-Silver Core-Shell Nanoparticles Using *in Situ* Second Harmonic Generation and Extinction Spectroscopy. *J. Chem. Phys.* **2019**, *151*, 224701.
(246) de Jonge, N.; Ross, F. M. Electron Microscopy of Specimens in Liquid. *Nature Nanotech.* **2011**, *6*, 695–704.
(247) Ross, F. M. Opportunities and Challenges in Liquid Cell Electron Microscopy. *Science* **2015**, *350*, aaa9886-1.
(248) Ahmad, N.; Wang, G.; Nelayah, J.; Ricolleau, C.; Alloyeau, D. Exploring the Formation of Symmetric Gold Nanostars by Liquid-Cell Transmission Electron Microscopy. *Nano Lett.* **2017**, *17*, 4194–4201.
(249) Ahmad, N.; Le Bouar, Y.; Ricolleau, C.; Alloyeau, D. Growth of Dendritic Nanostructures by Liquid-Cell Transmission Electron Microscopy: A Reflection of the Electron-Irradiation History. *Adv. Struct. Chem. Imag.* **2016**, *2*, 9:1-10.
(250) Woehl, T. J.; Evans, J. E.; Arslan, I.; Ristenpart, W. D.; Browning, N. D. Direct *in Situ* Determination of the Mechanisms Controlling Nanoparticle Nucleation and Growth. *ACS Nano* **2012**, *6*, 8599–8610.
(251) Ahmad, N.; Wang, G.; Nelayah, J.; Ricolleau, C.; Alloyeau, D. Driving Reversible Redox Reactions at Solid-Liquid Interfaces with the Electron Beam of a Transmission Electron Microscope. *J. Microsc.* **2018**, *269*, 127–133.
(252) Sutter, E.; Jungjohann, K.; Bliznakov, S.; Stach, E. A.; Courty, A.; Wong, S.; Lewis, C.; Sutter, P. In-Situ Liquid Cell Electron Microscopy of the Solution Growth of Core-Shell Nanostructures. *Microsc. Microanal.* **2014**, *20*, 1504–1505.
(253) Liao, H.-G.; Niu, K.; Zheng, H. Observation of Growth of Metal Nanoparticles. *Chem. Commun.* **2013**, *49*, 11720–11727.
(254) Tan, S. F.; Chee, S. W.; Lin, G.; Bosman, M.; Lin, M.; Mirsaidov, U.; Nijhuis, C. A. Real-Time Imaging of the Formation of Au-Ag Core-Shell Nanoparticles. *J. Am. Chem. Soc.* **2016**, *138*, 5190–5193.
(255) Wu, J.; Gao, W.; Wen, J.; Miller, D. J.; Lu, P.; Zuo, J.-M.; Yang, H. Growth of Au on Pt Icosahedral Nanoparticles Revealed by Low-Dose In Situ TEM. *Nano Lett.* **2015**, *15*, 2711–2715.
(256) Murphy, C. J.; Gole, A. M.; Hunyadi, S. E.; Stone, J. W.; Sisco, P. N.; Alkilany, A.; Kinard, B. E.; Hankins, P. Chemical Sensing and Imaging with Metallic Nanorods. *Chem. Commun.* **2008**, 544–557.
(257) Amendola, V.; Meneghetti, M. Size Evaluation of Gold Nanoparticles by UV-Vis Spectroscopy. *J. Phys. Chem. C* **2009**, *113*, 4277–4285.
(258) Slyusarenko, K.; Abécassis, B.; Davidson, P.; Constantin, D. Morphology of Gold Nanoparticles Determined by Full-Curve Fitting of the Light Absorption

Spectrum. Comparison with X-Ray Scattering and Electron Microscopy Data. *Nanoscale* **2014**, *6*, 13527–13534.
(259) Haiss, W.; Thanh, N. T. K.; Aveyard, J.; Fernig, D. G. Determination of Size and Concentration of Gold Nanoparticles from UV-Vis Spectra. *Anal. Chem.* **2007**, *79*, 4215–4221.
(260) Henkel, A.; Schubert, O.; Plech, A.; Sönnichsen, C. Growth Kinetic of a Rod-Shaped Metal Nanocrystal. *J. Phys. Chem. C* **2009**, *113*, 10390–10394.
(261) Avrami, M. Kinetics of Phase Change. I General Theory. *J. Chem. Phys.* **1939**, *7*, 1103–1112.
(262) Hutzler, A.; Schmutzler, T.; Jank, M. P. M.; Branscheid, R.; Unruh, T.; Spiecker, E.; Frey, L. Unravelling the Mechanisms of Gold-Silver Core-Shell Nanostructure Formation by in Situ TEM Using an Advanced Liquid Cell Design. *Nano Lett.* **2018**, *18*, 7222–7229.
(263) Lohse, S. E.; Burrows, N. D.; Scarabelli, L.; Liz-Marzán, L. M.; Murphy, C. J. Anisotropic Noble Metal Nanocrystal Growth: The Role of Halides. *Chem. Mater.* **2014**, *26*, 34–43.
(264) Mehtala, J. G.; Zemlyanov, D. Y.; Max, J. P.; Kadasala, N.; Zhao, S.; Wei, A. Citrate-Stabilized Gold Nanorods. *Langmuir* **2014**, *30*, 13727–13730.
(265) Vigderman, L.; Zubarev, E. R. High-Yield Synthesis of Gold Nanorods with Longitudinal SPR Peak Greater than 1200 Nm Using Hydroquinone as a Reducing Agent. *Chem. Mater.* **2013**, *25*, 1450–1457.
(266) Zhu, X.; Zhuo, X.; Li, Q.; Yang, Z.; Wang, J. Gold Nanobipyramid-Supported Silver Nanostructures with Narrow Plasmon Linewidths and Improved Chemical Stability. *Adv. Funct. Mater.* **2016**, *26*, 341–352.
(267) Lu, G.; Keersmaecker, H. D.; Su, L.; Kenens, B.; Rocha, S.; Fron, E.; Chen, C.; Uji-i, H. Live-Cell SERS Endoscopy Using Plasmonic Nanowire Waveguides. *Adv. Mater.* **2014**, *26*, 5124–5128.
(268) Lim, B.; Jiang, M.; Tao, J.; Camargo, P. H. C.; Zhu, Y.; Xia, Y. Shape-Controlled Synthesis of Pd Nanocrystals in Aqueous Solutions. *Adv. Funct. Mater.* **2009**, *19*, 189–200.
(269) Lim, B.; Kobayashi, H.; Yu, T.; Wang, J.; Kim, M. J.; Li, Z.-Y.; Rycenga, M.; Xia, Y. Synthesis of Pd-Au Bimetallic Nanocrystals via Controlled Overgrowth. *J. Am. Chem. Soc.* **2010**, *132*, 2506–2507.
(270) Al-Saidi, W. A.; Feng, H.; Fichthorn, K. A. Adsorption of Polyvinylpyrrolidone on Ag Surfaces: Insight into a Structure-Directing Agent. *Nano Lett.* **2012**, *12*, 997–1001.
(271) Marks, L. D. Experimental Studies of Small Particle Structures. *Rep. Prog. Phys.* **1994**, *57*, 603–649.
(272) Nehl, C. L.; Liao, H.; Hafner, J. H. Optical Properties of Star-Shaped Gold Nanoparticles. *Nano Lett.* **2006**, *6*, 683–688.
(273) Gennaro, S. D.; Rahmani, M.; Giannini, V.; Aouani, H.; Sidiropoulos, T. P. H.; Navarro-Cía, M.; Maier, S. A.; Oulton, R. F. The Interplay of Symmetry and Scattering Phase in Second Harmonic Generation from Gold Nanoantennas. *Nano Lett.* **2016**, *16*, 5278–5285.
(274) Pantazis, P.; Maloney, J.; Wu, D.; Fraser, S. E. Second Harmonic Generating (SHG) Nanoprobes for in Vivo Imaging. *Proc. Natl. Acad. Sci. USA* **2010**, *107*, 14535–14540.
(275) Malkinson, G.; Mahou, P.; Chaudan, É.; Gacoin, T.; Sonay, A. Y.; Pantazis, P.; Beaurepaire, E.; Supatto, W. Fast *In Vivo* Imaging of SHG Nanoprobes with Multiphoton Light-Sheet Microscopy. *ACS Photonics* **2020**, *7*, 1036–1049.

(276) Slaughter, L. S.; Willingham, B. A.; Chang, W.-S.; Chester, M. H.; Ogden, N.; Link, S. Toward Plasmonic Polymers. *Nano Lett.* **2012**, *12*, 3967–3972.
(277) Klinkova, A.; Thérien-Aubin, H.; Ahmed, A.; Nykypanchuk, D.; Choueiri, R. M.; Gagnon, B.; Muntyanu, A.; Gang, O.; Walker, G. C.; Kumacheva, E. Structural and Optical Properties of Self-Assembled Chains of Plasmonic Nanocubes. *Nano Lett.* **2014**, *14*, 6314–6321.
(278) Citrin, D. S. Plasmon Polaritons in Finite-Length Metal-Nanoparticle Chains: The Role of Chain Length Unravelled. *Nano Lett.* **2005**, *5*, 985–989.
(279) Barrow, S. J.; Funston, A. M.; Gómez, D. E.; Davis, T. J.; Mulvaney, P. Surface Plasmon Resonances in Strongly Coupled Gold Nanosphere Chains from Monomer to Hexamer. *Nano Lett.* **2011**, *11*, 4180–4187.
(280) Xi, C.; Marina, P. F.; Xia, H.; Wang, D. Directed Self-Assembly of Gold Nanoparticles into Plasmonic Chains. *Soft Matter* **2015**, *11*, 4562–4571.
(281) Taylor, R. W.; Lee, T.-C.; Scherman, O. A.; Esteban, R.; Aizpurua, J.; Huang, F. M.; Baumberg, J. J.; Mahajan, S. Precise Subnanometer Plasmonic Junctions for SERS within Gold Nanoparticle Assemblies Using Cucurbit[*n*]Uril "Glue." *ACS Nano* **2011**, *5*, 3878–3887.
(282) Caswell, K. K.; Wilson, J. N.; Bunz, U. H. F.; Murphy, C. J. Preferential End-to-End Assembly of Gold Nanorods by Biotin-Streptavidin Connectors. *J. Am. Chem. Soc.* **2003**, *125*, 13914–13915.
(283) Lin, S.; Li, M.; Dujardin, E.; Girard, C.; Mann, S. One-Dimensional Plasmon Coupling by Facile Self-Assembly of Gold Nanoparticles into Branched Chain Networks. *Adv. Mater.* **2005**, *17*, 2553–2559.
(284) Hamon, C.; Bizien, T.; Artzner, F.; Even-Hernandez, P.; Marchi, V. Replacement of CTAB with Peptidic Ligands at the Surface of Gold Nanorods and Their Self-Assembling Properties. *J. Colloid Interface Sci.* **2014**, *424*, 90–97.
(285) Shibu Joseph, S. T.; Ipe, B. I.; Pramod, P.; Thomas, K. G. Gold Nanorods to Nanochains: Mechanistic Investigations on Their Longitudinal Assembly Using α,ω-Alkanedithiols and Interplasmon Coupling. *J. Phys. Chem. B* **2006**, *110*, 150–157.
(286) Liu, K.; Nie, Z.; Zhao, N.; Li, W.; Rubinstein, M.; Kumacheva, E. Step-Growth Polymerization of Inorganic Nanoparticles. *Science* **2010**, *329*, 197–200.
(287) Nie, Z.; Fava, D.; Kumacheva, E.; Zou, S.; Walker, G. C.; Rubinstein, M. Self-Assembly of Metal–Polymer Analogues of Amphiphilic Triblock Copolymers. *Nat. Mater.* **2007**, *6*, 609–614.
(288) Hanske, C.; Tebbe, M.; Kuttner, C.; Bieber, V.; Tsukruk, V. V.; Chanana, M.; König, T. A. F.; Fery, A. Strongly Coupled Plasmonic Modes on Macroscopic Areas via Template-Assisted Colloidal Self-Assembly. *Nano Lett.* **2014**, *14*, 6863–6871.
(289) González-Rubio, G.; González-Izquierdo, J.; Bañares, L.; Tardajos, G.; Rivera, A.; Altantzis, T.; Bals, S.; Peña-Rodríguez, O.; Guerrero-Martínez, A.; Liz-Marzán, L. M. Femtosecond Laser-Controlled Tip-to-Tip Assembly and Welding of Gold Nanorods. *Nano Lett.* **2015**, *15*, 8282–8288.
(290) Herrmann, L. O.; Valev, V. K.; Tserkezis, C.; Barnard, J. S.; Kasera, S.; Scherman, O. A.; Aizpurua, J.; Baumberg, J. J. Threading Plasmonic Nanoparticle Strings with Light. *Nat. Commun.* **2014**, *5*, 4568.
(291) Fontana, J.; Charipar, N.; Flom, S. R.; Naciri, J.; Piqué, A.; Ratna, B. R. Rise of the Charge Transfer Plasmon: Programmable Concatenation of Conductively Linked Gold Nanorod Dimers. *ACS Photonics* **2016**, *3*, 904–911.

(292) Klinkova, A.; Therien-Aubin, H.; Choueiri, R. M.; Rubinstein, M.; Kumacheva, E. Colloidal Analogs of Molecular Chain Stoppers. *Proc. Natl. Acad. Sci. USA* **2013**, *110*, 18775–18779.
(293) Stewart, A. F.; Lee, A.; Ahmed, A.; Ip, S.; Kumacheva, E.; Walker, G. C. Rational Design for the Controlled Aggregation of Gold Nanorods *via* Phospholipid Encapsulation for Enhanced Raman Scattering. *ACS Nano* **2014**, *8*, 5462–5467.
(294) Stewart, A. F.; Gagnon, B. P.; Walker, G. C. Forming End-to-End Oligomers of Gold Nanorods Using Porphyrins and Phthalocyanines. *Langmuir* **2015**, *31*, 6902–6908.
(295) Yang, M.; Chen, G.; Zhao, Y.; Silber, G.; Wang, Y.; Xing, S.; Han, Y.; Chen, H. Mechanistic Investigation into the Spontaneous Linear Assembly of Gold Nanospheres. *Phys. Chem. Chem. Phys.* **2010**, *12*, 11850–11860.
(296) Han, X.; Goebl, J.; Lu, Z.; Yin, Y. Role of Salt in the Spontaneous Assembly of Charged Gold Nanoparticles in Ethanol. *Langmuir* **2011**, *27*, 5282–5289.
(297) Schuller, J. A.; Barnard, E. S.; Cai, W.; Jun, Y. C.; White, J. S.; Brongersma, M. L. Plasmonics for Extreme Light Concentration and Manipulation. *Nat. Mater.* **2010**, *9*, 193–204.
(298) Zhu, W.; Esteban, R.; Borisov, A. G.; Baumberg, J. J.; Nordlander, P.; Lezec, H. J.; Aizpurua, J.; Crozier, K. B. Quantum Mechanical Effects in Plasmonic Structures with Subnanometre Gaps. *Nat. Commun.* **2016**, *7*, 11495.
(299) Pérez-González, O.; Zabala, N.; Borisov, A. G.; Halas, N. J.; Nordlander, P.; Aizpurua, J. Optical Spectroscopy of Conductive Junctions in Plasmonic Cavities. *Nano Lett.* **2010**, *10*, 3090–3095.
(300) Teulle, A.; Bosman, M.; Girard, C.; Gurunatha, K. L.; Li, M.; Mann, S.; Dujardin, E. Multimodal Plasmonics in Fused Colloidal Networks. *Nat. Mater.* **2015**, *14*, 87–94.
(301) Fang, L.; Wang, Y.; Liu, M.; Gong, M.; Xu, A.; Deng, Z. Dry Sintering Meets Wet Silver-Ion "Soldering": Charge-Transfer Plasmon Engineering of Solution-Assembled Gold Nanodimers From Visible to Near-Infrared I and II Regions. *Angew. Chem. Int. Ed.* **2016**, *55*, 14296–14300.
(302) Lee, J.-H.; You, M.-H.; Kim, G.-H.; Nam, J.-M. Plasmonic Nanosnowmen with a Conductive Junction as Highly Tunable Nanoantenna Structures and Sensitive, Quantitative and Multiplexable Surface-Enhanced Raman Scattering Probes. *Nano Lett.* **2014**, *14*, 6217–6225.
(303) Shao, L.; Woo, K. C.; Chen, H.; Jin, Z.; Wang, J.; Lin, H.-Q. Angle-and Energy-Resolved Plasmon Coupling in Gold Nanorod Dimers. *ACS Nano* **2010**, *4*, 3053–3062.
(304) Janicek, B. E.; Hinman, J. G.; Hinman, J. J.; hyun Bae, S.; Wu, M.; Turner, J.; Chang, H.-H.; Park, E.; Lawless, R.; Suslick, K. S.; Murphy, C. J.; Huang, P. Y. Quantitative Imaging of Organic Ligand Density on Anisotropic Inorganic Nanocrystals. *Nano Lett.* **2019**, *19*, 6308–6314.
(305) Liu, K.; Ahmed, A.; Chung, S.; Sugikawa, K.; Wu, G.; Nie, Z.; Gordon, R.; Kumacheva, E. *In Situ*Plasmonic Counter for Polymerization of Chains of Gold Nanorods in Solution. *ACS Nano* **2013**, *7*, 5901–5910.
(306) Gesztelyi, R.; Zsuga, J.; Kemeny-Beke, A.; Varga, B.; Juhasz, B.; Tosaki, A. The Hill Equation and the Origin of Quantitative Pharmacology. *Arch. Hist. Exact Sci* . **2012**, *66*, 427–438.

(307) Kékicheff, P.; Contal, C. Cationic-Surfactant-Coated Mica Surfaces below the Critical Micellar Concentration: 1. Patchy Structures As Revealed by Peak Force Tapping AFM Mode. *Langmuir* **2019**, *35*, 3087–3107.
(308) Li, Z.; Wang, W.; Yin, Y. Colloidal Assembly and Active Tuning of Coupled Plasmonic Nanospheres. *Trends Chem.* **2020**, *2*, 593–608.
(309) Odian, G. G. *Principles of Polymerization*, 4th ed.; Wiley-Interscience: Hoboken, N.J, 2004.
(310) Langhammer, C.; Yuan, Z.; Zorić, I.; Kasemo, B. Plasmonic Properties of Supported Pt and Pd Nanostructures. *Nano Lett.* **2006**, *6*, 833–838.
(311) Dacosta Fernandes, B.; Spuch-Calvar, M.; Baida, H.; Tréguer-Delapierre, M.; Oberlé, J.; Langot, P.; Burgin, J. Acoustic Vibrations of Au Nano-Bipyramids and Their Modification under Ag Deposition: A Perspective for the Development of Nanobalances. *ACS Nano* **2013**, *7*, 7630–7639.
(312) Besteiro, L. V.; Kong, X.-T.; Wang, Z.; Hartland, G.; Govorov, A. O. Understanding Hot-Electron Generation and Plasmon Relaxation in Metal Nanocrystals: Quantum and Classical Mechanisms. *ACS Photonics* **2017**, *4*, 2759–2781.
(313) Quan, Z.; Fang, J. Superlattices with Non-Spherical Building Blocks. *Nano Today* **2010**, *5*, 390–411.
(314) Damasceno, P. F.; Engel, M.; Glotzer, S. C. Predictive Self-Assembly of Polyhedra into Complex Structures. *Science* **2012**, *337*, 453–457.
(315) Torquato, S.; Jiao, Y. Dense Packings of the Platonic and Archimedean Solids. *Nature* **2009**, *460*, 876–879.
(316) Liao, C.-W.; Lin, Y.-S.; Chanda, K.; Song, Y.-F.; Huang, M. H. Formation of Diverse Supercrystals from Self-Assembly of a Variety of Polyhedral Gold Nanocrystals. *J. Am. Chem. Soc.* **2013**, *135*, 2684–2693.
(317) Meijer, J.-M.; Pal, A.; Ouhajji, S.; Lekkerkerker, H. N. W.; Philipse, A. P.; Petukhov, A. V. Observation of Solid-Solid Transitions in 3D Crystals of Colloidal Superballs. *Nat. Commun.* **2017**, *8*, 14352.
(318) Huang, M. H.; Thoka, S. Formation of Supercrystals through Self-Assembly of Polyhedral Nanocrystals. *Nano Today* **2015**, *10*, 81–92.
(319) Onsager, L. The Effects of Shape on the Interaction of Colloidal Particles. *Ann. N. Y. Acad. Sci.* **1949**, *51*, 627–659.
(320) Zong, C. Packing, Covering and Tiling in Two-Dimensional Spaces. *Expo. Math.* **2014**, *32*, 297–364.
(321) Kepler, J.; Aiton, E. J.; Duncan, A. M.; Field, J. V. *The Harmony of the World*; American Philosophical Society: Philadelphia, Pa., 1997.
(322) Rao, M. Exhaustive Search of Convex Pentagons Which Tile the Plane. *Cornell University* **2017**.
(323) Schattschneider, D. Tiling the Plane with Congruent Pentagons. *Math. Mag.* **1978**, *51*, 29–44.
(324) Sadoc, J.-F.; Mosseri, R. *Geometrical Frustration*; Cambridge, UK: Cambridge University Press, 1999.
(325) Hales, T.; Kusner, W. Packings of Regular Pentagons in the Plane. **2016**.
(326) Henley, C. L. Sphere Packings and Local Environments in Penrose Tilings. *Phys. Rev. B* **1986**, *34*, 797–816.
(327) Daniel, S. D. *A Grammar of Chinese Lattice*; Harvard University Press, Cambridge, Mass. 2.
(328) Kuperberg, G.; Kuperberg, W. Double-Lattice Packings of Convex Bodies in the Plane. *Discrete. Comput. Geom.* **1990**, *5*, 389–397.

(329) Schilling, T.; Pronk, S.; Mulder, B.; Frenkel, D. Monte Carlo Study of Hard Pentagons. *Phys. Rev. E* **2005**, *71*, 036138.
(330) Winckelmans, N.; Altantzis, T.; Grzelczak, M.; Sánchez-Iglesias, A.; Liz-Marzán, L. M.; Bals, S. Multimode Electron Tomography as a Tool to Characterize the Internal Structure and Morphology of Gold Nanoparticles. *J. Phys. Chem. C* **2018**, *122*, 13522–13528.
(331) Liu, M.; Guyot-Sionnest, P. Mechanism of Silver(I)-Assisted Growth of Gold Nanorods and Bipyramids. *J. Phys. Chem. B* **2005**, *109*, 22192–22200.
(332) Chateau, D.; Liotta, A.; Vadcard, F.; Navarro, J. R. G.; Chaput, F.; Lermé, J.; Lerouge, F.; Parola, S. From Gold Nanobipyramids to Nanojavelins for a Precise Tuning of the Plasmon Resonance to the Infrared Wavelengths: Experimental and Theoretical Aspects. *Nanoscale* **2015**, *7*, 1934–1943.
(333) Donev, A.; Stillinger, F. H.; Chaikin, P. M.; Torquato, S. Unusually Dense Crystal Packings of Ellipsoids. *Phys. Rev. Lett.* **2004**, *92*, 255506.
(334) Trovato, A.; Hoang, T. X.; Banavar, J. R.; Maritan, A. Symmetry, Shape, and Order. *Proc. Natl. Acad. Sci. U.S.A.* **2007**, *104*, 19187–19192.
(335) Haji-Akbari, A.; Engel, M.; Glotzer, S. C. Degenerate Quasicrystal of Hard Triangular Bipyramids. *Phys. Rev. Lett.* **2011**, *107*, 215702.
(336) Haji-Akbari, A.; Chen, E. R.; Engel, M.; Glotzer, S. C. Packing and Self-Assembly of Truncated Triangular Bipyramids. *Phys. Rev. E* **2013**, *88*, 012127.
(337) Solomon, M. J.; Boger, D. V. The Rheology of Aqueous Dispersions of Spindle-Type Colloidal Hematite Rods. *J. Rheol.* **1998**, *42*, 929–949.
(338) Li, S.; Wang, L.; Liu, B. Fabrication of Magnetic Colloidal Bicones and Their Switchable Self-Assembly. *Soft Matter* **2020**, *16*, 8024–8032.
(339) Roller, J.; Laganapan, A.; Meijer, J.-M.; Fuchs, M.; Zumbusch, A. Observation of Liquid Glass in Suspensions of Ellipsoidal Colloids. *Proc. Natl. Acad. Sci. USA* **2021**, *118*, e2018072118.
(340) O'Brien, M. N.; Jones, M. R.; Mirkin, C. A. The Nature and Implications of Uniformity in the Hierarchical Organization of Nanomaterials. *Proc. Natl. Acad. Sci. USA* **2016**, *113*, 11717–11725.
(341) Hamon, C.; Sanz-Ortiz, M. N.; Modin, E.; Hill, E. H.; Scarabelli, L.; Chuvilin, A.; Liz-Marzán, L. M. Hierarchical Organization and Molecular Diffusion in Gold Nanorod/Silica Supercrystal Nanocomposites. *Nanoscale* **2016**, *8*, 7914–7922.
(342) Van der Hoeven, J. E. S.; Van der Wee, E. B.; De Winter, D. A. M.; Hermes, M.; Liu, Y.; Fokkema, J.; Bransen, M.; van Huis, M. A.; Gerritsen, H. C.; de Jongh, P. E.; van Blaaderen, A. Bridging the Gap: 3D Real-Space Characterization of Colloidal Assemblies *via* FIB-SEM Tomography. *Nanoscale* **2019**, *11*, 5304–5316.
(343) De Graaf, J.; Filion, L.; Marechal, M.; van Roij, R.; Dijkstra, M. Crystal-Structure Prediction via the FloppyBox Monte Carlo Algorithm: Method and Application to Hard (Non)Convex Particles. *J. Chem. Phys.* **2012**, *137*, 214101-1–11.
(344) Gómez-Graña, S.; Hubert, F.; Testard, F.; Guerrero-Martínez, A.; Grillo, I.; Liz-Marzán, L. M.; Spalla, O. Surfactant (Bi)Layers on Gold Nanorods. *Langmuir* **2012**, *28*, 1453–1459.
(345) Donald, E. S. Introduction to Crystallography, (Dover Publications, 2012) (accessed Feb 17, 2022).

(346) Dshemuchadse, J. Soft Matter Crystallography-Complex, Diverse, and New Crystal Structures in Condensed Materials on the Mesoscale. *J. Appl. Phys.* **2022**, *131*, 020901-1–14.
(347) Langer, J.; Jimenez de Aberasturi, D.; Aizpurua, J.; Alvarez-Puebla, R. A.; Auguié, B.; Baumberg, J. J.; Bazan, G. C.; Bell, S. E. J.; Boisen, A.; Brolo, A. G.; Choo, J.; Cialla-May, D.; Deckert, V.; Fabris, L.; Faulds, K.; García de Abajo, F. J.; Goodacre, R.; Graham, D.; Haes, A. J.; Haynes, C. L.; Huck, C.; Itoh, T.; Käll, M.; Kneipp, J.; Kotov, N. A.; Kuang, H.; Le Ru, E. C.; Lee, H. K.; Li, J.-F.; Ling, X. Y.; Maier, S. A.; Mayerhöfer, T.; Moskovits, M.; Murakoshi, K.; Nam, J.-M.; Nie, S.; Ozaki, Y.; Pastoriza-Santos, I.; Perez-Juste, J.; Popp, J.; Pucci, A.; Reich, S.; Ren, B.; Schatz, G. C.; Shegai, T.; Schlücker, S.; Tay, L.-L.; Thomas, K. G.; Tian, Z.-Q.; Van Duyne, R. P.; Vo-Dinh, T.; Wang, Y.; Willets, K. A.; Xu, C.; Xu, H.; Xu, Y.; Yamamoto, Y. S.; Zhao, B.; Liz-Marzán, L. M. Present and Future of Surface-Enhanced Raman Scattering. *ACS Nano* **2020**, *14* (1), 28–117.
(348) Atkins, P. W.; De Paula, J.; Atkins, P. W. *Physical Chemistry*; New York, 2006.
(349) Press, W. H.; Teukolsky, S. A.; Vetterling, W. T.; Flannery, B. P. *Numerical Recipes in C: The Art of Scientific Computing*, 3rd ed.; Cambridge University Press: Cambridge; New York, 2007.
(350) Cohen, M. D.; Fischer, E. 588. Isosbestic Points. *J. Chem. Soc.* **1962**, 3044–3052.

Publication list

I. **Lyu, J.**; Geertsen, V.; Hamon, C.; Constantin, D. Determining the Morphology and Concentration of Core–Shell Au/Ag Nanoparticles. *Nanoscale Adv.* **2020**, *2* (10), 4522–4528. https://doi.org/10.1039/D0NA00629G.

II. **Lyu, J.**; Alloyeau, D.; Hamon, C.; Constantin, D. Two-Step Assembly Kinetics of Gold Nanoparticles. *J. Mater. Chem. C* **2021**, *9* (5), 1730–1739. https://doi.org/10.1039/D0TC05076H.

III. **Lyu, J**.; Chaâbani, W.; Modin, E.; Chuvilin, A.; Bizien, T.; Smallenburg, F.; Impéror-Clerc, M.; Constantin, D.; Hamon, C. Double-Lattice Packing of Pentagonal Gold Bipyramids in Supercrystals with Triclinic Symmetry. *Adv. Mater.* **2022**, 2200883. https://doi.org/10.1002/adma.202200883.

IV. **Lyu, J**.; Rondepierre, F.; Jonin, C.; Brevet, P.-F.; Hamon, C.; Constantin, D. Shape-Controlled Second-Harmonic Scattering from Gold Nano-Tetrapods. *J. Phys. Chem. C*, **2022**, *126*, (23), 9831–9835. https://doi.org/10.1021/acs.jpcc.2c01867.

V. Li, X.; **Lyu, J.**; Goldmann, C.; Kociak, M.; Constantin, D.; Hamon, C. Plasmonic Oligomers with Tunable Conductive Nanojunctions. *J. Phys. Chem. Lett.* **2019**, *10* (22), 7093–7099. https://doi.org/10.1021/acs.jpclett.9b03185.

VI. Aliyah, K.; **Lyu, J.**; Goldmann, C.; Bizien, T.; Hamon, C.; Alloyeau, D.; Constantin, D. Real-Time *In Situ* Observations Reveal a Double Role for Ascorbic Acid in the Anisotropic Growth of Silver on Gold. *J. Phys. Chem. Lett.* **2020**, 2830–2837. https://doi.org/10.1021/acs.jpclett.0c00121.

VII. **Lyu, J**.; Alloyeau, D.; Matthews, L.; Zinn, T.; Hamon, C.; Constantin, D. Reshaping Kinetics of Nano-Tetrapods. In preparation.